Improved Glacial Isostatic Adjustment Models for Northern Canada

by

Karen Simon
B.Sc., University of Victoria, 2004
M.Sc., Dalhousie University, 2007

A Dissertation Submitted in Partial Fulfillment of the
Requirements for the Degree of

DOCTOR OF PHILOSOPHY

in the School of Earth and Ocean Sciences

Improved Glacial Isostatic Adjustment Models for Northern Canada

by

Karen Simon
B.Sc., University of Victoria, 2004
M.Sc., Dalhousie University, 2007

Supervisory Committee

Dr. Thomas James, Supervisor
(School of Earth and Ocean Sciences)

Dr. George Spence, Co-supervisor
(School of Earth and Ocean Sciences)

Dr. Roy Hyndman, Departmental Member
(School of Earth and Ocean Sciences)

Dr. Kelin Wang, Departmental Member
(School of Earth and Ocean Sciences)

Dr. Dan Smith, Outside Member
(Department of Geography)

Supervisory Committee

Dr. Thomas James, Supervisor
(School of Earth and Ocean Sciences)

Dr. George Spence, Co-supervisor
(School of Earth and Ocean Sciences)

Dr. Roy Hyndman, Departmental Member
(School of Earth and Ocean Sciences)

Dr. Kelin Wang, Departmental Member
(School of Earth and Ocean Sciences)

Dr. Dan Smith, Outside Member
(Department of Geography)

ABSTRACT

In northern Canada, the glacial isostatic adjustment (GIA) response of the Earth to the former Pleistocene Laurentide and Innuitian ice sheets contributes significantly to the Earth's past and ongoing sea-level change and land deformation. In this dissertation, measurements of Holocene sea-level change and observations of GPS-measured vertical crustal uplift rates are employed as constraints in numerical GIA models that examine the thickness and volume history of the former ice sheets in northern North America. The study is divided into two main sections; the first provides new measurements of Holocene sea-level change collected west of Hudson Bay, while the second presents a GIA modelling analysis for the entire study area of northern Canada.

Radiocarbon dating of post-glacial deposits collected in an area just west of central Hudson Bay provides several new constraints on regional Holocene sea-level change. The field collection area is near a former load centre of the Laurentide Ice Sheet (LIS), and the sea-level measurements suggest that following deglaciation, regional sea level fell rapidly from a high-stand of nearly 170 m elevation just after 8000 cal yr BP to 60 m elevation by ∼5200 cal yr BP. Sea level subsequently fell at a decreased rate (approximately 30 m since 3000 cal yr BP).

The fit of GIA model predictions to relative sea-level (RSL) data and present-day GPS-measured vertical land motion rates from throughout the study area constrains the peak thickness of the LIS to be ∼3.4-3.6 km west of Hudson Bay, and up to 4 km east of Hudson Bay. The ice model thicknesses inferred for these two regions represent, respectively, a ∼30% decrease and an average ∼20-25% increase to the load thickness relative to the ICE-5G reconstruction (Peltier 2004), generally consistent with other studies focussing on space geodetic measurements of vertical crustal motion. Around Baffin Island, the fit of GIA model predictions to RSL data indicate peak regional ice thicknesses of 1.2-1.3 km, a modest reduction compared to ICE-5G.

A new reconstruction of the Innuitian Ice Sheet (IIS), which covered the Queen Elizabeth Islands at LGM, incorporates the current glacial-geological constraints on its spatial extent and timing history. The new IIS reconstruction provides RSL predictions that are more consistent with regional observations of post-glacial sea-level change than ICE-5G. The results suggest that the peak thickness of the IIS was ∼1600 m, approximately 400 m thicker than the minimum peak thickness indicated by glacial geology studies, but between ∼1000-1500 m thinner than the peak thicknesses used in previous regional ice sheet reconstructions.

On Baffin Island and in the Queen Elizabeth Islands, however, the modelled elastic crustal response of the Earth to present-day ice mass changes is large. Accounting for this effect improves the agreement between GPS measurements of vertical crustal motion and the GIA model predictions. However, improvements such as the inclusion of spatially non-uniform mass loss and a sensitivity analysis that examines uncertainties of this effect should be incorporated into the modelling of present-day changes to glaciers and ice caps.

Table of Contents

List of Tables

List of Figures

List of Abbreviations Used

AMS	accelerator mass spectrometry
CAA	Canadian Arctic Archipelago
cal	calibrated
CGS	Canadian Geodetic Survey
EWHC	equivalent water height change
GIA	glacial isostatic adjustment
GIC	glaciers and ice caps
GPS	Global Positioning System
GRACE	Gravity Recovery and Climate Experiment
GRIS	Greenland Ice Sheet
GSC	Geological Survey of Canada
GSD	Geodetic Survey Division
IIS	Innuitian Ice Sheet
ITRF	International Reference Frame
ka, kyr	kiloannum, kiloyears
KID	Keewatin Ice Divide
LIS	Laurentide Ice Sheet
LGM	Last Glacial Maximum
MID	M'Clintock Ice Divide
MSE	mean squared error
mwp-1a, mwp-1b	meltwater pulse 1a, meltwater pulse 1b
PDB	Pee Dee Belemnite
PPP	Precise Point Positioning
QEI	Queen Elizabeth Islands
RMS	root mean square
RSL	relative sea level
TAM	Transantarctic Mountains

ACKNOWLEDGEMENTS

Above all, I would like to thank my supervisor, Thomas James. I feel very fortunate to have worked with Tom for my PhD research; I have learned a lot from him, and I have always benefitted from his support, suggestions and encouragement. I would also like to thank all members of my supervisory committee: George Spence, Roy Hyndman, Kelin Wang, and Dan Smith. I am grateful for their support over the years, and my research project was continually improved by their comments and their wide range of knowledge on the subject matter. I also thank Glenn Milne for kindly agreeing to act as my external examiner, and for providing insightful questions and suggestions for the work.

This work has also benefitted from contributions and assistance from several collaborators. Arthur Dyke provided access to the relative sea-level database as well as valuable insight into the regional glacial history. Donald Forbes offered his significant expertise to several aspects of the sea-level fieldwork, including interpretation of the Holocene deglacial history, as well as logistical planning and execution. Significant help with the GPS data processing was kindly provided by Joe Henton. Work with Erik Ivins in the early stages of the research contributed to the development of the ocean loading methodology. Alice Telka identified and prepared collected samples of relative sea-level indicators for radiocarbon dating, and offered great insight into the interpretation of the depositional history of many samples. I also gratefully acknowledge support for this work from the ArcticNet Network of Centres of Excellence, Natural Resources Canada, and the University of Victoria.

During my PhD research, I was fortunate to be able to visit Nunavut with my supervisor to pursue the collection of new data. I would like to thank the community members of Arviat for their support during the fieldwork, especially Jerry Panegoniak and David Vetra. In addition, I thank Andrea Darlington for her assistance in the field. Numerous people assisted with various aspects relating to the GPS equipment and processing, especially Lisa Nykolaishen, Michael Schmidt, Brian Schofield, J.C. Lavergne, Phil Lamothe and Jason Silliker. I also thank Jan Bednarski and Robert Mott for their identification of the collected shell and wood samples.

I wish to sincerely thank everyone at the Pacific Geoscience Centre; it was a pleasure to study in such an excellent and friendly working environment. At the University of Victoria, I am grateful for support from the School of Earth and Ocean Sciences. In particular, I thank Allison Rose, the departmental graduate secretary,

who has always been very helpful and friendly with administrative matters. In addition, Belaid Moa from the University Systems Department has provided useful advice and assistance with the university's computing resources.

I would like to thank my friends and fellow students for their friendship and for the good times over the years. Finally, I owe my thanks to my family (Jean and David, Brian, and Bill). The work has always been made easier by their support and encouragement.

Chapter 1

Introduction

1.1 Topic of Thesis Research

During the last Pleistocene glaciation, much of the continental land masses were covered by thick ice sheets, including Greenland and northern North America and Europe in the northern hemisphere (Figure 1.1), and Patagonia and Antarctica in the southern hemisphere. On the North American continent, the Laurentide Ice Sheet covered central and western Canada and parts of the northern United States, and was confluent with the Cordilleran Ice Sheet to the west and the smaller Appalachian Ice Complex to the east. In the north, the much smaller Innuitian Ice Sheet covered the Queen Elizabeth Islands, and converged with the Laurentide Ice Sheet to the south, and the Greenland Ice Sheet to the east. In North America, the pattern of glacial flow directions suggests that the Laurentide Ice Sheet had major load centres over Keewatin (west of Hudson Bay), Quebec-Labrador (east of Hudson Bay), and in Foxe Basin (south of Baffin Island) (Dyke et al. 1982, Dyke et al. 2002).

At the last glacial maximum (LGM), $\sim$26 ka BP, globally averaged sea level was approximately 120-125 m lower than at present due to the large volume of water stored on land in the ice sheets (Fairbanks 1989, Peltier and Fairbanks 2006). In regions proximal to the ice sheets, however, the large depression of the Earth's surface generated by the weight of the ice caused local sea levels to be up to 450 m higher than at present. As deglaciation proceeded throughout the late Pleistocene and early Holocene, globally averaged sea-level rose. In regions near the diminishing ice sheets, the response of the Earth to deglaciation caused the land to uplift, and relative sea-level (RSL) fell rapidly.

This thesis focuses on the use of numerical models to predict the displacement of the Earth's surface and changes to the gravitational potential owing to surface load variations induced by the growth and ablation of ice sheets, a process known as

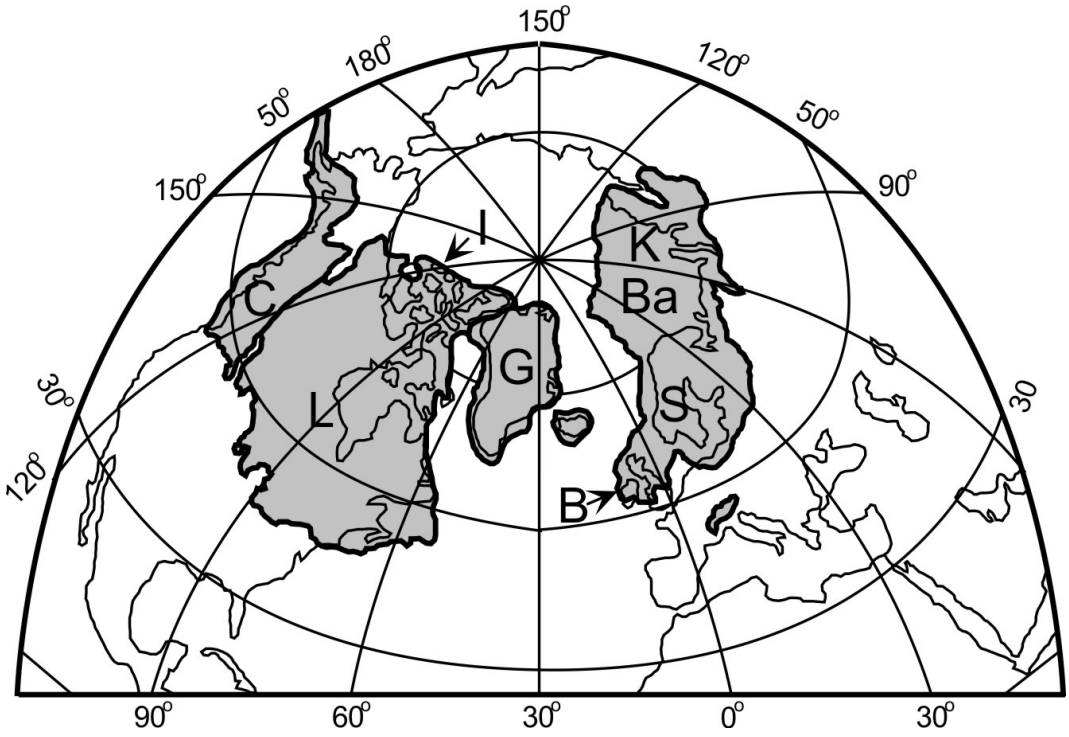

Figure 1.1: Map of maximum northern hemisphere glaciation at the last glacial maximum (LGM), with the major ice sheets labelled by letter. B-British, Ba-Barents Sea, C-Cordilleran, G-Greenland, I-Innuitian, K-Kara Sea, L-Laurentide, S-Scandinavian. Figure from Clark and Mix (2002), and based on Denton and Hughes (1981).

glacial isostatic adjustment (GIA). GIA models consist of an ice sheet history model applied as a surface load to an Earth model. GIA models of varying complexity have been developed, but modern models typically feature an Earth model with realistic, seismically-constrained, radially-varying density and elastic structure and a radially-varying viscosity structure. Ice sheet models are constrained by reconstructions of the areal extent, retreat history (typically constrained by ages from radiocarbon and other dating techniques), and inferences of former flow directions of the ice, and may also be informed by glaciological considerations of varying sophistication. Generally GIA modelling exercises seek to improve understanding of the viscosity structure of the Earth and/or the ice sheet history. The general study area for this research project is northern Canada ($\gtrsim$60° N).

An important constraint on GIA models are RSL observations because measurements of sea-level change record the combined response of the Earth to glacial unloading and the filling of the ocean basins over time. In this study, RSL data are the dominant constraint for the GIA models, although GPS-measured rates of present-

day vertical land motion, which record the Earth's ongoing GIA response, are also used as a supplementary constraint. Although there is an extensive database of RSL measurements available for much of northern Canada (Figure 1.2), RSL data from the region west of the coast of Hudson Bay (the eastern margin of the Keewatin load centre) are sparse. A key component of this project is dedicated to the collection of sea-level measurements from this region. The new RSL data complement the large existing RSL data set. RSL histories from a number of locations in northern Canada are used to constrain a GIA modelling analysis that examines variations to the ice sheet reconstruction. The remainder of this thesis project focusses on providing improved understanding of Laurentide and Innuitian ice sheet history.

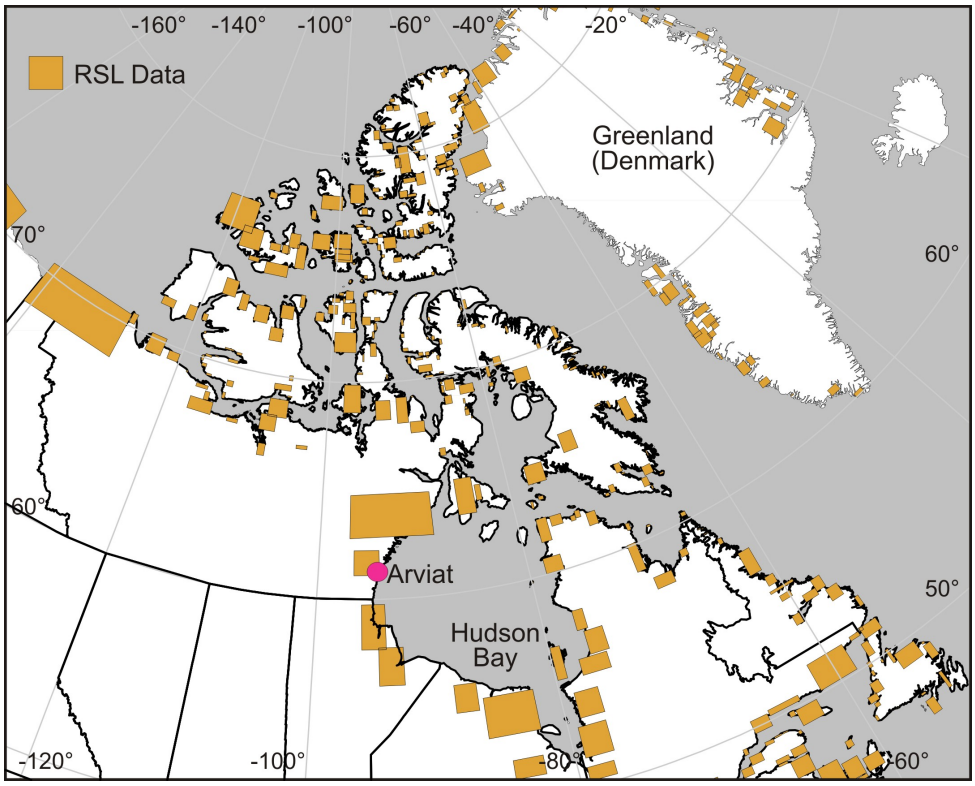

Figure 1.2: Distribution of available relative sea-level data in central and northern Canada. Each orange box shows the location for which a relative sea-level history exists; the spatial extent of each box indicates the area over which the measurements that comprise a given relative sea-level history have been compiled. The location of the community of Arviat, where new relative sea-level measurements are collected in this study, is shown by the pink circle. Database of RSL measurements provided by A. Dyke (personal communication, 2010).

1.2 Motivation

Improved forward models of the glacial isostatic adjustment process are needed to constrain better Earth properties and structure, and the spatial extent and thickness (and thence volume) of the ice sheets. Accurate volume estimates of the continental ice sheets are needed to construct the global sea-level budget from the LGM to present-day (Peltier 2009, Tamisiea 2011), the magnitude of which is approximated by records of far-field sea-level change. By performing a detailed GIA modelling analysis in northern Canada, this study contributes to understanding ice sheet history in the study area, as well as providing sector-specific estimates of North America's contribution to globally averaged sea level. Accurate prediction of GIA motions can also contribute to the understanding of continental deformation patterns and earthquake occurrence (James and Bent 1994, Argus et al. 1999, Milne et al. 2001, Mazzotti and Adams 2005, Calais et al. 2006, Tiampo et al. 2012).

The area west of Hudson Bay is one of the former load centres of the Laurentide Ice Sheet, and is thus a particularly important region for inferring ice sheet history and thickness and Earth rheology through analysis of the Earth's glacial isostatic adjustment response. Before this study, there was a paucity of relative sea-level data from the central west coast of Hudson Bay. New relative sea-level measurements collected from around the vicinity of Arviat, Nunavut (Figure 1.2), substantially improve the history of regional post-glacial sea-level change in the area. GIA modelling of the new observations places strong constraints on the history of Laurentide Ice Sheet thickness.

Improved GIA models also provide benefits and uses in a variety of related disciplines. For example, much focus has been placed on assessing the regional and global societal impact of recent changes to the Earth's cryosphere, atmosphere and oceans, including constraining the mass loss of present-day ice cover, and the prediction of future rates of sea-level change (e.g., Rahmstorf 2007, Grinsted et al. 2009, Shepherd et al. 2012, IPCC 2014). An important application of improved GIA model predictions is the correction of gravity data collected by the Gravity Recovery and Climate Experiment (GRACE) for the GIA effect. This correction allows the isolation of hydrological signals (soil moisture, river and lake levels, groundwater, and components of the cryosphere) that are of interest for a variety of applications. In regions where GPS measurements of vertical crustal motion are sparse, GIA model predictions also allow interpolation of vertical velocities. This application is useful, for example, in

generating robust projections of sea-level change.

1.3 Objectives of the Research

The overarching objective of this research is to arrive at an improved GIA model for northern Canada. Improvements to both the Laurentide and Innuitian ice sheet histories are sought by comparison to new and previously available measurements of relative sea-level change and GPS-measured rates of vertical crustal motion.

The specific objectives of this thesis project are:

1. To incorporate a global, gravitationally self-consistent solution to the sea-level equation into an existing GIA code;
2. To improve the observational record of Holocene sea-level change west of Hudson Bay through the collection of sea-level measurements in the field;
3. To refine models of the evolution of the central and northern Laurentide Ice Sheet, as well as the Innuitian Ice Sheet, using new and previously available relative sea-level measurements and GPS-measured rates of vertical uplift as constraints for GIA models;
4. To use the best-fit ice sheet reconstruction developed in the previous two items to compute sector-specific contributions to the global sea-level budget from North America.

1.4 Organization of the Thesis

Chapters 5, 6, and 7 contain the main results of the thesis, and are written as journal articles. Chapter 5 has already been published in Quaternary Research (Simon et al. 2014), while Chapters 6 and 7 are currently in preparation for submission. The main content of each of these chapters is written in the format of a stand-alone journal article, with each article having its own introduction, methods, results and conclusion sections.

Chapter 1 provides an introduction to the thesis topic, describes the scientific motivation and objectives of the research, and contains an outline of the thesis structure.

Chapter 2 gives a detailed background to GIA theory. This chapter includes descriptions of various types of Earth rheology, the calculation of the Earth's GIA response to surface loading and unloading, the solution of the global sea-level equation, and observational constraints typically used to constrain the GIA process.

Chapter 3 describes the implementation of the global sea-level equation used to calculate the effect of ocean loading within the GIA computer code.

Chapter 4 provides a brief summary of the glacial and tectonic history of the study area, and summarizes the independent geophysical constraints that may be used *a priori* to inform the selection of the Earth model within the GIA models.

Chapter 5 includes an article published in Quaternary Research. The article presents new measurements of relative sea-level change collected from the west coast of Hudson Bay, and discusses their application within GIA models.

Chapter 6 contains the results of a GIA modelling analysis that examines the history of the Laurentide Ice Sheet. This chapter includes GIA model results that explore variations to the ice sheet history for the regions west and east of Hudson Bay, and parts of the Canadian Arctic Archipelago. The impact of the new ice sheet reconstruction on the global sea-level budget is also evaluated.

Chapter 7 consists of a GIA modelling analysis focussed on the Innuitian Ice Sheet, including the development of a new Innuitian Ice Sheet reconstruction, and its ability to generate predictions that fit measurements of relative sea-level change and present-day rates of vertical uplift.

Chapter 8 evaluates the outcome of the thesis research relative to the objectives stated in Section 1.3. Avenues for future research are also suggested.

Appendix A presents a detailed derivation of an analytical expression for the gradient of the spherical harmonics, as discussed in Chapter 2.

Appendix B consists of an article that was published in the Journal of Geodesy (Simon et al. 2010). The research presented within the article formed part of the PhD research, and explored a simplified version of the sea-level equation in preparation for incorporation of the full global sea-level theory discussed in Chapter 3.

Appendix C provides the supplementary information to the Quaternary Research article presented in Chapter 5.

Chapter 2

Glacial Isostatic Adjustment and the Sea-Level Equation

2.1 Earth Rheology

Rheology describes the way in which a material deforms in response to an applied stress. For different time-scales and pressure-temperature conditions, it is possible for the Earth to behave elastically, viscously, plastically, or some combination of the three. The assumed rheology is therefore important in any GIA model, as it will determine the fundamental nature of the Earth's response to loading and unloading. This section outlines the types of rheology that are useful for modelling the GIA process.

2.1.1 Elastic Rheology

The behaviour of an elastic body provides one important and relatively simple description of rock rheology. Elastic deformation is given by Hooke's Law

$$\sigma_{ij} = \lambda \epsilon_{kk} \delta_{ij} + 2\mu \epsilon_{ij}, \tag{2.1}$$

where σ_{ij} and ϵ_{ij} are the components of the stress and strain tensors, respectively, δ_{ij} is the Kronecker delta, ϵ_{kk} is the trace of the strain tensor (also called the volumetric deformation or cubical dilatation), and λ and μ are two elastic Lamé parameters (e.g., Ranalli 1987).

Following Ranalli (1987), tensor contraction of equation 2.1 yields

$$\sigma_{ii} = (3\lambda \ + 2\mu)\epsilon_{ii} \tag{2.2}$$

which, setting

$$\lambda + \frac{2}{3}\mu = k \tag{2.3}$$

gives

$$\sigma_{ii}/3 = k\epsilon_{ii}. \tag{2.4}$$

Equation 2.4 is an expression for the mean normal stress. Each side of equation 2.4 can be subtracted from equation 2.1, which using equation 2.3, gives

$$\sigma_{ij} - \frac{\sigma_{kk}}{3}\delta_{ij} = \lambda\epsilon_{kk}\delta_{ij} + 2\mu\epsilon_{ij} - (\lambda + \frac{2}{3}\mu)\epsilon_{kk}\delta_{ij}, \tag{2.5}$$

which can be re-written as

$$\sigma_{ij} - \frac{\sigma_{kk}}{3}\delta_{ij} = 2\mu(\epsilon_{ij} - \frac{\epsilon_{kk}}{3}\delta_{ij}). \tag{2.6}$$

If only the deviatoric ($i \neq j$) parts of the stress and strain tensors are considered, equation 2.6 can be written as

$$\sigma'_{ij} = 2\mu\epsilon'_{ij}, \tag{2.7}$$

where the primes indicate the deviatoric part of the tensor. Equation 2.7 proportionally relates the deviatoric stress to the deviatoric strain, and its rearrangement yields an expression for the Lamé parameter μ

$$\mu = \frac{\sigma'_{ij}}{2\epsilon'_{ij}}. \tag{2.8}$$

The parameter μ is called the shear modulus or rigidity, while the parameter k, which relates μ and λ, is called the bulk modulus. All of μ, λ, and k have units of stress.

Equation 2.1 governs elastic deformation until the stress threshold for the rock is exceeded, at which point permanent deformation such as rupture occurs. By equation 2.1, the resulting strain is linearly proportional to the applied stress. Generally, rocks will deform elastically at relatively low stresses and temperatures (i.e., much of the upper lithosphere). For low temperatures, the time-rate of change of the strain is zero, even if the stress is applied for a long duration. It is also possible for a medium with a high temperature to behave elastically if the stress is applied for only a short duration, such as when seismic waves propagate through the Earth's mantle. By Hooke's Law, strain in an elastic body will be non-zero only for the duration over which the stress is applied; strain will be fully recovered following removal of the stress. This time-independence of Hooke's Law means that elastic deformation and recovery occur instantaneously.

However, not all strain in the Earth is recoverable, and elastic deformation describes only one type of rheological response to deformation. At high temperatures and pressures, and over long time-scales, rocks may deform as a viscous fluid. As discussed in Sections 2.1.2 and 2.1.3, the viscous flow law may have a linear (Newtonian) or non-linear (non-Newtonian) form.

2.1.2 Linear Viscous Rheology

For a linear or Newtonian rheology, the stress, σ, is linearly proportional to the strain-rate, $\dot{\epsilon}$. The introduction of time-dependence means that unlike in an elastic body, neither deformation nor recovery of a viscous body is instantaneous. The constitutive equation for a linear viscous material is

$$\sigma_{ij} = \frac{\sigma_{kk}}{3}\delta_{ij} - \frac{2}{3}\eta\dot{\epsilon}_{kk}\delta_{ij} + 2\eta\dot{\epsilon}_{ij} \tag{2.9}$$

where η is the Newtonian viscosity. Rearranging equation 2.9 and again using the deviatoric expressions for the stress and strain tensors yields

$$\sigma'_{ij} = 2\eta\dot{\epsilon'}_{ij}. \tag{2.10}$$

The Newtonian (linear) viscosity of a fluid (e.g., the mantle) is therefore half the ratio of the deviatoric stress and strain-rate, or

$$\eta = \frac{\sigma'_{ij}}{2\dot{\epsilon'}_{ij}}. \tag{2.11}$$

Equation 2.11 for the linear viscosity is analogous to equation 2.8 for the rigidity of a purely elastic body.

2.1.3 Non-Linear Viscous Rheology

Viscous mantle deformation may also be described by a non-linear flow law. The most common deformation mechanisms for non-linear and linear rheology in the mantle are dislocation creep and diffusion creep, respectively. For a linear or Newtonian rheology, the stress, σ, is linearly proportional to the strain-rate, $\dot{\epsilon}$ (equation 2.10). Deformation typically occurs as the result of diffusive mass transport through vacancies within grains or along grain boundaries (diffusion creep). For a non-linear or power-law rheology, the strain-rate increases non-linearly with increasing stress (i.e., $\dot{\epsilon} \propto \sigma^n$,

with a stress exponent $n > 1$). Deformation of a power-law rheology usually takes place as a process of creation and annihilation of dislocations or imperfections in the crystal grains (dislocation creep). A linear form of dislocation creep (Harper-Dorn creep) also exists, but is rarely observed (Ranalli 1987).

Assuming a power-law rheology, the uniaxial time-rate of strain for either diffusion or dislocation creep can be expressed by

$$\dot{\epsilon_1} = Ad^{-m} f_{H_2O}^r \sigma_1^n \exp -\frac{E + PV}{RT}, \tag{2.12}$$

where A is a rheological scaling factor for uniaxial compression, d is grain size, f_{H_2O} is the water content, m and r are the grain size and water content exponents, respectively, σ_1 is the uniaxial stress, n is the power-law exponent, E is the activation energy, P is pressure, V is the activation volume, R is the gas constant, and T is temperature (Karato and Wu 1993). The quantities A, m, n, E, and V are material specific properties that are independent of stress and temperature, and their values are constrained by deformation experiments. For both diffusion and dislocation creep, the values of these rheological parameters are typically derived from laboratory experiments on olivine, the most abundant mineral in the upper mantle (e.g., Karato and Wu 1993).

The state of stress is a critical parameter for determining the type of flow observed in the mantle. Generally, at relatively low stresses and small grain sizes, the mantle will deform by linear diffusion creep (e.g., Karato and Wu 1993). In this case, $n = 1$, and the dependence of strain-rate on stress is linear. Conversely, at higher stresses and larger grain sizes, the mantle will generally deform by non-linear dislocation creep. For dislocation creep, $m = 0$, and the resulting deformation is grain-size insensitive. At a given temperature and pressure, the mechanism that yields the higher strain-rate will be dominant.

Equation 2.12 may be expressed in terms of an effective viscosity, which can be defined relative to either a constant stress or a constant strain-rate. Using the relationship for viscous flow, the effective viscosity is given by

$$\eta_{\text{eff}} = \frac{\sigma_{\text{s}}}{2\dot{\epsilon_{\text{s}}}}, \tag{2.13}$$

where σ_{s} is maximum shear stress and $\dot{\epsilon_{\text{s}}}$ is the maximum strain-rate. Under uniaxial

compression,

$$\sigma_{\mathrm{s}} = 3^{\frac{1}{2}}\sigma'_E = \sigma_1 \tag{2.14}$$

and

$$\dot{\epsilon_{\mathrm{s}}} = \frac{3^{\frac{n+1}{2}}}{2}\dot{\epsilon_1}, \tag{2.15}$$

where σ'_E is the effective shear stress (Ranalli 1987, p.77-78). Substituting equations 2.12, 2.14 and 2.15 into equation 2.12 gives an expression for the effective viscosity in terms of the stress

$$\eta_{\mathrm{eff}} = \frac{1}{\frac{3^{\frac{n+1}{2}}}{2}A^*\sigma_1^{n-1}}, \tag{2.16}$$

where here $A^* = Ad^{-m}f_{H_20}^r \exp -\frac{E+PV}{RT}$ (a similar generalized equation can be derived using tensor notation, as in, e.g., Wu (1998)). Thus, by equation 2.16, the higher the stress, the lower the effective viscosity of the mantle.

2.1.4 Maxwell Viscoelasticity

The previous sections discussed elastic deformation (Section 2.1.1) and both linear and non-linear viscous deformation (Sections 2.1.2, 2.1.3). Specifically, Sections 2.1.2 and 2.1.3 considered the rheology of a mantle that is viscous and deforms by steady-state creep according to a power-law relationship between stress and strain-rate. The power-law exponent determines the linearity: for $n = 1$ ($n > 1$), the stress-strain-rate relationship is linear (non-linear). Transitions between the two viscous flow types are thermally and rheologically controlled. Transitions between elastic and viscous deformation will also depend on temperature and depth, as well as the time-scale of the deformation response.

Depending on the geophysical process being studied, neither an elastic nor viscous rheology alone may adequately describe the Earth's response to loading. The glacial isostatic adjustment process is a classical example of a phenomenon for which the observed deformation is best described by more than one rheological component. Typically, the GIA response to loading and unloading of the lithosphere by large ice sheets is described in terms of both an instantaneous elastic response and a time-dependent viscous response.

Although the linearity of the viscous flow law is debatable (Section 2.1.5), the rheological model used most frequently in GIA modelling studies is that of a Maxwell solid, which combines an elastic rheology with a linear viscous rheology. This type of

composite formulation is often presented as being conceptually equivalent to electrical circuit theory, where strain-rate and stress are analogous to current and voltage, respectively. For a Maxwell rheology, the elastic component (mechanically represented by a spring) is combined in series with the viscous component (represented by a dashpot, Figure 2.1). Although only Maxwell bodies are discussed here, there are many other rheological models that are variations on this arrangement.

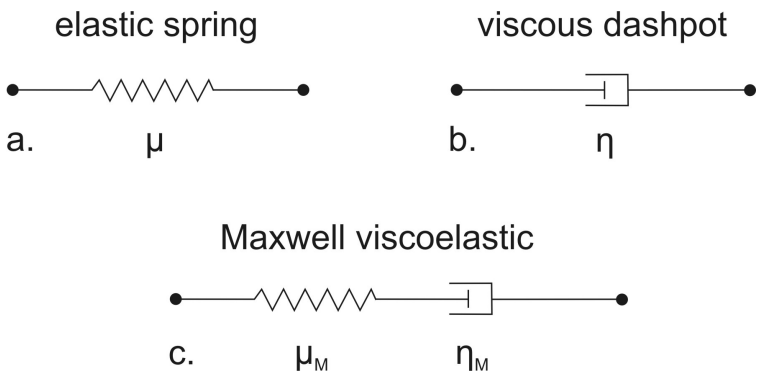

Figure 2.1: Various rheological models after Ranalli (1987). a. An elastic (Hooke) spring, with rigidity μ, b. A viscous (Newtonian) dashpot with viscosity η, and c. A Maxwell viscoelastic body with a spring and dashpot connected in series, where μ_M and η_M are the Maxwell-rigidity and Maxwell-viscosity, respectively.

Since the elastic and viscous components of a Maxwell body are combined in series, the strain-rates of each component can be combined to yield the total strain-rate. The constitutive equation for a Maxwell body is therefore obtained by adding the strain-rates of equations 2.9 and 2.1. After some rearranging and differentiating equation 2.1 with respect to time, the strain-rates of the elastic and viscous components are

$$2\mu\dot{\epsilon}_{ij} = \dot{\sigma}_{ij} - \lambda\dot{\epsilon}_{kk}\delta_{ij} \tag{2.17a}$$

$$2\mu\dot{\epsilon}_{ij} = \frac{\mu}{\eta}\left(\sigma_{ij} - \frac{\sigma_{kk}}{3}\delta_{ij}\right) + \frac{2}{3}\mu\dot{\epsilon}_{kk}\delta_{ij}. \tag{2.17b}$$

Glacial isostatic adjustment models with a Maxwell viscoelastic rheology typically assume that material is elastically compressible, and viscously incompressible. Incompressibility assumes changes in pressure cause no change in density or volume, and for an incompressible medium, the cubical dilatation is zero, or $\epsilon_{kk} = \dot{\epsilon}_{kk} = 0$. Assuming the term σ_{kk} is independent of $\dot{\epsilon}_{kk}$ (Ranalli 1987), and does not go to zero,

equation 2.17b for the viscous component reduces to

$$2\mu\dot{\epsilon}_{ij} = \frac{\mu}{\eta}\left(\sigma_{ij} - \sigma_{kk}\delta_{ij}\right). \tag{2.18}$$

Summation of the elastic and viscous strain-rate equations 2.17a and 2.18 yields the Maxwell constitutive equation for a linear viscoelastic material

$$\dot{\sigma}_{ij} + \frac{\mu}{\eta}\left(\sigma_{ij} - \frac{1}{3}\sigma_{kk}\delta_{ij}\right) = 2\mu\dot{\epsilon}_{ij} + \lambda\dot{\epsilon}_{kk}\delta_{ij}, \tag{2.19}$$

(e.g., Peltier 1974, Wu and Peltier 1982).

The Maxwell constitutive equation is also often presented in terms of the deviatoric parts of the stress and strain tensors. Combining the strain-rates of equation 2.10 with the time derivative of equation 2.7 after some rearranging gives

$$\dot{\epsilon'}_{ij} = \frac{\dot{\sigma'}_{ij}}{2\mu} + \frac{\sigma'_{ij}}{2\eta}. \tag{2.20}$$

Assuming that a stress is applied at time $t = 0$ and is maintained thereafter, integration of equation 2.20 with respect to time yields

$$\epsilon'_{ij} = \frac{\sigma'_{ij}}{2\mu} + \frac{\sigma'_{ij}}{2\eta}t, \tag{2.21}$$

so that the elastic strain is instantaneous, and the linear viscous strain depends on time t; only the elastic strain is recovered upon removal of the applied stress.

2.1.5 Linear Versus Non-linear Rheology for GIA Models

Whether mantle deformation is dominated by a linear or a non-linear flow law remains an important question in the study of mantle dynamics. Accounting for varying spatial and temporal scales, the sublithospheric mantle can behave as either a linear or a non-linear medium, and it is likely that transitions between the two flow types occur as the result of variations in both depth and tectonic setting. The governing rheological flow law of the mantle will critically control the viscosity-depth profile, the spatial and temporal characteristics of mantle convection, and shear localization of deformation (e.g., Karato and Wu 1993). However, rheological transitions between linear and non-linear flow are neither well constrained by experimental determination of the controlling parameters, nor straightforward to identify through geophysical

observation.

Equation 2.16 relates the effective viscosity of the mantle to the values of its rheological and thermal parameters for a given differential stress. It is useful to express the effective viscosity as a function of stress since deformation experiments performed on mantle rocks are typically done by subjecting the rock or mineral sample to a known stress. By assuming the geotherm and the rheological properties of the mantle are known, the effective viscosity can be calculated as a function of depth (or pressure) for both diffusion and dislocation creep using equation 2.16. The mechanism which yields the lower effective viscosity at any given pressure and temperature will be the principal mode of deformation.

Near mid-ocean ridges and subduction zones, it is likely that the shallow upper mantle deforms by non-linear dislocation creep since the high temperatures there promote a low viscosity. Conversely, the colder geotherm associated with less tectonically active cratonic regions favours deformation by linear diffusion creep in the upper mantle. The rheological transition between dislocation and diffusion creep in the upper mantle is also highly sensitive to stress (Karato and Wu 1993). The high stress associated with some tectonic settings (e.g., collisional or continental rifting environments) will promote a transition in the upper mantle from dislocation to diffusion creep through a stress induced reduction in grain size.

In addition to microphysical experimentation on rocks, geophysical observations have been applied to constrain the linear or non-linear nature of the mantle. Geophysical data used to infer mantle rheology can be provided by microstructural analysis of rocks, measurements of the mantle's seismic properties, and observations of the GIA process. An important question however is whether observations of the glacial isostatic adjustment process can actually be used to successfully distinguish between a linear and non-linear rheology. If the answer to this question is 'yes', the natural subsequent goal is to determine which deformation mechanism is supported by GIA observations.

To evaluate the capability of GIA to 'see' a non-linear rheology, it is useful to consider the magnitude of deformation resulting from this process. Typical stress, strain and strain-rate magnitudes for GIA are, respectively, 10^{-1}–10 MPa, 10^{-6}–10^{-4}, and, assuming a time-scale of 1–10 kyr, 10^{-16}–10^{-14} s^{-1} (Karato 1998). The corresponding values estimated for mantle convection are 10^{-1}–10 MPa, 10^{-1}–10, and, assuming a time-scale of 100–1000 Myr, 10^{-16}–10^{-15} s^{-1} (Karato 1998). The strain magnitude of GIA is thus several orders of magnitude smaller than that for

plate tectonic processes.

The stress magnitude of GIA forms the basis of one argument against GIA observations being able to differentiate between linear and non-linear deformation. Specifically, if the background tectonic stress is larger than the GIA-induced stress, then the deformation resulting from the GIA process will appear linear, even if the mantle is governed by a non-linear creep law (Schmeling 1987), an argument which assumes interaction and superposition of GIA-induced and tectonic stresses. However, the degree to which tectonic and GIA stresses interact is debatable. Karato (1998) stated that because the strain magnitudes of GIA are small relative to those of tectonic processes, the dislocation density is unlikely to change significantly during the GIA process; Karato (1998) concluded that because GIA strain is typically smaller than tectonic strain, and because the time scale of deformation is also shorter, that there is little interaction between tectonic and GIA stresses. Various studies (Wu 1992, Wu 1993, Karato and Wu 1993, Wu and Wang 2008) have appealed to this argument, or, equivalently, have assumed a negligible ambient stress.

In a study that considered non-negligible tectonic stress, it was shown by Wu (2001) that in the Laurentide region, Schmeling's (1987) assertion that a power-law mantle will behave linearly for the GIA process holds only for a narrow window of parameter space (the ambient stress level must be $\sim$10 MPa and the rheological scaling factor $A \sim 10^{-35}$ Pa^{-3} s^{-1}). Wu (1995, 1998) also demonstrated that at larger ambient stresses, the ability of predicted GIA motions to discriminate between a linear or a non-linear mantle appears to depend on proximity to the load centre. In these models, GIA deformation of a power-law mantle is not strongly time-dependent near the centre of the load, and therefore can appear linear. Otherwise, relative sea-level change predicted by GIA models generally displays sensitivity to the type of flow law and thus in most cases can be used to distinguish between a linear and non-linear rheology (Wu 1995).

The use of a purely steady-state power-law rheology has been questioned by Karato (1998), who argued that transient creep is an important component of the GIA process. Several GIA modelling studies (Karato and Wu 1993, Wu 1995, Wu 1998, Wu and Wang 2008, van der Wal et al. 2010), however, assume that the GIA process can be represented by steady-state creep within a power-law rheology. Many studies have modelled the GIA process using a non-linear viscous rheology (e.g., Wu 1995, 1998, 2001), as well as a composite viscous rheology in which deformation can be simultaneously linear and non-linear (Gasperini et al. 1992, Giunchi and Spada

2000, Dal Forno et al. 2005, van der Wal et al. 2010). Although the specific conclusions of these studies vary, the results often suggest that GIA observations can be better fit by predictions using a non-linear or composite rheology when compared to predictions from a purely linear rheology.

The rationale for this study adopting a linear flow law for the mantle therefore are: i) the study area of northern Canada is almost entirely limited to tectonically quiescent cratonic regions, which with their colder geotherms, likely favour diffusion creep (linear deformation); ii) much of the study area can be considered to be near the load centre, where GIA deformation can appear less time-dependent (more linear); iii) there is no strong consensus in the literature as to which deformation mechanism dominates in both the upper and lower mantle; and, iv) the effective viscosity of a non-linear mantle can vary greatly owing to very large uncertainties in quantifying the controlling parameters. As well, this study uses the ICE-5G ice sheet reconstruction of Peltier (2004), which was developed assuming that the GIA response of the Earth follows that of a Maxwell viscoelastic body. Use of a linear rheology is therefore a practical starting point, because one of the goals of this study is to propose modifications to ICE-5G that may result in an improved fit between model predictions and observations. These points do not however preclude the future consideration of non-linear viscous rheologies to similarly examine the research objectives. A non-linear flow law may be more appropriate for the margins of the study area, where the second point may not be true.

2.2 GIA Response Theory

Originally recognized by Jamieson (1865), glacial isostatic adjustment (GIA, also sometimes referred to as postglacial rebound) is the process by which the Earth's surface deforms in response to loading and unloading by ice sheets and glaciers. The magnitude of this response provides a means for inferring internal rheological properties of the Earth, such as the viscosity of the mantle. Numerical methods for quantifying loading-induced deformations to the Earth's surface and gravitational potential were first introduced by Haskell (1935) for a homogeneous viscous half-space model. Since then, analytical solutions have evolved to describe the response of increasingly complex Earth models.

The general problem of computing the Earth's response to surface loading can be solved using a Green's function approach, as demonstrated by Farrell (1972),

who provided the full solution for the loading response of an elastic Earth. Peltier (1974, 1976, 1985) subsequently described in detail the impulse response of a more complex Maxwell Earth to a time-variable surface mass load. As discussed in Section 2.1.4, a Maxwell rheology is the most commonly used rheology in GIA models. This section therefore describes the method by which the response of a Maxwell Earth due to surface loading is calculated. The response of a simple impulsive point load is considered first; Section 2.2.4 describes the solution for a spatially and temporally variable surface load. The aim of this section is to provide a summary of the important steps for solving the GIA problem. Peltier (1974, 1976, 1985), Wu and Peltier (1982), James (1991), and Mitrovica et al. (1994) all provide more detailed descriptions of the methods outlined here.

2.2.1 Governing Equations

The constitutive equation for a Maxwell body defines the relationship between stress and strain, and is given by

$$\dot{\sigma}_{ij} + \frac{\mu}{\eta}\left(\sigma_{ij} - \frac{1}{3}\sigma_{kk}\delta_{ij}\right) = 2\mu\dot{\epsilon}_{ij} + \lambda\dot{\epsilon}_{kk}\delta_{ij}, \tag{2.22}$$

which is the same as equation 2.19 in Section 2.1.4. Peltier (1974) showed that the viscoelastic problem may be solved by first expressing equation 2.22 in the Laplace transform domain as

$$\sigma_{ij}(s) = \lambda(s)\epsilon_{kk}\delta_{ij} + 2\mu(s)\epsilon_{ij} \tag{2.23}$$

where s is the Laplace transform variable and has units of frequency, and $\mu(s)$ and $\lambda(s)$ are s-dependent functions of the time domain equivalent Lamé parameters μ and λ. Equation 2.23 is equivalent in form to the constitutive equation for a purely elastic body (equation 2.1). The correspondence principle then allows the time-dependent viscoelastic response to be constructed through the repeated solution of the equivalent elastic problem for many values of the Laplace transform variable.

The equations of motion and mass conservation for the response to loading of a Maxwell Earth are the linearized equation for conservation of momentum, Poisson's

equation for gravitational potential, and the continuity equation, and are given by

$$\nabla \cdot \sigma - \nabla(\rho_0 g \mathbf{u} \cdot \mathbf{e}_r) - \rho_0 \nabla \phi + g \nabla \cdot (\rho_0 \mathbf{u}) \mathbf{e}_r = 0 \tag{2.24a}$$

$$\nabla^2 \phi = -4\pi G \nabla \cdot (\rho_0 \mathbf{u}) = 4\pi G \rho_1 \tag{2.24b}$$

$$\rho_1 = -\rho_0 \nabla \cdot \mathbf{u} - \mathbf{u} \cdot (\frac{\partial}{\partial r} \rho_0) \mathbf{e}_r \tag{2.24c}$$

where σ is the stress, $\mathbf{u}$ is the displacement vector, ϕ is the gravitational potential, ρ_0 and ρ_1 are the initial and perturbed densities, respectively, and $\mathbf{e}_r$ is the basis vector in the radial (r) direction. The second term in equation 2.24a is the advection of the hydrostatic prestress that the Earth is subject to prior to loading (Peltier 1974, 1985). The third term in equation 2.24a is the body force, while the fourth term is the buoyancy force.

In the simplified case where the Earth is assumed to be elastically incompressible, the density remains constant, and as such $(\frac{\partial}{\partial r} \rho_0) = 0$, $\rho_1 = 0$, and the buoyancy term in equation 2.24a vanishes. For an incompressible Earth model, the governing equations therefore reduce to

$$\nabla \cdot \sigma - \nabla(\rho_0 g \mathbf{u} \cdot \mathbf{e}_r) - \rho_0 \nabla \phi = 0 \tag{2.25a}$$

$$\nabla^2 \phi = 0 \tag{2.25b}$$

$$\nabla \cdot \mathbf{u} = 0. \tag{2.25c}$$

The choice of whether to employ a compressible or incompressible Earth model depends on the particular modelling study; the following discussion applies for the more general compressible case, but can be simplified to an incompressible case through equations 2.25.

Solutions to equations 2.24 can be obtained for the deformation (described by $\mathbf{u}$ and ϕ) of a spherically symmetric Earth by a surface load. These equations are typically solved in the spherical polar coordinate system, (r, θ, ψ), where the coordinates are the radial component, the colatitude, and the east longitude, respectively. For the simplest case of an axially symmetric point load, the longitudinal dependence will vanish due to symmetry, and the response of a Maxwell Earth can be expressed as

an expansion of spherical harmonics

$$\mathbf{u} = \sum_{n=0}^{\infty} \left(U_n(r,s) P_n(\cos\theta)\mathbf{e}_r + V_n(r,s)\partial \frac{P_n(\cos\theta)}{\partial\theta}\mathbf{e}_\theta \right) \tag{2.26a}$$

$$\phi = \sum_{n=0}^{\infty} \phi_n(r,s) P_n(\cos\theta) \tag{2.26b}$$

$$\nabla \cdot \mathbf{u} = \sum_{n=0}^{\infty} X_n(r,s) P_n(\cos\theta), \tag{2.26c}$$

where U_n and V_n are, respectively, the vertical and horizontal components of the total displacement $\mathbf{u}$, $P_n(\cos\theta)$ is the Legendre polynomial for degree n, and $\mathbf{e}_\theta$ is the polar basis vector (Peltier 1974, Wu and Peltier 1982). Note that here, and in all subsequent expressions using spherical harmonics, the variables n and m are now used to refer to degree and order, respectively.

The combination of equations 2.26 with the stress-strain transforms derived from the Maxwell constitutive equation gives a coupled first-order system of differential equations that can be solved as a boundary value problem in the Laplace transform domain. The resulting transformed response can then be inverted to obtain the time-dependent response, which is described in the following sections.

2.2.2 Time-Dependent Love Numbers

In the preceding section, the equations for calculating the response were expressed in the transform domain to allow simplified solution of the Maxwell constitutive equation. In general, transformation from the frequency domain to the time domain of any function $f(t)$ can be given by $f(t) = L^{-1}[f(s)]$, where L^{-1} is the inverse of the standard Laplace transform. In the following sections, the response is expressed as a function of time. Equations 2.24-2.26 are equally valid in either the transform or time domain.

It is conventional to express the point load response in terms of dimensionless time-dependent Love numbers. Accordingly, the response for a given Legendre degree n is

$$\begin{bmatrix} U_n(a,t) \\ V_n(a,t) \\ \phi_n(a,t) \end{bmatrix} = \frac{a g_0}{M} \begin{bmatrix} h_n(a,t)/g_0 \\ l_n(a,t)/g_0 \\ -(k_n(a,t)+1) \end{bmatrix}, \tag{2.27}$$

where a is the radius of the Earth, g_0 is the unperturbed gravitational acceleration

at radius $r = a$, M is the mass of the Earth, and h_n, l_n, and k_n are, respectively, the vertical, horizontal and gravitational surface load Love numbers.

The total Love numbers can be expressed as a sum of instantaneous elastic and time-dependent viscoelastic Love numbers

$$\begin{bmatrix} h_n(t) \\ l_n(t) \\ k_n(t) \end{bmatrix} = \begin{bmatrix} h_n^{el}\delta(t) + h_n^{v}(t) \\ l_n^{el}\delta(t) + l_n^{v}(t) \\ k_n^{el}\delta(t) + k_n^{v}(t) \end{bmatrix} \tag{2.28}$$

where el indicates the elastic component, v indicates the viscoelastic component, $\delta(t)$ is the Dirac delta, and the radial component at $r = a$ is now implicit. The h_n^{el}, l_n^{el}, and k_n^{el} components of equations 2.28 are the surface load Love numbers for the purely elastic component of the response. The viscoelastic Love numbers can be approximated as an exponential series so that the expression for the total Love number takes the form

$$h_n(t) = h_n^{el}\delta(t) + \sum_{i=1}^{J} r_i^n \exp(-s_i^n t) \tag{2.29}$$

where r_i^n are the residues of the loading Love numbers, $s_i^n = 1/\tau_i^n$ are the inverse relaxation times, and summation occurs over J viscoelastic modes (Peltier 1974, Wu and Peltier 1982). Only the vertical Love number is shown in equation 2.29, but analogous expressions exist for $l_n(t)$ and $k_n(t)$.

The solutions for r_i^n and s_i^n are found by the normal mode method described by Peltier (1985) and used by James (1991). The values of s_i^n are the zeros of a secular determinant and lie on the negative part of the real s-axis. The r_i^n values are the inverse of the slope of the determinant as it passes through the zero value of the associated s_i^n value. A more detailed description of the method of solution can be found in Wu and Peltier (1982), Peltier (1985) and James (1991).

In any radially symmetric Earth model, each boundary within the model will give rise to a decay mode. There are several prominent modes, and they are conventionally called the M0, M1, M2, L0, and C0 modes. The M modes are mantle modes; M0 is the fundamental mantle mode arising from the density contrast across the surface of the model, and M1 and M2 are due to the 440 km and 670 km discontinuities, respectively (Wu and Peltier 1982, Peltier 1985). The L0 mode is due to the presence of the lithosphere, and the C0 mode is due to the presence of the core-mantle bound-

ary. Transition (T) modes also exist, and arise due to viscosity contrasts within the assumed Earth model (James 1991). Relaxation times for varying spherical harmonic degree for each of the main modes are shown for a typical Earth model in Figure 2.2.

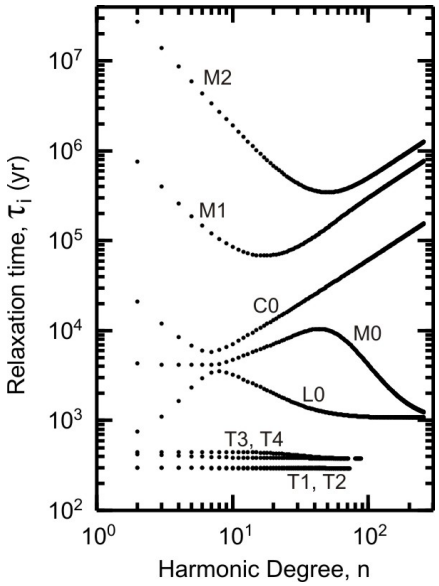

Figure 2.2: Spectrum of relaxation times τ_i for a typical spherically symmetric viscoelastic Earth model for the main modes in the mantle for spherical harmonic degree $n = 1$, 256. The M modes are mantle modes, the C mode is due to the core-mantle boundary, the L mode is a lithospheric mode, and the T modes are transition modes.

2.2.3 Space-Time Green's Functions for an Impulsive Point Load

The total impulse response (or the space-time Green's function) is obtained by summing over Legendre degree the infinite series of the n-dependent response functions and the Legendre polynomials, and can be expressed as a combination of equations 2.26a, 2.26b and 2.27

$$G_u(\theta, t) = \frac{a}{M} \sum_{n=0}^{\infty} h_n(t) P_n(\cos\theta) \tag{2.30a}$$

$$\underline{G}_v(\theta, t) = \frac{a}{M} \sum_{n=0}^{\infty} l_n(t) \partial \frac{P_n(\cos\theta)}{\partial\theta} \tag{2.30b}$$

$$G_\phi(\theta, t) = -\frac{a g_0}{M} \sum_{n=0}^{\infty} (k_n(t) + 1) P_n(\cos\theta) \tag{2.30c}$$

where $G_u(\theta,t)$, $\underline{G}_v(\theta,t)$ and $G_\phi(\theta,t)$ are the Green's functions for the total vertical, horizontal, and gravitational potential responses, respectively (e.g., Peltier 1974), and the underbar on $\underline{G}_v(\theta,t)$ indicates that the horizontal response is a vector quantity. Using equation 2.28 the elastic and viscoelastic components of the Love numbers in equation 2.30 can be separated as

$$\begin{aligned} G_u(\theta,t) &= \frac{a}{M}\sum_{n=0}^{\infty}\left(h_n^{el}\delta(t)+h_n^v(t)\right)P_n(\cos\theta) \\ \underline{G}_v(\theta,t) &= \frac{a}{M}\sum_{n=0}^{\infty}\left(l_n^{el}\delta(t)+l_n^v(t)\right)\partial\frac{P_n(\cos\theta)}{\partial\theta} \\ G_\phi(\theta,t) &= -\frac{ag_0}{M}\sum_{n=0}^{\infty}\left(k_n^{el}\delta(t)+1+k_n^v(t)\right)P_n(\cos\theta). \end{aligned} \tag{2.31}$$

Using the relation given by equation 2.29, equation 2.31 can be rewritten in the form

$$G_u(\theta,t) = \frac{a}{M}\sum_{n=0}^{\infty}\left(h_n^{el}\delta(t)+H(t)\sum_{i=1}^{J}h_i^n\exp(-s_i^n t)\right)P_n(\cos\theta) \tag{2.32a}$$

$$\underline{G}_v(\theta,t) = \frac{a}{M}\sum_{n=0}^{\infty}\left(l_n^{el}\delta(t)+H(t)\sum_{i=1}^{J}l_i^n\exp(-s_i^n t)\right)\partial\frac{P_n(\cos\theta)}{\partial\theta} \tag{2.32b}$$

$$G_\phi(\theta,t) = -\frac{ag_0}{M}\sum_{n=0}^{\infty}\left((k_n^{el}+1)\delta(t)+H(t)\sum_{i=1}^{J}k_i^n\exp(-s_i^n t)\right)P_n(\cos\theta), \tag{2.32c}$$

where h_i^n, l_i^n, and k_i^n are the vertical, horizontal and gravitational equivalents of the generic residues r_i^n given in equation 2.29, and $H(t)$ is the Heaviside function with $H(t)=1$ for $t\geq 0$ and $H(t)=0$ for $t<0$. The component of the response with $\delta(t)$ dependence in equation 2.32 is the elastic Green's function (solved by Farrell (1972)), while the component of the response with the $\exp(-s_i^n t)$ dependence is the viscoelastic Green's function.

2.2.4 Spatially and Temporally Variable Surface Loads

The description of Peltier (1974, 1985) assumes a simple impulsive point load. To obtain the Earth's response to surface loading by large ice sheets, a more complex representation of the load is required. In general, the full response to more realistic loads may be obtained through the convolution of the Green's function describing the

point load response with a load history that varies in space and time.

The surface load may consist of both an ice and an ocean component, and is typically expressed as a surface mass density in the form

$$L(\theta, \psi, t) = L_i(\theta, \psi, t) + L_o(\theta, \psi, t), \tag{2.33}$$

where the i and o subscripts denote the respective ice and ocean components of the total load, $L(\theta, \psi, t)$. The surface mass density is related to the load thickness by

$$L_i(\theta, \psi, t) = \rho_i I(\theta, \psi, t) \tag{2.34a}$$

$$L_o(\theta, \psi, t) = \rho_w SL(\theta, \psi, t) O(\theta, \psi, t), \tag{2.34b}$$

where $I(\theta, \psi, t)$ and $SL(\theta, \psi, t)$ are the ice thickness and sea-level, respectively, ρ_i and ρ_w are the respective ice and ocean water densities, and

$$O(\theta, \psi, t) = \begin{cases} 1, \text{ where ocean exists} \\ 0, \text{ where no ocean exists} \end{cases} \tag{2.35}$$

is the ocean function. The presence of the ocean function prevents ice and ocean water from being coincident at a given location (θ, ψ, t). The ocean function is an important part of the sea-level equation, and is discussed more in Section 2.3.2.

The surface mass density of the load can be expanded in spherical harmonics in a manner similar to equations 2.26. However, in the more general case where the load is not axially symmetric, the expansion will also depend on the longitude. In this case, the Legendre polynomials in equation 2.26 can be replaced with normalized vector spherical harmonics of the form

$$\overline{Y}^j_{nm}(\theta, \psi) = \overline{P}_{nm}(\cos\theta) c_j(m\psi), \tag{2.36}$$

where $P_{nm}(\cos\theta)$ are the associated Legendre polynomials of degree n and order m, $c_j(m\psi)$ are the even and odd parts of the longitudinal solution, with $c_1(m\psi) = \cos(m\psi)$ and $c_2(m\psi) = \sin(m\psi)$, and the overbar denotes normalization (e.g., Ivins et al. 1993, Mitrovica et al. 1994).

The following discussion refers to the ice component of the surface mass density, although an analogous treatment exists for the ocean water component. Using

equation 2.36, the surface mass density of the ice load can be expanded as

$$L_i(\theta,\psi,t) = \sum_{n=0}^{\infty}\sum_{m=0}^{n}(\sigma_{nm1}(t)c_1(m\psi) + \sigma_{nm2}(t)c_2(m\psi))\overline{P}_{nm}(\cos\theta)$$

or

$$L_i(\theta,\psi,t) = \sum_{n=0}^{\infty}\sum_{m=0}^{n}\sum_{j=1}^{2}\sigma_{nmj}(t)\overline{Y}^{j}_{nm}(\theta,\psi), \tag{2.37}$$

where here $\sigma_{nmj}(t)$ are the spherical harmonic coefficients of the ice load (and σ does not relate to stress). When the $\overline{Y}^{j}_{nm}(\theta,\psi)$ values are substituted in place of the Legendre polynomials, the summations take the same general form as equations 2.26, except that the single sum over degree n is replaced by summation over both n and m, for $m \leq n$.

The $\overline{Y}^{j}_{nm}(\theta,\psi)$ are normalized according to

$$\int_S \overline{Y}^{j}_{nm}(\theta,\psi)\overline{Y}^{j'}_{n'm'}(\theta,\psi)\sin\theta d\theta d\psi = 4\pi\delta_{nn'}\delta_{mm'}\delta_{jj'}, \tag{2.38}$$

where the $\int_S$ indicates integration over the spherical surface (Mitrovica et al. 1994, James and Ivins 1998). Through the use of equation 2.38, the values of $\sigma_{nmj}(t)$ are solved as

$$\sigma_{nmj}(t) = \frac{1}{4\pi}\int_S L_i(\theta,\psi,t)\overline{Y}^{j}_{nm}(\theta,\psi)\sin\theta d\theta d\psi, \tag{2.39}$$

where the t dependence of $\sigma_{nmj}(t)$ does not represent a formal integration over time, but simply indicates that the calculation must be repeated for every time t in the loading history.

2.2.5 Calculating the Earth's Response to an Arbitrary Load

The response to an arbitrary ice load can be obtained through the convolution of $L_i(\theta,\psi,t)$ with the appropriate Green's function from equation 2.32. Following Mitrovica et al. (1994), the total vertical, horizontal, and gravitational responses to the

ice load are therefore given by

$$u_i(\theta,\psi,t) = \int_{-\infty}^{t} dt' \int_S a^2 L_i(\theta',\psi'\,t') G_u(\alpha, t-t') \sin\theta' d\theta' d\psi' \tag{2.40a}$$

$$\mathbf{v}_i(\theta,\psi,t) = \int_{-\infty}^{t} dt' \int_S a^2 L_i(\theta',\psi'\,t') \underline{G}_v(\alpha, t-t') \sin\theta' d\theta' d\psi' \tag{2.40b}$$

$$\phi_i(\theta,\psi,t) = \int_{-\infty}^{t} dt' \int_S a^2 L_i(\theta',\psi'\,t') G_\phi(\alpha, t-t') \sin\theta' d\theta' d\psi', \tag{2.40c}$$

where (θ,ψ,t) are the coordinates of the observation point, (θ',ψ',t') are the coordinates of the load point, and α is the angular distance between these two points given by the law of cosines

$$\cos\alpha = \cos\theta\cos\theta' + \sin\theta\sin\theta'\cos(\psi-\psi'). \tag{2.41}$$

It is useful for the purposes of analytical calculation to obtain a spectral form of equation 2.40. The scalar quantities u and ϕ are shown first; the vector horizontal displacement takes a slightly different form and is shown separately. Following a treatment similar to Mitrovica et al. (1994), the spectral form for equations 2.40a and 2.40c can be obtained by substituting the values in equations 2.37, 2.30a and 2.30c to give

$$\begin{aligned} u_i(\theta,\psi,t) &= \frac{a^3}{M}\int_{-\infty}^{t} dt' \sum_{n=0}^{\infty} h_n(t-t') \times \sum_{n'=0}^{\infty}\sum_{m'=0}^{n'}\sum_{j'=1}^{2} \sigma_{n'm'j'}(t') \\ &\times \int_S \overline{Y}^{j'}_{n'm'}(\theta',\psi') P_n(\cos\alpha)\sin\theta' d\theta' d\psi' \end{aligned} \tag{2.42a}$$

$$\begin{aligned} \phi_i(\theta,\psi,t) &= \frac{a^3 g_0}{M}\int_{-\infty}^{t} dt' \sum_{n=0}^{\infty} (k_n(t-t')+1) \times \sum_{n'=0}^{\infty}\sum_{m'=0}^{n'}\sum_{j'=1}^{2} \sigma_{n'm'j'}(t') \\ &\times \int_S \overline{Y}^{j'}_{n'm'}(\theta',\psi') P_n(\cos\alpha)\sin\theta' d\theta' d\psi'. \end{aligned} \tag{2.42b}$$

The addition theorem for spherical harmonics (e.g., Arfken and Weber 2001), allows

the Legendre polynomials to be expressed as

$$P_n(\cos\alpha) = \frac{1}{2n+1}\sum_{m=0}^{n}\sum_{j=1}^{2}\overline{Y}^{j}_{nm}(\theta,\psi)\overline{Y}^{j}_{nm}(\theta',\psi'). \tag{2.43}$$

Use of equation 2.43 in 2.42 gives

$$\begin{aligned} u_i(\theta,\psi,t) &= \frac{a^3}{M}\int_{-\infty}^{t} dt' \sum_{n=0}^{\infty} h_n(t-t') \times \sum_{n'=0}^{\infty}\sum_{m'=0}^{n'}\sum_{j'=1}^{2}\sigma_{n'm'j'}(t') \\ &\times \int_S \overline{Y}^{j'}_{n'm'}(\theta',\psi')\sin\theta' d\theta' d\psi' \\ &\times \frac{1}{2n+1}\sum_{m=0}^{n}\sum_{j=1}^{2}\overline{Y}^{j}_{nm}(\theta,\psi)\overline{Y}^{j}_{nm}(\theta',\psi') \end{aligned} \tag{2.44a}$$

$$\begin{aligned} \phi_i(\theta,\psi,t) &= \frac{a^3 g_0}{M}\int_{-\infty}^{t} dt' \sum_{n=0}^{\infty}(k_n(t-t')+1) \times \sum_{n'=0}^{\infty}\sum_{m'=0}^{n'}\sum_{j'=1}^{2}\sigma_{n'm'j'}(t') \\ &\times \int_S \overline{Y}^{j'}_{n'm'}(\theta',\psi')\sin\theta' d\theta' d\psi' \\ &\times \frac{1}{2n+1}\sum_{m=0}^{n}\sum_{j=1}^{2}\overline{Y}^{j}_{nm}(\theta,\psi)\overline{Y}^{j}_{nm}(\theta',\psi') \end{aligned} \tag{2.44b}$$

which, after adopting the shorthand notation $\sum_{nmj} = \sum_{n=0}^{\infty}\sum_{m=0}^{n}\sum_{j=1}^{2}$ and performing some simplification gives

$$\begin{aligned} u_i(\theta,\psi,t) &= \frac{a^3}{M}\sum_{nmj}\sum_{n'm'j'}\frac{\sigma_{n'm'j'}(t')}{2n+1}\int_{-\infty}^{t} dt' h_n(t-t')\overline{Y}^{j}_{nm}(\theta,\psi) \\ &\times \int_S \overline{Y}^{j}_{nm}(\theta',\psi')\overline{Y}^{j'}_{n'm'}(\theta',\psi')\sin\theta' d\theta' d\psi' \end{aligned} \tag{2.45a}$$

$$\begin{aligned} \phi_i(\theta,\psi,t) &= \frac{a^3 g_0}{M}\sum_{nmj}\sum_{n'm'j'}\frac{\sigma_{n'm'j'}(t')}{2n+1}\int_{-\infty}^{t} dt'(k_n(t-t')+1)\overline{Y}^{j}_{nm}(\theta,\psi) \\ &\times \int_S \overline{Y}^{j}_{nm}(\theta',\psi')\overline{Y}^{j'}_{n'm'}(\theta',\psi')\sin\theta' d\theta' d\psi'. \end{aligned} \tag{2.45b}$$

Finally, recalling the orthonormality relation in equation 2.38, equation 2.45 becomes

$$u_i(\theta,\psi,t) = \frac{4\pi a^3}{M}\sum_{nmj}\frac{\sigma_{nmj}(t')}{2n+1}\int_{-\infty}^{t} dt' h_n(t-t')\overline{Y}^{j}_{nm}(\theta,\psi) \tag{2.46a}$$

$$\phi_i(\theta,\psi,t) = \frac{4\pi a^3 g_0}{M}\sum_{nmj}\frac{\sigma_{nmj}(t')}{2n+1}\int_{-\infty}^{t} dt' (k_n(t-t')+1)\overline{Y}^{j}_{nm}(\theta,\psi). \tag{2.46b}$$

As shown by Mitrovica et al. (1994), the derivation for the horizontal displacement follows in a similar manner, with

$$\begin{aligned}\mathbf{v}_i(\theta,\psi,t) &= \frac{a^3}{M}\int_{-\infty}^{t} dt' \sum_{n=0}^{\infty} l_n(t-t') \times \sum_{n'=0}^{\infty}\sum_{m'=0}^{n'}\sum_{j'=1}^{2}\sigma_{n'm'j'}(t') \\ &\times \int_S \overline{Y}^{j'}_{n'm'}(\theta',\psi')\frac{\partial}{\partial\alpha}P_n(\cos\alpha)\hat{\alpha}\sin\theta' d\theta' d\psi',\end{aligned} \tag{2.47}$$

which using the relation $\dfrac{\partial}{\partial\alpha}P_n(\cos\alpha)\hat{\alpha} = \nabla P_n(\cos\alpha)$ becomes

$$\begin{aligned}\mathbf{v}_i(\theta,\psi,t) &= \frac{a^3}{M}\int_{-\infty}^{t} dt' \sum_{n=0}^{\infty} l_n(t-t') \times \sum_{n'=0}^{\infty}\sum_{m'=0}^{n'}\sum_{j'=1}^{2}\sigma_{n'm'j'}(t') \\ &\times \int_S \overline{Y}^{j'}_{n'm'}(\theta',\psi')\nabla P_n(\cos\alpha)\sin\theta' d\theta' d\psi'.\end{aligned} \tag{2.48}$$

Using the addition theorem, equation 2.48 can be rewritten as

$$\begin{aligned}\mathbf{v}_i(\theta,\psi,t) &= \frac{a^3}{M}\sum_{nmj}\sum_{n'm'j'}\frac{\sigma_{n'm'j'}(t')}{2n+1}\int_{-\infty}^{t} dt' l_n(t-t')\nabla\overline{Y}^{j}_{nm}(\theta,\psi) \\ &\times \int_S \overline{Y}^{j}_{nm}(\theta',\psi')\overline{Y}^{j'}_{n'm'}(\theta',\psi')\sin\theta' d\theta' d\psi',\end{aligned} \tag{2.49}$$

which after some simplification finally gives

$$\mathbf{v}_i(\theta,\psi,t) \;=\; \frac{4\pi a^3}{M}\sum_{nmj}\frac{\sigma_{nmj}(t')}{2n+1}\int_{-\infty}^{t} dt' l_n(t-t')\nabla\overline{Y}^{j}_{nm}(\theta,\psi). \tag{2.50}$$

Mitrovica et al. (1994) derived an expression for $\nabla\overline{Y}^{j}_{nm}(\theta,\psi)$ in complex spherical coordinates; for the present study, however, a direct expression for $\nabla\overline{Y}^{j}_{nm}(\theta,\psi)$ in real spherical coordinates was derived. The details of the derivation are given in Appendix A.

Equations 2.46 and 2.50 give a form of the solution for the Earth's vertical, gravitational, and horizontal response to an arbitrary ice load that can be calculated analytically. It is these equations that are implemented within this study's GIA model. The preceding discussion was restricted to the response to only the ice sheet component of the total surface load. The response of the Earth to a changing ocean load takes a completely analogous form to equations 2.46 and 2.50. As will be shown in the next section, the only significant difference is that sea-level and the ocean function must be iteratively solved for through use of the sea-level equation.

2.3 The Sea-Level Equation and Ocean Loading Theory

The decay and growth of ice sheets on land redistributes water into and out of the world's oceans, resulting in changing sea-level. These sea-level variations are non-uniform over the surface of the ocean, and depend on both the glacial isostatic displacement of the Earth's surface, and the direct gravitational effect of the imposed load. This phenomenon was first described by Woodward (1888) and has been subsequently addressed by many others, including Daly (1925), Farrell and Clark (1976), Mitrovica and Peltier (1991), Johnston (1993), Milne (1998), Peltier (1998a), Okuno and Nakada (2001), and Mitrovica and Milne (2003).

During times of glaciation, relative sea-level will be high in the vicinity of an ice sheet, owing to both glacial isostatic depression of the solid surface, and the gravitational attraction of the ocean towards the ice mass. In contrast, locations that are distant from any ice sheets experience little direct isostatic adjustment, and sea-level will be lower there due to increased water storage on land. During and following deglaciation, far-field sea-level rises; conversely, near the decaying ice sheet, local or relative sea-level falls as the surface rebounds upwards, and the gravitational

attraction towards the load is reduced (Figure 2.3).

Section 2.2 quantified these GIA-induced changes to the Earth's surface and gravitational potential. The final form of the response presented in Section 2.2.5 was restricted to consider only the changing ice sheet load. However, a large component of the total surface load is comprised of the load associated with changing water volumes in the ocean. The equations to calculate the response to a changing ocean load are identical to equations 2.46 and 2.50 if the spherical harmonic coefficients of the surface load are replaced with those of the ocean load.

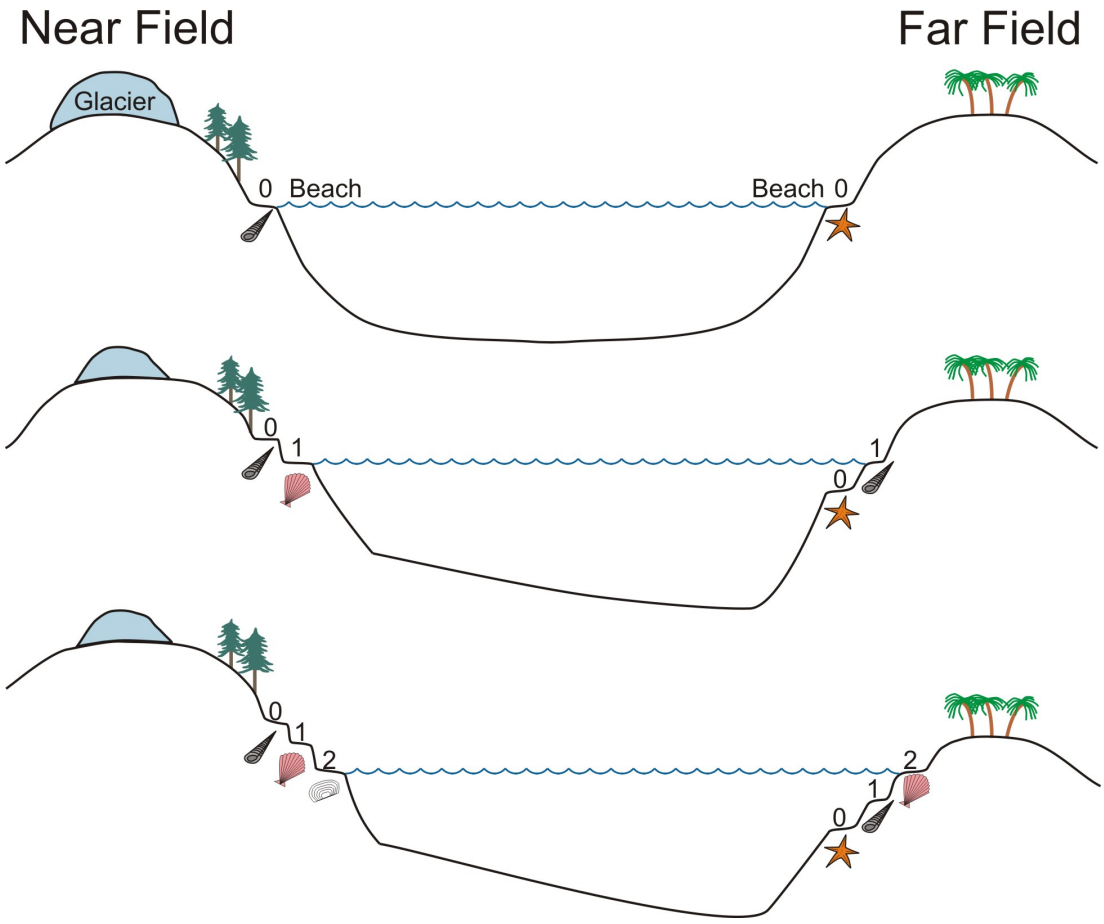

Figure 2.3: Schematic depiction of near and far-field sea-level change as the result of deglaciation. At time $t = 0$, the load is at isostatic equilibrium, and beaches exist both near the ice sheet, and in far-field locations (top panel). The ice sheet shrinks, and instantaneous elastic uplift causes sea-level to fall in the near-field, while increased ocean volume causes sea-level to rise in the far-field (middle panel). At time $t = 2$, the Earth has viscously relaxed near the ice sheet, again causing near-field sea-level fall, and far-field sea-level rise (bottom panel). As a result, a series of raised (drowned) beaches are created in the near (far) field. Approximate tilting of the ocean floor has also been shown. Modified after Farrell and Clark (1976).

Quantifying the Earth's response to a varying ice load is relatively straightforward, at least insofar as there is no feedback between ice mass changes and displacement of the surface - if ice diminishes, the surface rebounds. In contrast, the response to a varying ocean load is more complicated, since the ocean load's final value is dependent on changes to the ocean load itself. This dependency arises because variations in the ocean load depend not only on the amount of water entering or exiting the ocean, but also on the vertical displacement of the Earth's surface and the geoid, which themselves depend on variations to the ocean load. Thus, sea-level variations must be calculated iteratively, until convergence between successive iterations is reached.

This section describes the theory behind the sea-level equation, including how to incorporate the effects of grounded marine-based ice, and the variation of shoreline position over time. Observations of far-field sea-level change are also introduced since an important feature of any GIA model is the ability to reasonably reproduce these observations. Specific details of the implementation of the sea-level equation within the GIA code are addressed later in Chapter 3.

2.3.1 Displacement of the Solid Surface, and the Geoid

Two quantities of fundamental importance for calculating sea-level variations are the position of the solid surface, and the position of the geoid. The geoid is defined as a surface of gravitational equipotential that corresponds to the surface of present-day sea-level. Computing the position of the geoid may be understood by considering the reference gravitational potential prior to any changes in the surface load, and the perturbed gravitational potential that results when the surface load varies. The reference gravitational potential is constant on the surface of the Earth ($r = a$) and is given by

$$\phi_0(a) = -\frac{GM}{a}, \tag{2.51}$$

where for simplicity only the radial dependence of ϕ is shown and the spatial and temporal coordinates have been suppressed.

If the mass of the surface load changes, then the reference gravitational potential field is perturbed, and equation 2.51 is replaced by an expression that at $r = a$ also depends on the angular distance away from the location of mass change. Therefore, the gravitational potential at $r = a$ can no longer be considered an equipotential since it is not the same everywhere on the Earth's surface. There is however some distance ΔN away from the surface of the Earth where the perturbed potential at $r = a + \Delta N$

equals the reference potential at $r = a$

$$\phi_1(a + \Delta N) = \phi_0(a), \tag{2.52}$$

where the 0 and 1 subscripts indicate the unperturbed and perturbed potentials, respectively. By assuming that $N \ll a$, expansion of equation 2.52 in a Taylor series to first order gives

$$\phi_1(a) + \Delta N \cdot (\nabla\phi_1(a)) = \phi_0(a). \tag{2.53}$$

The gradient of the perturbed gravitational potential to sufficient accuracy is the same as that of the reference gravitational potential, and is given by

$$\nabla\phi_1(a) \approx \nabla\phi_0(a) = \frac{GM}{a^2} = g_0, \tag{2.54}$$

where g_0 is the acceleration due to gravity on the Earth's surface. Substitution of equation 2.54 into equation 2.53 gives

$$\Delta N = -\frac{(\phi_1(a) - \phi_0(a))}{g_0} = -\frac{\Delta\phi}{g_0} \tag{2.55}$$

where ΔN represents the deflection of the geoid resulting from the change to the gravitational potential. It can be seen from equation 2.55 and Figure 2.4 that the absolute position of the deflected geoid is given by

$$N = a + \Delta N = a + -\frac{\phi_1}{g_0} + \frac{\phi_0}{g_0}, \tag{2.56}$$

which since $\dfrac{\phi_0}{g_0} = -a$ finally gives

$$N = -\frac{\phi_1}{g_0}. \tag{2.57}$$

However, equation 2.57 does not take into account the mass exchange between the ocean and the ice sheet. In order to conserve mass, a constant c must be introduced such that

$$N^\dagger = -\frac{\phi_1}{g_0} + c. \tag{2.58}$$

While both equations 2.57 and 2.58 represent equipotentials, only equation 2.58 also conserves mass in the system. The constant c can be approximated by distributing

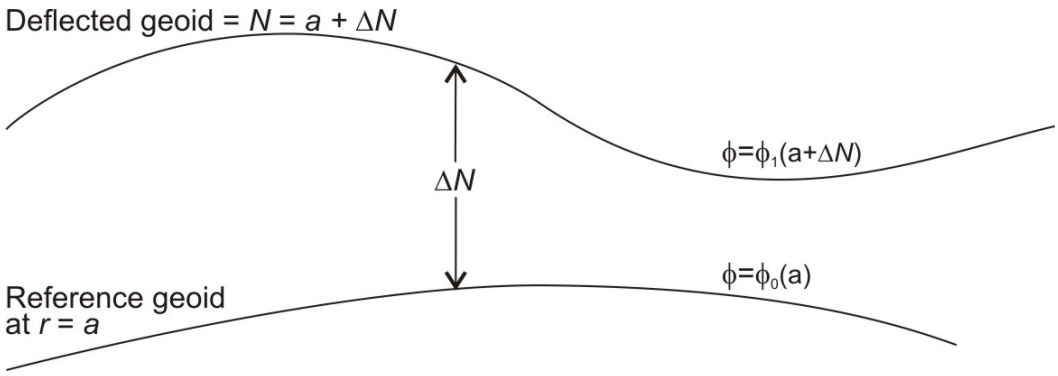

Figure 2.4: Illustration of the reference geoid at $r = a$, and the deflected geoid at $r = a+\Delta N$ (in this notation, the geoid is uncorrected for mass conservation). The surface N represents a gravitational equipotential. Modified after Turcotte and Schubert (2002).

the volume of ice lost (or gained) over the area of the ocean, and its calculation is discussed more in Chapter 3.

In the presence of a mass excess, such as a large ice sheet, the geoid will initially be deflected upwards. As mass is lost, or the ice sheet melts, the subsequent deflection will be downwards. The response of the geoid to changes in surface load is thus opposite to that of the position of the solid surface, U. As will be seen in the next section, it is the position of both $N^{\dagger}$ and U that defines sea-level.

2.3.2 The Sea-Level Equation

The Farrell and Clark 1976 Formulation

In 1976, Farrell and Clark derived a gravitationally self-consistent solution for sea-level changes due to GIA, assuming a viscoelastic non-rotating Earth. Their sea-level equation expresses the change in sea-level over time $\Delta SL(\theta, \psi, t)$ as

$$\begin{aligned}\Delta SL(\theta,\psi,t) = &\frac{\rho_i}{g_0} G_\phi(\theta,t) * I(\theta,\psi,t) \\ &+ \frac{\rho_w}{g_0} G_\phi(\theta,t) * \Delta SL(\theta,\psi,t) O(\theta,\psi,t) + c(t),\end{aligned} \tag{2.59}$$

where, recalling from Section 2.2, $G_\phi(\theta, t)$ is the Green's function for the gravitational potential, $I(\theta, \psi, t)$ is the ice load, $O(\theta, \psi, t)$ is the ocean function as defined by equation 2.35, ρ_i and ρ_w are the respective ice and water densities, $c(t)$ is the conservation of mass term, and the $*$ symbol denotes convolution over the ice surface (first term) and the ocean surface (second term). Equation 2.59 also illustrates how

since $\Delta SL(\theta, \psi, t)$ appears on both sides of the equation, the total change in sea-level is itself dependent on sea-level variations.

In their formulation, Farrell and Clark (1976) assumed that the ocean is bounded by continents with steep vertical cliffs, so that shoreline position does not change even as relative sea-level rises or falls. They also did not incorporate the effects of marine-based ice on shoreline geometry. These assumptions remove the time-dependence of the ocean function, and $O(\theta, \psi, t)$ becomes $O(\theta, \psi)$. Perturbations to the ocean height $S(\theta, \psi, t)$ are then simply equivalent to sea-level perturbations mapped onto the ocean function according to

$$\Delta S(\theta, \psi, t) = \Delta SL(\theta, \psi, t) O(\theta, \psi). \tag{2.60}$$

Equation 2.60 is valid over much of the global ocean. However, GIA-induced changes to the ocean-continent boundary do occur over time, either as the result of onlap or offlap of water on continental shelves, or through the growth and ablation of marine-based ice. Mitrovica and Milne (2003) updated the sea-level equation of Farrell and Clark (1976) to include the effects of both migrating shorelines and marine-based ice. In the derivation of the sea-level equation that follows, the methodology, as well as much of the notation, follows Mitrovica and Milne (2003). First, the effect of shoreline migration is considered through the use of a time-dependent ocean function. The effect of including marine-based ice is then discussed.

Time-Varying Shorelines

Following the treatment of Mitrovica and Milne (2003), it is first useful to express sea-level with a generalized sea-level equation of the form

$$SL(\theta, \psi, t) \equiv N(\theta, \psi, t) - U(\theta, \psi, t) + c(t), \tag{2.61}$$

where both the $N(\theta, \psi, t)$ and $c(t)$ components of the geoid have been explicitly shown. Sea-level is therefore the difference between the geoid position and the position of the solid surface. If $N(\theta, \psi, t) + c(t) > U(\theta, \psi, t)$, then the sea surface is above the solid surface and ocean exists; conversely dry land is present where $U(\theta, \psi, t) \geq N(\theta, \psi, t) + c(t)$ (Figure 2.5). It immediately follows that topography $T(\theta, \psi, t)$ is defined as simply

$$T(\theta, \psi, t) \equiv -SL(\theta, \psi, t). \tag{2.62}$$

The ocean height, $S(\theta, \psi, t)$, can be defined as a projection of sea-level onto the ocean function such that

$$S(\theta, \psi, t) = SL(\theta, \psi, t)O(\theta, \psi, t). \tag{2.63}$$

Use of the time-varying ocean function $O(\theta, \psi, t)$ allows the incorporation of changing shoreline position owing to relative sea-level rise or fall (Figure 2.6).

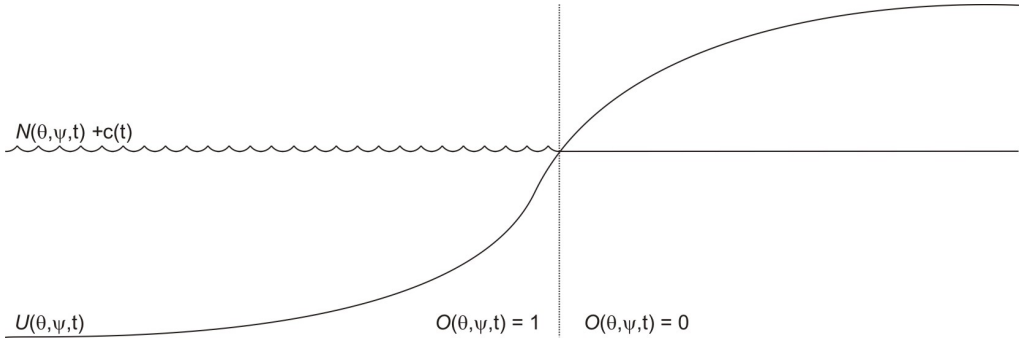

Figure 2.5: The distance between the solid surface $U(\theta, \psi, t)$ and the geoid $N^{\dagger}(\theta, \psi, t) = N(\theta, \psi, t) + c(t)$ determines sea-level. If $U(\theta, \psi, t) < N^{\dagger}(\theta, \psi, t)$, sea-level is positive and ocean exists; if $U(\theta, \psi, t) \geq N^{\dagger}(\theta, \psi, t)$ sea-level is negative, and dry land is present. The ocean function $O(\theta, \psi, t)$ distinguishes land from ocean. Modified from Mitrovica and Milne (2003).

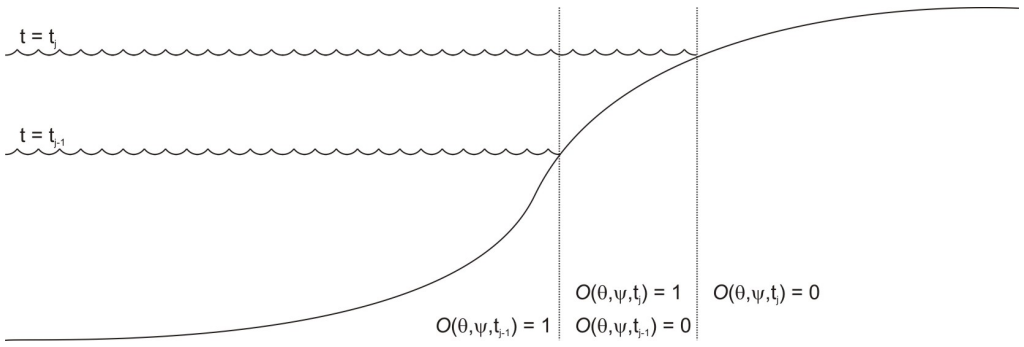

Figure 2.6: Onlap of water onto the continental shelf from relative sea-level rise, illustrating the time-dependent ocean function.

While equation 2.63 is a useful representation of the ocean height at any given time, GIA models typically calculate the changes over time of U, N, SL, T, and S, rather than their absolute values. The changes in these values at a particular time

$t = t_j$ relative to a time $t = t_0$ prior to the onset of glaciation are given by

$$\Delta U(\theta, \psi, t_j) = U(\theta, \psi, t_j) - U(\theta, \psi, t_0) \tag{2.64}$$

$$\Delta N(\theta, \psi, t_j) = N(\theta, \psi, t_j) - N(\theta, \psi, t_0) \tag{2.65}$$

$$\Delta SL(\theta, \psi, t_j) = SL(\theta, \psi, t_j) - SL(\theta, \psi, t_0) \tag{2.66}$$

$$\Delta T(\theta, \psi, t_j) = T(\theta, \psi, t_j) - T(\theta, \psi, t_0) \tag{2.67}$$

$$\Delta S(\theta, \psi, t_j) = S(\theta, \psi, t_j)O(\theta, \psi, t_j) - S(\theta, \psi, t_0)O(\theta, \psi, t_0). \tag{2.68}$$

From equations 2.61, 2.64, and 2.65 it can be seen that $\Delta SL(\theta, \psi, t_j)$ can be rewritten as

$$\Delta SL(\theta, \psi, t_j) = \Delta N(\theta, \psi, t_j) - \Delta U(\theta, \psi, t_j) + \Delta c(t_j), \tag{2.69}$$

where $\Delta c(t_j)$ is the change in the conservation of mass constant over the same time interval. Equation 2.69 represents one form of sea-level variations that can be directly calculated by a GIA model.

An equation for the change in ocean height, rather than the change in sea-level, can be found in a similar manner. Substituting the value for $SL(\theta, \psi, t_j)$ from equation 2.66 into equation 2.63, $S(\theta, \psi, t)$ at $t = t_j$ can be written as

$$S(\theta, \psi, t_j) = \left[SL(\theta, \psi, t_0) + \Delta SL(\theta, \psi, t_j)\right] O(\theta, \psi, t_j) \tag{2.70}$$

or, using equation 2.62,

$$S(\theta, \psi, t_j) = \left[-T(\theta, \psi, t_0) + \Delta SL(\theta, \psi, t_j)\right] O(\theta, \psi, t_j). \tag{2.71}$$

Using equation 2.71, ΔS in equation 2.68 can be rewritten as

$$\begin{aligned} \Delta S(\theta, \psi, t_j) = &\left[-T(\theta, \psi, t_0) + \Delta SL(\theta, \psi, t_j)\right] O(\theta, \psi, t_j) \\ &- \left[-T(\theta, \psi, t_0) + \Delta SL(\theta, \psi, t_0)\right] O(\theta, \psi, t_0), \end{aligned} \tag{2.72}$$

which assuming that $\Delta SL(\theta, \psi, t_0) \equiv 0$, simplifies to

$$\begin{aligned} \Delta S(\theta, \psi, t_j) = &\Delta SL(\theta, \psi, t_j)O(\theta, \psi, t_j) \\ &- T(\theta, \psi, t_0)\left[O(\theta, \psi, t_j) - O(\theta, \psi, t_0)\right]. \end{aligned} \tag{2.73}$$

Equation 2.73 highlights a salient point when computing ocean load variations,

that is, the change in ocean height at any location (θ, ψ, t_j) is equal to the change in sea-level projected onto the ocean function at that location *only* if the ocean geometry does not change over that time interval, or $O(\theta, \psi, t_j) = O(\theta, \psi, t_0)$. If changes to the ocean-continent boundary occur, then in addition to the perturbative change to the ocean height resulting from sea-level change, there is also a non-perturbative contribution proportional to the topography at that location. Equation 2.60 of the original Farrell and Clark (1976) formulation therefore breaks down in regions of changing shoreline geometry.

An alternative form of equation 2.73 can be obtained to consider incremental perturbations to the ocean load, rather than perturbations relative to time $t = t_0$. An incremental representation can be useful, since many GIA models, including the one used in this study, consider the changes to the surface load from time step to time step, rather than from the beginning of the loading history. As in Mitrovica and Milne (2003), for a timing history with $t_j = 0, ..., t_p$, where t_p is the present-day, the incremental change in ocean height can be expressed as

$$\begin{aligned}
\delta S(\theta, \psi, t_j) &= S(\theta, \psi, t_j) - S(\theta, \psi, t_{j-1}) \\
&= SL(\theta, \psi, t_j) O(\theta, \psi, t_j) - SL(\theta, \psi, t_{j-1}) O(\theta, \psi, t_{j-1}) \qquad (2.74) \\
&= \left[-T(\theta, \psi, t_0) + \Delta SL(\theta, \psi, t_j)\right] O(\theta, \psi, t_j) \\
&\quad - \left[-T(\theta, \psi, t_0) + \Delta SL(\theta, \psi, t_{j-1})\right] O(\theta, \psi, t_{j-1}). \qquad (2.75)
\end{aligned}$$

Either of equations 2.73 or 2.75 can be used to calculate GIA-induced ocean load variations with time-varying shorelines. Initially, the topography value $T(\theta, \psi, t_0)$ is not known; however, its value can be iteratively improved upon using the starting guess of $T(\theta, \psi, t_0) = T(\theta, \psi, t_p)$.

Marine-Based Ice

In addition to the onlap and offlap of water along shorelines, the presence of marine-based ice will also introduce a time varying component to the ocean function. During the last glaciation, parts of the major ice sheets extended off land and bordered directly with the ocean. Retreat of this ice caused an instantaneous influx of water into the isostatically depressed region directly in front of the ice sheet (Figure 2.7). This phenomenon has been called 'water dumping' (Milne 1998), or alternatively described as 'implicit ice' (Peltier 1998a).

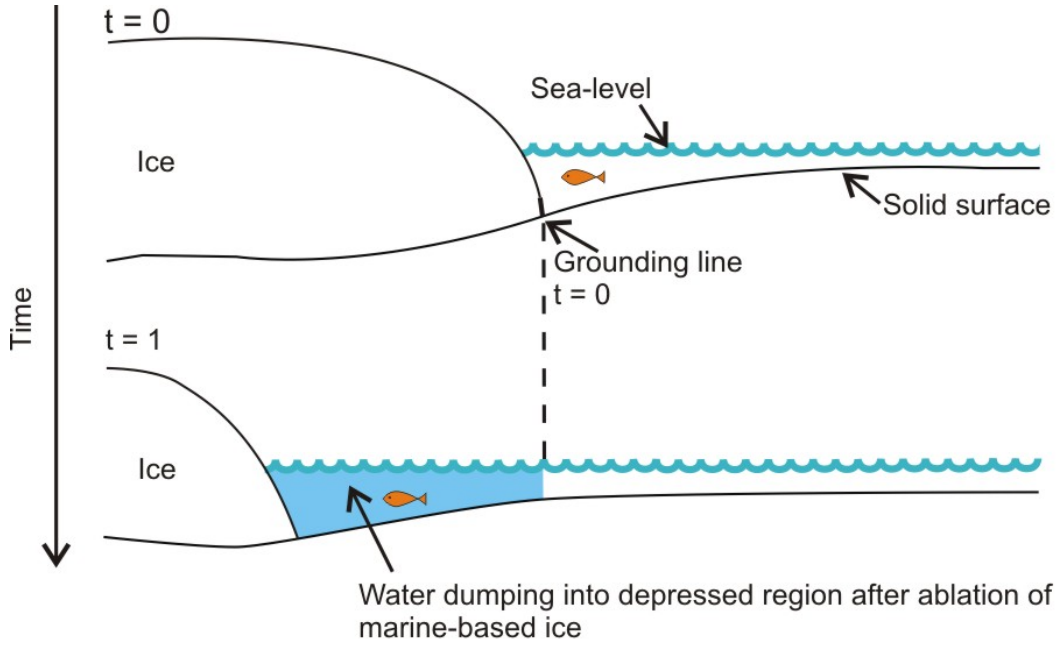

Figure 2.7: Conceptual depiction of the 'water dumping' effect. Marine-based ice retreats from its original grounding line between times $t = 0$ and $t = 1$. At $t = 1$, water infills the isostatically depressed region in front of the new grounding line of the ice sheet, an effect which is effectively instantaneous (non-perturbative). The ocean load from this water dumping effect partially offsets the loss of the ice load. Figure modified after Mitrovica and Milne (2003).

To account for this effect, the ocean function must be modified to include the variation of the ice sheet grounding line. An new function can be introduced that will consider grounded marine ice part of the ice load instead of part of the ocean load. The grounding function is defined as

$$\beta(\theta, \psi, t) = \begin{cases} 1, \text{ where there is no grounded marine ice} \\ 0, \text{ where grounded marine ice exists.} \end{cases} \tag{2.76}$$

The ocean height in equation 2.63 therefore becomes

$$S(\theta, \psi, t) = SL(\theta, \psi, t)O(\theta, \psi, t)\beta(\theta, \psi, t). \tag{2.77}$$

The grounded parts of the ice sheet contribute towards the total surface load. Ice shelves conversely are not in contact with the solid surface, and therefore do not contribute to the surface load. Using equation 2.77 to represent the ocean height, the

incremental change to ocean height expressed in equations 2.74 and 2.75 becomes

$$\begin{aligned}\delta S(\theta,\psi,t_j) &= S(\theta,\psi,t_j) - S(\theta,\psi,t_{j-1}) \\ &= SL(\theta,\psi,t_j)O(\theta,\psi,t_j)\beta(\theta,\psi,t_j) - SL(\theta,\psi,t_{j-1})O(\theta,\psi,t_{j-1})\beta(\theta,\psi,t_{j-1}) \qquad (2.78)\end{aligned}$$

$$\begin{aligned}&= \left[-T(\theta,\psi,t_0) + \Delta SL(\theta,\psi,t_j)\right] O(\theta,\psi,t_j)\beta(\theta,\psi,t_j) \\ &- \left[-T(\theta,\psi,t_0) + \Delta SL(\theta,\psi,t_{j-1})\right] O(\theta,\psi,t_{j-1})\beta(\theta,\psi,t_{j-1}). \qquad (2.79)\end{aligned}$$

Using equation 2.67, and the relationship $\Delta T(\theta,\psi,t_j) = -\Delta SL(\theta,\psi,t_j)$, an expression for topography can be written as

$$T(\theta,\psi,t_j) = T(\theta,\psi,t_0) - \Delta SL(\theta,\psi,t_j). \qquad (2.80)$$

By subtracting equation 2.80 with the same equation expressed for time t_{j-1}, the following relationship, as shown by Mitrovica and Milne (2003), can be derived

$$T(\theta,\psi,t_j) = T(\theta,\psi,t_{j-1}) + \Delta SL(\theta,\psi,t_{j-1}) - \Delta SL(\theta,\psi,t_j). \qquad (2.81)$$

The substitution of equation 2.81 into equation 2.78, and the use of the relationship between topography and sea-level gives

$$\begin{aligned}\delta S(\theta,\psi,t_j) = &- \left[T(\theta,\psi,t_{j-1}) + \Delta SL(\theta,\psi,t_{j-1}) - \Delta SL(\theta,\psi,t_j)\right] O(\theta,\psi,t_j)\beta(\theta,\psi,t_j) \\ &+ T(\theta,\psi,t_{j-1})O(\theta,\psi,t_{j-1})\beta(\theta,\psi,t_{j-1}). \qquad (2.82)\end{aligned}$$

Rearranging equation 2.82 yields

$$\begin{aligned}\delta S(\theta,\psi,t_j) = &\, O(\theta,\psi,t_j)\beta(\theta,\psi,t_j)\left[\Delta SL(\theta,\psi,t_j) - \Delta SL(\theta,\psi,t_{j-1})\right] \\ &+ T(\theta,\psi,t_{j-1})\left[O(\theta,\psi,t_{j-1})\beta(\theta,\psi,t_{j-1}) - O(\theta,\psi,t_j)\beta(\theta,\psi,t_j)\right]. \qquad (2.83)\end{aligned}$$

Equation 2.83 is equivalent to equation 39 of Mitrovica and Milne (2003), and provides a useful numerical expression for calculating the incremental change to the ocean load. It is this equation that is implemented within the GIA computer code (discussed further in Chapter 3).

2.3.3 Observations of Far-Field Sea-Level

Globally-averaged (or eustatic) sea-level change is defined as the variation through time of the volume of water in the global ocean averaged over its area (and generally assumes a fixed ocean basin geometry). Defined in this way, globally-averaged sea-level is a spatially uniform value, and is therefore more of a theoretical construct than a observable quantity. In practice however, observational records of sea-level change at far-field sites that are located well away from former or current ice sheets provide a reasonable approximation for global sea-level because these locations will be relatively insensitive to the presence of the ice sheets. In order for a far-field location to provide a good approximation of eustatic sea-level change, the site should also experience little tectonic movement (or the sea-level measurements are corrected for this effect).

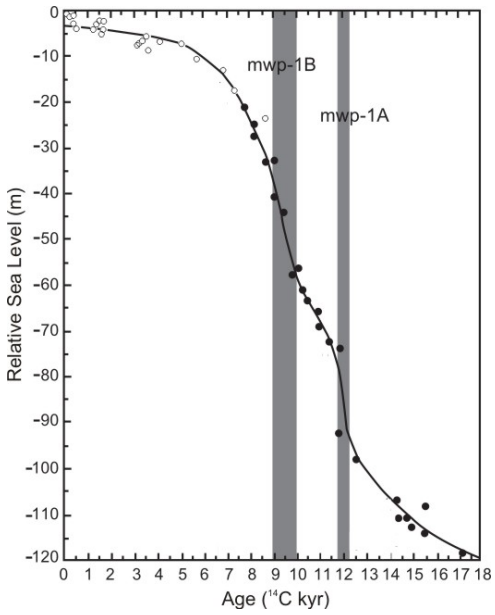

Figure 2.8: The far-field sea-level record at Barbados published by Fairbanks (1989). The timing and duration of meltwater pulses 1a and 1b (mwp-1a, mwp-1b) are shown by the grey-shaded boxes. The black line fits the data points and represents the interpreted sea-level history at Barbados. Figure modified from Licht (2004).

The sea-level record at Barbados published by Fairbanks (1989) was obtained from Uranium-Thorium (U-Th) dating of coral reef cores, and has been frequently used as a proxy for eustatic sea-level change (Figure 2.8). This sea-level history indicates an $\sim$120 m low-stand at the last glacial maximum, and is characterized by two significant periods of rapid sea level rise, termed respectively meltwater pulses 1a and 1b (mwp-1a, mwp-1b). The Barbados sea-level record has since been extended

(Peltier and Fairbanks 2006). Although these authors placed the timing of the last glacial maximum at approximately 26 cal kyr BP (5 kyr earlier than most estimates), the low-stand of ∼120 m at Barbados was shown to be robust.

Although the Barbados far-field sea-level history is the most complete, other far-field sea-level records have been established for Tahiti (Bard et al. 1996), the Sunda Shelf (Hanebuth et al. 2000), and other locations in the south Pacific (Figure 2.9). The sea-level history of the Sunda Shelf indicates a last glacial maximum low-stand of ∼120 m, consistent with the observed low-stand at Barbados. In Tahiti, recent work has confirmed the existence of mwp-1a, but questioned the existence of mwp-1b (Bard et al. 2010). Identification of the ice sheet(s) from which mwp-1a originated has also been controversial (Bassett et al. 2005, Peltier 2005). Recent studies still differ on the proposed source of mwp-1a, with Deschamps et al. (2012) favouring a significant contribution from Antarctica, and Gregoire et al. (2012) and Wickert et al. (2013) suggesting a dominant North American contribution.

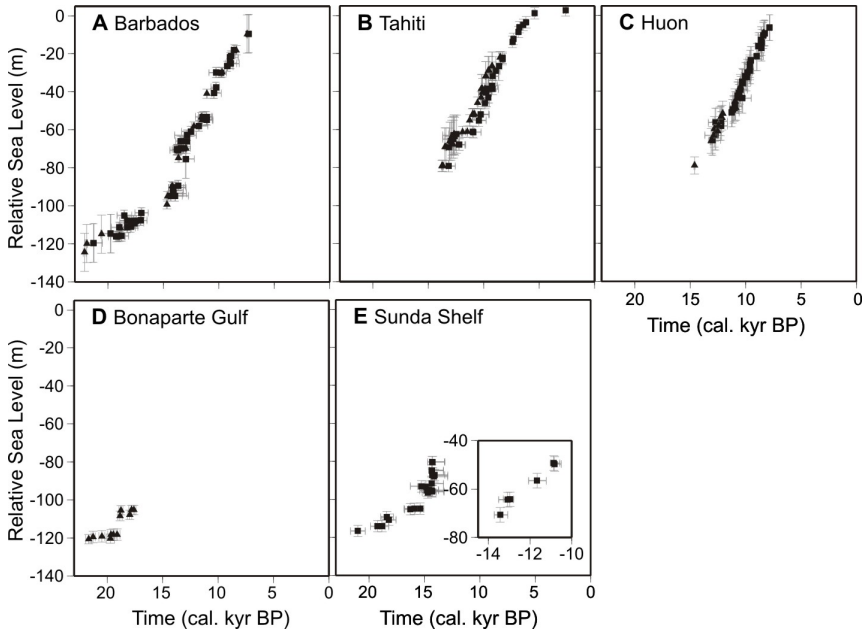

Figure 2.9: Examples of five far-field sea-level records, which can be used as proxies for eustatic sea-level change. The data consist of U-Th dated corals (triangles) and radiocarbon dated organic material (squares). Figure modified from Bassett et al. (2005).

Identification of the continental source of mwp-1a has important implications for Pleistocene and Holocene climate trends, as well as for the development of global ice sheet reconstructions, including the description of ice sheet growth and retreat. Far-field records of sea-level also provide important constraints for the total volume

history of global ice sheet models. Differences in far-field sea-level records indicate that no true measure of eustatic sea-level exists, as all locations will experience a component of (non-eustatic) sea-level change owing to surface load variations. Milne and Mitrovica (2008) examined a suite of GIA sea-level predictions and identified far-field sites in the Indian Ocean and the Mediterranean Sea as being among the least sensitive to model parameter variations. These sites are therefore the least influenced by non-eustatic surface load variations, and may provide optimal locations for obtaining sea-level measurements that approximate eustatic sea-level change with the least uncertainty.

2.3.4 Effect of the Earth's Rotation

The GIA-induced redistribution of ice and ocean masses on the Earth's surface will perturb the Earth's rotation vector (e.g., Wu and Peltier 1984). This change to the rotation vector will deform both the geoid and the solid surface, and thus result in an additional component of sea-level change not discussed in the sea-level theory of Section 2.3.2. The rotational feedback effect on sea-level predictions was investigated by Mitrovica and Milne (1998). These authors found the effect of rotation, while non-negligible, is generally small. The maximum change to predicted paleo-sea-level may reach 7-8 m at some locations (Mitrovica and Milne 1998). The rotational effect also perturbs present-day rates of sea-level change by a maximum of ∼0.22 mm/yr (Mitrovica et al. 2005, Mitrovica and Wahr 2011). The variation in present-day sea-surface height predicted by Mitrovica and Wahr (2011) (using the ICE-5G ice sheet reconstruction and VM2 viscosity profile) is shown in Figure 2.10.

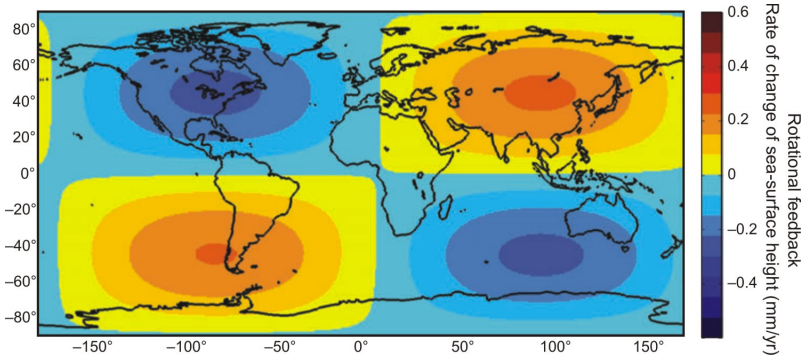

Figure 2.10: Effect of rotational feedback on predicted present-day sea-surface height rates of change using the ICE-5G ice sheet reconstruction and VM2 viscosity profile and the theory of Mitrovica et al. (2005). Figure taken from Mitrovica and Wahr (2011).

2.4 Observational Constraints and the GIA Process

2.4.1 Relative Sea-Level Change and Marine Limits

Measurements of past relative sea-level are one of the most frequently applied constraints to the GIA modelling problem. Relative sea-level data record the changing position of sea-level over time, and provide an indication of how the Earth's surface has responded over time to loading and unloading by large ice sheets. Because relative sea-level data span time through the Holocene (and sometimes also the Pleistocene), they offer valuable insight into temporal variations of the GIA response, and thus can be used to infer both past and present-day GIA motions (e.g., Tushingham and Peltier 1991, Lambeck et al. 1998, Peltier 2004, James et al. 2009). One fundamental limitation of RSL data is their inherent spatial restriction to (post-glacial) shoreline regions, although the history of land tilting can be derived at inland locations from paleo-lake shorelines.

Typical relative sea-level indicators include marine shells, bones of marine mammals, and terrestrial material, such as plant detritus (peat, driftwood, twigs). The material type and stratigraphic context of a sea-level indicator allows its position at the time of deposition to be classified as above, below, or near the position of sea-level. This type of classification is also known as the 'indicative meaning' of an observation (Shennan 2007). Marine samples provide a lower limit on relative sea-level (the position of sea-level was at least as high as the sample, or higher), while terrestrial samples provide an upper limit on relative sea-level (sea-level was no higher than the sample, or lower). These types of observations usually only provide upper-limiting or lower-limiting constraints on sea-level position, and thus the uncertainty associated with interpreting the exact position of sea level can be large (for example, many bivalve species can live at water depths of up to 200 m). However, some samples may originate from nearshore environments (e.g., seaweed), and some bivalve species (e.g., *Mytilus edulis*) are reliably known to live within $\sim$5 metres of sea level. These types of samples provide tight constraint on the position of sea level, as the uncertainty associated with their vertical position relative to sea level is generally low. The best constraint on the position of sea level is thus provided by either sea-level measurements from interpreted nearshore environments, or a combination of upper-limiting and lower-limiting observations that have approximately the same age and elevation.

A relative sea-level datum for a given location is the measured elevation of the sample combined with its age. Ideally, for any given location or region, a series of

relative sea-level measurements can be obtained and compiled to give the variation in sea-level over time for that area. Sample ages are usually determined by the radiocarbon dating method, although U-Th dating can also be used. This thesis project will use a large existing database of RSL histories for northern Canada to constrain the GIA models. This database, as well as the method of radiocarbon dating, are discussed further in Chapter 5.

Regional marine limits mark the maximum extent of marine incursion relative to the present-day shoreline, and are defined by the surface of the highest observable beach strandlines. Radiocarbon ages from samples collected near or at a regional marine limit can provide a lower estimate for the time of peak marine inundation, while the position of the marine limit bounds the extent to which the ocean extended past the present-day shoreline. Marine limit elevations have been compiled for North America by Dyke et al. (2005).

2.4.2 GPS, Tide-Gauge and Absolute Gravity Measurements

During the last decade, the magnitude of ongoing GIA motions has been increasingly well-constrained by a growing body of observational data. In particular, Global Positioning System (GPS) measurements record both the vertical and horizontal motions of the Earth's surface. Sella et al. (2007) used GPS observations to constrain the present-day GIA response in North America. In a similar study, Milne et al. (2001) used GPS observations from the BIFROST permanent network to constrain present-day GIA motions in Fennoscandia. The Fennoscandian GPS observations were later updated and expanded on by Lidberg et al. (2007). Generally, these studies show reasonable agreement between GPS-measured vertical uplift rates and those predicted by GIA models, suggesting that most of the current uplift observed in central North America and Fennoscandia is attributable to the GIA process.

High precision measurements of absolute gravity change rates have also been used to infer GIA motions in central North America (Lambert et al. 2001, 2006). These measurements record variations to the gravity field over time, which in regions of former glaciation are primarily a consequence of the glacial isostatic adjustment response of the crust and underlying mantle. Lambert et al. (2001, 2006) measured absolute gravity change rates along a transect of sites in North America and found that the largest change rates were closest to the former load centre of the Laurentide Ice Sheet; the maximum gravity change rate was recorded at Churchill at -1.9

μGal/yr.

Tide-gauge records measure the total rate of change of the position of present-day sea-level, and thus in some ways offer a marine analogue to GPS and absolute gravity measurements. A large component of observed changes to present-day sea-level is attributable to the ongoing GIA response of the Earth to the last glaciation. However, a significant component of tide-gauge rates are also a result of recent and ongoing changes to the volume of the cryosphere. Thus, in order for GIA model predicted rates of sea-level change to be comparable directly to measured tide gauge rates, the sea-level change signal attributable to present-day mass loss of ice sheets and glaciers must be accurately known (or vice versa).

A common limitation among GPS, absolute gravity and tide-gauge measurements is that they can be used to infer only the present-day GIA motions of the Earth. These data sets therefore offer limited insight into the past GIA response. As well, the spatial resolution of GPS, absolute gravity and tide gauge measurements is restricted to specific locations or regions. As noted by Craymer et al. (2006) there are few GPS sites and tide gauge records in northern Canada compared to the more southern regions of North America. Three years of GPS data are needed to obtain a first estimate of vertical motion at any location, and ten years of tide gauge data are required to obtain sea-level change estimates at an accuracy level of 2 mm/yr (Craymer et al. 2006). It could therefore be several decades before GPS and tide gauge data sets with good spatial resolution and small uncertainties exist for northern Canada.

2.4.3 GIA and GRACE

The twin satellites of the Gravity Recovery and Climate Experiment (GRACE) measure spatial and temporal gravity field variations and therefore provide a valuable method by which to approximate large-scale mass changes, such as those caused by GIA (e.g., Velicogna and Wahr 2006). Several studies have used GRACE data as a means to constrain GIA motions in North America (Paulson et al. 2007, Tamisiea et al. 2007, Tregoning et al. 2009). GRACE, however, senses only total mass changes, and cannot distinguish between mass variations that occur as the result of present-day changes to the Earth's cryosphere and hydrosphere, or the long-term GIA response of the underlying mantle to the last glaciation. Thus, to estimate GIA motions from GRACE data, other signals, such as changes to continental water storage on land and

present-day ice mass loss, must first be quantified and removed.

In North America, however, significant uncertainties exist in the estimation of water storage changes, and these uncertainties will limit the ability of GRACE data to accurately constrain GIA motions resulting from Laurentide glaciation (van der Wal et al. 2008, Wang et al. 2012). In northern Canada, interpretation of GRACE-observed gravity rates will be similarly complicated by the uncertainties associated with separating the long-term GIA signal from the present-day mass loss signal from regional glaciers and ice caps and the nearby Greenland Ice Sheet. However, although the calculated absolute and relative magnitudes vary between the analyses, the studies of Paulson et al. (2007), Tamisiea et al. (2007), van der Wal et al. (2008), and Tregoning et al. (2009) all consistently show that when corrected for estimated hydrological changes, GRACE observes two large domes of present-day uplift west and southeast of Hudson Bay. Assuming that the variations observed by GRACE are primarily attributable to GIA, this pattern of uplift suggests that the Laurentide Ice Sheet was characterized by large domes both west and southeast of Hudson Bay. Despite the associated uncertainties, the GRACE observations therefore represent an independent data set that can be used to evaluate the relative geometry and magnitude of LIS reconstructions.

2.4.4 Constraints Used in This Study

Although all of the methods discussed in Sections 2.4.1 - 2.4.3 can be used to constrain GIA models, relative sea-level data form the primary constraint for this study. GPS-measured rates of present-day vertical land motion also provide secondary constraint on the GIA models. Chapter 5 discusses the collection of both new RSL measurements and GPS data from a site location within the study area.

Chapter 3

Development of the Ocean Loading Code

3.1 The Existing GIA Code: A Brief Summary

This study uses and expands on a glacial isostatic adjustment computer code developed by James (1991) and further described in James and Ivins (1997, 1998). The GIA code that existed at the outset of this study can incorporate approximations of the local ocean load and the water dumping effect (Simon et al. 2010). This method is used and described in more detail in the study contained in Appendix B. However, the ocean loading computation of Simon et al. (2010) is not global, and thus does not model effects such as the global redistribution of water due to equatorial ocean syphoning (e.g., Mitrovica and Peltier 1991) or the more subtle changes to shoreline position due to the on lap and off lap of water over time (discussed in Section 2.3.2).

The ocean loading treatment that is incorporated into the GIA calculation follows closely the methods developed and tested by other researchers (notably, Milne 1998, Mitrovica and Milne 2003, Kendall et al. 2005). The incorporation of the global solution for the sea-level equation into the existing GIA code represented substantial effort and is a significant methodological development. The results of the implementation are therefore summarized here in a stand-alone chapter.

3.1.1 Method of Solution

The computer code developed by James (1991) follows the methodology outlined in Section 2.2.5 wherein the GIA response is obtained through convolution of the surface load reconstruction with the appropriate Green's function for the Earth model. Decay times of incompressible Earth models are solved for using the normal mode method described by Peltier (1985), while the Earth model response for elastically compressible models uses an adaptation of the elastic Love number code of Dahlen

(1976) and also incorporates Peltier's (1985) normal mode method.

3.1.2 The Reference Ice Sheet Reconstruction, ICE-5G

The global ICE-5G model of Peltier (2004) is the reference ice sheet reconstruction for the development of both the ocean loading code and the subsequent modelling analyses. The history of ICE-5G starts at 122 kyr BP and extends to present-day. The timing of the load has been discretized at 10 kyr intervals from 122 kyr BP to 32 kyr BP and at 1 kyr intervals from 21 kyr to 0 kyr BP. Ice thicknesses are also specified at 26, 21, 0.5, and 0.1 kyr BP. Ice thicknesses of ICE-5G at 26 cal kyr BP are shown in Figure 3.1.

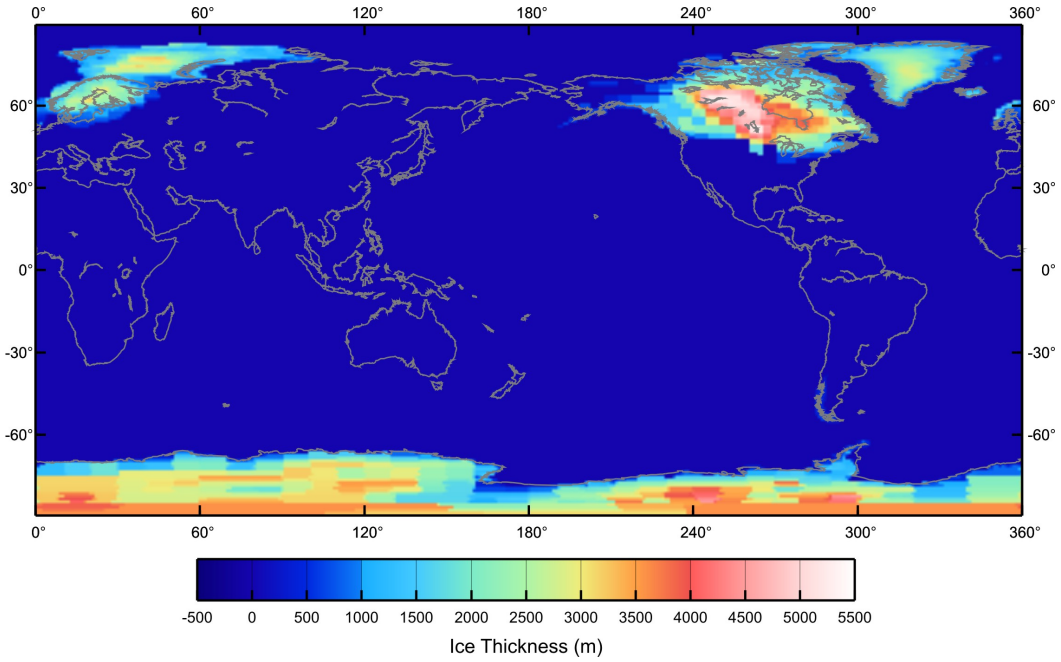

Figure 3.1: The global ICE-5G ice sheet reconstruction of Peltier (2004) at 26 kyr BP.

3.1.3 Spatial Discretization of the Surface Load

In this study, the surface load is discretized over the surface of the Earth in rectangular grid elements. The grid used is a Gaussian grid, which contains 256 × 512 elements. Because the grid is Gaussian, the latitudes are unevenly spaced (the grid is latitudinally denser towards the poles) while the longitudes are evenly spaced.

3.1.4 Temporal Discretization of the Surface Load

The timing history of the model calculations follows the discretization of the ICE-5G model described in Section 3.1.2. Between time steps, the calculation linearly interpolates the value of the surface load. The calculation does not use a Heaviside (or step-wise) temporal variation to the surface load.

3.2 Adding Gravitationally Self-Consistent Global Ocean Loading

3.2.1 Global Topography and the Present-day Ocean Function

The ocean function is fundamental to the solution of the sea-level equation. A basic approach assumes a steady (unchanging) ocean function, while a more sophisticated approach includes the effect of time-varying shorelines. The ocean function is defined with a value of 1 where ocean exists, and 0 elsewhere. In the GIA code, the initial global ocean function is defined using the publicly available global topography database ETOPO1 (Figure 3.2); the values of this data set are extracted onto the calculation grid, and values of the present-day ocean function are assigned according to equation 2.35, where values of 1 are assigned if the topography is negative, and values of 0 are assigned if the topography is positive.

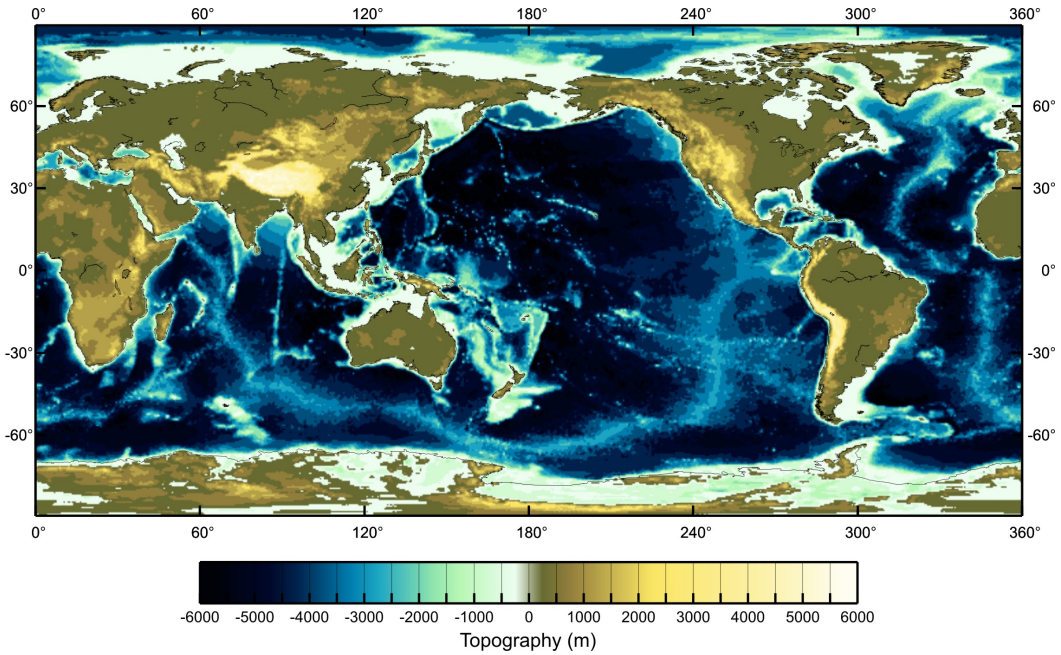

Figure 3.2: Global bedrock topography from the ETOPO1 data set, extracted onto the 256° calculation grid.

The definition of the ocean function used in this study does not take into account land that lies below sea level. The definition of the ocean function, however, does take into account the presence of grounded ice using the grounding function defined in equation 2.76, so that in practice the 'full' ocean function becomes

$$O^*(\theta, \psi, t) = O(\theta, \psi, t)\beta(\theta, \psi, t). \tag{3.1}$$

This expression of the ocean function follows the same notation that was introduced in Chapter 2 (although in Chapter 2, $O(\theta, \psi, t)$ and $\beta(\theta, \psi, t)$ were always stated explicitly). For a solution to the sea-level equation that does not include time-varying shorelines, $O^*(\theta, \psi, t) = O(\theta, \psi)$, and the present-day ocean function holds at all times in the loading history. When the solution to the sea-level equation does include time-varying shorelines, $O(\theta, \psi, t)$ must be solved for through iterative solution of the paleo-topography field (Section 3.3). Figure 3.3 shows the present-day ocean function.

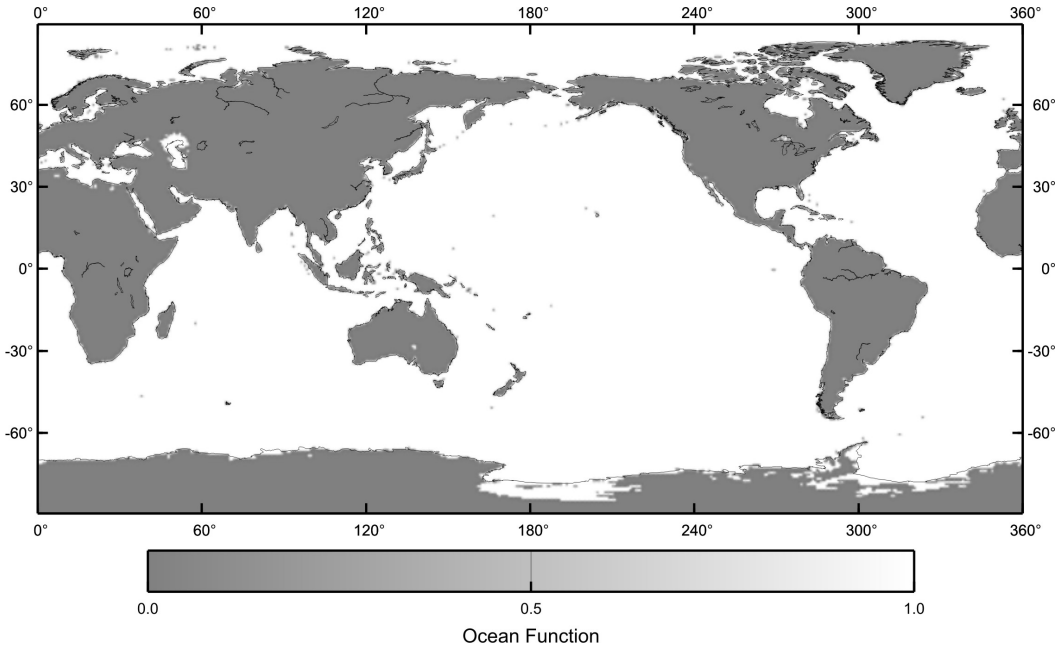

Figure 3.3: The full global ocean function at present-day. The ocean function has a value of 1 where ocean is present (white) and a value of 0 elsewhere (grey). Note that negative bedrock topography in areas of Greenland and Antarctica (Figure 3.2) has a value of 0 in the full ocean function if grounded ice with a thickness greater than the topography value is also present (via equation 3.1).

3.2.2 Conservation of Mass, Static Shorelines

As discussed in 2.3.2, Farrell and Clark (1976) introduced a solution for GIA-induced changes to sea-level, assuming a viscoelastic non-rotating Earth. The Farrell and Clark (1976) derivation expresses ocean water depth, S, as

$$S(\theta, \psi, t) = N(\theta, \psi, t) - U(\theta, \psi, t) + c(t), \tag{3.2}$$

where N is the geoid, U is the displacement of the solid surface, $c(t)$ is a term introduced to conserve mass, θ and ψ are the spatial coordinates, and t is time. The $c(t)$ term is a uniform shift to the geoid that exists to conserve mass within the system. In order to conserve mass, the amount of water entering (exiting) the ocean must equal the amount of ice retreating from (accumulating on) the continents. This requirement can be expressed

$$\Delta M_i + \Delta M_w = 0 \tag{3.3}$$

where ΔM_i and ΔM_w are the changes in mass to the ice load and water load, respectively. Making use of the relationship $M = \rho V = \rho h A$ (where ρ is density, V is volume, h is a height, and A is an area), equation 3.3 can be rewritten as an integral equation in the form

$$\rho_i \int h dS_i + \rho_w \int S dS_w = 0 \tag{3.4}$$

where ρ_i is the density of ice, h is the ice thickness, dS is the incremental area of either the ice or the water load, ρ_w is the water density, S is ocean height, and the coordinates have been suppressed. Integrating the left-hand side of equation 3.4 and substituting equation 3.2, equation 3.4 can be rewritten as

$$\rho_i \bar{h} A_i = -\rho_w \int \left[c(t) - (U - N)\right] dS_w, \tag{3.5}$$

where $\bar{h}$ denotes a uniform ice thickness over the area of the ice load. Since $c(t)$ is a spatial constant, it can be taken out of the integral, and solved for following

$$\rho_i \bar{h} A_i = -\rho_w c(t) A_o + \rho_w \int (U - N) dS_w \tag{3.6}$$

$$c(t) = \frac{\rho_i \bar{h} A_i + \rho_w \int (U - N) dS_w}{-\rho_w A_o} \tag{3.7}$$

where A_i is the area of the ice, and A_o is the area of the global ocean. Because the value of $(U - N)$ depends on the ocean load itself, the calculation must iteratively solve for the value of $(U-N)$ until the value of S has converged. For the first iteration, the displacement field (and thus $(U - N)$) is zero, and equation 3.6 for $c(t)$ becomes

$$c(t) = \frac{\rho_i \bar{h} A_i}{-\rho_w A_o} = \frac{\rho_i V_i}{-\rho_w A_o}, \tag{3.8}$$

where V_i is the total volume of ice.

3.2.3 Conservation of Mass, Time-Varying Shorelines

For the case of time-varying shorelines, the calculation of the conservation of mass term follows a similar form as in Section 3.2.2 and is expressed by

$$c(t) = \frac{\rho_i \bar{h} A_i - \rho_w \int (\Delta U - \Delta N) O_j^* dS_w + \rho_w \int -T(O_j^* - O_{j-1}^*) O_j^* dS_w}{-\rho_w A_o(t)}, \tag{3.9}$$

where the j and $j-1$ subscripts represent the j^{th} and $(j-1)^{st}$ time steps in the surface load history. The two main differences are the time-dependence given to the area of the ocean, $A_o(t)$, and the inclusion of the final term which relates to the topography, T. The topography term arises because if the value of the ocean function changes between time steps, then the component of the conservation of mass term which covers the area of changing ocean geometry is no longer a perturbative term; rather, it becomes a non-perturbative function of the topography. As with the static shorelines formulation, the displacement term $(\Delta U - \Delta N)$ is zero for the first iteration, where here the incremental (between time steps) nature of the displacements is stated explicitly.

3.3 Methodology for Full Ocean Loading

This section lists in point form the steps used in the implementation of the time-varying solution of the sea-level equation.

1. Construct a loading history for ICE-5G. The selected timing history discussed in Section 3.1.2 (36 times) is used, and ice thickness values are written out onto the 256° Gaussian grid. Compute the spherical harmonic coefficients of the ice load.

2. Perform a normalization check of the spherical harmonic coefficients. That is, sum up the calculated spherical harmonics over the entire globe on the 256° Gaussian grid (approximately $0.7° \times 0.7°$ grid). The sum of the calculated spherical harmonics over the surface of the Earth should be consistent with the normalization introduced in Chapter 2,

$$\int_S \overline{Y}_n^{mj}(\theta,\psi)\overline{Y}_{n'}^{m'j'}(\theta,\psi)dS = 4\pi\delta_{nn'}\delta_{mm'}\delta_{jj'}. \tag{3.10}$$

3. Take the ETOPO1 data base, and extract topography values onto the 256° Gaussian grid.

4. Using the topography field and the ice loading history, create an initial set of ocean functions, $O^*(\theta,\psi,t)$. In this step, floating ice is checked for in the model. Grounded marine ice is also located (the density difference between water and ice is taken into account). The initial definition of $O^*(\theta,\psi,t)$ is the product of the present-day ocean function ($O(\theta,\psi)_p$, where $O(\theta,\psi)_p = 0$ where topography is positive, and 1 where topography is negative) and the grounding function $\beta(\theta,\psi,t)$. Note that this definition of the ocean function does not account for land that lies below sea level. Compute the ocean function coefficients.

5. Using the computed spherical harmonic coefficients of the initial ocean function, compute the time-varying area of the ocean, $A_o(t)$, which is based on the value of the degree and order zero spherical harmonic coefficient.

6. Create the initial ocean load. The first iteration value of $c(t)$ is computed according to

$$c^0(t) = \frac{\rho_i\bar{h}A_i + \rho_w\int -T(O_j^* - O_{j-1}^*)O_j^*dS}{-\rho_w A_o(t)}. \tag{3.11}$$

Compute the ocean load coefficients.

7. Using the ocean load coefficients in combination with the ice load coefficients, compute the first iteration displacements on a global $5° \times 5°$ grid (2664 points).

8. Interpolate the computed displacements (specifically, $U - N$) onto the 256° grid.

9. Construct a new ocean load using the newly computed displacements. The generic

form of $c(t)$ can be computed using equation 3.9. Compute the new (absolute) ocean load, S, according to

$$S_j = (\delta S_j + S_{j-1})O_j^* \tag{3.12}$$

$$\delta S_j = O_j^*[\Delta SL_j - \Delta SL_{j-1}] - T_{j-1}[O_j^* - O_{j-1}^*] \tag{3.13}$$

$$\Delta SL_j = c(t)_j - (\Delta U - \Delta N)_j. \tag{3.14}$$

Equation 3.13 is the same as equation 39 of Milne and Mitrovica (2003) which is also equivalent to equation 19 of Kendall et al. (2005). Assume that $S_0 = 0$ (i.e., at time t_0 prior to the onset of glaciation, the glacially perturbed part of the ocean load is equal to zero).

10. Compute the spherical harmonic coefficients of the new ocean load.

11. Check for convergence between the coefficients of the ocean load of the current iteration and the last iteration. If convergence has not been reached, return to step 7, and repeat until convergence is reached. A convergence criterion similar to that described by Kendall et al. (2005) (their equation 83) is used. Specifically, to determine if convergence has been reached, compute

$$\xi_j^{i,k} = \frac{\Sigma_{l,m}|[S_{l,m}(t_j)^{i,k}]| - \Sigma_{l,m}|[S_{l,m}(t_j)^{i-1,k}]|}{\Sigma_{l,m}|[S_{l,m}(t_j)^{i-1,k}]|}, \tag{3.15}$$

where l and m are the spherical harmonic degree and order of the coefficients, respectively, i is the ocean load iteration number, j is the time step number, and k is the topography field iteration number. If $\xi_j^{i,k} < \epsilon_1$ for all j times in the loading history, where ϵ_1 is taken to be $\sim 10^{-4}$, then convergence has been reached.

12. If the ocean load has converged, update the topography field using

$$T_j = T_p - RSL_j. \tag{3.16}$$

13. Check for convergence of the topography field between the current iteration and the previous iteration. If the topography field has not converged, go back to step 4 and use the new topography field. Repeat the sea-level and topography iterations until convergence of both fields is reached.

3.4 Comparisons Between 'Farrell and Clark' and 'Full' Ocean Loading

This section compares the solutions to the sea-level equation for the standard 'Farrell and Clark' formulation to the full, moving shorelines formulation. All calculations shown in this section use ICE-5G and the VM5a viscosity profile. Although the studies on which this methodology is based (e.g., Milne 1998, Kendall et al. 2005) used the ICE-3G reconstruction, the results shown in the following sections qualitatively compare well with those studies.

3.4.1 The Ocean Function

Figure 3.4 shows the converged ocean function at 26 cal kyr BP for the full formulation. This figure shows that at 26 ka regions with grounded marine-based ice are zero in the ocean function. As well, regions currently characterized by shallow continental shelves have zero values in the ocean function.

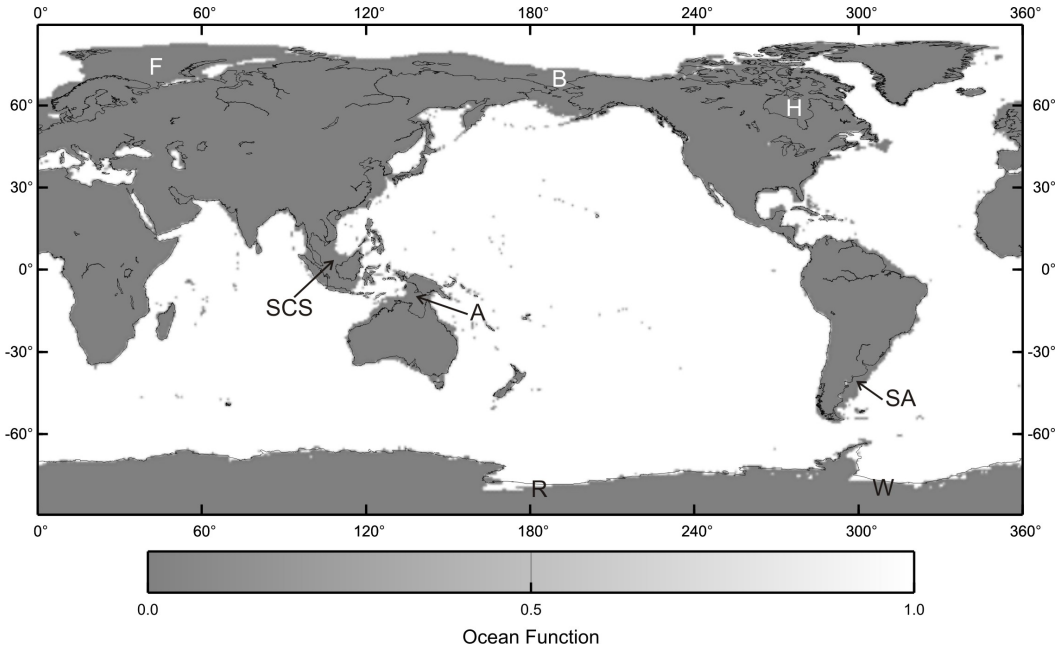

Figure 3.4: The converged global ocean function at 26 cal kyr BP, approximately the time of the last glacial maximum. At LGM, the presence of marine-based ice in large areas around Hudson Bay (H), Fennoscandia (F), and the Ross (R) and Weddell (W) seas, results in a zero (land) value for the ocean function. Similarly, shallow present-day continental shelves around northern Australia (A), the South China Sea and Indonesia (SCS), the Bering Sea (B) and southeastern South America (SA) are emergent at LGM due to the larger amount of water stored on land, and are also defined with a zero (land) value in the ocean function. Calculated for the reference ICE-5G/VM5a model.

3.4.2 Ocean Height

Figure 3.5 shows maps of predicted ocean heights, S, for the Hudson Bay region for two different time steps in the load history. The predicted differences between the two formulations is similar to those shown by Milne (1998) and Kendall et al. (2005). In the Farrell and Clark (FC) formulation there are large positive ocean heights in Hudson Bay at 26 ka owing primarily to the large downward vertical displacement of the Earth from the load (remembering that ocean height is expressed in this formulation as $S = c(t) - (U - N)$). In the updated formulation, however, the grounded ice present in Hudson Bay at this time yields a zero value for the ocean function, and thus also the ocean height. At 8 ka in the FC formulation, the ocean height in Hudson Bay is still positive, but has decreased relative to the 26 ka time because of the upward rebound of the Earth's surface. In the full formulation, the 8 ka time in the load history corresponds to the ablation of marine-based ice in Hudson Bay, which results in water dumping and yields positive ocean heights. At 8 ka, the time-dependent nature of the ocean function also allows expression of the incursion of the sea to the west of the present-day shoreline of Hudson Bay. The full formulation also predicts that the Grand Banks area off the east coast of Newfoundland is emergent at both 26 and 8 ka.

Similar to Figure 3.5, Figure 3.6 shows maps of predicted ocean heights at two different times in the load history in the region around Australia. This region can be considered to be located in the far-field relative to the location of the former ice sheets. In the FC formulation, the ocean function does not change through time, and the regions that are currently shallow continental shelf are not predicted to have been emergent at any time in the past. Conversely, in the updated formulation, these regions are predicted to be emergent at 18 ka because of the decreased volume of water in the global ocean. In the FC formulation, the ocean heights increase in value between 18 ka and 5 ka as a result of global deglaciation causing globally averaged sea-level to rise (because displacements are calculated globally, this increase in ocean height does not represent true 'eustatic' sea-level rise, but as a far-field region, it is a reasonably close approximation). The predicted ocean heights for both times in the FC formulation are negative because they represent an expression of the GIA-induced perturbation to the background regional ocean, which in far-field regions, is dominated by the 'missing' mass of the ocean stored on land. In the full formulation, the negative ocean heights change very similarly between 18 ka and 5 ka. However,

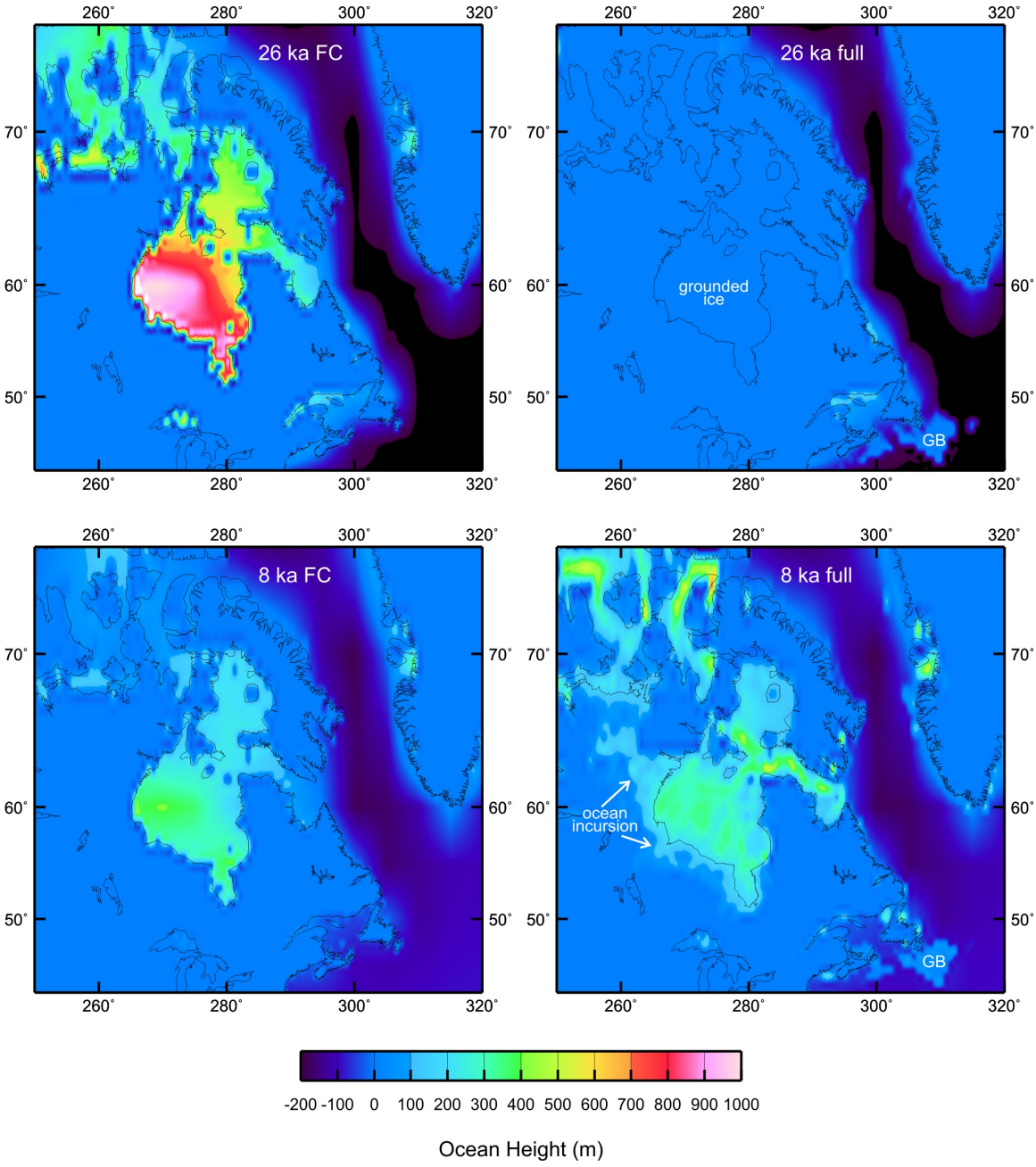

Figure 3.5: Ocean heights around near-field Hudson Bay, predicted for both the Farrell and Clark (FC) and full formulations, at 26 ka and 8 ka. The full formulation accounts for grounded marine ice in Hudson Bay at 26 ka. At 8 ka, the full formulation also predicts water dumping associated with the ablation of marine-based ice in Hudson Bay, as well as the incursion of the sea relative to the present-day coastline of Hudson Bay. At both times, the full formulation also predicts emergence of shallow present-day bathymetry, such as the Grand Banks (GB).

as globally averaged sea-level rises in this formulation, the areas surrounding the present-day Australian coastline that are emergent at 18 ka are submerged by 5 ka, and are characterized by small positive ocean heights. These ocean heights are positive because they represent a non-perturbative addition to the total ocean load at these locations.

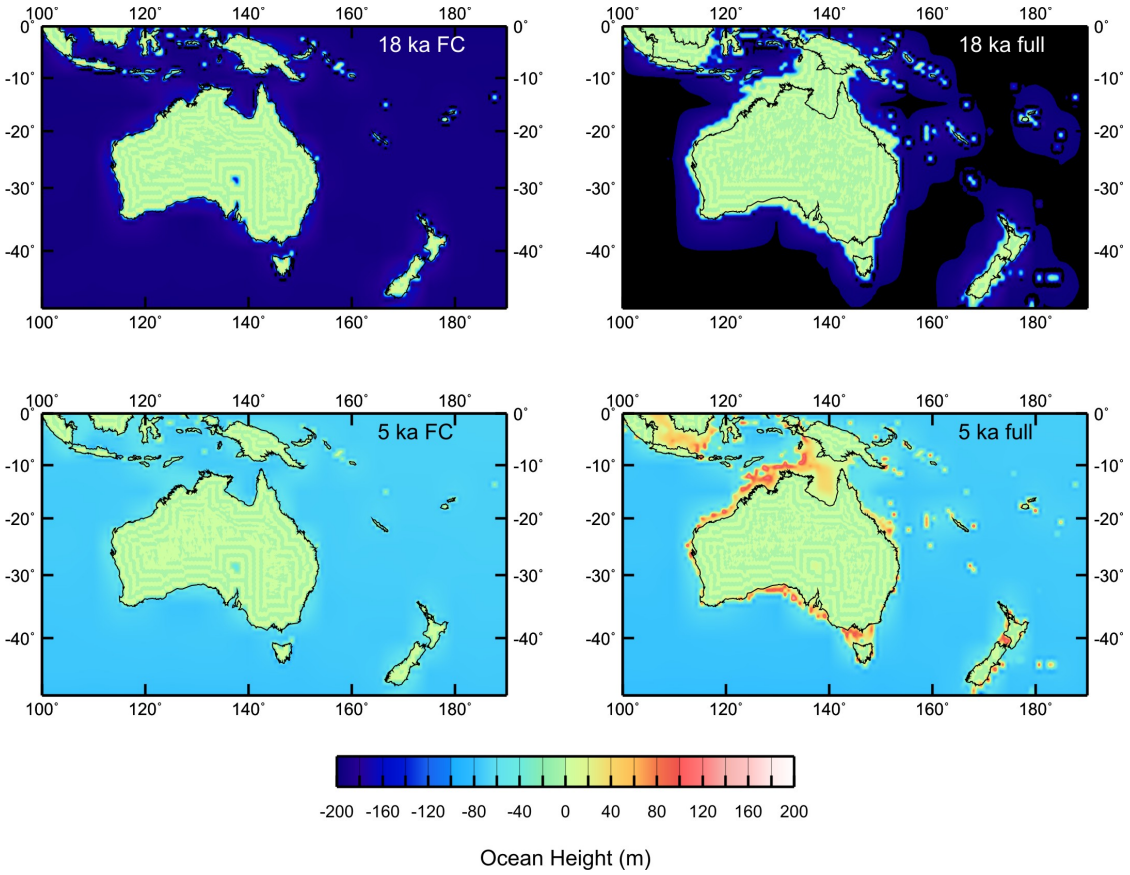

Figure 3.6: Ocean heights around the far-field Australian region, predicted for both the Farrell and Clark (FC) and full formulations, at 18 ka and 5 ka. The full formulation accounts for the emergence of shallow present-day continental shelves in the past, as well as their subsequent submergence in response to rising globally-averaged sea-level.

3.4.3 Relative Sea-level

Figures 3.7-3.8 show the difference in predicted relative sea-level for the FC and full formulations of the sea-level equation for both the near-field Hudson Bay and far-field Australian regions. Again, the predicted differences between the two formulations qualitatively compare well with the results of Milne (1998) and Kendall et al. (2005). The difference between the full and FC formulations (full-FC) results in a negative

relative sea-level difference in Hudson Bay, with a maximum predicted difference of approximately 140 m at 8 ka (Figure 3.7). Because both formulations predict relative sea-level to be positive (and decreasing through time), the negative RSL anomaly means that the FC formulation overpredicts relative sea-level change. This difference occurs because the water dumping effect included in the full formulation offsets the loss of mass from the removed ice load, which in turn results in smaller GIA displacements and thus smaller changes to the position of relative sea-level.

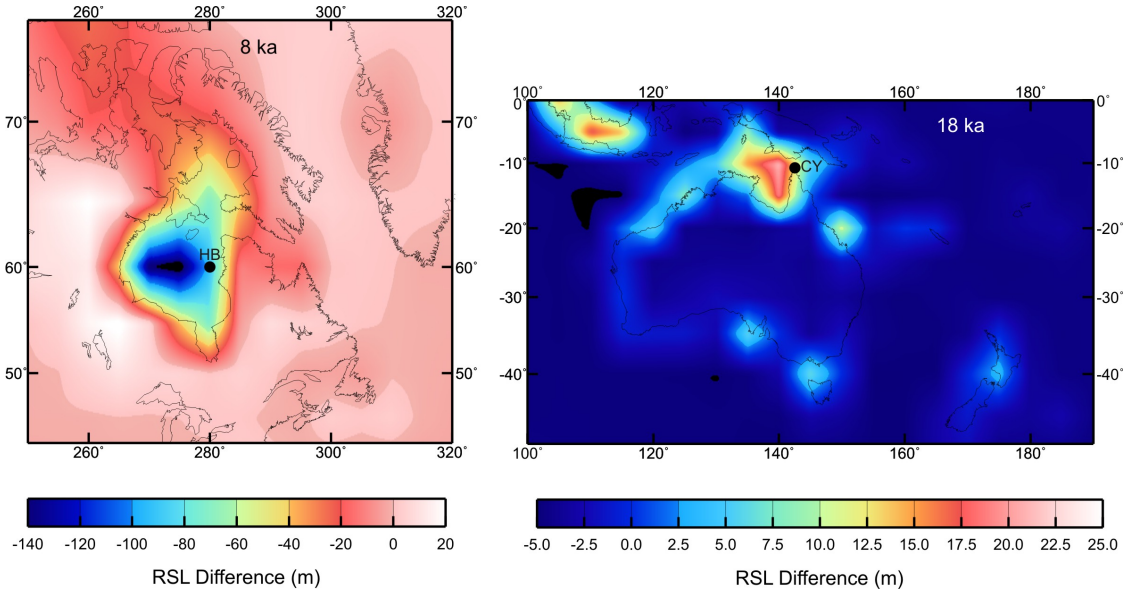

Figure 3.7: Maps of the predicted difference in relative sea-level for the Farrell and Clark formulation versus the full formulation (shown are the 'full' values minus the FC values). In near-field Hudson Bay (left), the full formulation allows the water dumping effect to offset the effect of ice retreat; thus, the magnitude of the surface load variation is less than in the FC theory, and predicted relative sea-level is lower by up to 140 m at 8 ka. Around far-field Australia (right), the full formulation accounts for the effect of a shallow and sloping continent-ocean boundary; incorporation of the shallower shelf topography reduces the predicted ocean heights relative to the FC case, which decreases the predicted local subsidence of the surface, and thus also decreases predicted relative sea-level. Two sites locations in Hudson Bay (HB, left) and in northern Australia (Cape York, CY, right) are shown with black dots and their relative sea-level change through time is plotted in Figure 3.8.

The opposite is however true for the far-field Australian region (Figures 3.7-3.8). Here, the difference between the full and FC formulations (full-FC) results in a smaller (<25 m), positive anomaly to predicted relative sea-level (shown at 18 ka in Figure 3.7). Because both formulations predict relative sea-level to be negative (and increasing through time), the positive RSL anomaly means that the FC formulation

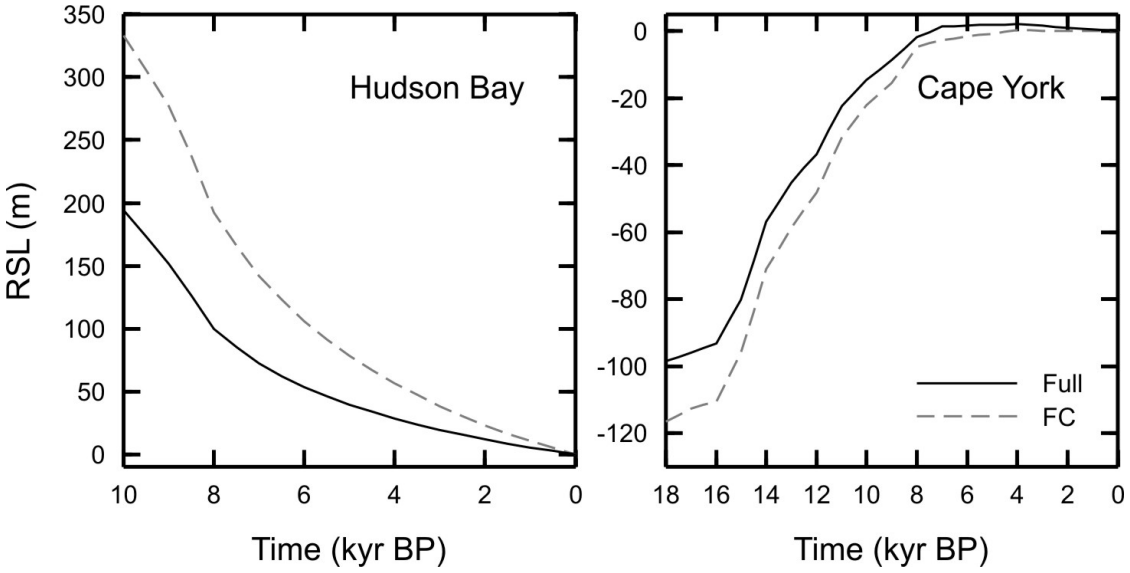

Figure 3.8: Predicted relative sea-level change for the Farrell and Clark formulation (grey dashed line) versus the full formulation (black solid line) plotted through time. Near-field Hudson Bay (left) and far-field Cape York, Australia (right), are shown. See caption of Figure 3.7 for explanation of the difference between the full and FC predictions. Site locations are plotted as black dots in Figure 3.7.

overpredicts the magnitude of the lowstand north of Australia. This overprediction occurs because the FC formulation assumes that the continent-ocean boundary is everywhere characterized by steep vertical cliffs. This assumption leads to overpredicted ocean heights, and thus overpredicted local subsidence of the Earth's surface.

3.5 Summary

This chapter has summarized the incorporation of the full solution to the sea-level equation into the existing GIA code. The ocean loading treatment followed the methods of Mitrovica and Milne (2003), and the results shown in Section 3.4 compare well with those described in the studies of Milne (1998) and Kendall et al. (2005). The results further show that the incorporation of moving shoreline geometry into the sea-level equation can significantly influence GIA model predictions, and is particularly important in regions of marine-based ice retreat, such as around Hudson Bay. The full formulation is used for the GIA calculations shown in Chapters 5-7.

Chapter 4

Glacial and Geological History of Northern Canada

This chapter briefly summarizes the glacial history and aspects of the tectonic evolution of northern Canada. The chapter includes descriptions of the evolution of the Laurentide and Innuitian ice sheets during the most recent glaciation (Section 4.1), the tectonic and geological setting of the study area (Section 4.2), and available geophysical constraints on Earth structure and mantle rheology (Section 4.3). Although a much more extensive review of these topics would be possible, only the key points are summarized, and their relevance to the current GIA modelling study are discussed (Section 4.4).

4.1 Ice Sheet History

During the last major glaciation, much of the North American continent was covered by a large ice sheet complex (Figure 4.1). The three major ice sheets of this complex were the Laurentide Ice Sheet, centred over Hudson Bay and the Canadian Shield, the Innuitian Ice Sheet, which covered the Queen Elizabeth Islands, and the Cordilleran Ice Sheet to the west of the Rocky Mountains (Dyke 2004). The smaller Appalachian Ice Complex covered the maritime region of Canada. During the last glaciation, all three of the North American ice sheets were confluent, as were the Innuitian and Greenland ice sheets. The main focus of this project is on the evolution of the northern sector of the Laurentide Ice Sheet and the Innuitian Ice Sheet. Other aspects of the evolution of both the Laurentide Ice Sheet and the Innuitian Ice Sheet are also summarized in Chapters 5-7.

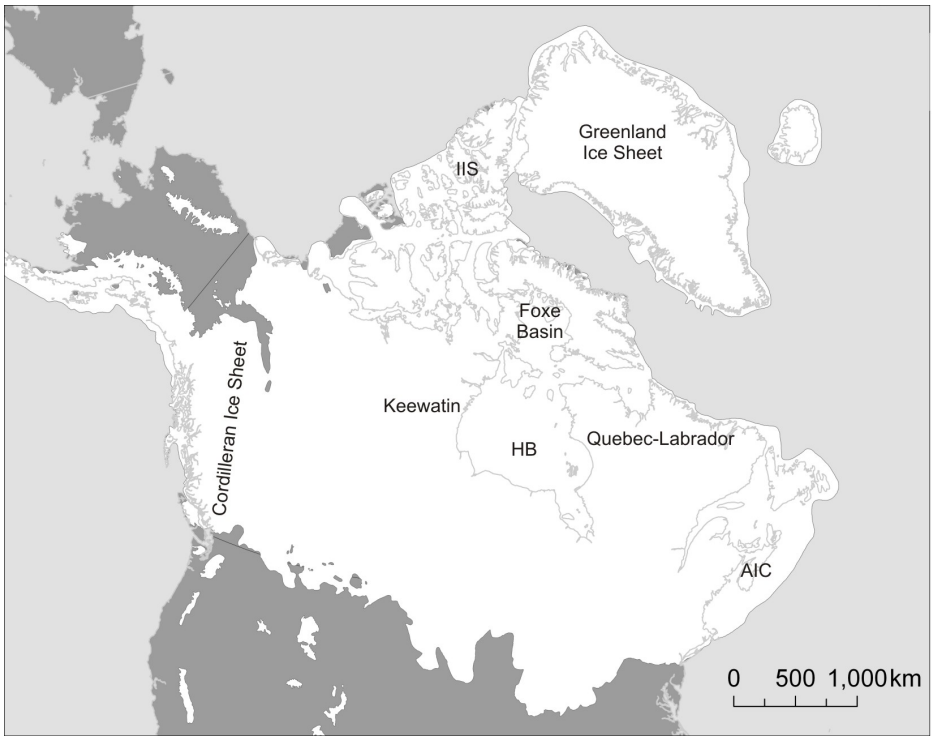

Figure 4.1: Map of the Laurentide Ice Sheet and surrounding ice cover at LGM. The Laurentide Ice Sheet was confluent with the Cordilleran Ice Sheet to the west, the Appalachian Ice Complex to the east, and the Innuitian Ice Sheet to the north. The ice sheet had three major load centres over Keewatin, Quebec-Labrador and Foxe Basin. AIC - Appalachian Ice Complex, HB - Hudson Bay, IIS - Innuitian Ice Sheet.

4.1.1 Laurentide Ice Sheet

Growth of the Laurentide Ice Sheet from its last interstadial minimum commenced approximately 30-27 ^{14}C kyr BP in the late Wisconsinan (Dyke et al. 2002). The peak extent of the Laurentide Ice Sheet was reached by approximately 24-21 ^{14}C kyr BP. In the global sea-level record, the advance of the Laurentide Ice Sheet is coincident with an observed rapid drop in eustatic sea level. The onshore limit of the Laurentide Ice Sheet at its maximum extent is marked by moraines and till deposits, and margin chronology is constrained by radiocarbon dates on subtill organic material (Dyke et al. 2002). On the eastern margins of the LIS, as well as much of the northern margin, the ice sheet terminated offshore and its boundaries are less well constrained. On a continental scale, deglaciation was minor until about 14 ^{14}C kyr BP. Therefore, while the LGM is typically defined as occurring at approximately 18 ^{14}C kyr BP, the maximal period of Laurentide glaciation both preceded and persisted long after this time. The main phase of deglaciation of the Laurentide Ice Sheet occurred between

14 and 7 ^{14}C kyr BP, during which time there was a nearly linear 90% reduction in the area of the ice sheet complex relative to its area at LGM (Dyke 2004). By 5 ^{14}C kyr BP, deglaciation of North America was nearly complete, leaving the Greenland Ice Sheet as the only major ice sheet remaining in the northern hemisphere.

On a continental scale, observed flow direction patterns suggest that the Laurentide Ice Sheet consisted of three major ice domes over the Keewatin region, Quebec-Labrador, and Foxe Basin (Figure 4.1). Detailed regional studies have indicated that in both Keewatin and Quebec-Labrador regional ice divides migrated throughout the last glacial cycle. In Keewatin, detailed mapping of ice flow direction indicators has revealed a complex history of ice-divide migration and reversal throughout the last glacial cycle, with ice divides shifting orientation and position by as much as 500 km during different evolutionary phases of the LIS (McMartin and Henderson 2004a,b, McMartin et al. 2006). In Labrador, prior to the LGM, the regional ice divide migrated northwestward towards Hudson Bay to form a loading centre near Richmond Gulf (Dyke et al. 2002). After the LGM, the divide then migrated east towards Schefferville to form a load centre farther east of Hudson Bay which included a component of regional flow northward towards Ungava Bay.

While the retreat and advance of the Laurentide Ice Sheet can be inferred from relative sea-level histories and the spatial and temporal distribution of meltwater channels, moraines and glacial erratics, direct estimates of ice thickness are sparse. Relative ice thicknesses can be inferred from flow direction indicators which suggest the presence of regional loading centres, minimum thickness estimates can be obtained from overtopped mountains, and ice surface elevations can be determined where the ice terminated on land (Dyke et al. 2002). Aside from these few observational constraints, Laurentide Ice Sheet thicknesses, particularly in interior regions, are generally estimated using predictions from glacial isostatic adjustment and, to a lesser extent, glaciological models.

4.1.2 Innuitian Ice Sheet

The extent of the last glaciation in the Queen Elizabeth Islands and the existence of the Innuitian Ice Sheet were debated for over a century (Dyke 1999 provides a good review), and competing interpretations of the regional glacial history were typically divided into two general hypotheses. In the first hypothesis, the most recent glaciation was not extensive in the QEI, and no continuous ice sheet was present. Rather,

glaciers and ice caps thickened and extended beyond their present-day boundaries, and ice coverage consisted of a series of discontinuous ice caps with peak ice thicknesses likely not exceeding 1000 m (e.g., England 1976, Dyke and Prest 1987). The second hypothesis, which was based largely on the pattern of Holocene emergence, featured extensive ice coverage over the QEI and the presence of a continuous ice sheet during the LGM (Blake 1970).

The present consensus is that a continuous Innuitian Ice Sheet did exist, and that it consisted of an alpine sector and a lowland sector (England et al. 2006). In the northeast, the alpine sector developed over the mountain ranges and fiords of Axel Heiberg and Ellesmere islands. The lowland sector of the IIS lay to the southwest, where ice covered the coastal plain topography of the southern QEI and filled the inter-island channels and bays. At its maximum extent, the IIS was confluent along its southern margin with the LIS in Parry Channel, and along its eastern margin with the GRIS in Nares Strait. The position of the western margin of the IIS is not well defined, although morainal topography indicates it extended onto the continental shelf of the Arctic Ocean, and terminated below sea level (Dyke et al. 2002, Figure 4.2).

The timing of the growth and retreat of the Innuitian Ice Sheet during the last glaciation is out of phase with that of the Laurentide Ice Sheet by several thousand years. Radiocarbon ages of redeposited marine shells provide maximum ages for the advancement of the IIS of between 27-23 ^{14}C kyr throughout most of the QEI (Dyke et al. 2002), while on southern Ellesmere Island, ice-transported shells and subtill organics indicate that the ice sheet began advancing in that region as late as 19 ^{14}C kyr BP (England et al. 2004). Prior to the growth of the IIS, ice cover in the QEI from $\sim$50-19 ^{14}C kyr BP was likely similar to present-day ice cover, with discontinuous ice caps existing on Devon, Axel Heiberg, and Ellesmere islands (England et al. 2004).

The presence of extensive ice coverage throughout the Queen Elizabeth Islands is supported by numerous data sets of glacial flow direction indicators and geomorphological features. In the alpine sector, granite erratic dispersal trains and lateral meltwater channels indicate that during glaciation ice flowed outwards from regional ice divides that overtopped the topographic high points of Axel Heiberg and Ellesmere islands (Bednarski 1998, Ó Cofaigh et al. 2000). These ice flows coalesced at lower elevations in Eureka and Nansen sounds. In the central lowland sector, numerous observations of glacial striae, till deposits, recessional moraines and lateral meltwater channels extending to a Holocene marine limit all suggest that ice flowed outwards

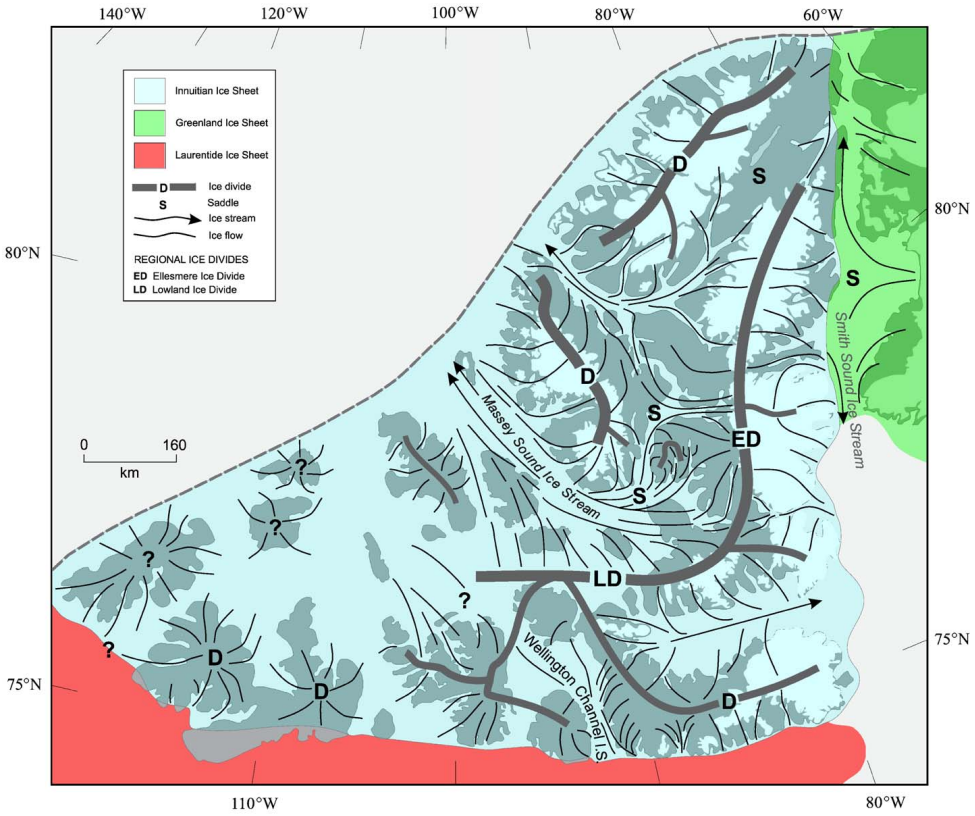

Figure 4.2: Schematic depiction of the Innuitian Ice Sheet during the last glaciation. Ice divides existed on the topographic high points in the alpine sector, coalesced in interior saddles and converged in the Massey Sound Ice Stream. Smaller ice domes existed on the islands in the lowland sector. The IIS was confluent with the Greenland Ice Sheet on its eastern margin (green shading) and with the Laurentide Ice Sheet to the south (red shading). Figure from England et al. (2006).

from a central ice divide on Devon Island (Dyke 1999). In the westernmost QEI, glaciation is recorded by striae, erratics, lateral meltwater channels and glacial landforms on Amund and Ellef Ringnes islands, and the deglacial chronology of these features can be constrained to early Holocene time (Atkinson 2003).

Retreat of the IIS did not begin until between 11-10 ^{14}C kyr BP, and recession of the IIS was asynchronous along its western and eastern margins. The retreat of the IIS began in the lowland sector along its southwestern margin. Due to its large component of marine-based ice, this sector may have been particularly vulnerable to ablation triggered by pre-Holocene global sea-level rise (Atkinson and England 2004). By 10 ^{14}C kyr BP, the marine-based portion of the lowland IIS had disappeared, and by 9 ^{14}C kyr BP only localized ice caps remained in the lowland sector. On southeastern Ellesmere Island, ice began retreating from fiords at approximately 9

^{14}C kyr BP and was mostly gone by 8 ^{14}C kyr BP (England et al. 2004). Elsewhere in the alpine sector, deglaciation followed a similar timing as marine water inundated Eureka and Nansen sounds between 8.5-8 ^{14}C kyr BP, leaving the fiords in Eureka Sound ice-free by 8 ^{14}C kyr BP (England et al. 2006).

4.2 Tectonic and Geological Setting

The study area for this research includes the Canadian Shield of central and northern North America, and also includes Baffin Island and the high north region of the Arctic. Much of central North America consists of Archean cratons that were brought together by episodes of Proterozoic orogenesis (Trettin 1991). The Archean core of the study area is dominated by the Slave, Rae-Hearne and Superior provinces (Figure 4.3). The Proterozoic Trans-Hudson Orogen extends across south-central Hudson Bay and its northeastward expression is represented by the Proterozoic Rinkian terrane that extends across central Baffin Island. Baffin Island otherwise consists of reworked and deformed Archean rocks.

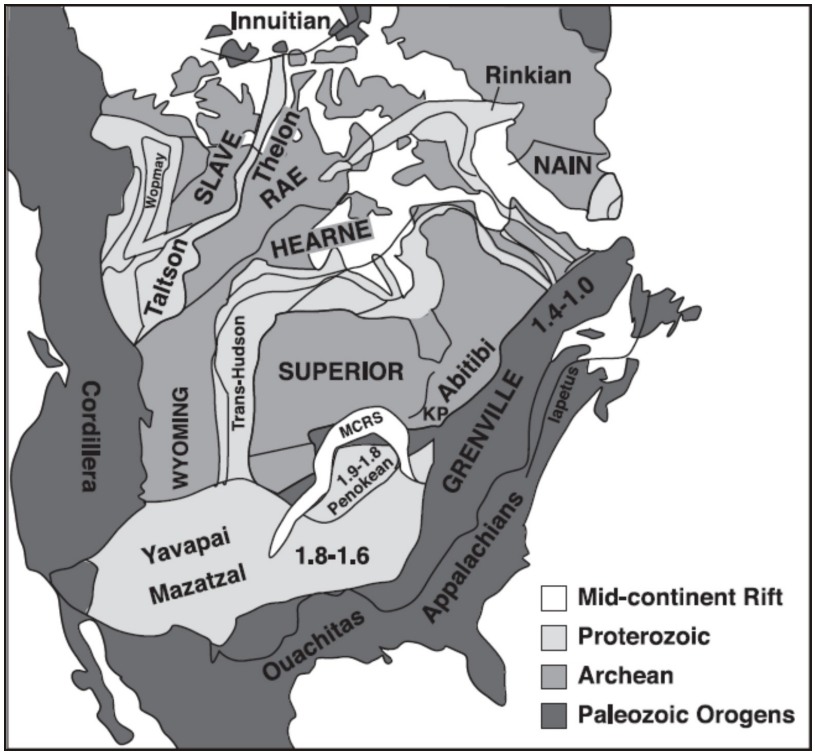

Figure 4.3: Tectonic provinces of North America. MCRS - Mid-continent rift system. Figure from Griffin et al. (2004).

The northernmost part of the Canadian Shield is exposed on the Boothia Peninsula as part of the Boothia Uplift, which is a north-south trending region of tectonic uplift that formed in the Late Silurian to the Early Devonian (Okulitch et al. 1991). The Boothia Uplift is approximately 1000 km long, and consists of an uplifted and exposed Archean basement block that is fault-bounded to both the east and west (Figure 4.4). The Boothia Uplift may have been triggered by north-northwest trending plate convergence associated with the Caledonian orogeny since uplift of north-trending structural features would have been favoured by the nearly perpendicular compressive stress (Okulitch et al. 1991). To the northeast, the Canadian Shield is bordered by the Arctic Platform, with the boundary between the two regions occurring somewhere to the south and southwest of Victoria Island (Figure 4.4). The Arctic Platform consists mainly of Phanerozoic units that have not been regionally deformed (Trettin 1991).

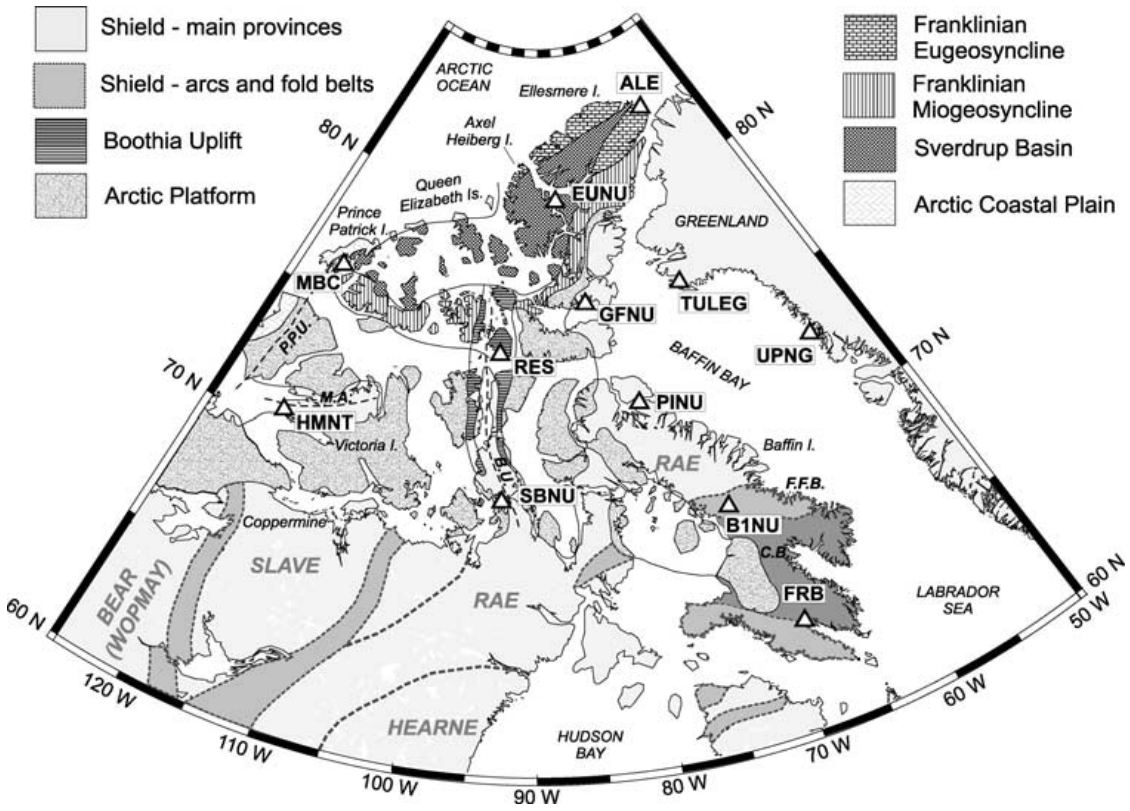

Figure 4.4: Geological and tectonic provinces of the high Arctic, and names of features and locations mentioned in the text, including the main tectonic provinces of the Canadian Shield, the Boothia Uplift, the Arctic Platform, Victoria Island, Franklinian fold belts, and Sverdrup Basin. (White triangles and site names mark the locations of broadband seismic stations in the region). B.U. - Boothia Uplift (near the station labelled SBNU). Figure from Darbyshire (2003).

The Paleozoic Innuitian tectonic province borders the Arctic Platform to the north (Figure 4.3), and is characterized by a complex tectonic history. Between the Late Devonian to the early Carboniferous, the Ellesmerian Orogeny produced the fold belts of the Franklinian mobile belt (or Franklinian Geosyncline, Figure 4.4). The Ellesmerian Orogeny was followed in the Carboniferous by extension and formation of Sverdrup Basin. The basin is exposed in the central Innuitian orogen, and overlies and is bordered to the south and east by Franklinian fold belts (Figure 4.4). Between the Carboniferous to the Late Cretaceous periods, the Sverdrup Basin underwent cycles of rifting, thermal subsidence and deposition, and consists of up to ∼15 km of sedimentary sequences (Trettin 1991). Deposition in the Sverdrup Basin was terminated in the Cretaceous by the Eurekan Orogeny, which resulted from convergence between Greenland and Ellesmere Island and caused deformation throughout the Canadian Arctic Archipelago (Oakey and Stephenson 2008).

4.3 Geophysical Constraints on Earth Properties and Inferences for Mantle Viscosity

4.3.1 Crustal Thickness

Continental to global scale seismic refraction studies indicate that the average crustal thickness of the Canadian Shield varies from approximately 35-40 km (Mooney et al. 1998, Perry et al. 2002). In the high Arctic, a regional analysis of teleseismic receiver functions has indicated crustal thickness varies across much of the Canadian Arctic Archipelago (Darbyshire 2003). The southern CAA and the Boothia Peninsula have a crustal thickness of ∼35 km, while on Baffin Island crustal thicknesses range from approximately 40-45 km. The thinnest crust is present in the Innuitian Orogen, with crustal thicknesses of ∼33-37 km in the Sverdrup Basin area and 27-32 km on northern Ellesmere Island (Darbyshire 2003). In the Innuitian region, the inversion of gravity observations has yielded crustal thicknesses that generally compare well with those derived from the receiver function analysis (Oakey and Stephenson 2008). Oakey and Stephenson (2008), who calculated crustal thicknesses by subtracting depth-to-basement values from the modelled Moho depths, indicated that the Sverdrup Basin has undergone crustal thinning from an average unthinned value of ∼35 km to ∼24 km in the central basin (Figure 4.5).

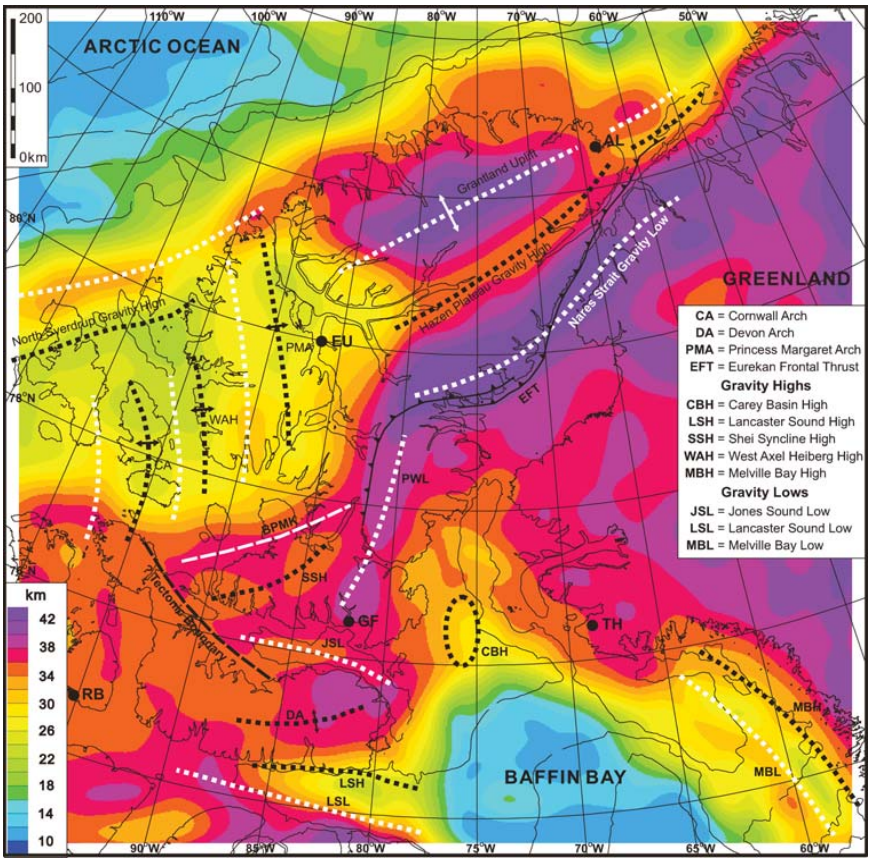

Figure 4.5: Map of modelled crustal thicknesses in the high Arctic region. The Sverdrup Basin in the interior of the Innuitian region, has undergone crustal thinning of ∼30% (average crustal thicknesses of 35 km thin to 24 km within the central basin). Figure from Oakey and Stephenson (2008).

4.3.2 Elastic Lithospheric Thickness

The effective elastic thickness of the lithosphere is the thickness of an equivalent elastic plate that would deflect by the same amount as the lithosphere in response to applied loads. The effective elastic lithospheric thickness relates to both the flexural rigidity of the lithosphere, and its elastic properties, and is essentially a measure of the lithosphere's mechanical strength or its resistance to loading (e.g., Turcotte and Schubert 2002). Studies suggest that the effective elastic thickness of the lithosphere within the Canadian Shield can vary from ∼40 km to >100 km over distances of approximately 500 km (Wang and Mareschal 1999, Audet and Mareschal 2004, Mareschal et al. 2005, Figure 4.6).

The studies of both Wang and Mareschal (1999) and Audet and Mareschal (2004) show large elastic thicknesses in the western Canadian Shield, with values in the

Trans-Hudson Orogen and Hearne Provinces locally reaching >120 km (Figure 4.6). By comparison, the Interior Platform to the west is characterized by much lower values of approximately 20-40 km. Audet and Mareschal (2004) indicate much larger elastic thickness values beneath Hudson Bay Basin than Wang and Mareschal (1999), but both studies indicate that with values reaching up to ∼70 km, the elastic thickness east of Hudson Bay is thinner than that found west of Hudson Bay (Figure 4.6).

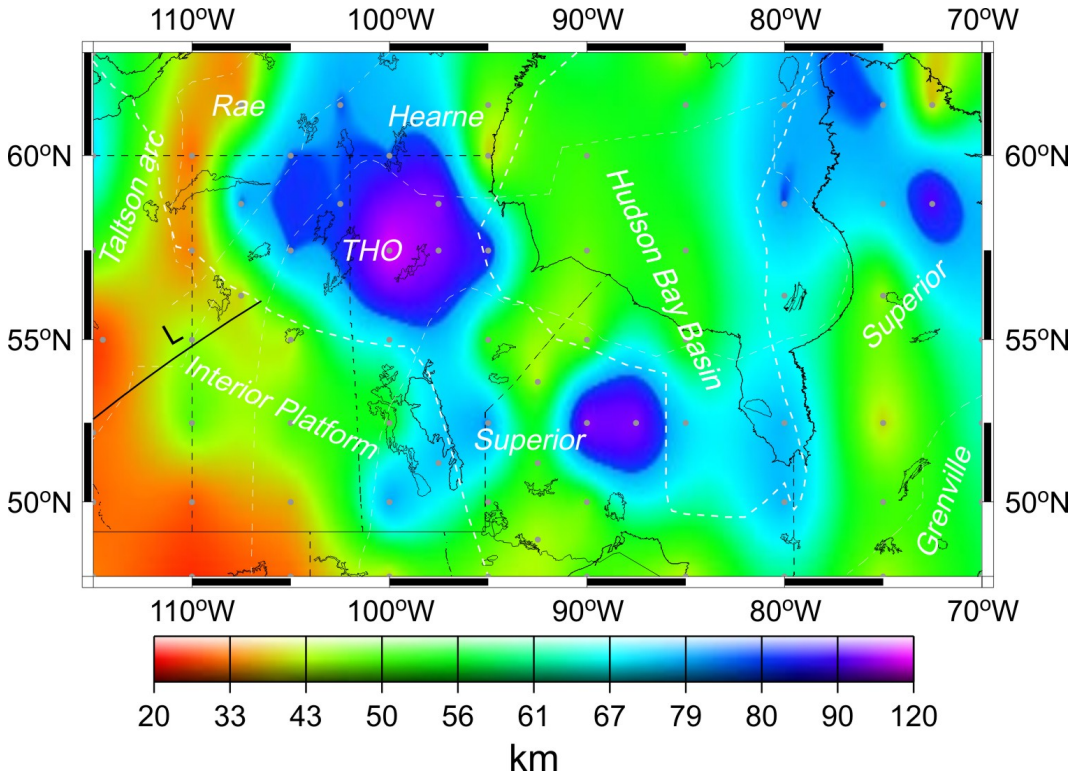

Figure 4.6: Effective elastic lithosphere thickness variations in the Canadian Shield. The major tectonic provinces are delineated by the white dashed lines. THO - Trans-Hudson Orogen. Figure from Wang and Mareschal (1999).

There is generally a lack of elastic lithospheric thickness estimates north of approximately 60° N. However, based on a compilation of geotherms from continental provinces of different age, Artemieva (2006) determined a relationship between the age and thermal state of the lithosphere and produced a global map of the depth to the 550°C isotherm on a 1° × 1° grid (Figure 4.7). For lithosphere older than 200 Ma, the depth to the 550°C isotherm can be used as a proxy for the depth to the brittle-ductile transition in olivine (Artemieva 2006). This depth can therefore also be used as a relative or proportional measure of the mechanical strength of the lithosphere (and thus also its equivalent elastic thickness). In the Canadian Shield,

the trends on the global map compare with the results of Wang and Mareschal (1999) and Audet and Mareschal (2004) with the mechanically stronger lithosphere in the region around Hudson Bay surrounded by the overall weaker lithosphere of the Interior Platform (Figure 4.7). Although this method provides only an indirect inference of elastic lithospheric thickness, and despite the lack of detail shown for the high Arctic, the global map indicates that the Innuitian portion of the study area appears to be characterized by the lowest values to the depth to the 550°C isotherm (∼30 km). This region therefore likely has the mechanically weakest (or thinnest equivalent elastic) lithosphere of the study area.

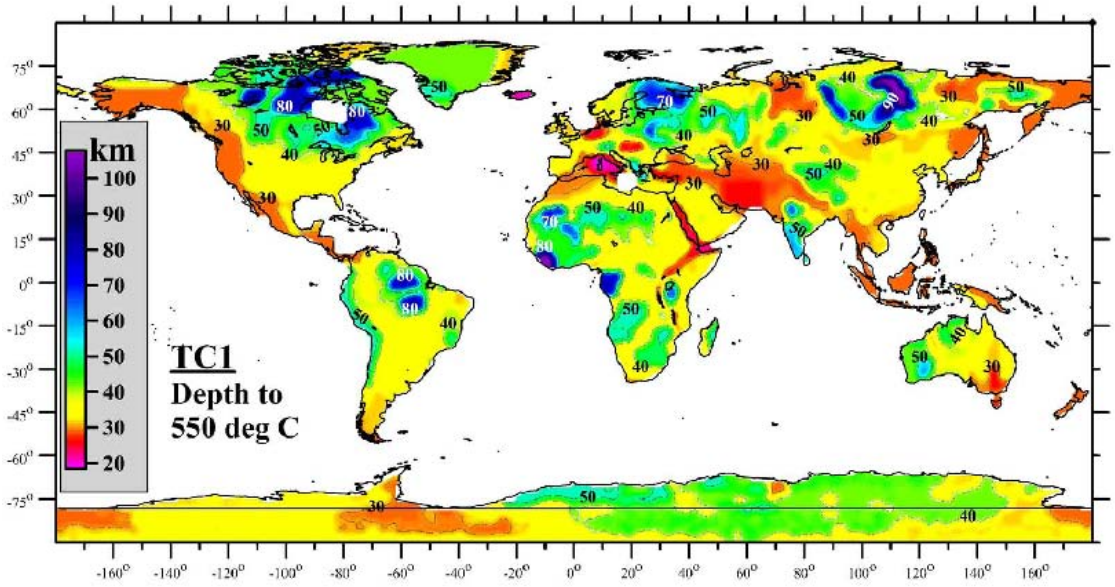

Figure 4.7: Global map of the depth to the 550°C isotherm constrained on a 1° × 1° grid. The depth to the 550°C isotherm can be used as an approximate measure of elastic thickness of the lithosphere. Figure from Artemieva (2006).

4.3.3 Heat Flow

A map derived from a summary of North American heat flow values shows clear variations in heat flow across the continent (Blackwell and Richards 2004). Within the study area, the lowest heat flow values (∼22-32 mW/m^2) occur over Hudson Bay and northern Quebec (Mareschal and Jaupart 2004). To the west and north of Hudson Bay, a zone of higher heat flow borders the region of lower heat flow values. The Slave and Rae-Hearn provinces as well as Baffin Island have estimated heat flow values that range from 40-60 mW/m^2 (Blackwell and Richards 2004, Mareschal et al.

2004). The largest range of heat flow values in the study area (and highest values overall) occur within the Innuitian region, with values ranging from 40-90 mW/m^2; Sverdrup Basin has a mean heat flow value of 57 mW/m^2 (Majorowicz and Embry 1998).

4.3.4 Mantle Temperature Inferences from Seismology

Global surface wave data sets can be inverted to obtain depth-dependent estimates of regional perturbations in shear wave velocity relative to an average reference model. The perturbations can be used to infer regional thermal profiles, with seismically fast perturbations inferring a colder (and thus more viscous) mantle (and vice versa). Figure 4.8 shows a North American map of shear wave velocity perturbations relative to an average global model at 150 km depth taken from the surface wave inversion of Nettles and Dziewonski (2008). The seismically fast anomaly beneath the Canadian Shield extends to at least 250 km depth, and implies the presence of cold and refractory mantle lithosphere.

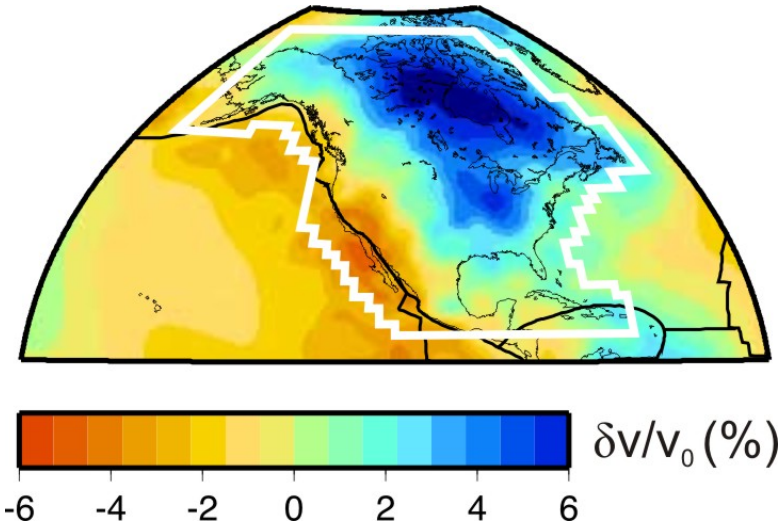

Figure 4.8: Perturbations to shear wave velocity at 150 km depth for North America relative to a global average. Blue colours indicate positive perturbations (faster velocities) relative to the global average reference model and red colours indicate slower velocities relative to the global average. Figure from Nettles and Dziewonski (2008).

4.4 Summary in the Context of GIA Models

Forward GIA modelling studies generally define a model that consists of a spatial-temporal reconstruction of ice sheet coverage applied to an Earth model that describes the elastic lithospheric thickness and the mantle viscosity profile. The fit of GIA model predictions to observational data sets is then typically used to constrain parameters relating to ice sheet evolution or Earth properties. However, the dependence of GIA model predictions on the ice sheet model and Earth model is coupled, and without sufficient independent constraints, the GIA model predictions may not be able to distinguish these parameters independently. The incorporation of independent glacial-geological constraints on ice sheet evolution or the constraints on the Earth's physical and rheological properties is therefore useful for definition of the initial model.

The reference Earth model used in this study assumes an elastic lithospheric thickness of 90-100 km, and a viscosity profile that approximates the global VM2 average of Peltier (1996). However, independent observations of elastic lithospheric thickness, surface heat flow, and mantle temperature all suggest the presence of fundamentally different tectonic domains throughout the study area, an idea that also is supported by geological and petrological evidence (e.g., Griffin et al. 2004). The presence of different lithospheric domains could be accounted for as an *a priori* model constraint either by developing a set of 1-D regional earth models to represent each major domain in the study area, or through the use of a three-dimensional Earth model. This approach would allow evaluation of how the variability in elastic lithospheric thickness influences predicted GIA behaviour. In particular, data from the Innuitian region, including the tectonic history and observations that show or infer thinned crust, thin elastic lithosphere and high heat flow, suggest that Earth properties in this region may depart significantly from those of the reference Earth model. Earth models with elastic lithospheric thicknesses that are thinner than the reference model may be more appropriate in this region, as may be mantle viscosity profiles that are characterized by lower viscosities than the reference model.

Sections 4.1-4.3 summarized some of the observations that can be used to infer or constrain independently ice sheet and Earth properties. This study uses the ICE-5G global ice sheet reconstruction of Peltier (2004) as the starting ice model. Adjustments to this model that could be made within the Laurentide component of the ice model are discussed in Chapter 6. Section 4.1.2 summarized the current geological

constraints on Innuitian Ice Sheet history. Since the paper that summarizes many of these IIS constraints (e.g., England et al. (2006)) post-dates the development of the ICE-5G model, Chapter 7 examines the effect on GIA model predictions of developing a revised IIS reconstruction that incorporates these constraints.

Chapter 5

Relative Sea-Level Data: New Observations West of Hudson Bay

This chapter focuses on the collection of relative sea level observations in the Kivalliq region of Nunavut. Section 5.1 briefly describes the existing observational database of relative sea level measurements, while Section 5.2 outlines some of the key points concerning radiocarbon dating of collected relative sea level indicators. As described in Section 5.3, the main body of the chapter appears in Section 5.4, which consists of an adapted journal article (Simon et al. 2014) about the collection and analysis of relative sea-level data in the vicinity of Arviat, Nunavut. A summary is given in Section 5.5, and supplementary material for Section 5.4 is given in Appendix C.

5.1 Existing Relative Sea-Level Database

Almost all of the relative sea-level data that is used to constrain the GIA models for this thesis project come from a large database of sea-level measurements from North America and Greenland. The database is a compilation of relative sea-level measurements collected by many different researchers over the last several decades, and was compiled and provided by Arthur S. Dyke, from the Geological Survey of Canada (Ottawa). In Canada, the spatial extent of the relative sea-level measurements includes western Canada, the Canadian Arctic Islands, Hudson Bay, the Maritimes, and the Gulf of St. Lawrence. In Chapter 1, Figure 1.2 shows the distribution of relative sea-level data in northern Canada. In Figure 1.2, each box represents one relative sea-level history, and is based on a number of radiocarbon ages of samples collected from features having an identifiable relation to past sea level. The area of the box shows the spatial extent of the observations that comprise that history.

5.2 Radiocarbon Dating

A radiogenic isotope of carbon, ^{14}C, forms in the upper atmosphere when cosmic rays react with atmospheric ^{14}N (Libby 1946). ^{14}C will continuously be incorporated into organisms until their time of death, after which the concentration of ^{14}C in the organism will exponentially decrease by radioactive decay. As shown first by Libby et al. (1949), radiocarbon dating establishes the age of a sample by measuring the sample's concentration of remaining ^{14}C, which has a known half-life of 5730±40 years (Godwin 1962). Instead of counting β decays using the methods of Libby et al. (1949), ^{14}C atoms are now often counted directly using accelerator mass spectrometry (AMS). Although the half-life of ^{14}C is now known to be 5730 years (Godwin 1962), radiocarbon dating typically assumes an earlier measured half-life of 5568 years (Arnold and Libby 1951), in order to maintain consistency with radiocarbon ages that pre-date the more accurate half-life (Stuiver and Polach 1977). Thermonuclear weapons testing in the 1950s contaminated the atmosphere with excess ^{14}C, making it impossible to date samples that died after this time (de Vries 1958); therefore, radiocarbon ages are given in years before 1950 AD. This section summarizes the corrections that need to be applied to measured radiocarbon ages.

5.2.1 Isotopic Fractionation

Living organisms use carbon in the atmosphere to carry out processes such as photosynthesis. The process of photosynthesis will discriminate against use of the heavier ^{14}C and ^{13}C isotopes in favour of ^{12}C. As a result of this fractionation, photosynthetic organisms will contain proportionally less ^{14}C and ^{13}C than the atmosphere. The concentration of ^{14}C in the organism is thus depleted relative to the atmosphere, and the depletion is not due to radioactive decay (Fleming 1976). During photosynthesis, ^{13}C will be used approximately twice as often as ^{14}C (Fleming 1976). Therefore, the measured ratio of the stable ^{13}C isotope to ^{12}C can be used to correct the radiocarbon age of a sample for its initial depletion of the unstable ^{14}C isotope.

The magnitude of the isotopic fractionation effect can be calculated by measuring the ^{13}C/^{12}C ratio of a given sample and comparing it to an established standard ^{13}C/^{12}C ratio. The conventional standard for carbon is given by the ^{13}C/^{12}C ratio of a belemnite limestone formation in Pee Dee, South Carolina, and is often just referred to as the Pee Dee belemnite (PDB) standard (Craig 1957). Isotopic fractionation ratios are expressed in parts per thousand as

$$\delta^{13}\mathrm{C} = \left(\frac{^{13}\mathrm{C}/^{12}\mathrm{C}_{\mathrm{sample}}}{^{13}\mathrm{C}/^{12}\mathrm{C}_{\mathrm{PDB}}} - 1 \right) \times 1000, \tag{5.1}$$

thus, for PDB, $\delta^{13}\mathrm{C} = 0‰$. The measured value of $^{13}\mathrm{C}/^{12}\mathrm{C} = 0.0112372$ for PDB is higher than that of most natural materials, and therefore the $\delta^{13}\mathrm{C}$ values of most samples will be negative (Craig 1957). The conventional normalization for all radiocarbon ages normalizes the ages relative to a $\delta^{13}\mathrm{C}$ value of -25‰, which is the average measured value of terrestrial wood (Stuiver and Polach 1977).

Using the equations of Stuiver and Polach (1977), and assuming normalization relative to $\delta^{13}\mathrm{C} = -25‰$, the isotopic fractionation age correction t_{corr} in years can be approximated as

$$t_{corr} \approx -8033 \ln \left(1 - \frac{2(25 + \delta^{13}\mathrm{C})}{1000} \right), \tag{5.2}$$

where -8033 years is the mean lifetime of $^{14}\mathrm{C}$, assuming a half-life of 5568 years. Using equation 5.2, it can easily be seen that a sample with a $\delta^{13}\mathrm{C}$ value of -25‰ gives an age correction of zero. Similarly, the age correction for marine shells, which typically have measured $\delta^{13}\mathrm{C} \approx 0‰$, is approximately +400 years.

5.2.2 Marine Reservoir Corrections

The radiocarbon ages of marine samples must also be corrected for the ocean reservoir effect (Stuiver and Polach 1977). This effect arises because the incorporation of atmospheric radiocarbon into ocean waters is slowed by ocean mixing and circulation. Since the ocean acts as a large reservoir for 'old' carbon, marine samples will have apparent radiocarbon ages that are typically several hundred years older than the ages of their equivalent terrestrial counterparts.

Marine reservoir correction values can be determined by radiocarbon dating marine and terrestrial material found in the same stratigraphic position (e.g., Hutchinson et al. 2004). The difference between the ages of the marine sample and the terrestrial sample is equivalent to the reservoir correction. Reservoir corrections can also be calculated by radiocarbon dating modern marine samples that were collected live prior to thermonuclear weapons testing in the 1950s (e.g., McNeely et al. 2006).

The average global marine reservoir correction is approximately -400 years (Stuiver and Braziunas 1993). However, reservoir corrections also depend on regional circulation and upwelling strength of deep water containing old carbon (e.g., Bard

1988, Hutchinson et al. 2004). For example, the average regional reservoir correction for the Canadian Arctic Islands is -720 years (McNeely et al. 2006), and can be as much as -1200 years in western Canada (Kovanen and Easterbrook 2002, Hutchinson et al. 2004). Regional reservoir corrections are therefore desirable for correcting radiocarbon ages. An exception to using a regional correction exists for marine samples that are obtained from highly migratory species, such as *Balaena mysticetus* and *Monodon monoceros* (bowhead whale, narwhal); for these samples, the global average reservoir correction is considered to be appropriate (Dyke, personal communication, 2008).

5.2.3 Calibration to Calendar Years

The radiocarbon dating method assumes that atmospheric concentrations of ^{14}C have remained constant through time. However, abundance of ^{14}C in the atmosphere has varied over time, and radiocarbon ages must be calibrated in order to determine equivalent calendar ages. The program Calib 5.1 (Stuiver and Reimer 1993) can be used to calibrate radiocarbon ages to calendar ages. Marine samples are calibrated using the Marine04 data set (Hughen et al. 2004), and terrestrial samples are calibrated using the IntCal04 data set (Reimer et al. 2004). The calibrated ages (cal BP) of the samples can be expressed as either the 1σ or 2σ probability range predicted by Calib.

5.3 Article Information

5.3.1 Author's, Coauthors', and Outside Contributions

Section 5.4 consists of a journal article published in Quaternary Research. The author of this thesis prepared all of the components of the manuscript (figures and text). As described in the paper, the author of this thesis also contributed significantly to the collection of the relative sea-level data in the field, assisted with processing the kinematic GPS data to obtain sample elevations, and calibrated the radiocarbon dates of the samples to calendar years. Coauthor Thomas James formulated much of the original research plan. Coauthors Thomas James and Donald Forbes also contributed significantly to collection of the relative sea-level data in the field. Coauthor Alice Telka identified and prepared macrofossils in our peat samples prior to their dating, and additionally brokered the radiocarbon dating of all of our samples with the Keck

Carbon Cycle AMS facility at the University of California, Irvine. Coauthor Arthur Dyke provided access to the original relative sea-level database (Section 5.1). Coauthor Joseph Henton assisted with much of the processing and interpretation of the GPS data from the campaign site. All coauthors provided feedback on this work and reviewed and revised earlier versions of the manuscript. Research scientist Jan Bednarski of the Geological Survey of Canada (GSC), Pacific Division (Sidney, BC) identified the marine shells prior to their dating, and palynologist emeritus Robert J. Mott of the Geological Survey of Canada (Ottawa, ON) identified the wood sample. Michael Schmidt and Lisa Nykolaishen of GSC Pacific (Sidney, BC), and J.C. Lavergne of the Canadian Geodetic Survey (Ottawa, ON), assisted with processing the GPS data.

5.3.2 Citation

Simon, K.M., James, T.S., Forbes, D.L., Telka, A.M., Dyke, A.S., and Henton, J.A, 2014. A relative sea-level history for Arviat, Nunavut, and implications for Laurentide Ice Sheet thickness west of Hudson Bay. Quaternary Research 82, 185-197.

5.3.3 Authors' Names and Affiliations

K.M. Simon[1,2*], T.S. James[2,1], D.L. Forbes[3,4], A.M. Telka[5], A.S. Dyke[6], J.A. Henton[7]

[1] School of Earth and Ocean Sciences, University of Victoria, Victoria, BC, V8P 5C2

[2] Geological Survey of Canada, Natural Resources Canada, Sidney, BC, V8L 4B2

[3] Geological Survey of Canada, Natural Resources Canada, Dartmouth, NS, B2Y 4A2

[4] Department of Geography, Memorial University, St. John's, NL, A1B 3X9

[5] Paleotec Services, Ottawa, ON, K1R 5K2

[6] Geological Survey of Canada, Natural Resources Canada, Ottawa, ON, K1A 0E8

[7] Geodetic Survey Division, Natural Resources Canada, Sidney, BC, V8L 4B2

[*] Corresponding author: ksimon@nrcan.gc.ca

5.3.4 Article Format

The text and figures included in Section 5.4 are taken directly from the Quaternary Research article, but have been reformatted and renumbered to maintain consistency with the rest of the thesis. The supplementary material to the article is given in Appendix C in the thesis. The references cited in the article are included with the final list of references for the thesis as a whole, and are not given separately. References to

the material presented in Section 5.4 should include the citation as given in Section 5.3.2.

5.4 A relative sea-level history for Arviat, Nunavut, and implications for Laurentide Ice Sheet thickness west of Hudson Bay

5.4.1 Abstract

Thirty-six new and previously published radiocarbon dates constrain the relative sea-level history of Arviat on the west coast of Hudson Bay. As a result of glacial isostatic adjustment (GIA) following deglaciation, sea level fell rapidly from a high-stand of nearly 170 m elevation just after 8000 cal yr BP to 60 m elevation by the mid Holocene (∼5200 cal yr BP). The rate of sea-level fall decreased in the mid and late Holocene, with sea level falling 30 m since 3000 cal yr BP. Several late Holocene sea-level measurements are interpreted to originate from the upper end of the tidal range and place tight constraints on sea level. A preliminary measurement of present-day vertical land motion obtained by repeat Global Positioning System (GPS) occupations indicates ongoing crustal uplift at Arviat of 9.3 ± 1.5 mm/yr, in close agreement with the crustal uplift rate inferred from the inferred sea-level curve. Predictions of numerical GIA models indicate that the new sea-level curve is best fit by a Laurentide Ice Sheet reconstruction with a last glacial maximum peak thickness of ∼3.4 km. This is a 30-35% thickness reduction of the ICE-5G ice-sheet history west of Hudson Bay. *Keywords: Kivalliq, Radiocarbon dating, Uplift rate, Glacial isostatic adjustment, Laurentide Ice Sheet, Tyrrell Sea*

5.4.2 Introduction

The region west of Hudson Bay is near the centre of the former Laurentide Ice Sheet (LIS) (Dyke and Prest 1987, Dyke 2004). The history of the LIS is constrained by radiocarbon ages documenting the evolution of its areal extent, but few direct measurements of ice thickness exist inland from the margins of the former ice sheet. The thickness of the LIS is needed to determine its former volume in order to construct the global sea-level budget from the last glacial maximum to present-day (Peltier 2004, 2009, Bassett et al. 2005, Tamisiea 2011). Reliable models of past ice-sheet thickness are also necessary to reproduce observed present-day vertical and horizontal crustal motions from glacial isostatic adjustment (GIA), and thereby contribute to

understanding crustal deformation and earthquake occurrence (James and Bent 1994, Argus et al. 1999, Milne et al. 2001, Mazzotti and Adams 2005, Calais et al. 2006, Tiampo et al. 2012).

Since few direct constraints on LIS ice thickness exist, its thickness history is often inferred from fitting the Earth's GIA response to available measurements of relative sea-level change (e.g., Tushingham and Peltier 1991, Lambeck 1993, Lambeck et al. 1998, Peltier 2004, James et al. 2009). Observations of past and present-day sea-level change and vertical crustal motion are therefore important for inferring LIS history and estimating the maximum thickness of the ice sheet. Prior to this study, however, the relative sea-level history of the region west of the coast of central Hudson Bay was relatively poorly constrained, especially in the mid and late Holocene. Only eight radiocarbon-constrained relative sea-level measurements were available for this region, and of these, only two were late Holocene.

In this paper, we present new radiocarbon ages and combine them with previously published ages to obtain an improved sea-level history for the region around Arviat (formerly Eskimo Point), Nunavut, on the west coast of Hudson Bay (Figure 5.1). A preliminary measurement of the rate of present-day crustal uplift obtained from repeated Global Positioning System (GPS) observations provides additional information on the ongoing GIA response at Arviat. We use the improved relative sea-level curve, as well as the present-day uplift rate, to constrain a GIA modelling sensitivity analysis that explores variations to ice-sheet thickness west of Hudson Bay in Peltier's (2004) ICE-5G reconstruction. The modelling analysis is consistent with the work of Lambert et al. (2006), Argus and Peltier (2010), and Mazzotti et al. (2011), which used GPS and gravity data and found that ICE-5G thicknesses are too large in the central sector of the former LIS. The sensitivity analysis constrains the reduction to the peak LIS model thickness west of Hudson Bay to be as much as ∼30-35%.

5.4.3 Regional setting and glacial history

During the last glaciation, the LIS was centred over the Canadian Shield, and flowed outwards onto the Interior Plains of North America. At its peak extent, the LIS was confluent with the Cordilleran Ice Sheet to the west, the Innuitian Ice Sheet to the north, and the Appalachian Ice Complex to the east (Dyke 2004). Geological mapping of ice divides and glacial flow indicators, as well as the observed pattern of gravity anomalies and present-day uplift rates, suggest that within the LIS, ice cover

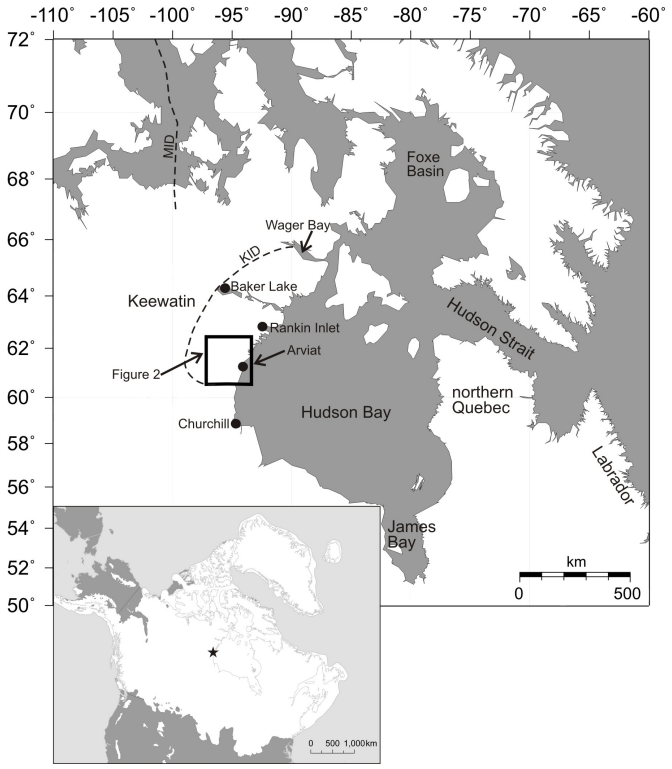

Figure 5.1: Location map showing the regional setting of the study and geographical names mentioned in the text. The former Laurentide Ice Sheet had three main load centres: Keewatin (now Kivalliq), northern Quebec-Labrador, and Foxe Basin. Approximate locations of the M'Clintock Ice Divide(MID) and its relict, the Keewatin Ice Divide (KID), are shown by the dashed lines (Dyke et al. 1982, Shilts et al. 1987, Dyke and Dredge 1989). The study area (black box) lies in the Keewatin region, and is shown in more detail in Figure 5.2. Bottom left inset map shows the extent of North American glaciation at the last glacial maximum. The GIA modelling analysis applies scaling factors to the starting ice-sheet reconstruction to a large region west of Hudson Bay while holding fixed the rest of the North American load.

nucleated in three major sectors over Keewatin, Quebec-Labrador, and Foxe Basin (Figure 5.1, Dyke et al. 1982, Dyke et al. 2002).

The study area lies within the Kivalliq (formerly Keewatin[1]) region, directly to the west of Hudson Bay (Figure 5.1). The Keewatin ice dome was located in the interior of the former LIS and reached its maximum extent by 22 ^{14}C ka BP (26.5 cal ka BP, Clark et al. 2009). Ice in this region generally flowed radially outwards from the approximately north-south trending M'Clintock Ice Divide located about 650 km west of Hudson Bay (Dyke and Dredge 1989). Just north of the study area, more recent

[1]To maintain consistency with previously published literature, we retain the Keewatin name when referring to remnant glacial features (e.g., the Keewatin ice dome, the Keewatin Ice Divide).

regional mapping has shown however that the locations of major ice divides within the Keewatin dome did not remain static throughout the last glaciation. Rather, detailed mapping of ice flow direction indicators in a region extending from just south of Rankin Inlet to north of Baker Lake (Figure 5.1), has revealed a complex history of ice-divide migration and reversal throughout the last glacial cycle, with ice divides shifting orientation and position by as much as 500 km during different evolutionary phases of the LIS (McMartin and Henderson 2004a,b, McMartin et al. 2006). On a continental scale, recession of the LIS was minor until about 14 ^{14}C ka BP (16.8 cal ka BP), after which more rapid deglaciation commenced (Dyke et al. 2002). By 10.5 ^{14}C ka BP (∼12.5 cal ka BP), retreat of Keewatin ice was well underway, and was relatively synchronous on the northern, western and southern margins of the ice dome (Dyke and Dredge 1989, Dyke 2004).

After 9 ^{14}C ka BP (10.2 cal ka BP), ice began to retreat from Hudson Strait, allowing an influx of ocean water into Hudson Bay, and triggering rapid retreat of Keewatin ice from 9.0 to 7.2 ^{14}C ka BP (10.2-8 cal ka BP, Dyke 2004). During this rapid retreat phase, marine-based ice disappeared from Hudson Bay, and continental ice shrank towards the Keewatin Ice Divide, located west of Hudson Bay. The Keewatin Ice Divide, a relict of earlier regional ice divides, developed as a late-glacial feature sometime after the last glacial maximum and generally migrated southeastward as the centre of the ice dome shifted. While the northern position of the Keewatin Ice Divide near Wager Bay remained fairly stable during deglaciation, the rest of the divide migrated to the southeast up to 250 km, reaching its final position between 8 and 7 ^{14}C ka BP (∼8.8-7.7 cal ka BP, McMartin and Henderson 2004a, McMartin and Dredge 2005, Figure 5.1).

The study area lies directly to the east of the final position of the Keewatin Ice Divide. Striations, and drumlin, esker, and moraine orientations, record a dominant southeastward ice-flow phase within the study area, and retreat of the ice sheet is marked by a series of margin-parallel recessional moraines (Lee 1959, Aylsworth and Shilts 1989). By 7.2 ^{14}C ka BP (8.0 cal ka BP) almost all of Hudson Bay was ice free, and after approximately 6.5 ^{14}C ka BP (7.5 cal ka BP), all lingering continental ice in the western Hudson Bay region had also disappeared (Dyke 2004). During deglaciation, ocean water flooded past present-day shorelines into the isostatically depressed lowland forming the Tyrrell Sea, the landward extension of Hudson Bay (Lee 1962). At its peak, the Tyrrell Sea extended past all of Hudson Bay's current margins into Nunavut, Manitoba, Quebec, and Ontario (Lee 1968).

The timing of deglaciation, subsequent marine inundation, and the gradual fall of sea level to its present-day position are constrained by relative sea-level measurements. Available data from the region suggest that the Tyrrell Sea likely reached its maximum extent in the study area sometime after 7.2-7.0 ^{14}C ka BP (8.0-7.7 cal ka BP), approximately 150 km inland from the present-day shoreline (Dyke 2004). The presence of ice-contact deltas indicates that prior to its final disappearance, remnant Keewatin ice terminated directly in the Tyrrell Sea (Shilts 1973). After reaching its landward maximum, the sea subsequently withdrew eastward as a result of glacial isostatic uplift.

Observations of gravity changes and uplift rates generally indicate large rates of ongoing glacial isostatic adjustment in the Kivalliq and surrounding regions (Lambert et al. 2001, Craymer et al. 2006, Sella et al. 2007, Tamisiea et al. 2007). However, spatial coverage of GPS stations in northern Canada is relatively sparse, and only two continuous GPS sites currently measure present-day vertical motion in the western Hudson Bay region. Baker Lake and Churchill both have observed uplift rates of approximately 11 mm/yr (Figure 5.1, Craymer et al. 2011).

5.4.4 Previous sea-level observations

Prior to this study, the relative sea-level history of the Arviat area was defined by only eight radiocarbon dates from the Geological Survey of Canada (GSC) radiocarbon dating laboratory (Table 5.1). Dyke and Dredge (1989) collated the available data and proposed a preliminary sea-level history for central Keewatin. Their emergence curve was restricted to the earlier half of the Holocene and provides constraint on the time of the maximum marine stand and the minimum time for deglaciation.

The regional marine limit marks the maximum extent of marine incursion relative to the present-day shoreline, and lies at ∼170 m elevation in the study area (Lee 1959, Craig and Fyles 1960, Craig 1969, Aylsworth et al. 1986, Dyke et al. 2005). A radiocarbon age of 6745± 250 ^{14}C yr BP (I(GSC)-8) from shells collected ≤15 km seaward of the marine limit provides a minimum estimate for the time of peak marine inundation (Lee 1959, Walton et al. 1961). The time of emergence of the 108 m elevation is constrained by the ages of shells and organic lake sediment to lie between 6600 and 5100 ^{14}C yr BP (GSC-5234 and GSC-2634, Shilts et al. 1976, Blake 1983, McNeely and Atkinson 1996), indicating that the present-day 108 m elevation was submerged at most for ∼1500 years.

Site (Fig. 5.2)	Latitude (° ' " N)	Longitude (° ' " W)	Elevation relative to high tide (m)	Material dated	Sample ID	Lab ID	Radiocarbon age (^{14}C yr BP)	Corrected age (^{14}C yr BP)	Calibrated 2σ age range (cal yr BP)	Median calibrated age (cal yr BP)	Sea-level position
1	60 55 9.93	95 42 55.728	158.8	*Carex* (sedge) achenes	10-50a	UCIAMS-92959	2855 ± 20	2855 ± 20	2884-3063	2968	Below
1	60 55 9.93	95 42 55.728	158.8	*Carex* achenes	10-50b	UCIAMS-92960	1890 ± 25	1890 ± 25	1737-1891	1843	Below
2	60 55 27	95 42 13.45	149.5	*Empetrum nigrum* (crowberry) seeds and *Carex* achenes	10-51a	UCIAMS-92961	1430 ± 45	1430 ± 45	1285-1401	1333	Below
2	60 55 27	95 42 13.45	149.5	Moss	10-51b	UCIAMS-92962	1360 ± 15	1360 ± 15	1278-1302	1292	Below
3[a]	61 56	96 27 55.0008	108 (ML 168)	*Hiatella arctica* shells	GSC-5234	GSC-5234	7200 ± 120	6570 ± 120	7235-7692	7470	Above
4[b,c]	61 40	96 33	108	Organic lake sediment	GSC-2634	GSC-2634	5080 ± 170	5080 ± 170	5474-6272	5834	Below
5	62 12 40.25	95 38 40.848	104.5	Charred *Empetrum nigrum* seeds and not charred leaves	10-48a	UCIAMS-92957	1950 ± 20	1950 ± 20	1830-1948	1899	Below
5	62 12 40.25	95 38 40.848	104.5	Marine alga blade fragment	10-48c	UCIAMS-92958	-425 ± 20	-1055 ± 20			Above
6	62 0 11.96	95 52 27.71	100	*Carabidae* (ground beetle) parts	10-46a	UCIAMS-92956	4155 ± 20	4155 ± 20	4585-4824	4701	Below
7	60 40 10.47	95 26 32.07	81.5	*Notiophilus* sp. (ground beetle) parts	10-52	UCIAMS-92963	1855 ± 20	1855 ± 20	1721-1865	1788	Below
8[d,e]	62 10	95 41	62 (ML 169)	Marine shells	I(GSC)-8	I(GSC)-8	7375 ± 250	6745 ± 250	7158-8144	7634	Above
9[f,g,h]	62 16	95 30	60	Twigs in deltaic marine sediment	GSC-1484	GSC-1484	4590 ± 220	4590 ± 220	4628-5856	5245	Marginal
10	61 6 48.4	94 47 46.168	59.6	*Agabus* sp. (predaceous diving beetle) parts	10-44	UCIAMS-92895	1380 ±20	1380 ± 20	1279-1331	1298	Below
9[f,g,h]	62 16	95 30	59 (ML 168)	*Mya truncata* shells	GSC-1434	GSC-1434	7000 ± 230	6370 ± 230	6737-7699	7264	Above
11[h]	61 48	95 41	59	*Clinocardium ciliatum* and *Macoma* sp. shells	GSC-1626	GSC-1626	6410 ± 180	5780 ± 180	6247-7086	6629	Above
12	61 8 22.21	94 49 1.78	53	*Hiatella arctica* shell fragment	10-42b	UCIAMS-90701	6615 ± 15	5985 ± 15	6735-6976	6858	Above
13[c]	62 17 30	95 20	51	Laminae of detrital organic matter	GSC-2688	GSC-2688	2370 ± 120	2370 ± 120	2147-2742	2443	Below
14	61 8 24.53	94 49 1.87	50.8	*Pterostichus (Cryobius) ventricosus* (ground beetle) parts	10-43a	UCIAMS-92955	360 ± 15	360 ± 15	320-492	438	Below
15	61 19 41.28	94 34 0.84	44.7	*Empetrum nigrum* seeds, *Carex* achenes and *Andromeda polifolia* (bog rosemary) seeds	10-53a	UCIAMS-92964	2540 ± 40	2540 ± 40	2488-2750	2621	Below
16	61 18 29.1	94 26 44.4	38.5	*Hiatella arctica* shell	09-11a	UCIAMS-72787	4300 ± 15	3670 ± 15	3961-4243	4106	Above
16	61 18 29.1	94 26 44.4	38.5	*Mytilus edulis* shell fragment	09-11b	UCIAMS-72788	4275 ± 15	3645 ± 15	3933-4215	4069	Above
16	61 18 29.1	94 26 44.4	38.5	*Balanus* sp. (barnacle) shell fragment	09-11c	UCIAMS-72789	4365 ± 15	3735 ± 15	4068-4365	4200	Above
17	61 14 52.7	94 7 28.4	28.2	*Picea* sp. (spruce) wood fragment	09-10w	UCIAMS-73105	2685 ± 20	2685 ± 20	2753-2844	2779	Marginal
17	61 14 52.7	94 7 28.4	27.8	*Empetrum nigrum* seed and leaf	09-1043T	UCIAMS-73107	2500 ± 20	2500 ± 20	2488-2721	2580	Marginal
17	61 14 52.7	94 7 28.4	27.8	Marine alga blade fragment	09-1043M	UCIAMS-73106	2950 ± 25	2450 ± 25	2437-2734	2607	Marginal
17	61 14 52.7	94 7 28.4	27.5	Twig and 2 *Vaccinium* sp. leaf fragments	09-1070T	UCIAMS-73109	-485 ± 20	-485 ± 20			Marginal
17	61 14 52.7	94 7 28.4	27.5	Marine alga blade fragment	09-1070M	UCIAMS-73108	3000 ± 20	2500 ± 20	2493-2768	2677	Marginal
18	61 16 21.96	94 14 29.52	26.9	*Mytilus edulis* shell fragment	10-65	UCIAMS-90702	3330 ± 15	2700 ± 15	2755-2993	2873	Above
19	61 14 24.62	94 6 9.82	12.3	*Empetrum nigrum* seeds and leaves	10-68aT	UCIAMS-92965	1210 ± 15	1210 ± 15	1067-1177	1131	Marginal
19	61 14 24.62	94 6 9.82	12.3	Marine alga fragments	10-68aM	UCIAMS-92966	1760 ± 15	1260 ± 15	1102-1306	1220	Marginal
19	61 14 24.62	94 6 9.82	12.3	*Empetrum nigrum* seeds	10-68c	UCIAMS-92967	130 ± 20	130 ± 20	-3-270	117	Below
20	61 12 57.06	94 6 27.3	10.7	*Empetrum nigrum* seeds	10-69	UCIAMS-92968	670 ± 15	670 ± 15	565-670	654	Below
21	61 5 23.3	94 3 11.1	9.3	Marine alga stipe fragments	09-05a	UCIAMS-73110	1355 ± 20	855 ± 20	691-905	800	Marginal
22	61 6 41.796	94 4 28.992	8.9	*Hiatella arctica* shell	09-07a	UCIAMS-72786	5050 ± 15	4420 ± 15	4965-5263	5118	Above
21	61 5 23.28	94 3 11.232	8.8	Marine alga stipe	09-16	UCIAMS-73111	1395 ± 20	895 ± 20	722-934	837	Marginal
23	61 9 10.08	94 5 15.03	6.5	Shell fragment	10-71	UCIAMS-90703	5110 ± 15	4480 ± 15	5039-5300	5192	Above
24	61 07 22.89484	94 06 17.60286	4.3	*Mya truncata* shell	09-18a	UCIAMS-72791	4105 ± 15	3475 ± 15	3700-3965	3843	Above
25[h]	61 6	94 5	2	*Mya truncata* shells	GSC-1427	GSC-1427	3630 ± 220	3000 ± 220	2737-3808	3255	Above

Table 5.1: Table of relative sea-level observations. All radiocarbon ages have been normalised for isotopic fractionation (δ^{13}C = -25‰) as discussed in the text. Corrected radiocarbon ages are marine ages that have been corrected for the marine reservoir effect. Elevations are referenced relative to the position of high tide by subtracting half the tidal range (2 m) from mean tide elevations (elevations of previously published observations were assumed to be reported relative to mean tide unless otherwise indicated). ML = marine limit, and appears for samples collected near the marine limit. Shaded entries represent the observations that provide useful constraint on the position of sea level. [a]McNeely and Atkinson (1996), [b]Shilts et al. (1976), [c]Blake (1983), [d]Lee (1959), [e]Walton et al. (1961), [f]Shilts (1973), [g]Ridler and Shilts (1974), [h]Lowdon and Blake (1979).

The radiocarbon age of twigs found in deltaic foreset beds directly overlying marine sediments indicates that the Tyrrell Sea had receded to the 60 m elevation by approximately 4600 ^{14}C yr BP (GSC-1484, Shilts 1973, Ridler and Shilts 1974, Lowdon and Blake, 1979). Two other radiocarbon dates constrain the late Holocene sea-level curve. The radiocarbon ages of shells (GSC-1427, Lowdon and Blake 1979), and organic matter from a lake core (GSC-2688, Blake 1983), place sea level between 2 and 51 m elevation between 3000 and 2400 ^{14}C yr BP.

5.4.5 Methods

The field work took place within the study area shown in Figure 5.2 during the summers of 2009 and 2010. To better constrain the late Holocene relative sea-level history, sample collection in 2009 was limited to low elevations (<40 m) within 35-40 km of Arviat. In 2010, several additional inland locations at elevations above 60 m, and up to ∼150 km inland, were reached by helicopter. Locations for sampling were determined by a combination of satellite imagery and air photo interpretation of raised beaches and other glacial landforms, as well as ease of accessibility through existing roads and trails. In addition, the study benefitted from traditional knowledge, as members of the local community provided information on inland locations where they had observed marine shells and algae.

The samples consist of marine shells and algae, wood, and peat. The marine shells, wood, and two of the algae samples were collected from gravel pits and road-cuts. The remaining algae samples and peat samples were acquired by digging shallow (<70 cm) pits (limited by the depth of seasonal thaw) and sampling from either the deepest level accessed or, where visible, directly above the contact between underlying clastic sediments (generally beach deposits) and overlying peat.

Precise site elevations were obtained by GPS measurements. A GPS base station was established at Government of Nunavut benchmark 6019210 for the 2009 fieldwork, and at a GSC bedrock campaign site, ARVI, for the 2010 fieldwork (Figure 5.2). The elevations of the base stations, relative to mean sea level, were obtained by adding the geoidal correction to the ellipsoidal height determined from processing the GPS observations with the Natural Resources Canada Geodetic Survey Division (GSD) Precise Point Positioning (PPP) GPS analysis software (Kouba and Héroux 2001). At each sampling location, site elevations were determined from static GPS measurements that were processed relative to the base station using the Ashtech Solu-

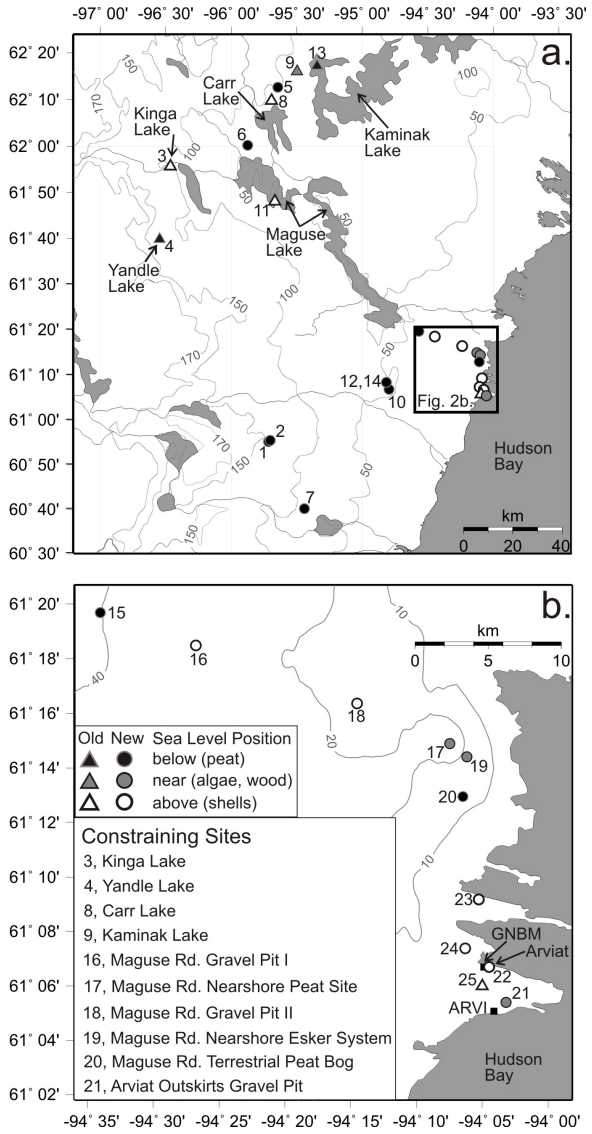

Figure 5.2: Site locations of the previously published and new relative sea-level observations. Data from higher elevations are found up to 150 km away from the current shoreline (a), while data from lower elevations are closer to the community of Arviat (b). Site locations are numbered sequentially from high to low elevation. Site locations new to this study are shown by circles, site locations of previously published radiocarbon ages are shown by triangles. Site locations are shaded according to whether the inferred position of sea level is above, near, or below the collected sample (white, grey, and black, respectively). Grey contours show regional elevations in metres. The regional marine limit is observed at approximately 170 m elevation. The sites that provide good constraints on the position of sea level are listed in the box in b and are discussed in detail in the Results section. The location of the campaign GPS bedrock site, ARVI, is shown by a black square. Government of Nunavut benchmark 6019210 is labelled GNBM (partially visible black square) and is located approximately 600 m west of site 22.

tions software. Several GPS observations were taken at the waterline at various times corresponding to different tidal states and were found to be in good agreement with the Arviat tide table[2]. These tidal observations indicate that the geoidal correction applied to the ellipsoidal site elevations corresponds to the approximate position of mean tide.

For this study, all sample elevations, including those of the previously published data, are referenced to the high-tide level, rather than mean tide. Many of the new observations are interpreted to relate to the elevation of the high-tide line, making the reference relative to high tide an appropriate choice. Because the maximum observed tidal range at Arviat is 4 m (footnote 2), high-tide elevations were obtained by subtracting half the tidal range (2 m) from the elevations referenced to mean tide. Site elevations are estimated to be accurate to within ±1 m.

Prior to radiocarbon dating, the peat samples were examined for datable material, such as seeds, leaves, and fossil insect remains. At two collection sites, macroscopic fragments of marine algae blades and stipes were isolated, but macrofossils extracted from peat otherwise consisted of terrestrial material. In all cases, identified macrofossils, rather than bulk peat samples, were dated. Radiocarbon dating of all samples was performed at the Keck Carbon Cycle AMS facility (University of California, Irvine) using the accelerator mass spectrometry (AMS) method.

It is now standard practice to normalise radiocarbon ages relative to a δ^{13}C value of -25‰. However, five of the previously published GSC marine shell ages did not follow this normalisation. Before 1986, only a selection of GSC samples had δ^{13}C measurements. Furthermore, prior to 1992, GSC marine shell ages with or without δ^{13}C values were not normalised to δ^{13}C = -25‰ (McNeely and Brennan 2005). The ages of samples I(GSC)-8, GSC-1427, GSC-1434, and GSC-1626 were originally reported without a δ^{13}C measurement. Sample GSC-5234 has a measured δ^{13}C value of +1.89‰, and later measurements performed on samples GSC-1427 and GSC-1626 yielded δ^{13}C values of +2.12 and +1.97‰, respectively (McNeely and Brennan 2005).

Because marine shells typically have a δ^{13}C value of approximately 0‰ (Stuiver and Polach 1977), the ages of I(GSC)-8 and GSC-1434 were normalised by adding 400 yr. The ages of GSC-1427, GSC-1626, and GSC-5234, all with measured δ^{13}C ≈ 2‰, were normalised by adding 430 yr (McNeely and Brennan 2005). The radiocarbon ages of all samples collected in the current study were normalised relative to a δ^{13}C

[2]http://www.tides.gc.ca/eng/station?type=0&date=2013%2F07%2F21&sid=5040&tz=CDT&pres=1. Accessed June 7, 2013.

value of -25‰, following the conventions of Stuiver and Polach (1977).

A regional marine reservoir correction of -630 ± 40 ^{14}C yr was calculated for the Hudson Bay region (McNeely et al. 2006). This reservoir correction was determined by radiocarbon-dating mollusk samples from Hudson Bay that were collected live prior to thermonuclear weapon tests in the 1950s. As discussed below, the ages of marine algae and terrestrial material collected from the same stratigraphic horizon in this study suggest a regional marine reservoir correction of approximately -500 ± 45 ^{14}C yr BP for marine algae samples from this study area. Therefore, a reservoir correction of -630 ± 40 ^{14}C yr is applied to marine shell ages, and a correction of -500 ± 45 ^{14}C yr is applied to marine algae ages.

All radiocarbon ages were calibrated to calendar years using the programme Calib 5.1 (Stuiver and Reimer 1993). Marine samples were calibrated using the Marine04 data set (Hughen et al. 2004), and terrestrial samples were calibrated using the IntCal04 data set (Reimer et al. 2004). The calibrated ages (cal yr BP) of the samples are expressed as the 2σ probability range computed by Calib. Unless otherwise indicated, the radiocarbon ages (^{14}C yr BP) of all samples referred to in the text have already been normalised for isotopic fractionation (δ^{13}C = -25‰) and, in the case of marine samples, corrected for the marine reservoir effect.

In addition to the collection of relative sea-level indicators, a campaign GPS site (ARVI) was installed near Arviat in 2009 (Figure 5.2). The site was established by drilling a stainless steel survey marker into bedrock and securing it with epoxy. The rock is a dark grey paragneiss with lenses of quartz (Tella et al. 2007) and the whaleback outcrop where the monument is located appears stable with no evidence of frost-heave or shattering, although heave of joint-bounded blocks has been observed elsewhere in the area. A GPS mast and choke-ring antenna were erected on the survey marker, levelled with a rotating level, and held vertical by three chains bolted to bedrock. The site was occupied for five days in 2009, and was reoccupied for three days in 2010 and 2012. The GPS data were aligned in the ITRF2005 reference frame, processed with the GSD PPP software, and plotted as a time series to determine the uplift rate.

5.4.6 Results

The marine reservoir correction for Arviat

The marine reservoir correction of -630 ± 40 ^{14}C yr applied to shells from the Hudson Bay region is the average reservoir correction of nine marine shells that were collected live prior to nuclear weapons testing in the 1950s (McNeely et al. 2006). The age difference between marine algae and terrestrial material collected from the same stratigraphic horizon at sites 17 and 19 indicates that the marine reservoir correction for algae differs from shells. At site 17, marine algae blade fragments gave a normalised, uncorrected radiocarbon age of 2950 ± 25 ^{14}C yr BP, while an *Empetrum nigrum* (crowberry) seed and leaf in the same layer gave a radiocarbon age of 2500 ± 20 ^{14}C yr BP. At site 19, marine algae fragments gave a normalised, uncorrected radiocarbon age of 1760 ± 15 ^{14}C yr BP, while *E. nigrum* seeds and leaves in the same layer yielded a radiocarbon age of 1210 ± 15 ^{14}C yr BP. The estimated reservoir correction is therefore -450 ± 45 ^{14}C yr BP for site 17, and -550 ± 30 ^{14}C yr BP for site 19. Both of these values are significantly less than the standard regional reservoir correction of -630 ± 40 ^{14}C yr derived from shells.

The difference in reservoir correction determined for the shells compared to that for the macrofossils of marine algae blades and stipes may reflect a different source of carbon for the two sample types. Cook et al. (2004) noted that many types of seaweed have the ability to obtain CO_2 from the atmosphere for photosynthesis when they are not submerged in the ocean. The incorporation of atmospheric CO_2 into the algae would result in a reduced reservoir correction (Lewis et al. 2008), an observation consistent with our smaller reservoir corrections for the marine algae samples compared to the regional shell reservoir correction. Thus, we apply a reservoir correction of -500 ±45 ^{14}C yr to the marine algae ages, which is the average of the two marine algae corrections mentioned above. A reservoir correction of -630 ± 40 ^{14}C yr is applied to all shell ages.

An updated sea-level curve for Arviat

We define a sea-level curve for the Arviat region with thirty-six radiocarbon ages, including the eight previously available GSC ages (Table 5.1, Figure 5.3). The stratigraphic context and nature of the material allows each sample to be classified accord-

ing to whether sea level was located above, below, or approximately at the elevation of the sample. The inferred relative sea-level curve is constrained by previously published radiocarbon ages before 5000 cal yr BP and by new ages after 5000 cal yr BP.

Some ages plot well away from the inferred curve, indicating that they do not provide a strong constraint on the relative sea-level history. There are, however, no discrepant ages, such as a peat age lying below the inferred curve, or a shell age lying above the inferred curve (Figure 5.3). The following section describes each of the samples that constrain sea level. The sites are ordered from highest elevation to lowest. The remaining observations are described in the Supplementary Material (Appendix C).

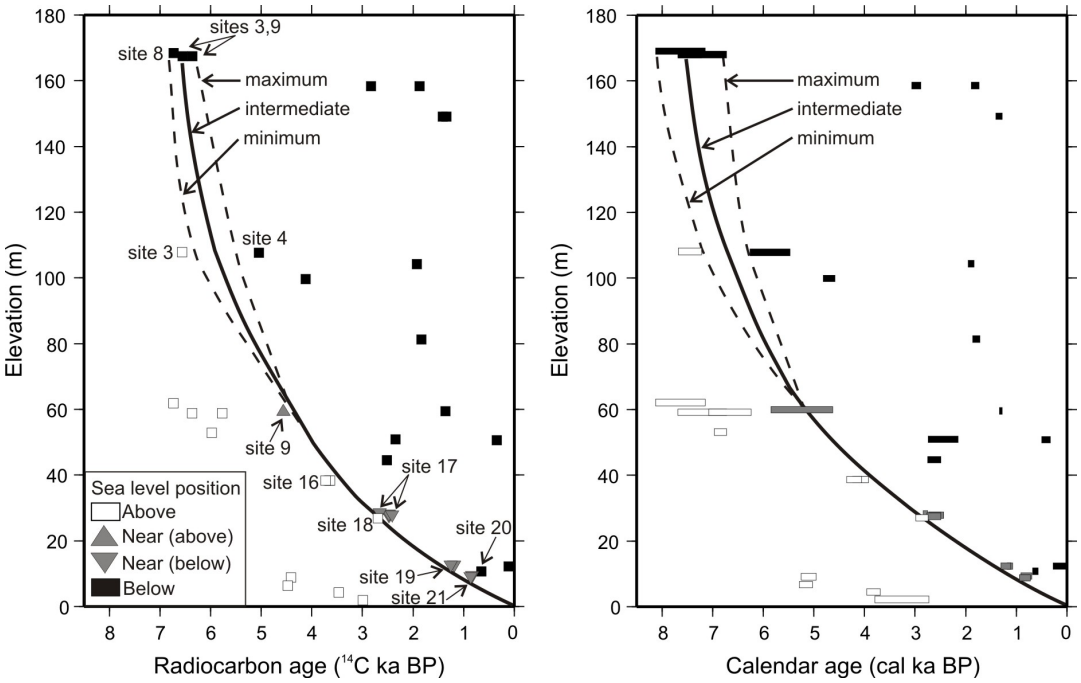

Figure 5.3: Inferred sea-level curve in radiocarbon years (left) and calendar years (right) for the Arviat region, with all sample elevations plotted relative to high tide. Observations that place sea level above, near, or below the observation are shown in white, grey and black, respectively. In the left panel, nearshore sea-level observations are shown by triangles pointing in the interpreted direction of sea level and constraining observations are identified by site number. Nearshore sea-level observations may lie within about 5 m of sea level. In the right panel, the age range of each data point reflects the minimum to maximum 2σ probability distribution. In both panels, the inferred intermediate sea-level curve is shown by the black line, and the minimum and maximum sea-level curves are shown by the dashed lines.

Site 3, Kinga Lake

Whole shells (*Hiatella arctica*, GSC-5234) collected near Kinga Lake at 108 m elevation yielded a radiocarbon age of 6570 ± 120 ^{14}C yr BP (7235-7692 cal yr BP, McNeely and Atkinson 1996). The shells were collected from the surface, and were underlain by till. The regional marine limit is observed at 168 ± 1 m elevation. Sea level at this site therefore was between 108 and 168 m elevation before 6570 ^{14}C yr BP.

Site 4, Yandle Lake

Two cores (1.94 m and 2.52 m long) collected within 20 m of each other in Yandle Lake consist of approximately 40 cm of freshwater sediment underlain by marine silty clay, with the contact occurring at the same stratigraphic position in both cores (GSC-2634, Shilts et al. 1976). Gyttja at the base of the freshwater sediment in both cores yielded a radiocarbon age of 5080 ± 170 ^{14}C yr BP (5474-6272 cal yr BP, Blake 1983). The cores were collected at an elevation of approximately 108 m. Sea level therefore had fallen below 108 m elevation before 5080 ^{14}C yr BP.

Site 8, Carr Lake

The first reported radiocarbon age from the study area comes from marine pelecypod shells collected at Carr Lake in 1952 (I(GSC)-8, Lee 1959). The shells gave a radiocarbon age of 6745 ± 250 ^{14}C yr BP (7158-8144 cal yr BP, Walton et al. 1961), and were collected in marine silty clays at 62 m elevation at the base of a hill extending to the marine limit (Lee 1959). This radiocarbon age suggests that at 6745 ^{14}C yr BP, sea level was somewhere above 62 m elevation, and below the marine limit of 168 m.

Site 9, Kaminak Lake

Twigs collected from the base of a silty sand unit near Kaminak Lake at 60 m elevation yielded a radiocarbon age of 4590 ± 220 ^{14}C yr BP (4628-5856 cal yr BP, GSC-1484, Ridler and Shilts 1974, Lowdon and Blake 1979). These sediments directly overlie marine clayey silt, which in turn overlies till. The twigs are interpreted to occur in the upper part of a marine unit in deltaic foreset beds; their age and depositional setting therefore indicate that sea level was at or just above 60 m elevation by 4600 ^{14}C yr BP. Of the observations constraining relative sea level in the early Holocene, only GSC-1484 provides a firm constraint on the position of sea level since its occurrence in an upper deltaic sequence indicates the site was just below sea level. However, the

calibrated age range of GSC-1484 is large.

At 59 m elevation, well-preserved marine shells (*Mya truncata*) collected at the base of the marine sediments from the same stratigraphic section as the twigs (GSC-1484), gave a radiocarbon age of 6370 ± 230 ^{14}C yr BP (6737-7699 cal yr BP, GSC-1434, Ridler and Shilts 1974, Lowdon and Blake 1979). This site is within 15 km of the observed marine limit. The age of the shells indicates that at 6400 ^{14}C yr BP, sea level at this site was above 59 m elevation, and below the marine limit of 168 m.

Site 16, Maguse Road gravel pit I

A gravel pit alongside Maguse Road, the road extending to the northwest from Arviat, exposed a 60 cm thick shell-rich layer of sand and gravel underlain by mud at 38.5 m elevation (Figure 5.4). There were several species of shells, and many were in an excellent state of preservation. Three radiocarbon ages were determined from samples collected from the surface sands and gravels. An articulated pair of *H. arctica* shells (09-11a) and a *Balanus* sp. barnacle fragment (09-11c) yielded radiocarbon ages of 3670 ± 15 ^{14}C yr BP (3961-4243 cal yr BP) and 3735 ± 15 ^{14}C yr BP (4068-4365 cal yr BP), respectively. In addition, a *Mytilus edulis* shell fragment (09-11b) gave a date of 3645 ± 15 ^{14}C yr BP (3933-4215 cal yr BP). *M. edulis* is a mollusk that lives only in shallow waters, and its abundance throughout the gravel pit suggests that this site was likely within approximately 5 m of sea level (e.g., Seed and Suchanek 1992, Witman and Dayton 2001). The radiocarbon ages of the shells therefore indicate that sea level was above, and likely near, 38.5 m elevation by 3645 ^{14}C yr BP.

Site 17, Maguse Road nearshore peat site

At an elevation of 28 m, excavation of a 70 cm deep hole exposed continuous layers of black fibrous peat (Figures 5.5, 5.6). Three bulk samples were collected at 43, 57 and 70 cm depth, with the deepest layer marking the depth to ice-bonded sediment. Macrofossil analyses of the upper and lower bulk samples revealed marine algae fragments interlayered with terrestrial material. Radiocarbon dating of marine algae (09-1043M) and *E. nigrum* seeds and leaves (09-1043T) in the upper layer yielded ages of 2450 ± 25 ^{14}C yr BP (2437-2734 cal yr BP) and 2500 ± 20 ^{14}C yr BP (2488-2721 cal yr BP), respectively. In the lower layer, radiocarbon dating of marine algae (09-1070M) and terrestrial twigs and leaves (09-1070T) yielded ages of 2500 ± 20 ^{14}C yr BP (2493-2768 cal yr BP) and -485 ± 20 ^{14}C yr BP, respectively.

Figure 5.4: Site 16, Maguse Road gravel pit I, 38.5 m elevation, with GPS staff and antenna for scale (approximately 2 m height). Top inset: 09-11a, articulated *Hiatella arctica* shells, with an age of 3670 ± 15 ^{14}C yr BP (3961-4243 cal yr BP). Bottom inset: 09-11b, shell fragments of *Mytilus edulis*, with an age of 3645 ± 15 ^{14}C yr BP (3933-4215 cal yr BP).

The negative age of the twigs and leaves indicates that the sample contains excess ^{14}C from nuclear bomb testing, and suggests that surface material was inadvertently incorporated into the basal sample. In addition, a wood sample from a large spruce log (09-10w, *Picea* sp.) enclosed in the surface peat and embedded below the top of ice-bonded sediment at 70 cm depth yielded a radiocarbon age of 2685 ± 20 ^{14}C yr BP (2753-2844 cal yr BP, Figure 5.5). Because the study area lies well north of the tree-line, and local rivers are not transporting logs from inland, the log is interpreted to represent driftwood. It is therefore probable that the log and marine algae represent storm surge deposits. Seasonal storms such as those currently observed in western Hudson Bay and the Arviat region (Prinsenberg 1987, Thomas 2008) likely periodically deposited driftwood and marine algae on the emerging shoreline at or slightly above the high tide mark. Since deposition by storms would likely have occurred over a relatively short time interval, this interpretation explains the lack of age progression with depth, and places sea level near, but up to 2 m below, 27.5-28.0 m elevation at approximately 2500 ^{14}C yr BP (Figure 5.6).

Figure 5.5: Site 17, Maguse Road nearshore peat site, 28 m elevation. Main photo shows the spruce (*Picea* sp.) log embedded in peat along the roadside. a) 09-10w, subsample of *Picea* log, with an age of 2685 ± 15 ^{14}C yr BP (2753-2844 cal yr BP), b) 09-1043T, *Empetrum nigrum* (crowberry) leaf, c) 09-1043T, *Empetrum nigrum* seed. Together b) and c) form sample 09-1043T, with an age of 2500 ± 20 ^{14}C yr BP (2488-2721 cal yr BP). d) 09-1043M, marine alga blade fragment, with an age of 2450 ± 25 ^{14}C yr BP (2437-2734 cal yr BP). Samples 09-1043T and 09-1043M are terrestrial and marine samples found intermixed in the same layer.

Site 18, Maguse Road gravel pit II

M. edulis shell fragments (10-65) collected from the surface of a roadside gravel pit yielded a radiocarbon age of 2700 ± 15 ^{14}C yr BP (2755-2993 cal yr BP). The presence of the shallow dwelling *M. edulis* suggests this site was just below sea level at that time. The shell fragments were found at an elevation of 26.9 m.

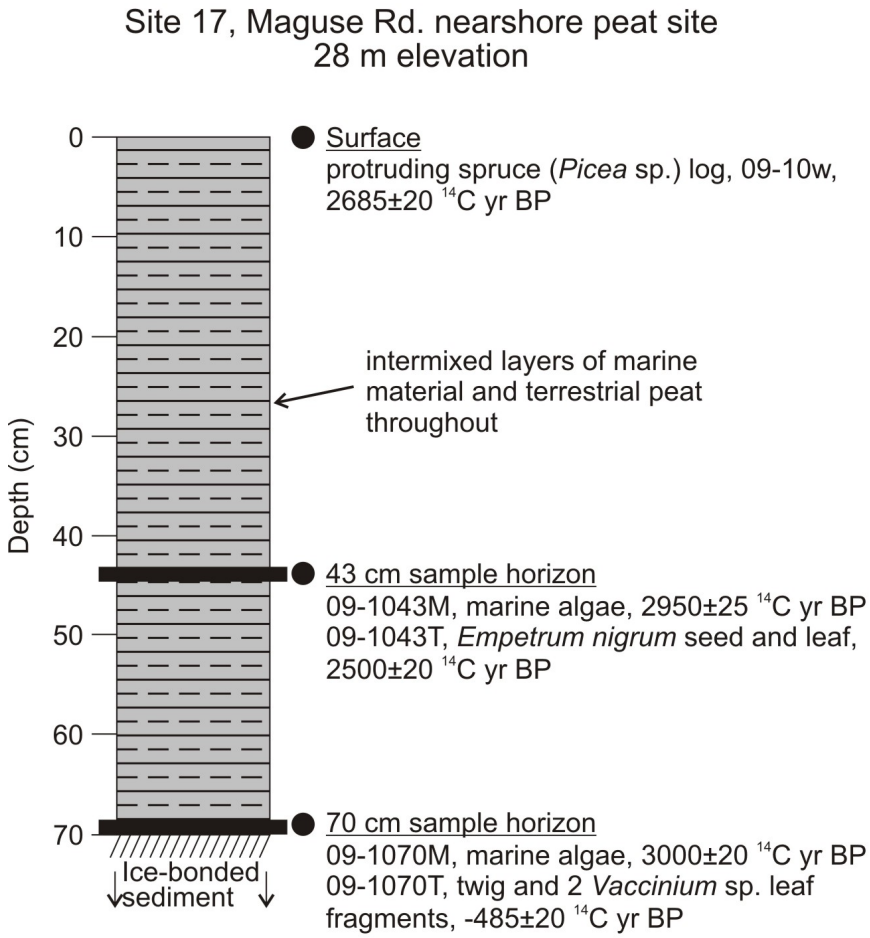

Figure 5.6: Stratigraphic sketch of samples collected at site 17, Maguse Road nearshore peat site, 28 m elevation. Samples are described in the text and shown in Figure 5.5. The depth of 70 cm marks the depth to ice-bonded sediment at the time of sampling in mid-July. Here, to explicitly show the determination of the reservoir correction for marine algae, the radiocarbon ages of the marine samples are shown uncorrected for the marine reservoir effect. The wood log is interpreted to represent driftwood and both the wood log and marine algae samples are interpreted to have been deposited onshore as storm-surge deposits.

Site 19, Maguse Road nearshore esker system

This site is located at 12.3 m elevation, and is approximately 200 m away from a large esker. Excavation of a 35 cm deep hole exposed peat overlying coarse pebbly sand. The peat occurred in alternating fibrous light brown and dark brown layers until it reached a sharp contact with underlying grey-brown sand at 24 cm depth. The surface 2 cm of dark peat was underlain by light brown peat from 2 to 6 cm

depth, dark brown peat from 6 to 14 cm, and light brown peat from 14 to 24 cm depth.

Samples from the lowermost light brown peat layer as well as the overlying dark brown peat layer were collected from 21 to 24 cm depth and 8 to 11 cm depth, respectively. Analysis of the basal peat sample revealed marine algae intermixed with terrestrial material, while the overlying layer showed no evidence of marine material. Many fly pupae from the *Ephydridae* family were also found in the basal sample, and although their species could not be confirmed with certainty, they were identified as likely being from the genus *Scatella*, found in lakeshore environments and the intertidal zone of beaches. Blade fragments of marine algae (10-68aM) and terrestrial *E. nigrum* seeds and leaves (10-68aT) from the lower layer gave radiocarbon ages of 1260 ± 15 ^{14}C yr BP (1102-1306 cal yr BP) and 1210 ± 15 ^{14}C yr BP (1067-1177 cal yr BP), respectively. *E. nigrum* seeds (10-68c) from the overlying layer gave a radiocarbon age of 130 ± 20 ^{14}C yr BP (0-270 cal yr BP).

The occurrence of marine and terrestrial material in the same stratigraphic horizon is interpreted to represent storm deposits or a setting resembling the high-tide level in a salt marsh, similar to the Maguse Road nearshore peat site. This interpretation suggests that the hightide line was near, but slightly below, 12.3 m elevation at 1260 ^{14}C yr BP. The sampling location for 10-68aT and 10-68aM is located at the base of a large esker. The side of the esker features a boulder rampart, which may have been deposited as the result of sea ice movement. The existence of the boulder rampart is consistent with very active shoreline processes at that site.

Site 20, Maguse Road terrestrial peat bog

Excavation of a 30 cm deep hole in a low-lying area near the roadside at 10.7 m elevation exposed layers of peat. Similar to site 19, the peat occurred in alternating light and dark layers, with the top 0-22 cm consisting of a light brown fibrous peat, followed by a dark brown peat with penetrating rootlets from 22 to 28 cm depth, and finally a light brown peat from 28 to 30 cm depth. The top of ice-bonded sediment was reached at 30 cm depth, and no lower contact for the deepest layer was observed. Unlike site 19, macrofossil analyses of the peat did not reveal the presence of any marine material. *E. nigrum* seeds isolated from a sample taken from 28 to 30 cm depth (10-69) yielded a radiocarbon age of 670 ± 15 ^{14}C yr BP (565-670 cal yr BP), indicating that sea level had fallen below 10.7 m elevation by that date.

Site 21, Arviat outskirts gravel pit

Two marine algae samples were recovered from the sandy gravel of an exposed esker located near the southern outskirts of Arviat. The crest of the esker was measured at 9.8 m elevation. The 2.5 m high exposure consisted of horizontally stratified beds of coarse sand and gravel between which two layers of matted organic material were observed 50 and 100 cm (9.3 and 8.8 m elevation) from the top of the exposure. Samples collected from each layer contained marine algae throughout. No terrestrial material was observed. The upper and lower samples yielded radiocarbon ages of 855 ± 20 ^{14}C yr BP (691-905 cal yr BP) and 895 ± 20 ^{14}C yr BP (722-934 cal yr BP), respectively. The continuity of the organic mats throughout the gravel pit exposure suggests that the exposure has not been disrupted. The sand and gravel layers intercalating and overlying the mats of algal material are interpreted to represent wind-wave washover deposits that likely formed as high tides and strong winds washed sediment over the top of the emerging esker. This interpretation places sea level near, but up to 2 m below, the crest of the esker at 855-895 ^{14}C yr BP.

Preliminary GPS uplift rate for Arviat

Campaign GPS occupations were carried out at Arviat in 2009, 2010 and 2012 at site ARVI. The three observations allow a preliminary present-day uplift rate for Arviat to be determined, although as noted by Craymer et al. (2006), the uncertainty of such a short dataset is large. Plotted as a time series, the GPS data yield an uplift rate of 9.3 ± 1.5 mm/yr. This GPS uplift rate is broadly compatible with the observed uplift rates at the two nearest continuous GPS sites, Churchill and Baker Lake (Craymer et al. 2011).

The rate of sea-level fall at any location is the sum of the rate of crustal uplift and the rate of change of the geoid, with the former effect providing the dominant contribution. The inferred sea-level curve for Arviat shows that the rate of sea-level fall, and thus crustal uplift, has steadily decreased throughout the Holocene (Figure 5.3). The slope of the inferred sea-level curve over the last 1000 cal yr yields an empirical 8.2 mm/yr rate of sea-level fall. When corrected for the displacement of the geoid at Arviat (estimated by GIA modelling at +1 mm/yr), the rate of recent sea-level fall gives an empirical estimate of the crustal uplift rate of 9.2 mm/yr, in close agreement with the present-day uplift rate determined from the GPS.

5.4.7 Discussion

Young basal peat ages and the timing of peatland inception

Many of the terrestrial samples extracted from basal peat layers yielded radiocarbon ages much younger than the inferred time of marine emergence (Figure 5.3). Of a total of twelve peat ages, eight are basal samples from directly above the contact between peat and underlying clastic sediments. Of the terrestrial macrofossils extracted from these eight basal peat samples, seven samples have radiocarbon ages of 3000 ^{14}C yr BP or younger, with the oldest sample having an age of 4155 $\pm$ 20 ^{14}C yr BP (4585-4824 cal yr BP). Their average age is 2130 $\pm$ 1305 cal yr BP (the uncertainty is the standard deviation of the mean). The ages are apparently independent of site elevation, which range from 10.7 to 158.8 m.

The prevalence of young ages from material taken from the basal peat samples indicates that regional environmental conditions were not favourable for peat formation until sometime after 4155 ^{14}C yr BP (4585-4824 cal yr BP). This suggestion is consistent with the observations of Zoltai (1995), whose compilation of basal peat dates from west-central Canada shows a series of basal ages from northeastern Keewatin ranging from 5110 $\pm$ 130 to 3850 $\pm$ 400 ^{14}C yr BP. The young ages are attributed to the lag time between deglaciation (or emergence) and peatland establishment, as peat formation directly over moist sandy ground is rare (Kuhry and Turunen 2006). Similarly, just south of the study area, along the southwest coast of Hudson Bay, peat formation was inhibited by late deglaciation and high soil salinity in raised marine sediments, and did not occur until 3700-2900 ^{14}C yr BP (Halsey et al. 1998).

Deglaciation occurred shortly after 8000 cal yr BP, but basal peat formation occurred mainly after 3000 cal yr BP, yielding an inferred lag time for the Arviat region greater than 5000 cal yr. This apparent lag time can be reduced by considering that peat formation following deglaciation would have been further limited by the retreat of the Tyrrell Sea. The lag time between land emergence and peat formation was determined for each basal peat age by subtracting the peat age at a given elevation from the time the inferred sea-level curve reached the same elevation. The average lag time between emergence and peat formation is 3900 $\pm$ 1490 cal yr, with minimum and maximum lag times of 1620 and 6070 cal yr, respectively. These results are generally consistent with the modelling study of Gorham et al. (2007), which showed that there is typically a 4000 cal year lag time between deglaciation and peatland

establishment. It is therefore possible that basal peat formation in the Arviat area was primarily controlled by a similar lag time. The scatters (standard deviations) of the basal peat ages and the lag times since emergence are, however, similar (1305 and 1490 cal yr, respectively). This observation indicates that our measurements give no clear preference for whether peatland formation was controlled by the time elapsed since emergence, or by the initiation of climatic conditions conducive to the growth of vegetation favourable to the formation of peat.

GIA modelling of Laurentide Ice Sheet thickness

To constrain better the history of the LIS near the former Keewatin load centre, we compare the inferred sea-level history for Arviat to sea-level predictions from a GIA model that examines variations to the ice-load thickness in the region west of Hudson Bay. The reference ice-sheet model is the global ICE-5G load history (Peltier 2004). Relative to the ICE-5G model, thinner ice cover in the former Keewatin region has been suggested by several authors (e.g., Lambert et al. 2006, Argus and Peltier 2010, Mazzotti et al. 2011). The current modelling study is presented as a sensitivity analysis, wherein we attempt to constrain the thickness overestimate of the LIS west of Hudson Bay by scaling the regional load history of the reference ICE-5G model over a range of thickness values. Each variation of the ice-load history is applied to a spherically symmetric Earth model with a 90 km thick elastic lithosphere and an underlying compressible linear viscoelastic mantle. The model viscosity profile approximates the VM2 profile derived by Peltier (1996), and has viscosities of 5×10^{20} Pa s from the base of the elastic lithosphere to 660 km depth, 1.6×10^{21} Pa s between 660 and 1160 km depth, and 3.2×10^{21} Pa s from 1160 km depth to the core-mantle boundary. The response of the Earth to surface loading is calculated following the methods described by James and Ivins (1998) for a viscoelastic Maxwell rheology. Using the theory developed by Mitrovica and Peltier (1991), the sea-level calculations include a gravitationally self-consistent global solution of the sea-level equation, and the effects of time-varying shorelines are incorporated following the methods of Mitrovica and Milne (2003). In the following we initially assume that Earth rheology is fixed, and only consider variations in ice sheet thickness. We then comment on the influence of Earth rheology.

As expected, the reference ICE-5G/VM2 model over-predicts sea level at Arviat (Figure 5.7), with over-predictions of nearly 100 m at 8000 cal yr BP, and 50 m at

5000 cal yr BP. Present-day rates of vertical crustal motion are also over-predicted by the reference ICE-5G/VM2 model. At Arviat, the reference model predicts a present-day uplift rate of 13.8 mm/yr, substantially larger than the preliminary observed rate of 9.3 ± 1.5 mm/yr, even considering the large GPS uncertainty. The over-prediction of both Holocene sea-level change and the present-day rate of vertical land motion at Arviat further support the suggestion that model ice-sheet thicknesses west of Hudson Bay are too large.

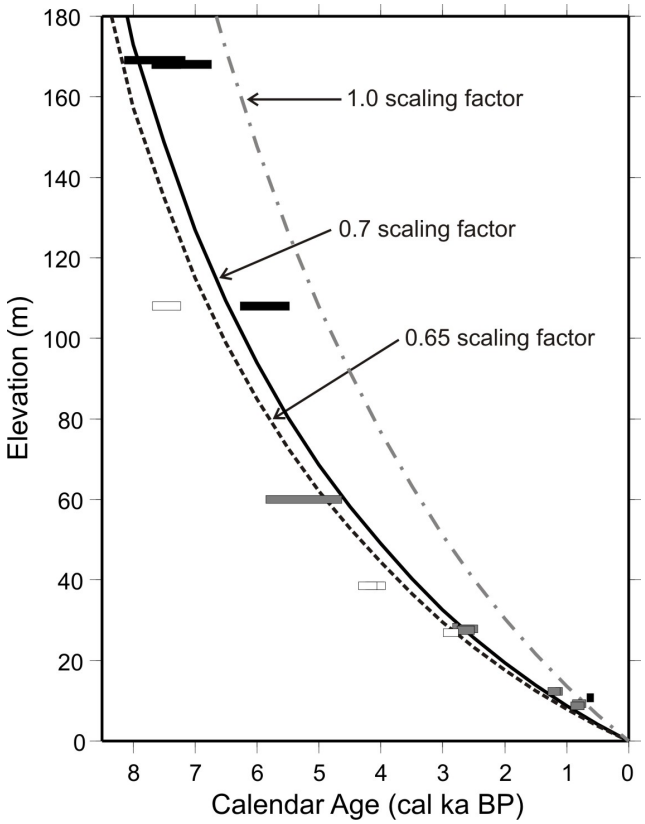

Figure 5.7: Model-predicted relative sea-level change at Arviat for ice sheet thickness scaling factors of 1, 0.7 and 0.65, applied to ICE-5G/VM2. The reference model has the load thickness scaled by a 1.0 scaling factor (grey dash-dot line) and over-predicts sea level relative to the data. GIA models with the ice-sheet thicknesses scaled down uniformly west of Hudson Bay by scaling factors of 0.65 (black dash line) and 0.7 (black solid line) better fit the observations. Only the constraining data, which are used in the calculation of the χ^2 misfit, are shown here.

To quantify the peak thickness of the LIS in this region, we apply uniform ice-sheet thickness scaling factors ranging from 0.5 to 1.3 to the reference ice-sheet history throughout the western Hudson Bay region. The scaling factors are applied only to a region west of Hudson Bay (Figure 5.1); the remainder of the global model,

including much of North America, is held fixed. For each scaling factor value, we compare the model-predicted relative sea-level curve to the constraining relative sea-level measurements (the shaded values in Table 5.1), and compute the statistical χ^2 measure of misfit (Figure 5.8). The smallest misfit between the model predictions and observations at Arviat is obtained for scaling factors of 0.65-0.7, suggesting that the ice-sheet thickness in the central sector of the LIS needs to be reduced by 30-35%. An ice-load model with a scaling factor of 0.7 predicts a present-day uplift rate of 8.6 mm/yr at Arviat, which is within the uncertainty of the measured 9.3 $\pm$ 1.5 mm/yr rate.

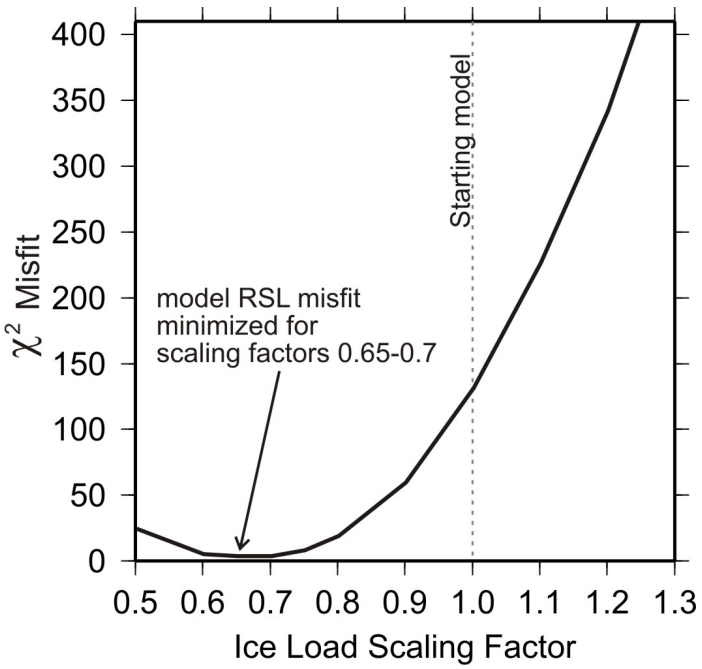

Figure 5.8: The calculated misfit between predicted and observed relative sea level (RSL) at Arviat where the thickness of the ice load reconstruction ICE-5G has been uniformly scaled within the western Hudson Bay region by factors ranging from 0.5 to 1.3. The misfit is expressed as χ^2 values, and is minimised for scaling factors of 0.65-0.70 (or a 30-35% reduction to the load thickness).

A 30-35% reduction to the ICE-5G load reconstruction west of Hudson Bay reduces the maximum thickness of the LIS in this region from over 5.2 km to approximately 3.4 km. This regional reduction decreases the global ICE-5G ice load by about 5%, and is equivalent to at least a 5 m reduction in the magnitude of the global sea-level lowstand. The global volume history of ICE-5G gives a eustatic sea-level low stand of $\sim$120 m, a value in accordance with observed sea-level low stands at far-field locations (Fairbanks 1989, Lambeck and Chappell 2001, Peltier and Fairbanks 2006).

Therefore, in order to maintain a volume history consistent with far-field records of sea level since the last glacial maximum, the volume reduction of ICE-5G west of Hudson Bay ultimately requires the addition of ice elsewhere in the global model. Argus and Peltier (2010) suggested that in addition to thinner ice west of Hudson Bay, ICE-5G requires thicker ice in southern and eastern Quebec, and along the northern British Columbia-Alberta border. The addition of thicker ice in these two regions of the model would at least partially offset the reduction to global sea level arising from the substantial decrease in ice thickness directly west of Hudson Bay, although Argus and Peltier (2010) do not directly quantify the contribution of each region to globally averaged sea level, and further note that the misfits of the model predictions to the geodetic data may alternatively be explained by changes to the temporal unloading history of the model.

The GIA model predictions are sensitive to both the ice model and the Earth model. Preliminary tests were performed where the ice load was kept constant at the reference ICE-5G thicknesses and the viscosities of the upper mantle (90-660 km depth) and lower mantle (below 660 km) were varied. The predictions for the initial ice load history provide a reasonable fit to the relative sea-level observations and crustal uplift rate only if the lower mantle viscosity is very large (10^{23} Pa s). This value for the lower mantle viscosity is larger than the estimates of most current geodynamic models (e.g., Mitrovica and Forte 2004). Additionally, the half-life decay time of the relative sea-level curve predicted by the higher viscosity model is much larger (by $\sim$1 ka) than the half-life decay times determined for the Hudson Bay region by Dyke and Peltier (2000). These factors suggest that changes to mantle viscosity, relative to the reference profile, play a subordinate role to ice-sheet thickness changes in improving the fit to the observations.

Based on the results of Argus and Peltier (2010), ICE-6G has been developed as a successor to ICE-5G, and features among its revisions thinner ice in and to the west of the study area (e.g., Peltier et al. 2012a). Although ICE-5G is still frequently used in GIA modelling, ICE-6G predictions have been employed in recent modelling analyses, including sea-level change predictions on the United States east coast and climate studies (e.g., Engelhart et al. 2011, Peltier et al. 2012b, Vettoretti and Peltier 2013). Vettoretti and Peltier (2013) stated that relative to ICE-5G, ICE-6G has been thinned by $\sim$1.5 km in central Canada, similar to the proposed reduction for the region west of Hudson Bay demonstrated by our modelling results. The results presented here use independent relative sea-level data to confirm and extend the conclusion of

previous studies indicating the need for a thinner LIS reconstruction west of Hudson Bay, and further indicate that the reduction is about 30%.

5.4.8 Conclusions

Prior to this study, few measurements constrained the sea-level history of the Arviat region, but the new data now provide tight constraints on sea-level fall in the late Holocene. The inferred sea-level curve shows that following deglaciation west of Hudson Bay, sea level in the Arviat region reached a high-stand of nearly 170 m elevation shortly after 8000 cal yr BP (Lee 1959). Sea level fell rapidly at first, dropping to 60 m elevation by approximately 5200 cal yr BP. After 5200 cal yr BP, the rate of sea-level fall decreased steadily as it reached its present day level, with sea level falling approximately 30 m in the last 3000 cal yr BP, and about 9 m in the last 1000 cal yr.

The new samples and radiocarbon ages provide an estimate of the reservoir correction for marine algae of -500 $\pm$ 45 ^{14}C yr in the study area, differing from the -630 $\pm$ 40 ^{14}C yr correction for marine shells in Hudson Bay. Additionally, basal peat ages suggest there was a nearly 4000 cal yr lag between the time of land emergence and the establishment of regional peatlands, consistent with previous studies. The observed lag time between emergence and peat formation indicates that basal peat ages do not provide a strong constraint on the position of sea level. To constrain better the early Holocene sea-level history in the Arviat area, future studies should focus on collection at higher elevations of lake cores and marine shells from exposed sequences of marine sediments.

A preliminary land uplift rate from a campaign GPS site indicates ongoing GIA at Arviat of 9.3 $\pm$ 1.5 mm/yr. This rate is in good agreement with the 9.2 mm/yr empirical uplift rate approximated from the inferred sea-level curve. The installation of a continuous GPS site at Rankin Inlet in 2012 and continuing occupations of the campaign site at Arviat will improve the precision of measured vertical uplift in the central Kivalliq region over the next decade.

The new relative sea-level curve and the GPS observations of vertical crustal motion at Arviat constrain a GIA modelling sensitivity analysis, which indicates the magnitude of the ICE-5G thickness overestimate could be as much as $\sim$30-35% in and to the west of our study area. This reduction to the load thickness corresponds to the Laurentide Ice Sheet having a peak thickness of 3.4 km west of Hudson Bay,

and decreases the contribution to global sea-level rise from this sector of the LIS by at least 5 m. Our results are generally consistent with the work of Lambert et al. (2006), Argus and Peltier (2010), and Mazzotti et al. (2011), who have also shown using gravity and GPS data that the ICE-5G ice-sheet reconstruction is too thick in the region of the former Keewatin load centre. Improved estimates of the volume of the Laurentide Ice Sheet are needed to constrain regional contributions to the global sea-level budget, and more comprehensive regional GIA modelling that incorporates sea-level data across northern Canada could help to further refine the Laurentide Ice Sheet history.

5.4.9 Acknowledgments

This work was supported by the ArcticNet Network of Centres of Excellence, the Nunavut Climate Change Partnership, and the Earth Sciences Sector (ESS) Climate Change Geoscience Program (CCGP). We gratefully acknowledge logistical support from the Polar Continental Shelf Project. We thank Andrea Darlington for assistance in the field; Jerry Panegoniak, David Vetra, Mitch Campbell, and numerous residents of the Hamlet of Arviat for support during the field work; Jan Bednarski for identification of the shell samples; Robert J. Mott for identification of the wood sample; Michael Schmidt, Lisa Nykolaishen, and J.C. Lavergne for assistance with the GPS equipment and data processing; Phil Lamothe and Jason Silliker for performing the third GPS occupation at Arviat; and Vaughn Barrie, Isabelle McMartin, and an anonymous reviewer for providing reviews that substantially improved the manuscript. KMS was supported through the ArcticNet Network of Centres of Excellence, the University of Victoria, and the ESS CCGP. This is ESS contribution number 20140009.

5.5 Summary

This chapter presented new relative sea-level data for Arviat, Nunavut. Together, the new and existing regional RSL data define a relative sea-level history for Arviat that is reasonably constrained in the early Holocene, and well constrained in the late Holocene. The GIA modelling study in Section 5.4.7 demonstrated the usefulness of this data set for constraining aspects of Laurentide Ice Sheet history. In Chapter 6, the Arviat data are used with many other RSL histories in a GIA modelling study that examines the history of the LIS over a larger region.

Chapter 6

GIA Models and History of the Laurentide Ice Sheet

6.1 Manuscript Information

6.1.1 Author's and Coauthors' Contributions

Section 6.2 consists of a manuscript in preparation for submission to Geophysical Journal International. The author of this thesis prepared all of the components of the manuscript (figures and text). Coauthor Thomas James developed, and provided access to, the GIA computer codes and formulated much of the research plan. Coauthor Joseph Henton assisted with much of the processing and interpretation of the GPS data. Coauthor Arthur Dyke provided access to the original relative sea-level database (Section 5.1).

6.1.2 Citation

Simon, K.M., James, T.S., Henton, J.A., and Dyke, A.S. Glacial Isostatic Adjustment Models in Northern Canada and the History of the Laurentide Ice Sheet. In preparation for submission to Geophysical Journal International.

6.1.3 Authors' Names and Affiliations

K.M. Simon[1,2*], T.S. James[2,1], J.A. Henton[3], A.S. Dyke[4,5]

[1] School of Earth and Ocean Sciences, University of Victoria, Victoria, BC, V8P 5C2

[2] Geological Survey of Canada, Natural Resources Canada, Sidney, BC, V8L 4B2

[3] Canadian Geodetic Survey, Natural Resources Canada, Sidney, BC, V8L 4B2

[4] Department of Earth Sciences, Dalhousie University, Halifax, NS, B3H 4R2

[5] Department of Anthropology, McGill University, Montreal, QC, H3A 2T4

[*] Corresponding author: ksimon@uvic.ca

6.1.4 Manuscript Format

The figures included in Section 6.2 have been numbered to maintain consistency with the rest of the thesis. The references cited in the manuscript are included with the final list of references for the thesis as a whole, and are not given separately.

6.2 Glacial Isostatic Adjustment Models in Northern Canada and the History of the Laurentide Ice Sheet

6.2.1 Abstract

The fit of glacial isostatic adjustment (GIA) model predictions to 24 relative sea-level histories and an additional 18 present-day GPS-measured vertical land motion rates from northern Canada constrains the thickness and the equivalent global sea-level contribution of the central and northern Laurentide Ice Sheet. The two data sets suggest that in the region west of Hudson Bay the last glacial maximum thickness of the Laurentide Ice Sheet likely did not exceed ∼3.4-3.6 km. Conversely, the GIA predictions indicate that ice may have been thicker throughout much of Quebec, and may have reached peak thicknesses there of over 4 km. The ice model thicknesses inferred for these two regions represent, respectively, a ∼30% decrease and an average ∼20-25% increase to the load thickness relative to the ICE-5G reconstruction, a result which is generally consistent with other studies that have focussed on Laurentide Ice Sheet history. In the Baffin Island region, the fit of GIA model predictions to relative sea-level data from central and northern Baffin Island indicate peak ice thicknesses of 1.2-1.3 km, a modest reduction relative to ICE-5G. Model predictions that include only the long-term viscoelastic GIA response to the last glaciation do not however simultaneously provide a good fit to relative sea-level and GPS measurements from around Baffin Island. Rather, the results suggest that vertical rates of uplift in the high north are significantly influenced by rapid present-day mass changes of regional glaciers and ice caps and the nearby Greenland Ice Sheet; correction of predicted present-day GIA uplift rates for this effect helps to reconcile the predicted rates with observations at sites that are close to present-day ice cover. The proposed modifications to the Laurentide Ice Sheet reconstruction correspond to a net change to globally averaged sea level at the last glacial maximum of up to -8 m, although, as proposed by others, this value may be partially offset by thickening the ice sheet model in regions of western Canada.

6.2.2 Introduction

During the last glaciation, large ice sheets covered much of North America, Greenland, Scandinavia, and Antarctica, and at the last glacial maximum (LGM), almost all of northern Canada was covered by the Laurentide and Innuitian ice sheets. The large amount of water stored on land in the ice sheets caused globally-averaged sea level to be ∼120 m lower at LGM than at present (Fairbanks 1989, Peltier and Fairbanks 2006), but the weight of the ice depressed the Earth's crust and mantle so that in the vicinity of the ice sheets, local sea level was tens to hundreds of metres higher than at present. Following deglaciation, glacial isostatic adjustment (GIA) caused the land in regions near the former ice sheets to uplift, and relative sea-level (RSL) rapidly fell. In part owing to the great length of shoreline in the Canadian Arctic Archipelago (CAA), the history of post-glacial sea-level change in northern Canada is generally well recorded.

Because relative sea-level measurements record the Earth's long-term GIA response to loading and unloading of the surface, they provide a valuable data set with which to constrain forward GIA models, including spatial and temporal aspects of ice sheet history and the Earth's rheological properties (e.g., Tushingham and Peltier 1991, Lambeck et al. 1998, Peltier 2004, James et al. 2009). Present-day Global Positioning System (GPS) measurements of land motion offer further insight into the ongoing GIA response to the last glaciation, including the GIA contribution to patterns of crustal deformation (e.g., Sella et al. 2007). Improved GIA models are needed to constrain better Earth properties and structure, as well as the spatial extent and volume of the ice sheets. Accurate volume estimates of the continental ice sheets are needed to construct the global sea-level budget from the LGM to present-day (Peltier 2009, Tamisiea 2011). In addition, much focus has been placed on assessing the regional and global impact of recent changes to the Earth's cryosphere, atmosphere and oceans, including the measurement of the Earth's response to present-day ice mass loss, and the prediction of future rates of sea-level change. A developing application of reducing the uncertainty of the present-day GIA response is the constraint and projection of future sea-level change in coastal communities (e.g., James et al. 2011).

In this paper, we refine GIA models in northern Canada by modifying the Laurentide component of the ICE-5G ice sheet reconstruction (Peltier 2004). Based on the misfit between model predictions and present-day gravity and GPS data (Lambert et al. 2006, Argus and Peltier 2010, Mazzotti et al. 2011), it was found that the

ICE-5G reconstruction is too thick in the central sector of the Laurentide Ice Sheet (LIS). Argus and Peltier (2010) additionally suggest that the ICE-5G model reconstruction features ice that is too thin near the British Columbia-Alberta border and in southern and eastern Quebec. The goal of this study is to perform a regional GIA modelling analysis to constrain the ice thickness relative to ICE-5G in four sectors of the Laurentide Ice Sheet. Determination of regional thickness corrections to ICE-5G provides an updated estimate of the North American ice-volume history and its net contribution to global sea level.

The study region is northern Canada ($\geq$55° N). Particular focus is placed on the Kivalliq (formerly Keewatin) region of Nunavut, northern Quebec, and the Canadian Arctic Archipelago (Figure 6.1). In contrast to the continental interior and the area that covers much of the southern extent of the last North American glaciation, which was the focus of Argus and Peltier (2010) and has extensive GPS coverage and little to no RSL data, most of northern Canada has abundant RSL measurements and few permanent GPS sites. We therefore use late Pleistocene and Holocene RSL data as the primary constraint for the GIA models, and available present-day GPS observations as a secondary constraint. In more southern portions of our study area, this approach will allow us to confirm and compare our results with those of Argus and Peltier (2010) through the use of an independent RSL data set. In northern regions of our study area, RSL data provide the dominant constraint on the GIA process.

6.2.3 Background and Previous Laurentide GIA Studies

The spatial extent, flow history and chronology of the last North American glaciation has been constructed through glacial-geological observations of end moraines and other ice-marginal features, flow direction indicators, glacial erratic distributions, and marine-limit and relative sea-level measurements. During the last interstadial minimum, the Laurentide Ice Sheet approximately covered the Canadian Shield; growth and expansion of the LIS from these margins commenced approximately 30-27 ^{14}C kyr BP at the middle to late Wisconsinan transition (Dyke et al. 2002). The LIS reached its peak extent by approximately 24-21 ^{14}C kyr BP, and was confluent with the smaller Cordilleran Ice Sheet in western Canada. Glacial flow indicators suggest that the thickest ice cover nucleated in three main regions over the area west of Hudson Bay, Quebec-Labrador, and Foxe Basin (Figure 6.1, Dyke et al. 1982, Dyke et al. 2002). The LIS remained at near LGM conditions over North America until

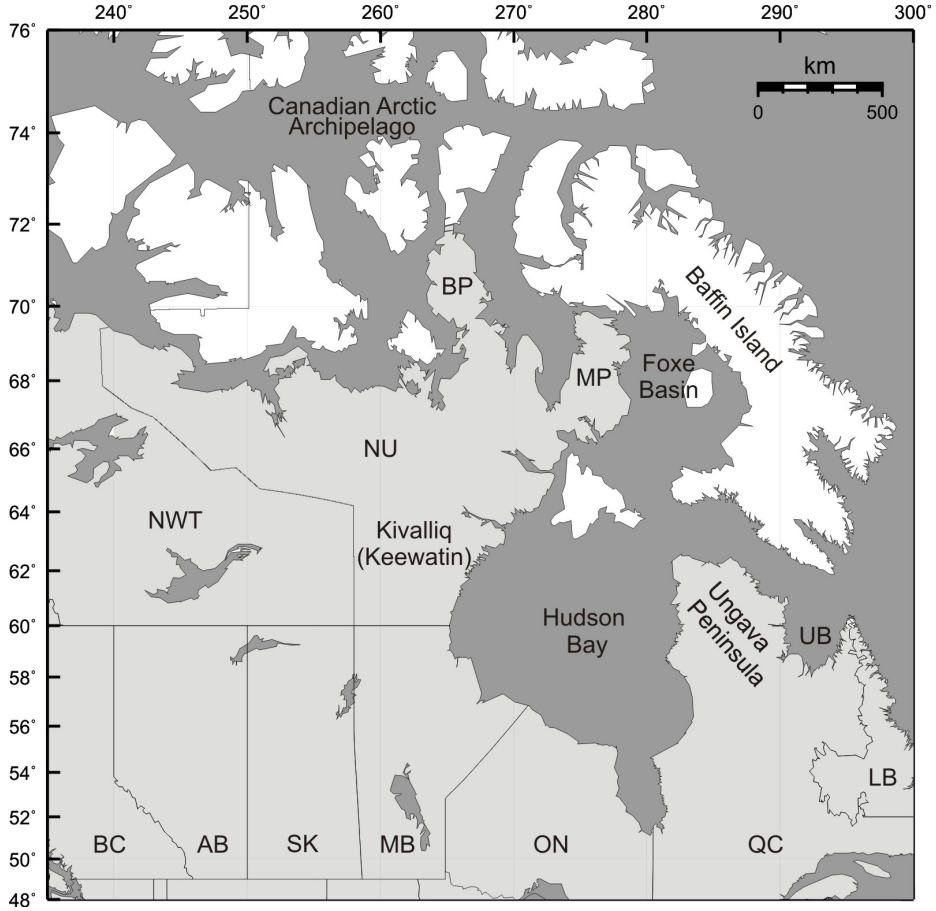

Figure 6.1: Regional map showing the study area and geographical place names mentioned in the text. Geographical place-name abbreviations are: BP - Boothia Peninsula, LB - Labrador, MP - Melville Peninsula, and UB - Ungava Bay. Canadian provincial and territorial abbreviations are: AB - Alberta, BC - British Columbia, SK - Saskatchewan, MB - Manitoba, ON - Ontario, and QC - Quebec, NU - Nunavut, NWT - Northwest Territories. The islands of the Canadian Arctic Archipelago are shaded white.

about 14 ^{14}C kyr BP. The main phase of deglaciation of the LIS occurred between 14 and 7 ^{14}C kyr BP, during which time there was a nearly linear 90% reduction in the area of the ice sheet complex relative to its area at LGM, including the ablation of marine-based ice in Hudson Bay between 8 and 7 ^{14}C kyr BP (Dyke 2004). By 5 ^{14}C kyr BP, deglaciation of North America was nearly complete.

In North America, many recent glacial isostatic adjustment studies have focused on the global ICE-5G ice sheet reconstruction of Peltier (2004). ICE-5G was developed as an update to the ICE-4G reconstruction (Peltier 1994); ICE-5G delivers a maximum eustatic sea-level low-stand of ∼120-125 m, in accordance with far-field sea-level measurements, and also generally well predicts sea-level measurements and

present-day vertical and horizontal motions over Fennoscandia (Peltier 2004, Argus and Peltier 2010). However, using present-day geodetic rates, several studies have suggested that the thickness of ICE-5G is too large in the central Laurentide region west of Hudson Bay (Lambert et al. 2006, Argus and Peltier 2010, Mazzotti et al. 2011). Argus and Peltier (2010) used the fit of model predictions to present-day rates of crustal motion from dense GPS coverage in southern Canada to also suggest that ICE-5G is too thick in Manitoba and near Yellowknife, and conversely too thin in western Canada and southeastern Quebec.

A successor model to ICE-5G, ICE-6G, has been developed to incorporate these revisions to the North American component of the ice sheet reconstruction, and its predictions have been used in recent sea level and climate modelling studies in other regions (e.g., Engelhart et al. 2011, Toscano et al. 2011, Vettoretti and Peltier 2013). As well, Tarasov et al. (2012) have also recently developed a glaciological model for the North American ice sheets that features less ice west of Hudson Bay than ICE-5G. In Vettoretti and Peltier (2013), the authors describe ICE-6G relative to ICE-5G as being approximately 1500 m thinner in central Canada, as well as less than 1000 m thicker in both western Canada and northern Quebec. At ∼120 m, the eustatic sea-level contribution of ICE-5G and ICE-6G are approximately equivalent (Vettoretti and Peltier 2013), and it seems that this conservation is achieved primarily through the redistribution of the load on the North American continent. In this study, we seek to constrain sector-specific contributions to the global sea-level budget of an LIS reconstruction that best fits the available RSL and GPS data from northern Canada.

6.2.4 Methods and Data

Model Description

The GIA model consists of an ice sheet reconstruction that varies in space and time, and an Earth model that describes the Earth's response to surface loading. The starting ice sheet model is the global ICE-5G reconstruction (Peltier 2004). The ice sheet history is applied to a spherically symmetric Earth model with an elastic lithosphere overlying a compressible linear viscoelastic mantle. The reference Earth model follows the VM5a profile of Peltier and Drummond (2008), and consists of a 60 km thick elastic lithosphere overlying a 40 km thick high-viscosity (10^{22} Pa s) layer. At greater depths, the VM5a viscosity profile is similar to the VM2 profile derived from the global mantle viscosity estimate of Peltier (1996). VM5a has viscosities of

5×10^{20} Pa s from 100-660 km depth, 1.6×10^{21} Pa s between 660-1160 km depth, and 3.2×10^{21} Pa s from 1160 km depth to the core mantle boundary. The Earth's density and rigidity parameters are averaged values from the Preliminary Reference Earth Model (Dziewonski and Anderson 1981).

The model calculations include a global, gravitationally self-consistent solution of the sea-level equation following the methods described by Mitrovica and Peltier (1991). The effects of time-varying ocean-continent geometry and water dumping into regions of formerly grounded marine-based ice are modelled following the methodology of Mitrovica and Milne (2003). The GIA model does not include perturbations to the Earth's rotation vector induced by the varying surface load. While the error associated with not including the rotational effect is non-negligible, it is likely small in most locations. Mitrovica and Milne (1998) estimated rotational effects may perturb relative sea-level predictions by up to a maximum of 7-8 m. The computational algorithm follows the pseudospectral approach of Mitrovica et al. (1994), and all calculations are truncated at spherical harmonic degree and order 128. A sensitivity test with truncation at degree and order 256 suggests that performing the calculations to spherical harmonic degree and order 128 adequately captures the GIA signal.

Selection and Analysis of the RSL Data

The primary constraint for the GIA models in this study are relative sea-level histories selected from a large database of measurements from the arctic and subarctic regions of Canada. The sea-level measurements consist of elevations and ages of radiocarbon-dated indicators of relative sea-level position, such as marine shells, driftwood, mammal bones, and plant material. The material type and stratigraphic context of the sea-level indicators allows each sample to be classified according to whether sea level was located above, below, or near the elevation of each observation (this type of classification is also sometimes referred to as the 'indicative meaning' of the observation, Shennan 2007). The history of sea-level change at a given location is then inferred by the line that most closely lies above the lower constraints and below the upper constraints. The position of sea level is most tightly constrained by measurements from interpreted nearshore environments, or marine-terrestrial pairs of similar age and elevation.

The RSL database assumes that observations that are geographically close to each other can be combined to construct the history of sea-level change for a particular

location. In some cases, especially in regions where data are sparse, measurements spaced up to ∼150 km apart are combined to form a single sea-level history. These larger sample areas, however, are used only in central glaciated regions where isostatic tilting is low. For sea-level histories that encompass areas that have either large geographical extent or a complex deglaciation history (e.g., Churchill, Ungava Bay), groups of discrepant ages (i.e., where a few marine ages lie above terrestrial ages, or a few terrestrial ages lie below marine ages) within the same sea-level history suggests that caution is needed when interpreting sea-level change at these locations.

Within the study area, 24 relative sea-level histories were chosen for comparison with the GIA model predictions (Figure 6.2). The selected data sets favour sea-level histories with observation points that: 1) lie geographically close together, 2) tightly constrain the position of sea level, and 3) display continuity, both spatially and temporally, such that a well-defined sea-level curve can be inferred. In addition, less well-defined sea-level histories are also used to supplement the observations in geographical regions of interest, such as near load centres of the former ice sheet, or locations at or near continuous GPS sites. Some relative sea-level histories include observations that fall far from the inferred sea-level curve, and thus place no additional constraint on the position of sea level. Because we calculate the fit of the model predictions relative to the individual measurements and not to the inferred sea-level curve, it is not statistically meaningful to compare the GIA model predictions to measurements that lie far from the inferred position of sea level. We therefore exclude all non-constraining measurements when calculating the fit of the models to the data.

The criteria used to retain or exclude any given observation are as follows. Marine ages that clearly lie far below other marine constraints are excluded, provided that additional constraints exist within a ±1 kyr time window of any excluded observation (Figure 6.3). Terrestrial ages that clearly lie well above other terrestrial constraints are excluded in a similar manner. In portions of the relative sea-level history where the position of sea level is unclear, or discrepant ages exist, all data points are retained in order to reflect the uncertainty of the observations (Figure 6.3). Where groups of either marine ages or terrestrial ages are spaced closely together, all data points are retained, as measurements that are clustered together will have little influence on the calculated misfit of the model to the data and a larger number of measurements will serve to reduce the uncertainty of the data set. In addition, all nearshore sea-level indicators, particularly shell ages from *Mytilus edulis*, a shallow-dwelling bivalve, are retained. Owing to their tendency to yield anomalously old radiocarbon ages

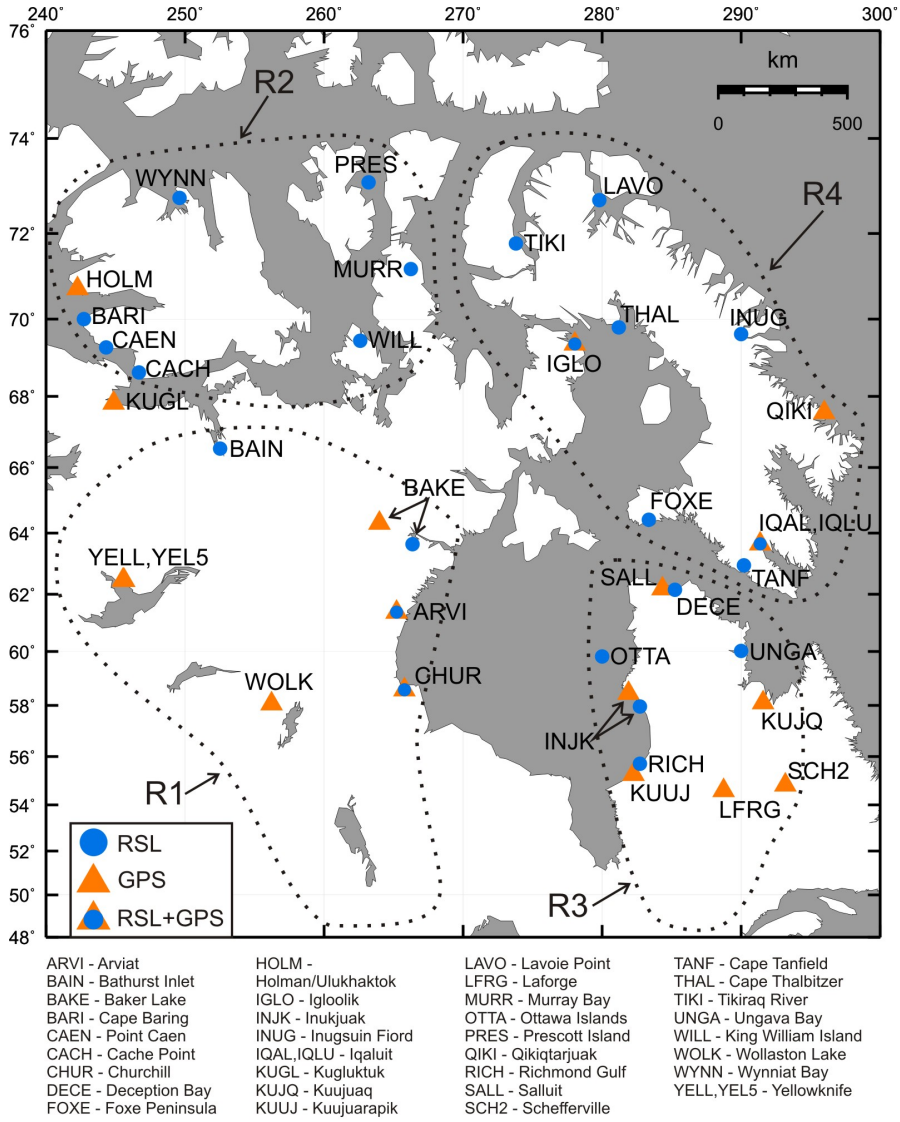

Figure 6.2: Site map showing the relative sea-level (RSL) and GPS site locations and names. RSL and GPS sites are shown by blue circles and orange triangles, respectively. Locations with both RSL and GPS data are shown by a blue circle within an orange triangle. Approximate boundaries of the four regions (R1-R4) of study are indicated by the black dashed lines.

(England et al. 2003, England et al. 2013), all *Portlandia arctica* shell ages are excluded. Exclusion of the clearly non-constraining measurements minimizes scatter of the data set, and allows better quantitative comparison between the sea-level data and the model predictions.

The difference between the relative sea-level measurements and model predictions is determined by calculating the shortest distance in space and time (s, t) between

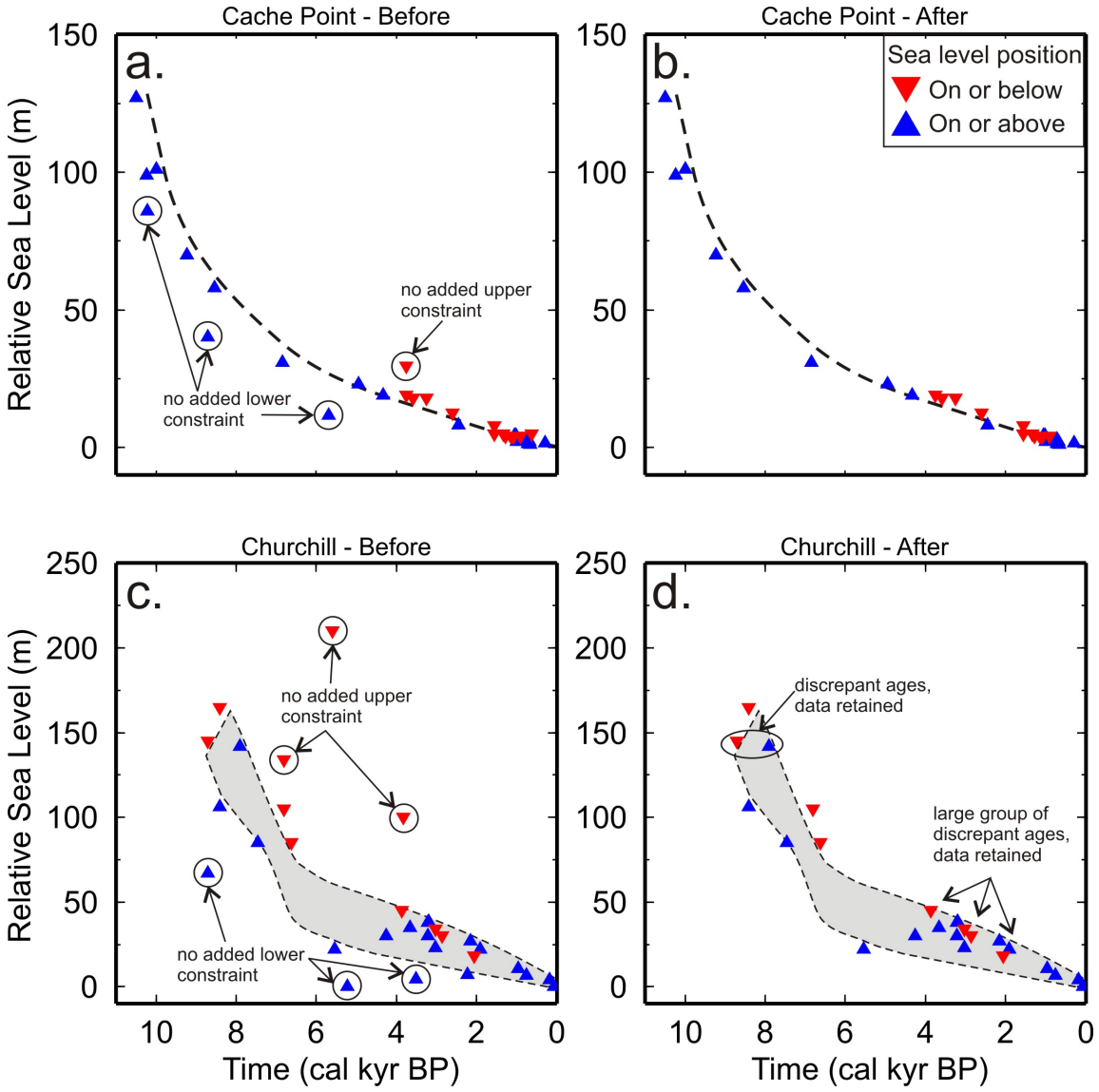

Figure 6.3: Examples of the criteria used for excluding or retaining data points from the relative sea-level histories. Marine ages occur below sea level and are shown by the blue triangles. Terrestrial ages occur above sea level and are shown by the red triangles (the triangles point in the direction of inferred sea level). Marine (terrestrial) ages that lie well below (above) the inferred position of sea level are excluded; ambiguous or discrepant ages are retained. The top panels show the relative sea-level history of a clearly constrained site location (Cache Point) before and after the filtering criteria are applied. At Cache Point, the inferred position of sea level is shown by the black dashed line. The bottom panels show the relative sea-level history of a less clearly constrained site location (Churchill) before and after the filtering criteria are applied. At Churchill, the inferred position of sea level is enclosed within the grey-shaded envelope. The larger scatter on the Churchill data set results in overall larger calculated misfit values.

each observation ($RSL^{o,s}$, $RSL^{o,t}$) to a point on the predicted sea-level curve ($RSL^{p,s}$, $RSL^{p,t}$) (e.g., Mitrovica et al. 2000, Paulson et al. 2007). The fit of the predictions to the observations at each site location is then evaluated by a χ^2 measure of misfit using

$$\chi^2_{RSL} = \frac{1}{N}\sum_{i=1}^{N}\left[\left(\frac{RSL_i^{o,s} - RSL_i^{p,s}}{\sigma_i^{o,s}}\right)^2 + \left(\frac{RSL_i^{o,t} - RSL_i^{p,t}}{\sigma_i^{o,t}}\right)^2\right], \qquad (6.1)$$

where $\sigma^{o,s}$ and $\sigma^{o,t}$ are the observational uncertainties in space and time, respectively, and N is the number of observations.

The temporal error of each observation is derived from the radiocarbon-laboratory estimate. The spatial errors of the observations reflect both the elevation measurement error and the uncertainty associated with the interpretation of the vertical position of each sample relative to past sea-level. Similar to Peltier (1998b), and as suggested by Dyke (personal communication), we calculate the vertical error as a function of sample elevation. For observations below 5 m, the vertical error is calculated as 20% of the measured elevation, with a minimum error of 0.5 m. Between 5-20 m elevation, observations are assigned a vertical error of $\pm$1 m. Above 20 m elevation, the vertical error is calculated as 5% of the observed elevation. In addition, we include a modest uncertainty of $\pm$5 m on each marine age to represent the uncertainty in vertical position owing to variations in tidal range, and in the case of marine shells, growth depth. Including this additional uncertainty has the overall effect of reducing the calculated χ^2 values, but the robustness of the solution does not appear to be affected by its use.

In the χ^2 calculation, the relative sea-level observations are categorized as either upper or lower constraints on the position of sea level (i.e., there is no additional category for nearshore constraints). Therefore, nearshore or marginal sea-level indicators (such as *Mytilus edulis* shell ages) are not more heavily weighted in the χ^2 calculation than the other constraints. Independent consideration of nearshore sea-level indicators, however, has the advantage that predicted sea-level is preferentially fit to the data points that provide the tightest constraint on the position of sea level; this method has recently been applied in GIA studies of sea-level change in Greenland (Simpson et al. 2009, Lecavalier et al. 2014).

Therefore, a limitation associated with not including a separate nearshore indicative meaning in the χ^2 calculations in this study is that computed χ^2 values for sea-level histories with more lower than upper constraints will be biased low. In these

cases, the low bias occurs because the misfit values will be minimized for predictions that fit observations that are predominately from below sea-level. However, the selection of relative sea-level histories that have a good distribution of both upper and lower constraints substantially mitigates this effect for most site locations in this study. For sea-level histories with a good distribution of lower and upper constraints, the method of data filtering described above is designed to yield a relative sea-level curve that constrains the possible vertical range of sea-level position to within the uncertainty of the data. The filtering also removes the effect of trying to fit χ^2 values to non-constraining points, which, for example, for a sea-level history with many lower constraints over a large elevation range, may also bias the misfit values low.

The radiocarbon ages of the relative sea-level measurements are normalized for isotopic fractionation relative to δ^{13}C = -25‰ following the conventions of Stuiver and Polach (1977), and marine ages are corrected for the reservoir effect using regional corrections (McNeely et al. 2006). The radiocarbon ages (and age errors) of the samples are calibrated to calendar years using the program Calib 5.1 (Stuiver and Reimer 1993). Marine ages are calibrated using the Marine04 data set (Hughen et al. 2004), and terrestrial ages are calibrated using the IntCal04 data set (Reimer et al. 2004). More recent calibration curves do exist (Reimer et al. 2013), but the differences between the calibrations during the Holocene are very small, and the use of a more recent calibration curve would likely not significantly impact the conversion of radiocarbon ages to calendar ages.

GPS Data

Within the study area, the measured vertical land motion rates of 18 GPS sites are considered (Figure 6.2). All GPS data, except for that from Arviat, are processed using the Bernese Software Version 5.0 (Dach et al. 2007). Using the Canadian Geodetic Survey's SINEX combination software, the data are aligned to the ITRF2008 reference frame (Altamimi et al. 2011). Arviat is a campaign GPS site whose processing is outlined in Chapter 5 and Simon et al. (2014). The misfit between the observed and predicted present-day rates of vertical land motion is calculated using a mean squared error (MSE) measure of misfit

$$MSE_{GPS} = \frac{1}{N}\sum_{i=1}^{N}\left(V_i^o - V_i^p\right)^2, \tag{6.2}$$

where V_i^o and V_i^p are the observed and predicted rates of vertical crustal motion at the i^{th} site location, respectively, and N is the number of GPS sites.

In the CAA, glaciers and ice caps are present on Baffin, Devon, Axel Heiberg and Ellesmere islands (Figure 6.4). These glaciers and ice caps (GIC), as well as the nearby Greenland Ice Sheet, are experiencing rapid present-day mass loss (e.g., Gardner et al. 2011, Rignot et al. 2011, Shepherd et al. 2012, Bolch et al. 2013, Gardner et al. 2013). In addition to uplift from the long-term GIA response, observed rates of vertical land motion in parts of our study area may contain a significant component of uplift attributable to the elastic response of the Earth to changes in present-day regional ice cover. Using an elastic Earth model and ice cover that approximates present-day changes to the northern GIC, and the Greenland Ice Sheet, we compute a correction for this effect.

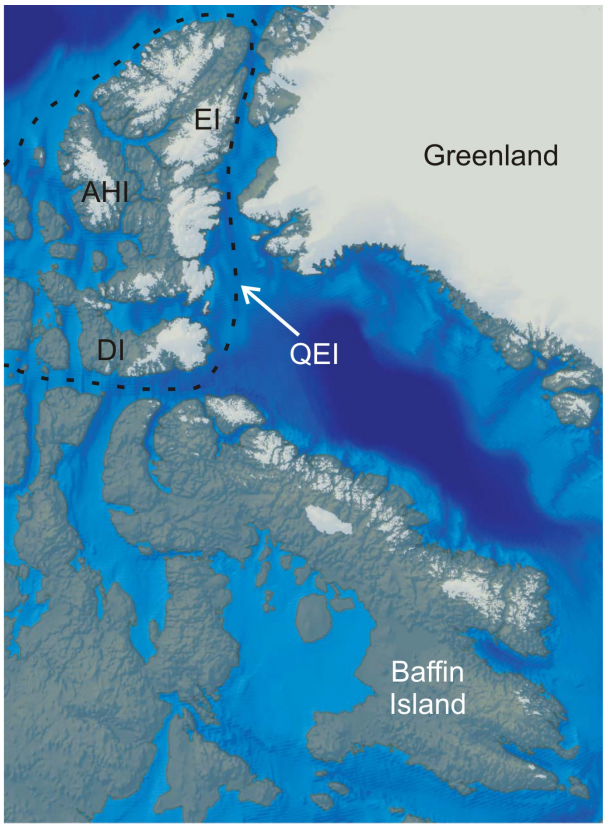

Figure 6.4: Present-day ice cover in the Canadian Arctic Archipelago and on Greenland. In the Canadian arctic, glaciers and ice caps are present on Baffin Island and the Queen Elizabeth Islands (QEI, enclosed by the dashed line). Within the QEI, ice cover exists on Devon, Axel Heiberg, and Ellesmere islands (DI, AHI, EI, respectively). Figure modified from Gardner et al. (2011).

Based on recent estimates, we specify rates of present-day mass loss of -60 Gt/yr and -142 Gt/yr for the Canadian Arctic GIC and Greenland, respectively (Shepherd et al. 2012, Gardner et al. 2013). Uniform mass loss is assumed for both regions. Bolch et al. (2013) found varying mass loss rates for specific sectors of Greenland glaciers and ice caps; although this study considered only Greenland GIC and not the ice sheet, it suggests that there may likely be significant error associated with the assumption of spatially uniform mass loss for Greenland. As well, the spatial resolution of the grid is coarse and the assumed mass loss rates are uncertain. Therefore, the predicted corrections for present-day mass loss should be considered preliminary estimates. In parts of our study area that are close to regions experiencing present-day ice mass loss (such as Baffin Island and to a lesser extent the Ungava Peninsula) estimating a correction for the mass loss effect will allow us to evaluate the relative importance of applying this correction to predicted vertical uplift rates.

Modelling Approach

Based on a combination of geographical and glaciological boundaries, the study area is divided into four smaller regions (Figure 6.2). The first region is the Kivalliq (formerly Keewatin) region west of Hudson Bay and is one of the former load centres of the Laurentide Ice Sheet. This region also includes parts of Hudson Bay, the Northwest Territories, Saskatchewan, and Manitoba. The southern portion of Region 1 (mainly Manitoba) has little RSL data, and thus is not an area of primary focus in our study. This area is however included in Region 1 to maintain regional continuity with the load reconstruction changes, and to be generally consistent with the results of Argus and Peltier (2010), which, although they do not comment directly on the Keewatin region to the north, suggest that significant thinning of ICE-5G is required in Manitoba. Region 2 lies to the north of Region 1 in a zone peripheral to the load centre, and includes the Boothia Peninsula and the southernmost islands of the Canadian Arctic Archipelago. Region 3 is east of Hudson Bay, and includes the Ungava Peninsula in northern Quebec. Similar to Region 1, Region 3 extends into southern Quebec to maintain consistency both with the regional treatment of the load, and with the results of Argus and Peltier (2010) which identify southern Quebec as an area of significant misfit between model predictions and observations. Region 4 consists of Baffin Island, Foxe Basin and the Melville Peninsula.

Each of the regions is considered sequentially, and the best-fit model of the pre-

ceding region is carried forward to the next region. The revisions to the GIA model explore variations to the thickness of the starting ice sheet reconstruction, and assume a fixed Earth model with the VM5a viscosity profile. The location of each predicted relative sea-level curve (and thus also its associated χ^2 value) is the average latitude and longitude of all of the data points that comprise that site's sea-level history, while present-day rates of vertical motion are computed at the precise locations of the GPS sites. RSL and GPS site locations that are close together may share the same site name (e.g., BAKE, INJK, IGLO, Figure 6.2). The ICE-5G load is discretized on a 256×512 degree Gaussian grid, and ice sheet thickness scaling factors are generally applied to groups of grid points within each region. Where finer spatial detail appears warranted, individual grid points are modified. In Regions 1-4, the timing history of ICE-5G is retained, and the ice sheet thicknesses are modified by applying scaling factors to the starting load values for all steps in the timing history.

6.2.5 Variations to Ice Sheet History

Regions 1 and 2

Of the regions considered in this study, Region 1 has the fewest available RSL measurements. The four main relative sea-level histories that exist in the region are located at Arviat, Baker Lake, the southern end of Bathurst Inlet, and Churchill (ARVI, BAKE, BAIN, and CHUR). At Arviat, Simon et al. (2014) recently updated the RSL history, and presented a preliminary campaign GPS uplift rate for site ARVI. Baker Lake and Churchill have permanent GPS sites (BAKE and CHUR), and within the continental interior of Region 1, there are also GPS sites at Wollaston Lake (WOLK) and Yellowknife (YELL, YEL5). The original ICE-5G model strongly overpredicts both Holocene RSL change and present-day vertical motion rates in Region 1 (Figures 6.5, 6.6).

Because Region 1 is very large and because both the RSL and GPS data sets are consistently overpredicted by the original model, we begin similar to Simon et al. (2014) by performing a sensitivity analysis wherein the thickness of the central LIS is uniformly scaled to identify a general best-fit scaling factor for this region. We then consider more localized adjustments to the load in Region 1. The applied scaling factors range from 0.4-1.2. At Arviat and Bathurst Inlet, the RSL misfit is minimized for scaling factors of 0.6-0.7 (Figure 6.7). At Baker Lake, which is located in a region slightly peripheral to the load centre, scaling factors of 0.7-0.8 provide the

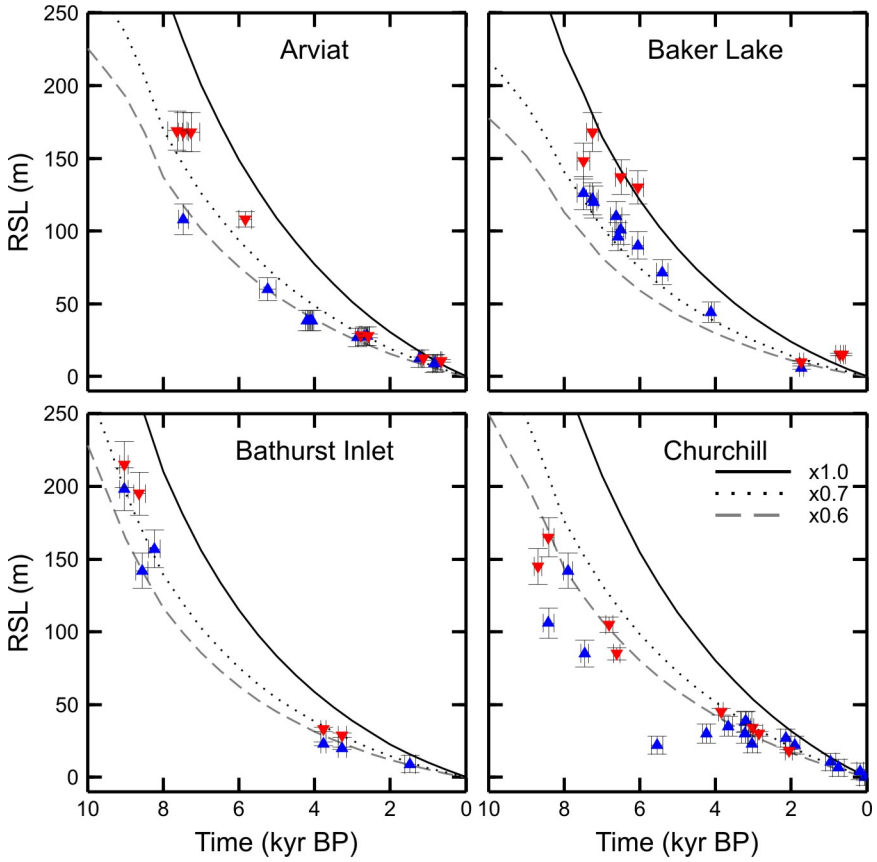

Figure 6.5: Relative sea-level predictions and measurements for Region 1. Lower observational constraints are shown by blue triangles; sea level was at or above these points. Upper observational constraints are shown by red triangles; sea level was at or below these points. Triangles point in the direction of the inferred position of sea level. The starting ice sheet reconstruction (black line, $\times 1.0$) overpredicts sea-level at all four locations in Region 1. Model predictions where the regional ice load has been scaled by factors of 0.7 (black dotted line) and 0.6 (grey dashed line) provide a better fit to the observations.

best fit to the RSL data. Finally, at Churchill, the misfit appears minimized for larger reductions to the load thickness, or scaling factors of 0.4-0.6. The large scatter on the Churchill data yields overall higher χ^2 values relative to the other sites, and the existence of discrepant ages within the Churchill data set suggests that the relative sea-level measurements require either more detailed filtering of the data or spatial separation of the measurements into two or more sea-level histories. At Churchill, models with higher scaling factors of 0.6-0.7 appear to fit well the late Holocene sea-level data despite the poor fit with the early Holocene data (Figure 6.5).

In Region 1, the GPS-measured present-day vertical land motion rates also indicate that a reduced load thickness relative to ICE-5G is needed (Figure 6.6). The

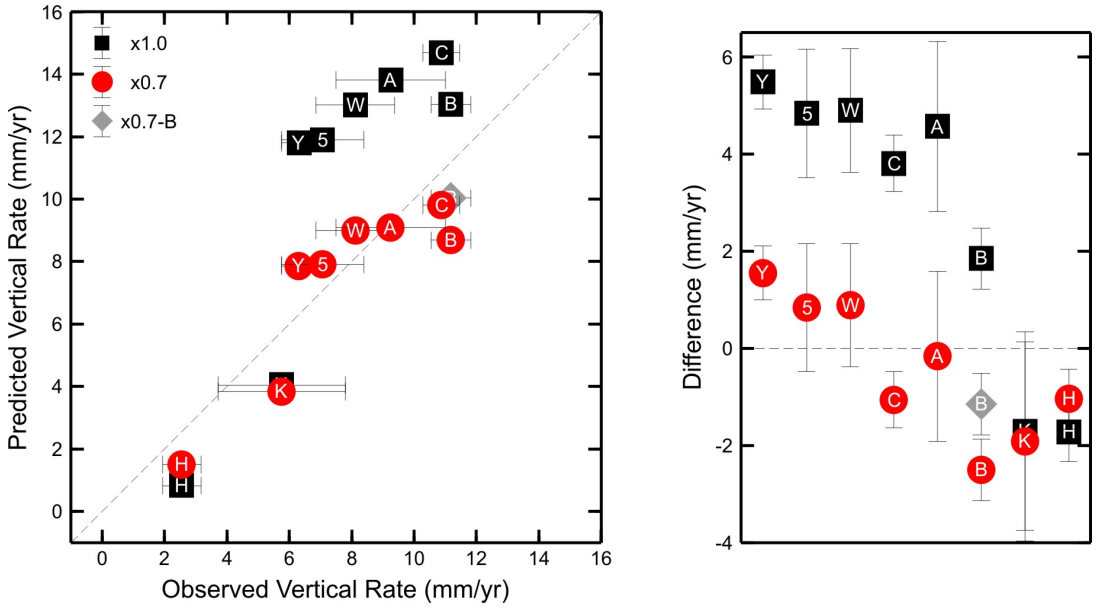

Figure 6.6: Predicted versus GPS-observed vertical rates of uplift in Regions 1 and 2 (left), and the differences between the predicted and observed rates (right). The 'Region 1' GPS sites are located in the northern part of Region 1, and the 'Region 2' GPS sites (Kugluktuk, Holman) are located near the boundary between Regions 1 and 2; thus, the area considered in this figure approximately corresponds to the northern portion of Region 1 shown in Figure 6.2. The starting model (black squares, $\times 1.0$) overpredicts rates of vertical uplift at all locations in Region 1, and underpredicts these values for both locations in Region 2. An ice sheet reconstruction reduced by 30% in Region 1 improves the fit of the predictions to the data (red circles). Additional local adjustments to the ice load around Baker Lake further improve the fit at that location (grey diamond). All predictions include the correction for the component of uplift resulting from present-day mass loss of Arctic glaciers and ice caps, and the Greenland Ice Sheet, as discussed in the text. A-Arviat, B-Baker Lake, C-Churchill, H-Holman, K-Kugluktuk, W-Wollaston Lake, Y-Yellowknife (site YELL), 5-Yellowknife (site YEL5)

original model overpredicts present-day uplift rates at all five sites, including Yellowknife, Baker Lake and Churchill, which were also shown to be overpredicted by Argus and Peltier (2010). The MSE misfit value of the present-day vertical rates is reduced from 15.2 for the original model (1.0 scaling factor), to 2.0 for the 0.7 scaling factor model. For the 0.7 scaling factor model, the fit of the present-day uplift rate is improved at Yellowknife, Wollaston Lake, Arviat and Churchill, although the predicted rate for Churchill is still not within observational uncertainty. At Baker Lake, the fit of the predicted uplift rate is worsened for the 0.7 scaling factor model relative to the original model, and the predicted rate also switches from being too large to being too small.

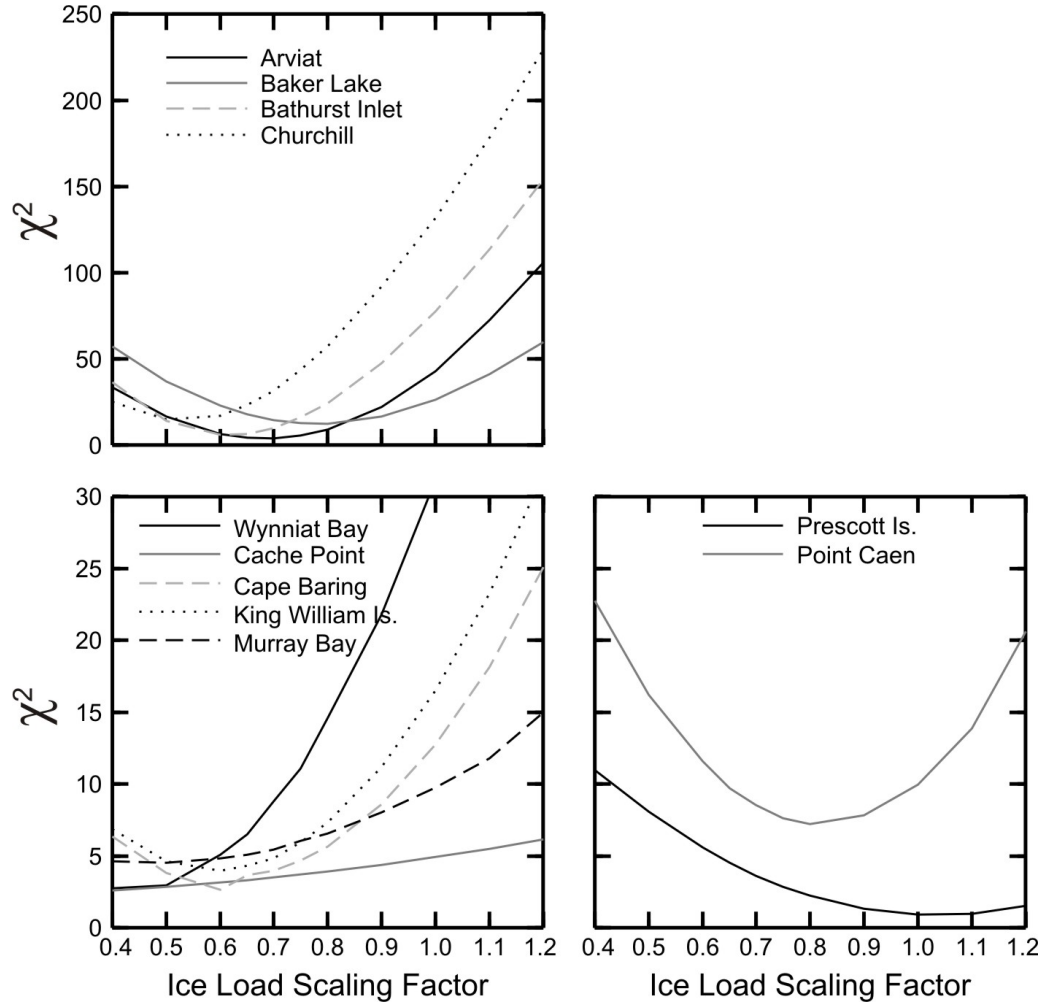

Figure 6.7: Calculated χ^2 misfits of the relative sea-level predictions, compared to the relative sea-level measurements, for Regions 1 and 2. For all panels, the sensitivity analysis scales the starting ICE-5G load reconstruction (equivalent to a 1.0 scaling factor) in Region 1 by scaling factors that range from 0.4-1.2, while the thickness history of Region 2 remains unchanged. In Region 1 (top panel), the misfit of RSL predictions to observations is minimized for an approximately ∼30% reduction to the starting load thicknesses within that region. In Region 2 (bottom panels), the fit of RSL predictions to RSL data also generally is improved for reduced versions of the ice sheet reconstruction in Region 1. The χ^2 misfits of most sites in Region 2 are minimized for Region 1 scaling factors of 0.5-0.7 (left bottom), although at Point Caen and Prescott Island, the misfit is minimized for larger scaling factors (right bottom).

While the reduction of the load thickness by the application of uniform scaling factors provides improved predictions overall for both the RSL and GPS data, the regional variability in the location of the minimum RSL χ^2 value suggests that some locations need more localized adjustments. In particular, at Baker Lake, both the

relative sea-level history and vertical uplift rate are underpredicted for a scaling factor of 0.7. We therefore apply larger scaling factors of 0.9 to the ice sheet thickness north of Baker Lake while maintaining the 0.7 scaling factor elsewhere. This localized ($<$150 km^2) modification yields an improved fit to the RSL data at Baker Lake, and increases the predicted present-day uplift rate from 8.6 to 10.0 mm/yr (Figure 6.6). The localized change to the load near Baker Lake does not significantly change the predicted RSL fall or rates of vertical uplift at other sites in Region 1. Improving the fit at Baker Lake further reduces the regional MSE misfit on the GPS observations from 2.0 to 1.3.

We do not locally decrease the ice load around Churchill based on the RSL χ^2 values because discrepant ages in the RSL data make the sea-level history harder to interpret, and because the late Holocene sea-level history is well fit by a 0.7 scaling factor. Also, although the predicted present-day uplift rate is improved for the 0.7 scaling factor model relative to the original model at Churchill, the predicted rate changes from being too large to too small, and further reductions to the ice sheet thickness would only worsen this trend. The best-fit model for Region 1 therefore has a scaling factor of 0.7 applied throughout most of the region, and larger scaling factors of 0.9 applied locally around Baker Lake.

Region 2 lies directly to the north of Region 1, in a zone peripheral to the Keewatin load centre of the LIS. The seven relative sea-level histories considered in this region are Cache Point, Point Caen, Cape Baring, Wynniat Bay, King William Island, Murray Bay and Prescott Island (CACH, CAEN, BARI, WYNN, WILL, MURR and PRES, respectively, Figure 6.2). In or near Region 2, continuous GPS sites exist at Kugluktuk (KUGL), and Ulukhaktok (formerly Holman, HOLM). We make no changes to the ice sheet thicknesses in Region 2. Instead, we note the effect of load reductions in Region 1 on the prediction of relative sea-level in Region 2. While reducing the ice sheet thickness in Region 1 also reduces the position of predicted sea level in that region, the reduced load thickness simultaneously increases the position of predicted sea level in Region 2 (Figure 6.8). This effect is the result of a decreased mantle forebulge to the north of the Keewatin sector of the LIS. The original (unscaled) ICE-5G model tends to underpredict sea level in Region 2, and overall the fit of the model predictions to the RSL data is improved for Keewatin scaling factors of less than 1 (Figure 6.7).

At Cape Baring, Wynniat Bay, King William Island, and Murray Bay, the misfit of the relative sea-level predictions to the observations is minimized for Keewatin scaling

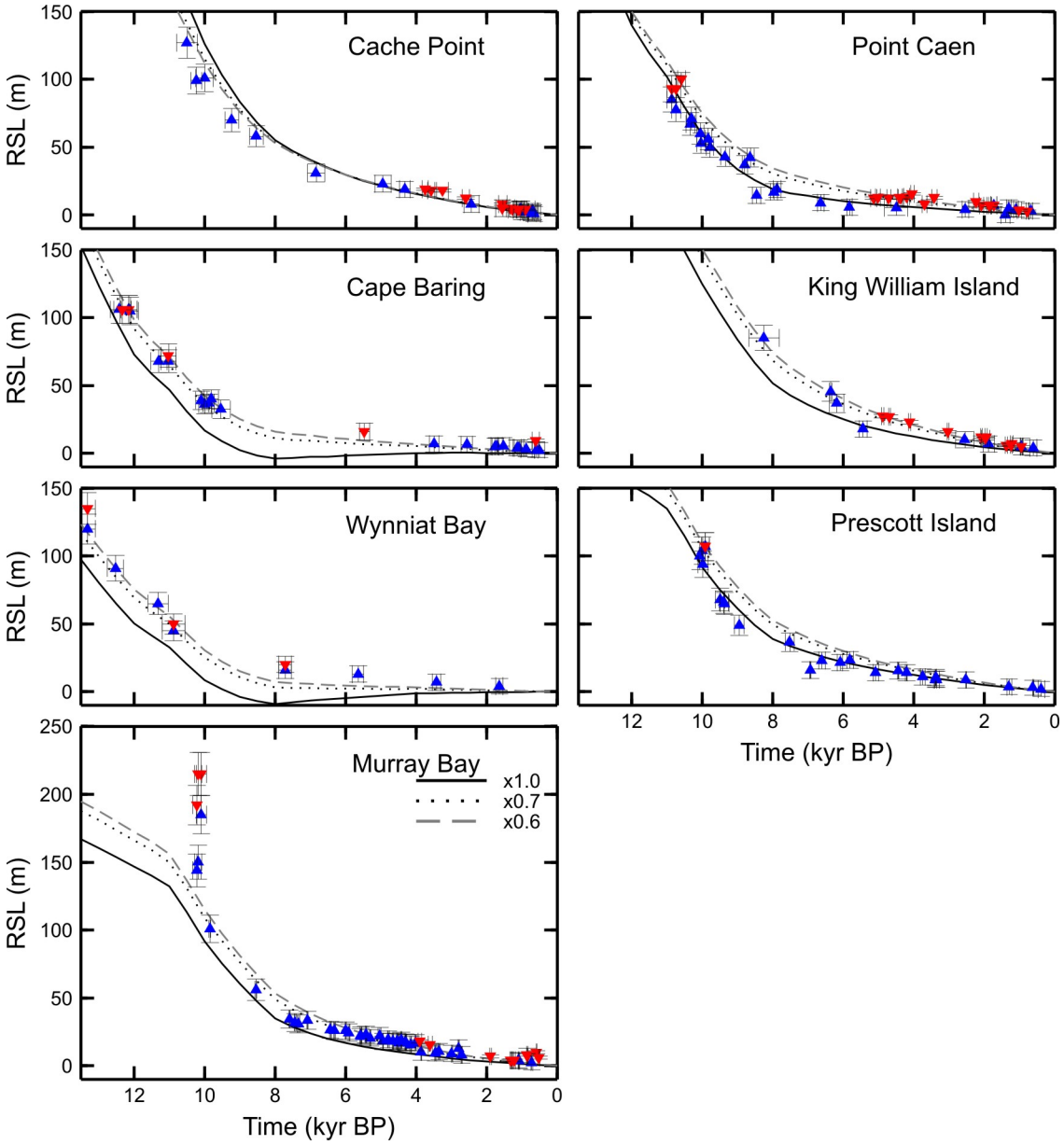

Figure 6.8: Relative sea-level predictions and measurements for Region 2. Sea-level measurements are plotted as described in the caption to Figure 6.5. The starting ice sheet reconstruction (black line, $\times 1.0$) underpredicts sea level at several locations in Region 2. Model predictions where the ice load in Region 1 has been scaled by factors of 0.7 (black dotted line) and 0.6 (grey dashed line) provide a better fit to the observations. The ice load in Region 2 has not been changed. The overall improved fit of predictions to data in Region 2 is the result of a reduced mantle forebulge that results from reducing the load in Region 1.

factors of 0.6-0.7 (Figure 6.7). The fit is also marginally improved at Cache Point for scaling factors less than 1, although overall this site appears largely insensitive

to changes in the ice sheet thickness, and likely is located near the transition point between the isostatically depressed central load region and the elevated peripheral region. At Point Caen, the RSL χ^2 misfit is minimized for scaling factors of around 0.8-0.9, although this result is largely due to a single marine observation at 42.5 m elevation with an approximate age of 8.6 kyr that is better fit by reduced scaling factors; the fit to many of the remaining points is slightly worsened for smaller scaling factors. The fit at Prescott Island is not improved for the reduced scaling factors, although the χ^2 value at this location for a scaling factor of 0.7 is still comparable to the minimized χ^2 values of the other sites. Prescott Island is the northernmost site in Region 2, and the lack of improved fit at this site may indicate it is farther north than the extent of the mantle forebulge region. Except for one upper constraint provided by the marine limit, the sea-level history at Prescott Island is comprised only of lower constraints on sea level, which may introduce a low bias into this site's χ^2 values. The total misfit value for all seven RSL sites for the 1.0 scaling model is $\chi^2_{tot}(1.0) = 10.4$, while for the 0.7 scaling factor model $\chi^2_{tot}(0.7) = 6.1$. Thus, reducing the load thicknesses in Region 1 simultaneously decreases the misfit to the RSL data in Region 2 by approximately 40%. For the reduced load thickness model, the predicted vertical motion rate at KUGL is unchanged, and is slightly improved for HOLM (Figure 6.6).

Region 3

Region 3 lies east of Hudson Bay, and encompasses much of Quebec. This region has only moderately well constrained relative sea-level histories. The sea-level histories considered in this region are from the Ottawa Islands, Inukjuak, Deception Bay, and the western shoreline of Ungava Bay (OTTA, INJK, DECE, UNGA, respectively). We also compare model predictions to the very well constrained sea-level record at Richmond Gulf (RICH), on the southeast coast of Hudson Bay. Unlike any of the other sea-level histories shown in this study, the marine ages shown in the sea-level curve for Richmond Gulf were obtained only from shells of the nearshore *Mytilus edulis* species, and therefore place a tight constraint on the position of sea level. On the Ungava Peninsula, there are GPS sites at Inukjuak, Salluit, and Kuujuaq (INJK, SALL, and KUJQ). East of Hudson Bay and south of the Ungava Peninsula, we also consider the GPS-measured vertical motion rates at Kuujjuarapik, LaForge, and Schefferville (KUUJ, LFRG, and SCH2).

The best-fit model from Regions 1 and 2 (i.e., unmodified in Region 3) underpre-

dicts relative sea-level at the Ottawa Islands and Inukjuak (Figure 6.9). This version of the model also underpredicts early Holocene sea-level fall at Deception Bay and Ungava Bay, although the model fits well the late Holocene history at both of these locations. The best-fit model from Regions 1 and 2 also fits well the RSL data at Richmond Gulf. However, this model underpredicts present-day vertical uplift rates at all six GPS sites in Region 3 by 2-5 mm/yr (Figure 6.10). The original ICE-5G model also underpredicts vertical motion rates in Region 3 by amounts similar to those of the starting best-fit model of Regions 1 and 2.

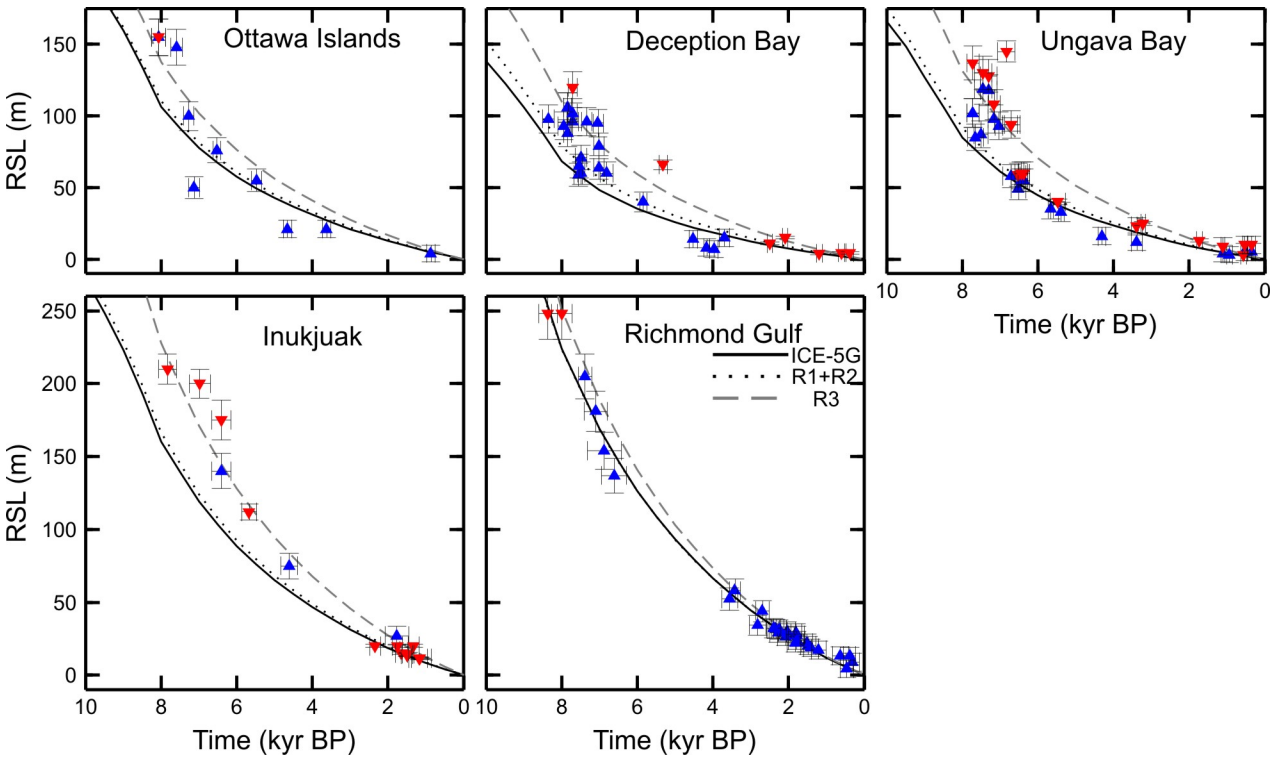

Figure 6.9: Relative sea-level predictions and measurements for Region 3. Sea-level measurements are plotted as described in the caption to Figure 6.5. Both the original model and the best-fit model from Regions 1 and 2 (solid black and dotted black lines, respectively) tend to underpredict the position of sea-level at all locations except Richmond Gulf. An ice sheet reconstruction with thickened ice in Region 3 improves the fit of the predictions to the data from Inukjuak. For the Ottawa Islands and Deception and Ungava bays, the thickened reconstruction leads to better agreement in the early Holocene, but sea-level is overpredicted in the mid- and late-Holocene (grey dashed line). All model predictions fit the data well at Richmond Gulf.

To seek a better fit to the strongly underpredicted regional GPS data, as well as the underpredicted sea-level change at the Ottawa Islands and Inukjuak, ice was thickened throughout Region 3. The addition of thicker ice increases the magnitude of all

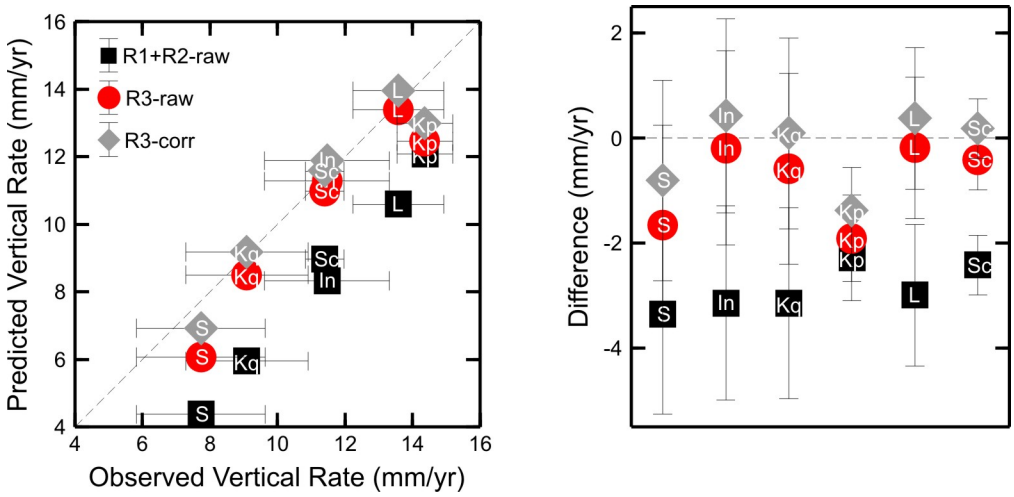

Figure 6.10: Predicted versus GPS-observed vertical rates of uplift in Region 3 (left), and the differences between the predicted and observed rates (right). The best-fit model from Regions 1 and 2 (black squares, R1+R2-raw) underpredicts rates of vertical uplift at all locations in Region 3. An ice sheet reconstruction with thickened ice in Region 3 improves the fit of the predictions to the data (red circles, R3-raw). The R1+R2-raw and R3-raw predictions are uncorrected for the component of uplift resulting from present-day mass loss of Arctic glaciers and ice caps, and the Greenland Ice Sheet. The R3-corr predictions (grey diamonds) include the correction for present-day mass loss of the nearby ice cover. L-LaForge, In-Inukjuak, Kp-Kuujjuarapik, Kq-Kuujuak, S-Salluit, Sc-Schefferville.

predictions of present-day uplift, and moves predictions at all sites but Kuujjuarapik to within the uncertainty of the measured rate (Figure 6.10). The correction for the present-day mass loss effect is shown explicitly in Figure 6.10, and reaches maximum values of approximately +0.6 to 0.8 mm/yr on the Ungava Peninsula. Although this correction is smaller than the uncertainty of the measured rates on the Ungava Peninsula, its addition to the predicted rates for just the long-term GIA response improves the fit of the total predicted rates to the measured rates. When corrected for the present-day mass loss effect, the MSE misfit of the GPS data for the best-fit model from Regions 1 and 2 (denoted R1+R2) is $\mathrm{MSE}_{ave}(\mathrm{R1+R2}) = 5.2$, while the modified Region 3 (R3) model has a misfit of $\mathrm{MSE}_{ave}(\mathrm{R3}) = 0.5$.

However, despite the much improved fit to the measured vertical uplift rates, thickened ice in this region does not significantly improve the fit of the GIA model predictions to the RSL measurements with the exception of Inukjuak (Figure 6.9). Relative to both the original ICE-5G and the R1+R2 model, the fit at Deception Bay and Ungava Bay is improved for the early Holocene portion of the curves, and worsened for the late Holocene portion of the curves. The net result is that the model

with thickened ice increases the overall χ^2 misfit of the predictions to the RSL data from both Deception and Ungava bays. At the Ottawa Islands, the fit of the modified R3 model is also worsened in the χ^2 sense relative to both ICE-5G and the R1+R2 model. All versions of the ice sheet reconstruction maintain a good fit with the RSL data from the Richmond Gulf control site.

The RSL histories at Deception and Ungava bays both have discrepant or otherwise difficult to interpret ages, and the inability of either the starting model or the model developed for Region 3 to adequately fit the record of both early and late Holocene sea-level change at these sites may indicate that separation of the data into more localized sea-level histories is required. Alternatively, a future improved fit of the model to the RSL measurements from Deception and Ungava bays could be obtained by modifying the timing history in the ice sheet reconstruction to feature more rapid initial deglaciation, or by exploring regional variations to the selected Earth model. It may, however, be difficult to find a GIA model that can simultaneously satisfy Deception and Ungava bays' late Holocene RSL histories, which imply relatively low rates of present-day uplift, and SALL and KUJQ's significantly larger observed vertical uplift rates from GPS.

Because of the differences between the sea-level histories and the measured rates of current vertical uplift, it is difficult to assert a strong preference for thickening the ice model directly on the Ungava Peninsula. However, GPS-measured uplift rates south of the Ungava Peninsula (KUUJ, LFRG and SCH2) strongly support the addition of ice in more central regions of Quebec, and relative to ICE-5G, Argus and Peltier (2010) identified southern Quebec as a region where crustal uplift is significantly underpredicted. We therefore retain the version of the ice sheet reconstruction developed for Region 3 because: 1) it provides a much better fit to all of the GPS data from the northern portion of the region; 2) there is uncertainty associated with interpretation of the RSL histories owing to discrepant or otherwise ambiguous ages; and, 3) it maintains regional continuity with the thicker ice in the southern portion of Region 3, where Argus and Peltier (2010) have also suggested thicker ice is needed.

Region 4

Region 4 includes Baffin Island, Foxe Basin and the Melville Peninsula. The RSL histories examined in this region are from Igloolik, Cape Thalbitzer, Foxe Peninsula, Tikiraq River, Lavoie Point, Inugsuin Fiord, Iqaluit, and Cape Tanfield (IGLO,

THAL, FOXE, TIKI, LAVO, INUG, IQAL, and TANF, respectively). This region is characterized by well constrained sea-level histories, particularly on central and northern Baffin Island (Tikiraq River, Lavoie Point, Inugsuin Fiord). Foxe Peninsula has few RSL measurements, but represents the southernmost available data set from near Foxe Basin, a former load centre of the LIS. The sea-level history at Cape Tanfield is well constrained overall, although there is a large gap in the data between ∼5-8 cal kyr BP. In Region 4 there are GPS-measured uplift rates from Igloolik and Qikiqtarjuak (IGLO, QIKI), and Iqaluit (IQAL, IQLU).

The best-fit model from Regions 1-3 reasonably predicts the sea-level record in the Foxe Basin area at Igloolik, Cape Thalbitzer and the Foxe Peninsula, but overpredicts sea level on Baffin Island at Tikiraq River, Lavoie Point, Inugsuin Fiord and Cape Tanfield (Figure 6.11). At Iqaluit there is a more complex sea-level history, including rapid initial emergence between 9 and 8 cal kyr BP. Because there are no marine measurements for Iqaluit after ∼7 cal kyr BP, the sea-level record cannot constrain whether the rapid sea-level fall was followed by continually decreasing emergence or a period of submergence. The starting model from Regions 1-3 underpredicts Iqaluit's early Holocene sea-level high stand, but overpredicts sea-level change after 8 cal kyr BP (Figure 6.11). The vertical uplift rates predicted by the model from Regions 1-3 tend to be underpredicted, although all predictions except that for QIKI are within the uncertainty of the measurements (Figure 6.12).

To fit better the GIA model predictions with the RSL measurements from Baffin Island, we reduce ice thicknesses across the island by factors ranging from 0.75-0.85. We do not alter ice coverage across Foxe Basin or Melville Peninsula because the fit of the model is already good in these locations. The reduced ice thicknesses result in significantly improved RSL predictions for all of the Baffin Island locations, except for Cape Tanfield, which is fit equally well by both models (Figure 6.11). At Foxe Peninsula, the χ^2 misfit of the model predictions to the RSL measurements is increased only slightly by the thinned ice coverage on Baffin Island.

Reducing ice thicknesses across Baffin Island reduces the predicted vertical uplift rates associated with the long-term GIA response at each of the GPS sites, although predicted rates at IGLO, IQAL and IQLU remain with the observational uncertainties (in part because the uncertainties at these sites are very large, Figure 6.12). However, because Baffin Island has ice caps, and is also relatively close to the Greenland Ice Sheet, the estimated present-day ice mass loss correction for Region 4 is large (+1.1-2.9 mm/yr). Figure 6.12 explicitly shows the estimated vertical uplift rate correction

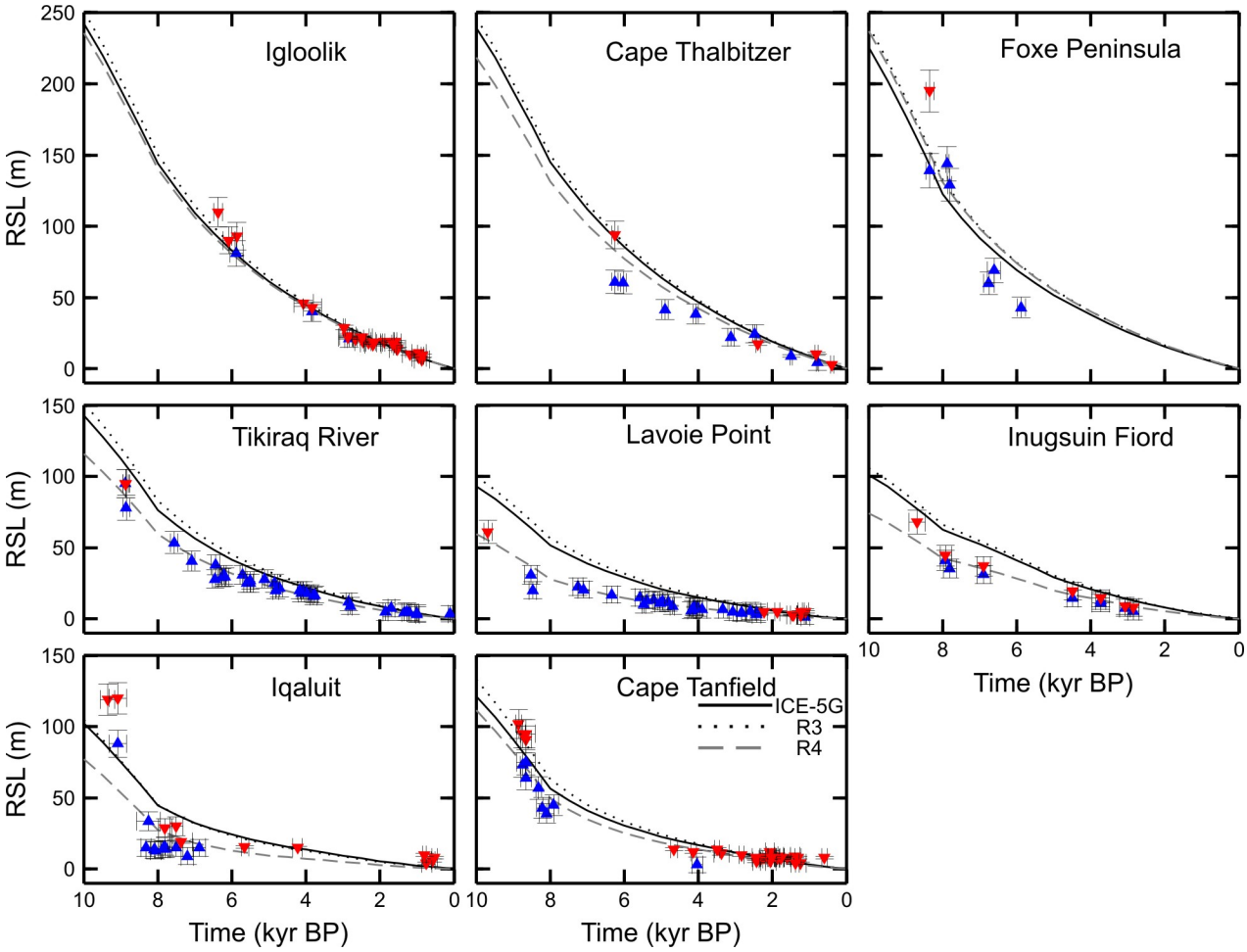

Figure 6.11: Relative sea-level predictions and measurements for Region 4. Sea-level measurements are plotted as described in the caption to Figure 4. Both the original model and the best-fit model from Region 3 (solid black and dotted black lines, respectively) well predict sea-level in the Foxe Basin region (top panel), but overpredict sea-level on northern Baffin Island (middle panel) and Iqaluit. An ice sheet reconstruction with thinned ice on Baffin Island improves the fit of the predictions to the data on northern Baffin Island and at Iqaluit, and maintains a good fit to the data from around Foxe Basin and Cape Tanfield (grey dashed line).

for present-day ice mass loss. The inclusion of this correction appears to be important for Region 4, and its addition to the predicted rates of uplift for the long-term GIA response helps to significantly improve the fit of the R4 model predictions to the GPS data. When corrected for the present-day mass loss effect, the MSE misfit of the GPS data for the best-fit model from Region 3 is MSE(R3) = 0.5, while the modified Region 4 model has a misfit of MSE(R4) = 1.2. Thus, the unmodified ice sheet reconstruction predicts the vertical uplift rates slightly better than the R4 model,

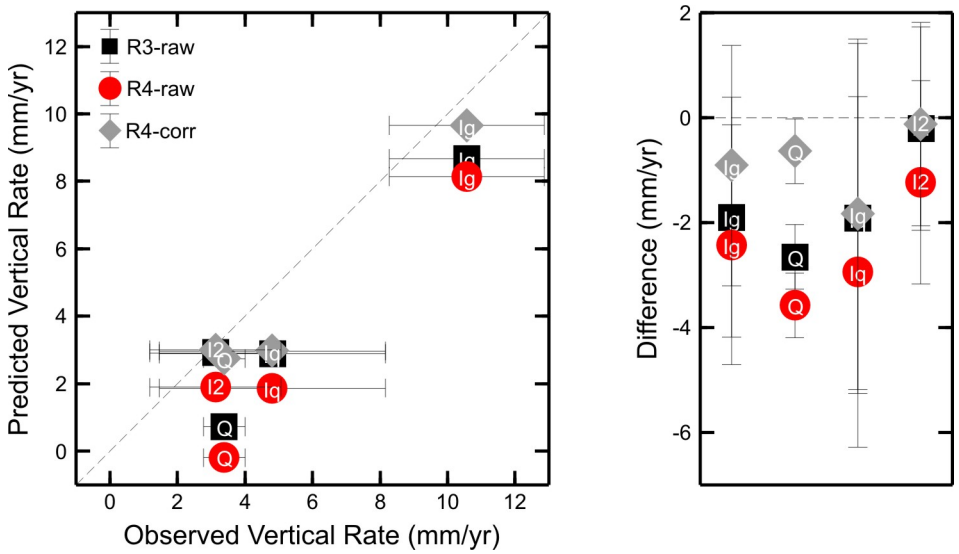

Figure 6.12: Predicted versus GPS-observed vertical rates of uplift in Region 4 (left), and the differences between the predicted and observed rates (right). The best-fit model from Region 3 (black squares, R3-raw) underpredicts rates of vertical uplift at all locations in Region 4. An ice sheet reconstruction with thinned ice in Region 4 worsens the fit of the predictions to the data (red circles, R4-raw). The R3-raw and R4-raw predictions are uncorrected for the component of uplift resulting from present-day mass loss of Arctic glaciers and ice caps, and the Greenland Ice Sheet. When corrected for this effect (grey diamonds, R4-corr) the fit of the predicted rates to the observed rates is significantly improved. Ig-Igloolik, Iq-Iqaluit (site IQAL), I2-Iqaluit (site IQLU), Q-Qikiqtarjuak.

although the MSE misfits of both models are relatively low.

6.2.6 Discussion

Regional Contributions to the Global Sea Level Budget

Plots of the region-specific changes to the LGM ice cover and global sea-level equivalent of the cumulative best-fit ice sheet reconstruction (i.e., the R4 model) relative to the original ICE-5G model are shown in Figures 6.13 and 6.14. At up to -10.0 m of global sea-level equivalent, the reduction to the ice thicknesses in Region 1 corresponds to the largest change to globally averaged sea level. This result is in part due to the fact that Region 1 is larger than any of the other regions, since it includes both the region west of Hudson Bay (Kivalliq/Keewatin), and the region south of there (Manitoba). Also, Region 1 had the largest original model ice thicknesses, and thus proportionally, the global sea-level equivalent values are more sensitive to load changes in Region 1 than in other regions. Approximately half of the 10.0 m total

reduction originates from the Keewatin region west of Hudson Bay; the remaining half originates from the southern half of Region 1. The thickened load in Region 3 contributes an additional +2.5 m to LGM globally averaged sea level. With changes to the LGM global sea-level equivalent of -0.4 m, the modifications to the ice sheet history in Region 4 do not result in a substantial change to the North American sea-level budget. The net change in global sea-level equivalent at LGM for North America for the modified ice sheet reconstruction is approximately -7.9 m.

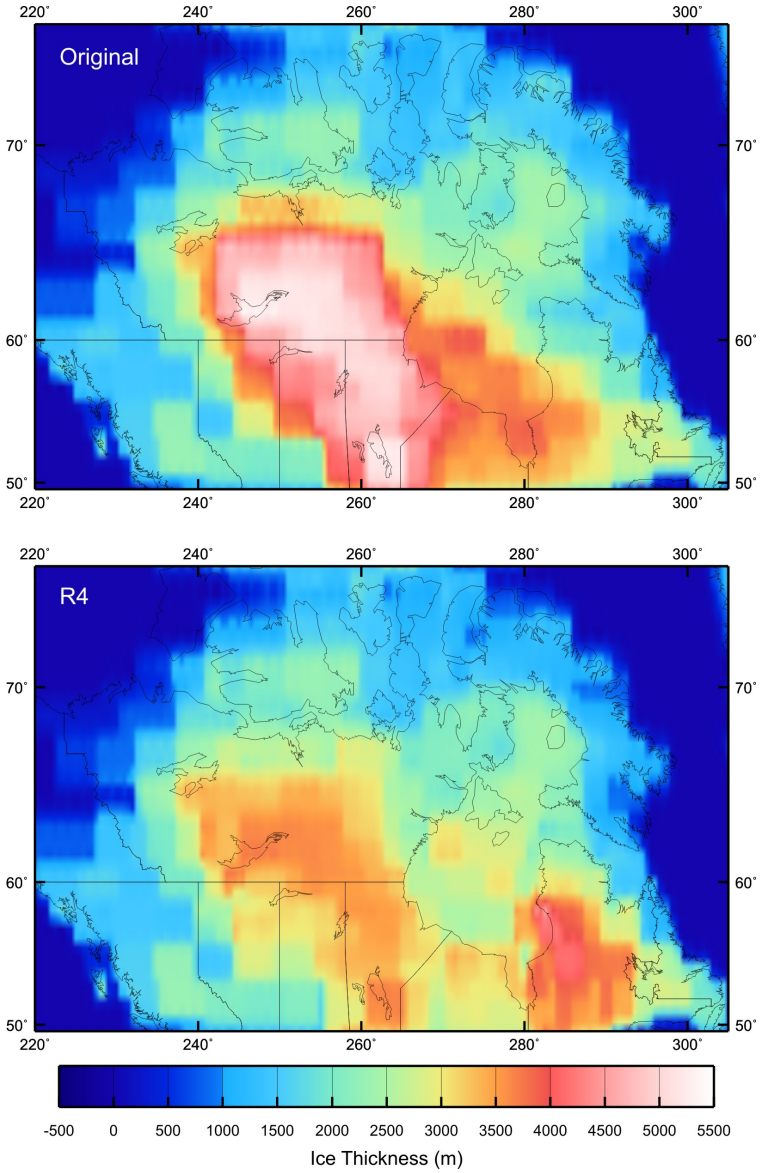

Figure 6.13: Last glacial maximum ice thicknesses of the original ice sheet reconstruction (top) and the best-fit (R4) ice sheet reconstruction (bottom).

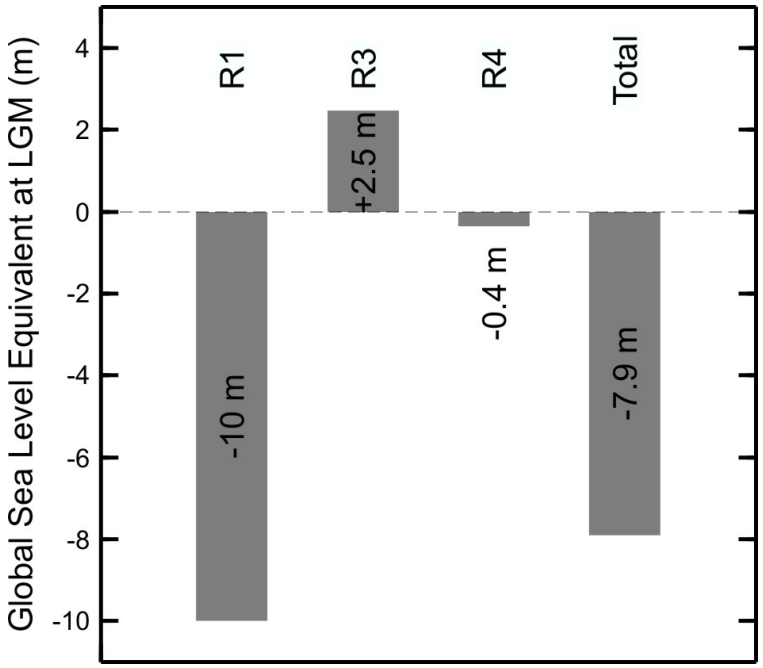

Figure 6.14: Calculated LGM global equivalent sea-level changes that result from the ice sheet reconstruction modifications in Regions 1, 3 and 4 (no changes were made to the ice load in Region 2). The reduction to the ice sheet reconstruction thicknesses in Region 1 (R1) corresponds to a substantial decrease in the global sea-level equivalent contribution, and is not substantially compensated by the effect of thickening the ice sheet reconstruction in Region 3 (R3). The changes to the ice sheet reconstruction over Baffin Island (R4) do not result in a substantial change to the contribution to global sea-level compared to Regions 1 and 3.

Although we have not directly considered GPS-measured uplift rates from more southern regions of Canada, we have computed differential vertical land motion rates predicted by the cumulative best-fit ice sheet model and the original ICE-5G model and compared to the results of Argus and Peltier (2010). The comparison suggests that additional thinning to the ice model may still be required in Manitoba to obtain a good fit with GPS uplift rates. Any additional thinning to the model in this region would increase the deficit to globally averaged sea level in Region 1.

We have not added ice on the northern British Columbia-Alberta border, although this area was identified by Argus and Peltier (2010) as an overly thin region in ICE-5G. Thickening the ice model here would result in an additional positive contribution to the total global sea-level equivalent, although it seems unlikely that this contribution would exceed that obtained for Region 3. Although ICE-5G and ICE-6G are indicated to have equivalent eustatic sea-level contributions (Vettoretti and Peltier 2013), it

is not clear from the current study that the deficit that arises from reducing ice thicknesses in the central Laurentide region can be completely offset by increased ice thicknesses in Quebec and near the northern British Columbia-Alberta border. It is possible that western Canada's contribution to globally averaged sea level may be further increased by thickening the ice model over the Cordilleran Ice Sheet, a modification which appears to be shown by Vettoretti and Peltier (2013).

At any rate, conservation of the North American contribution to globally averaged sea level will require substantial increases to ice sheet model thicknesses in other parts of the continent in order to offset the large deficit that arises from reducing the central Laurentide Ice Sheet. Although it is beyond the scope of this study, which focuses on northern North America, recent estimates of Antarctica's contribution to the global sea-level budget may introduce an additional deficit to globally averaged sea level. In ICE-5G, the global sea-level equivalent contribution of Antarctica is ∼17-18 m. This value is in excess of current estimates of ∼8-11 m for the Antarctic global sea-level equivalent contribution derived from ice sheet reconstructions developed to incorporate recent glacial-geological constraints (Ivins and James 2005, Whitehouse et al. 2012, Ivins et al. 2013) and suggests that the global sea-level deficit may be even larger than the amount derived from consideration of portions of the Laurentide Ice Sheet.

Summary of Laurentide Ice Sheet Reconstruction Results

In Figure 6.15, we compare the RSL χ^2 misfit values and GPS predictions of the original ICE-5G reconstruction to those of the cumulative best-fit ice sheet reconstruction throughout Regions 1-4. The χ^2 misfit value for all RSL measurements is reduced from 21.0 for the original model to 9.1 for the cumulative best-fit model. The MSE misfit value for all GPS measurements is reduced from 9.0 for the original model to 1.0 for the cumulative best-fit model. The best-fit ice sheet reconstruction developed in this study therefore provides an overall improved fit to the regional relative sea-level and GPS data. Region 1 shows the most significant improvement, although Regions 2 and 4 are also improved. As discussed below, Region 3 represents the only region for which clear improvement to the fit of the RSL data was not achieved.

Despite some variability in the scaling factor for which the minimum RSL χ^2 value was obtained, the results of the sensitivity analysis in Regions 1 and 2 agree with the conclusions of Lambert et al. (2006), Argus and Peltier (2010), and Mazzotti et al.

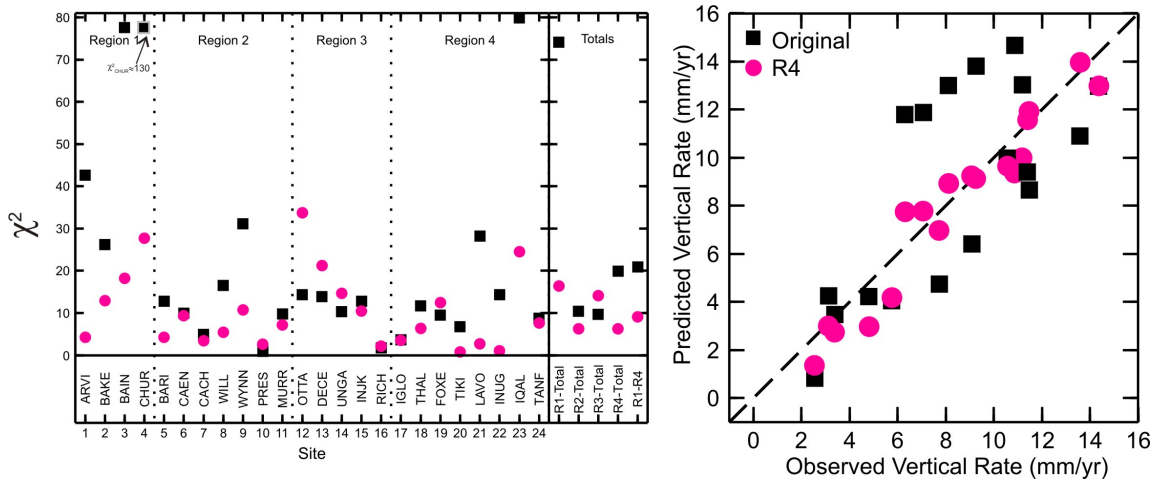

Figure 6.15: Summary of the fit of the original ice sheet reconstruction (black squares) and the best-fit ice sheet reconstruction (grey circles, R4) to all RSL and GPS measurements in Regions 1-4. The left panel shows the χ^2 misfit values for each of the individual RSL sites, as well as the cumulative χ^2 misfit values for each region (R1-Total, R2-Total, R3-Total, and R4-total) and all regions (R1-R4). The overall χ^2 misfit value on the RSL data decreases from 21.0 for the starting model to 9.1 for the best-fit R4 model. The R4 model contains all of the ice sheet modifications made in Regions 1-4 and therefore represents the final best-fit model for the study area as a whole. The right panel shows the predicted versus observed vertical uplift rates for the original model (black squares) and the R4 model (grey circles) for all 18 GPS sites. The overall MSE misfit value on the GPS data decreases from 9.0 for the starting model to 1.0 for the best-fit R4 model.

(2011) that the ice sheet thickness in ICE-5G is too large in Region 1. Ice thickness plots of the glaciological model of Tarasov et al. (2012) (shown in Lecavalier et al. (2014)) also show substantially reduced ice thicknesses west of Hudson Bay. In the current study, a uniform 30% reduction to the load thickness in Region 1 minimizes the misfit to most of the Holocene relative sea-level data as well as the observed present-day uplift rates. The exception is Baker Lake, located on the periphery of the former load centre, which locally requires less thinning than other sites in the region. The results show that the overprediction by the original model at Baker Lake is largely reconciled by the 30% reduction applied to the large area south and west of this site, and further suggest that Baker Lake is located near or just beyond the boundary of the portion of the LIS reconstruction that needs modification.

The ∼30% load reduction in Region 1 simultaneously improves the fit of the model to the RSL data in Region 2. In Region 2, no version of the ice sheet reconstruction is able to reproduce the rapid fall in sea level observed at Murray Bay at 10 kyr BP. This sharp drop in sea level may indicate a localized region where more rapid

deglaciation took place relative to that prescribed by the timing history of the ice sheet model. Alternatively, the rapid initial emergence at Murray Bay may reflect tectonic movement along faults of the Boothia Arch that became reactivated in the early Holocene by crustal uplift associated with deglaciation (Dyke et al. 1991).

In Region 3, compared to a model with thickened ice, the original ICE-5G model better predicts regional sea-level change in northern Quebec in the χ^2 sense, but strongly underpredicts all six regional GPS-measured uplift rates. In particular, it is challenging to reconcile late Holocene RSL change and present-day vertical uplift observations from the Ungava Peninsula. The sea-level histories of Deception and Ungava bays imply present-day rates of crustal uplift that appear significantly smaller than those observed by the nearest continuous GPS sites. The uplift rate inferred by Inukjuak's RSL curve is, however, large (Gray et al. 1993) and is in general agreement with the large GPS-measured uplift rate at INJK. Also, south of the Ungava Peninsula, a thickened ice sheet reconstruction is strongly supported by the GPS-measured present-day uplift rates at KUUJ, LFRG, and SCH2. This result is also consistent with the suggestion of Argus and Peltier (2010) that GPS-measured rates of vertical uplift indicate that more ice can be added to ICE-5G in southern and eastern Quebec. As well, GRACE observations over North America show a larger gravity anomaly signal east of Hudson Bay than west of Hudson Bay (Tregoning et al. 2009), an observation which suggests the presence of thicker ice there than is present in ICE-5G. It is less clear, however, whether the ice model should be thickened into northernmost Quebec. Predicted rates of vertical uplift on the Ungava Peninsula are moderately sensitive to the present-day mass loss of Greenland and Baffin Island. A higher rate of assumed mass loss for either of these locations would further increase predicted rates of vertical uplift and simultaneously reduce the magnitude of ice model thickening needed on the Ungava Peninsula.

At three locations in Region 3 (the Ottawa Islands, and Deception and Ungava bays), the RSL χ^2 misfit of the R3 model relative to ICE-5G is significantly increased (the R3 model is the version of the model that includes ice sheet modifications up to and including Region 3). This result is in part because of the worsened fit to the late Holocene RSL data at Deception and Ungava bays. However, we believe the increased misfit is also a side effect of our method of RSL data filtering. As discussed in Section 6.2.4, we have favoured data retention over data omission in the case of ambiguous RSL measurements in order to maintain the greatest objectivity possible when assessing the fit of the model to the data. The scatter on Deception and Ungava

bay's early Holocene RSL histories is large; both sites include groups of marine ages that span ∼50 m in elevation between 7-8 cal kyr BP. All of these marine ages were retained because at both sites shell ages from the (typically) nearshore *Mytilus edulis* species occur at the lower elevations. It could be argued that the uncertainty in interpreting the position of sea level that is introduced by the presence of three nearshore RSL indicators at the lower elevations is overcome by the presence of the substantially larger number (∼14) of marine ages that appear above these nearshore ages. At the Ottawa Islands, two marine ages at lower elevations have been similarly retained. Had we adopted a slightly less inclusive approach to the RSL data filtering and omitted more of the marine ages at lower elevations, the χ^2 misfit of the R3 model relative to ICE-5G would certainly be improved at Deception Bay, and possibly also at Ungava Bay and the Ottawa Islands.

In Region 4, a reduction of 15-25% to ICE-5G ice thicknesses across Baffin Island improves the fit of the model to the regional RSL measurements. This reduction corresponds to a modest decrease in peak ice thickness from approximately 1.6 km to between 1.2 and 1.35 km. However, the R4 model does not reproduce the sharp fall in relative sea-level observed at Iqaluit between 9 and 8 cal kyr BP. This result suggests that a combination of locally thicker ice prior to 9 cal kyr BP and more rapid initial deglaciation may be required in the ice model.

When uncorrected for the effect of present-day ice mass loss, the R4 model underpredicts present-day uplift rates at IGLO, IQAL and IQLU, and QIKI. However, due to the presence of ice caps and the nearby Greenland Ice Sheet, correction for this effect is important in Region 4 and significantly improves the fit of model predictions to measurements. At QIKI, the estimated present-day mass loss correction is particularly large (2.9 mm/yr) and corresponds to approximately 85% of QIKI's total observed rate of 3.4 mm/yr. This result suggests that QIKI is strongly influenced by the observed rapid present-day mass loss of the nearby Penny Ice Cap on the southeast coast of Baffin Island (Gardner et al. 2012, Zdanowicz et al. 2012).

In Region 4, if the correction for present-day ice mass loss is neglected, the variation to the starting ice sheet history favoured by the RSL data (thinning) appears contrary to the variation to the ice sheet history favoured by the uncorrected (and underpredicted) GPS measurements (thickening). However, when the GPS uplift rates are corrected for present-day ice-mass loss, the predicted present-day uplift rates fit the observed rates even in the reduced ice thickness model. This result therefore suggests that a thickened ice sheet reconstruction is likely not required to improve

the fit of model predictions to the sparse regional GPS data, and will also increase the misfit of the model to the more extensive regional RSL history.

6.2.7 Conclusion

The fit of GIA model predictions to four relative sea-level histories and six present-day rates of vertical motion from the region west of Hudson Bay indicates that the former Laurentide Ice Sheet reached a maximum thickness of ∼3.4-3.6 km in this region. This thickness represents a ∼30% reduction to the ice sheet relative to the original ICE-5G model throughout a broad area that includes the Kivalliq region of Nunavut, Manitoba, Saskatchewan, and parts of the Northwest Territories. This result is generally compatible with the 1.5 km thickness reduction to ICE-5G in central Canada indicated by Vettoretti and Peltier (2013). The reduction to the load history also reduces the size of the peripheral forebulge and increases the predicted position of sea level in load-marginal regions, an effect which improves the fit of model predictions to RSL data in a broad region to the north of the central LIS. The reduction in the ice sheet thicknesses in Region 1 corresponds to a total reduction to global sea-level equivalent of up to 10 m.

Conversely, relative sea-level data and present-day vertical uplift rates from northern and central Quebec support a thickened ice sheet in this region relative to ICE-5G. A model with ice thickened in this region decreases the MSE misfit of six continuous GPS sites in northern and central Quebec from 5.2 to 0.5. The cumulative χ^2 misfit to five RSL sites however is increased in Region 3 from 9.7 to 14.1. The worsened fit to the RSL data is due in part to the more challenging nature of the sea-level measurements, particularly at Deception and Ungava bays. No version of the GIA model explored in this study is able to simultaneously reproduce the rapid initial emergence and the slower rate of late Holocene emergence inferred by the RSL data at these sites. However, the relative sea-level histories at Inukjuak and Richmond Gulf, both located on the east coast of Hudson Bay, imply much higher rates of present-day uplift, an observation generally consistent with the high uplift rates measured at the GPS sites near these locations (INJK and KUUJ). Thus, the net outcome of fitting the GIA model predictions to the regional RSL and GPS measurements indicates a preference for a thickened ice sheet reconstruction on the Ungava Peninsula and in central Quebec, although the complex record of RSL change on the Ungava Peninsula suggests that considering more localized changes to the ice sheet history here may

be worthwhile. At present, the R3 model predicts vertical uplift rates within the uncertainty of the measured rates and provides predictions of RSL change that are at least broadly compatible with regional measurements. The increase to the model ice sheet thicknesses in Region 3 corresponds to a +2.5 m increase to globally averaged sea level at LGM.

In Region 4, the fit of the original ICE-5G model to the RSL data is generally good in the former load centre of Foxe Basin. Modest thinning (by approximately $\leq$300 m) to the ice sheet history on Baffin Island results in an improved fit to measurements of RSL, particularly on northern Baffin Island, and corresponds to peak regional thicknesses of approximately 1.3 km. This reduction to ice sheet thicknesses results in only a small (-0.4 m) reduction to globally averaged sea level.

When corrected for the estimated effect of present-day ice mass loss, the rates of vertical uplift predicted by model R4 also have a reasonable fit to the GPS-measured rates. Therefore, an important result from Region 4 is the demonstration that when the ice mass loss correction is included, predictions from a thinner ice sheet reconstruction (which better fit measurements of Holocene RSL change), can simultaneously be reconciled with the measured present-day vertical uplift rates. However, significant uncertainties exist for mass loss estimates of present-day ice cover. The assumption of a larger mass loss rate would increase the magnitude of the estimated correction (and vice versa).

Spatially denser continuous GPS coverage in the north, as well as longer observation times leading to reduced uncertainty of measurements of vertical uplift, will better constrain regional trends of present-day crustal uplift and thus benefit glacial isostatic adjustment studies. However, the use of relative sea-level measurements to constrain GIA models in northern Canada will continue because they provide a record of sea-level change, while vertical motion observations from GPS only provide a snapshot of present-day rates.

Chapter 7

GIA Models and History of the Innuitian Ice Sheet

7.1 Manuscript Information

7.1.1 Author's, Coauthors', and Outside Contributions

Section 7.2 consists of a manuscript in preparation for submission to Geophysical Journal International. The author of this thesis prepared all of the components of the manuscript (figures and text). Coauthor Thomas James developed, and provided access to, the GIA computer codes and also provided guidance with the research plan. Coauthor Arthur Dyke provided access to the original relative sea-level database (Section 5.1) and insight into the Quaternary glacial history of the study area. Joseph Henton assisted with much of the processing and interpretation of the GPS data.

7.1.2 Citation

Simon, K.M., James, T.S., and Dyke, A.S. A New Glacial Isostatic Adjustment Model of the Innuitian Ice Sheet, Arctic Canada. Submitted to Quaternary Science Reviews.

7.1.3 Authors' Names and Affiliations

K.M. Simon[1,2*], T.S. James[2,1], A.S. Dyke[3,4]

[1] School of Earth and Ocean Sciences, University of Victoria, Victoria, BC, V8P 5C2

[2] Geological Survey of Canada, Natural Resources Canada, Sidney, BC, V8L 4B2

[3] Department of Earth Sciences, Dalhousie University, Halifax, NS, B3H 4R2

[4] Department of Anthropology, McGill University, Montreal, QC, H3A 2T4

[*] Corresponding author: ksimon@uvic.ca

7.1.4 Manuscript Format

The figures included in Section 7.2 have been numbered to maintain consistency with the rest of the thesis. The references cited in the manuscript are included with the final list of references for the thesis as a whole, and are not given separately.

7.2 A New Glacial Isostatic Adjustment Model of the Innuitian Ice Sheet, Arctic Canada

7.2.1 Summary

A reconstruction of the Innuitian Ice Sheet is developed that incorporates current first-order constraints on its spatial extent and history as suggested by regional glacial geology studies. Glacial isostatic adjustment modelling of this ice sheet reconstruction provides relative sea-level predictions that are in good agreement with regional measurements of post-glacial sea-level change at 18 locations. The results indicate peak thicknesses of the Innuitian Ice Sheet of approximately 1600 m, up to 400 m thicker than the minimum peak thicknesses estimated from glacial geology studies, but between approximately 1000 to 1500 m thinner than the peak thicknesses utilized in previous depictions of the ice sheet. Although the thickness history of the Innuitian Ice Sheet model developed here differs from the ICE-5G reconstruction, both models provide a similar fit to relative sea-level measurements from the former alpine sector of the ice sheet. Conversely, the updated Innuitian Ice Sheet model provides an improved fit to sea-level measurements from the former lowland sector of the ice sheet. The vertical crustal motion predictions of the best-fit IIS model are in general agreement with limited GPS observations, after correction for a significant elastic crustal response to present-day ice mass change. The new model provides an approximately 2.7 m equivalent contribution to global sea-level rise, a change of +0.6 m compared to the Innuitian portion of ICE-5G.

7.2.2 Introduction

Glacial isostatic adjustment (GIA) models predict the solid Earth's loading and relaxation response to glacial cycles of growth and decay. They typically consist of a spatial-temporal reconstruction of ice sheet coverage applied to an Earth model in which key parameters are the elastic lithospheric thickness and the radial mantle viscosity profile. The fit of GIA model predictions to observations that are typi-

cally attributed to the GIA process, such as Holocene relative sea-level change, often yields information relating to ice sheet evolution and Earth properties. However, without sufficient independent constraints, GIA model predictions may not be able to distinguish these parameters independently. The incorporation of independent glacial-geological constraints on ice sheet evolution or geophysical constraints on the Earth's physical and rheological properties can therefore provide important additional information with which to construct initial model configurations.

In this study, we focus on the GIA response in the Queen Elizabeth Islands (QEI) within the islands of the Canadian Arctic Archipelago (Figure 7.1). Although the configuration and extent of ice coverage in the QEI during the last glaciation has been debated, the history of Holocene glacial isostatic uplift and relative sea-level fall following deglaciation is well-recorded by radiocarbon-dated material collected from raised beaches and marine sediments throughout the region. GPS-measured rates of crustal deformation are also available from the region, although there are only four continuous GPS sites installed throughout the QEI, and present-day crustal uplift is significantly less well-recorded than the history of sea-level change.

This study develops a trial model of Innuitian Ice Sheet (IIS) coverage that follows the current glacial-geological constraints on the evolution of the IIS summarized by England et al. (2006). We perform a GIA modelling analysis to test how well this model of the IIS can predict the well-recorded history of post-glacial sea-level change and to assess the sensitivity of the predicted GIA response to variations in the Earth model. The primary goal of the study is to evaluate whether the development of a revised IIS reconstruction can better explain observed Holocene sea-level change in the region. A secondary goal is to constrain better ice thickness estimates in the Innuitian region. We compare the predictions of the IIS model developed in this study to those of the ICE-5G reconstruction (Peltier 2004), which differs substantially in its ice coverage across the QEI. We also evaluate to what extent GPS-measured present-day uplift rates may be influenced by nearby ice mass loss, and quantify the global sea-level equivalent contribution of the IIS reconstruction that best fits the available relative sea-level data.

7.2.3 Background and Previous Innuitian GIA Studies

Relative to the Laurentide Ice Sheet, the much smaller Innuitian Ice Sheet has received considerably less attention in the history of North American glaciation as well as in

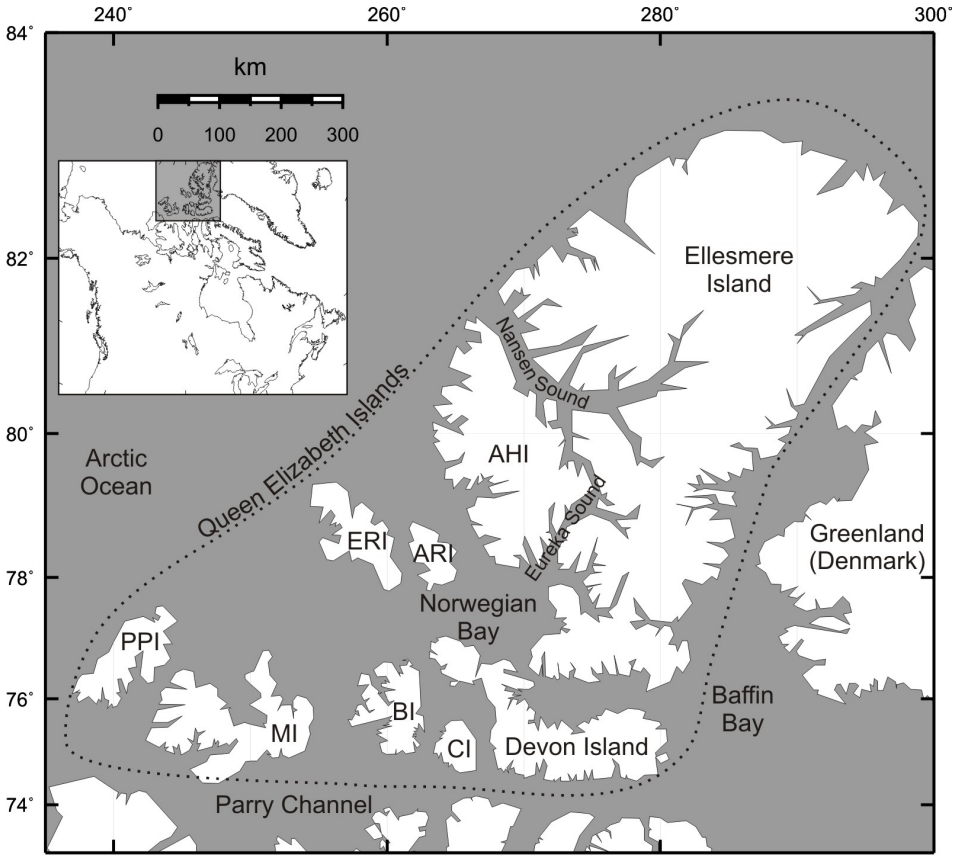

Figure 7.1: Map of the study area showing the Queen Elizabeth Islands (the region of the former Innuitian Ice Sheet) and geographical place names. AHI - Axel Heiberg Island, ARI - Amund Ringnes Island, BI - Bathurst Island, CI - Cornwallis Island, ERI - Ellef Ringnes Island, MI - Melville Island, PPI - Prince Patrick Island.

studies of glacial isostatic adjustment. The extent of the last glaciation in the Queen Elizabeth Islands and the existence of the IIS were debated for over a century (see Dyke 1999 for a review), and competing interpretations of the regional glacial history were typically divided into two general hypotheses. In the first hypothesis, the most recent glaciation was not extensive in the QEI, and no continuous ice sheet was present. Rather, glaciers and ice caps thickened and extended beyond their present-day boundaries, and ice coverage consisted of a series of discontinuous ice caps with peak ice thicknesses likely not exceeding 1000 m (e.g., England 1976, Dyke and Prest 1987). The second hypothesis, which was based largely on the observed pattern of Holocene emergence, featured extensive ice coverage over the QEI and the presence of a continuous ice sheet during the last glacial maximum (LGM, Blake 1970).

The two hypotheses were the subject of intense debate throughout the 1970's and

onward, with resolution proving elusive in part because the relative lack of observational data allowed multiple interpretations of glacial history. However, a growing number of observations of glacial flow directions, erratic dispersal trains, lateral meltwater channels, and new relative sea-level (RSL) measurements, as well as reinterpretations of previous data, have converged to support extensive ice coverage at the LGM and to provide improved constraint on IIS chronology (Bednarski 1998, Dyke 1999, Ó Cofaigh et al. 2000, Atkinson 2003, Atkinson and England 2004, England et al. 2004). The most recent consensus is that a continuous ice sheet existed in the Innuitian region. It consisted of an alpine sector to the northeast over Ellesmere and Axel Heiberg islands, and a lowland sector to the southwest. The IIS began advancing to its maximum extent after 27 ^{14}C kyr BP and as late as 19 ^{14}C kyr BP (and reached its LGM configuration up to 5 ^{14}C kyr after the Laurentide Ice Sheet). It did not begin retreating from its margins until 11-10 ^{14}C kyr BP (Dyke et al. 2002, England et al. 2006).

Tarasov et al. (2012) recently developed a glaciological model for the North American ice sheets, and this model includes an Innuitian Ice Sheet component that is constrained by regional RSL data. However, Innuitian Ice Sheet evolution was not the primary focus of the Tarasov et al. (2012) study, and there has been little recent detailed evaluation of Innuitian Ice Sheet evolution within forward GIA models. One of the only forward GIA modelling studies dedicated to the Innuitian region pre-dates the resolution of the IIS debate (Tushingham 1991a). In Tushingham's study, each end-member hypothesis for ice coverage was evaluated in terms of its ability to reproduce measurements of Holocene sea-level change. Tushingham (1991a,b) concluded that compared to a thinner, discontinuous ice sheet, a model with thicker, more extensive ice coverage better fit relative sea-level measurements throughout the region. The more successful ice sheet reconstruction used by Tushingham (1991a) was the ICE-3G model of Tushingham and Peltier (1991); as England et al. (1991) observed, ICE-3G was designed specifically to provide a best fit to relative sea-level data, and thus in the absence of independent constraints, its ability to reasonably predict Innuitian sea-level change could not discount the existence of alternative and equally viable ice sheet configurations.

The ICE-3G ice sheet model used by Tushingham (1991a) featured maximum Innuitian ice thicknesses of up to 2500 m, and was used in conjunction with an Earth model with a 120 km thick elastic lithosphere, an upper mantle (>670 km depth) viscosity of 10^{21} Pa s, and a lower mantle viscosity of 2×10^{21} Pa s. This upper

mantle viscosity value is somewhat higher than more recent global estimates of upper mantle viscosity ($\sim 4 \times 10^{20}$ Pa s, Mitrovica and Forte 2004). A change in the upper mantle viscosity in the ICE-3G calculations would affect the RSL predictions and require changes to the ice sheet thickness history. ICE-5G (Peltier 2004) is a more recent global ice sheet reconstruction, and it has been used by Lecavalier et al. (2013) to predict Innuitian sea-level change. This study, however, placed primary focus on the Greenland Ice Sheet, and obtained a best-fit of model predictions to sea-level measurements through variation of Earth model parameters, not ice sheet history. We use the most recent constraints on IIS configuration and chronology to guide the development of a revised IIS reconstruction, and then compare its GIA predictions with those of ICE-5G throughout the QEI.

7.2.4 Methods and Data

Model Description

We compare the predictions of the global ICE-5G model (Peltier 2004) to the predictions of a new ice-loading history of the Innuitian Ice Sheet (IIS). Our IIS model is embedded in a global ice-loading model that features an updated Laurentide Ice Sheet thickness history (Chapter 6) and, for the rest of the globe, the ICE-5G ice sheet history. We also explore the effects on RSL predictions of varying the thickness of the IIS within the new reconstruction. The Earth model follows the VM5a profile of Peltier and Drummond (2008), and consists of a 60 km thick elastic lithosphere overlying a 40 km thick layer of high viscosity (10^{22} Pa s). Below the lithosphere, the VM5a viscosity profile is an approximation of the VM2 profile derived by Peltier (1996), and has viscosities of 5×10^{20} Pa s from 100-660 km depth, 1.6×10^{21} Pa s between 660-1160 km depth, and 3.2×10^{21} Pa s from 1160 km depth to the core mantle boundary. The calculations solve for the response to surface loading of a viscoelastic Maxwell rheology following the description of James and Ivins (1998) and include a globally self-consistent solution of the sea-level equation following the methods of Mitrovica and Peltier (1991) and Mitrovica and Milne (2003).

Constraining Data (RSL and GPS)

Relative sea-level data from 18 locations within the QEI form the primary constraint for the GIA models. Of the selected RSL data, there are 9 locations from each of the former alpine and lowland sectors of the IIS (Figure 7.2). The RSL data sets are

selected, filtered for non-constraining data points, and assigned spatial uncertainties following the methods described in Chapter 6. A χ^2 measure of misfit is used to evaluate the level of fit between the model predictions and RSL measurements according to

$$\chi^2_{RSL} = \frac{1}{N}\sum_{i=1}^{N}\left[\left(\frac{RSL_i^{o,s} - RSL_i^{p,s}}{\sigma_i^{o,s}}\right)^2 + \left(\frac{RSL_i^{o,t} - RSL_i^{p,t}}{\sigma_i^{o,t}}\right)^2\right], \qquad (7.1)$$

where ($\mathrm{RSL}^{o,s}$, $\mathrm{RSL}^{o,t}$) and ($\mathrm{RSL}^{p,s}$,$\mathrm{RSL}^{p,t}$) are the respective observed (o) and predicted (p) RSL coordinates in space and time (s,t) of the i^{th} observation point, $\sigma^{o,s}$ and $\sigma^{o,t}$ are the respective observational uncertainties in space and time, and N is the number of RSL measurements (e.g., Mitrovica et al. 2000, Paulson et al. 2007).

GPS-measured vertical uplift rates from four site locations are also compared to model-predicted present-day uplift rates (Figure 7.2). The data are aligned in the ITRF 2008 reference frame. The misfit between the observed and predicted vertical uplift rates is calculated as

$$\chi^2_{GPS} = \frac{1}{N}\sum_{i=1}^{N}\left(\frac{V_i^o - V_i^p}{\sigma_i^o}\right)^2, \qquad (7.2)$$

where V_i^o and V_i^p are the observed and predicted rates of vertical crustal motion at the i^{th} site location, respectively, σ_i^o is the i^{th} observational uncertainty, and N is the number of GPS sites.

Due to the proximity of the GPS sites to present-day ice cover in the region (Figure 6.4), a component of the GPS-measured vertical land motion rates may be attributable to the present-day ice mass loss of Arctic glaciers and ice caps (GIC) and the Greenland Ice Sheet. We adjust the predicted long-term GIA uplift rates for this effect by adding them to the calculated purely elastic response of the Earth to changes in present-day ice cover. To compute the contribution of the elastic effect, rates of present-day mass loss are specified according to recent estimates. The GIC in the Canadian Arctic are currently experiencing an estimated mass loss of 60 $\pm$ 8 Gt/yr (Gardner et al. 2011, Gardner et al. 2013), and from 1992-2011, the Greenland Ice Sheet experienced an estimated mass loss of 142 $\pm$ 49 Gt/yr (Shepherd et al. 2012). Spatially uniform mass loss is assumed for both the Arctic GIC and the Greenland Ice Sheet; we do not include ice mass loss from other sources. The use of different mass loss scenarios (which are subject to large uncertainty), or the inclusion of spatially non-uniform mass loss would alter the predictions of the elastic contribu-

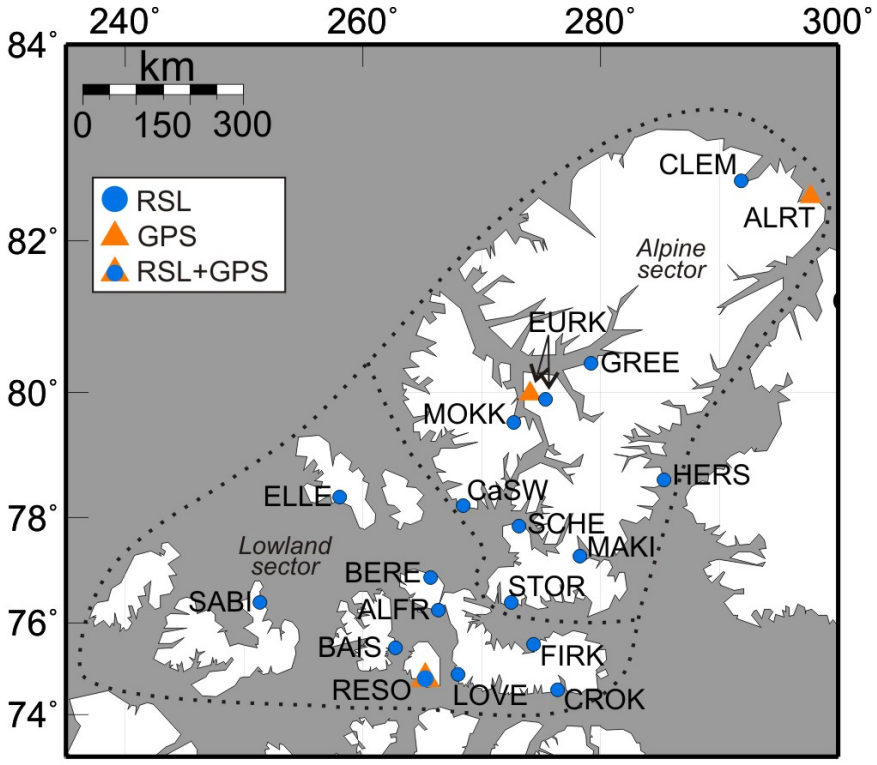

Figure 7.2: Site map of the relative sea-level (RSL) and GPS site locations and names. RSL sites are shown by the blue circles, GPS sites are shown by the orange triangles, and site RESO, which has both RSL and GPS data, is shown by a blue circle within an orange triangle. At Eureka (EURK), there is some spatial separation between the average location of the RSL data and the GPS site. The black dotted lines enclose the region of the former Innuitian Ice Sheet, including the approximate boundaries of the alpine sector to the northeast, and the lowland sector to the southwest.

tion. Therefore, the calculated predictions of the present-day mass loss effect should be considered preliminary estimates.

An Alternative Reconstruction of the Innuitian Ice Sheet

A representation of the IIS is developed that incorporates to first-order the glacial-geological constraints on ice sheet history recently presented by England et al. (2006) (Figure 7.3). These glacial-geological observations are used to guide the thickness history and margin chronology of the new model; other features such as ice physics and climate forcing are not incorporated. The revised IIS model is on a grid with a spacing of approximately $0.7^\circ \times 0.7^\circ$, and features 36 time slices from 122 kyr to present. Compared to the ICE-5G model (Peltier 2004), there are four main changes to the IIS reconstruction. First, the updated IIS model features continuous ice coverage over the entire Innuitian region, including grounded ice in the inter-island channels of the lowland sector. In contrast, ICE-5G features separated ice domes. Second, absolute ice thicknesses are based on topographically derived minimum peak thickness estimates. Based on the vertical distance between formerly ice-covered topographic high points and the depth of adjacent fiords ($\leq$600 m deep), Ó Cofaigh et al. (2000) and England et al. (2004) both suggested the minimum peak thickness of the IIS was approximately 1200 m. In contrast, the peak thickness of ICE-5G over Bathurst Island exceeds 3000 m. The thick ice cover on Bathurst Island is however localized to this region, and thinner ice is present in ICE-5G throughout the remaining Innuitian region. Third, the relative thickness distribution of the revised model is designed to correlate with the observed pattern of Holocene emergence. The emergence history suggests that ice was thickest in Eureka and Nansen sounds in the central alpine sector, and that thinner ice existed in the outer alpine sector and throughout the lowland sector. And fourth, the timing history of the revised IIS model incorporates the margin chronology of England et al. (2006), and features retreat of the lowland sector of the IIS after 13 cal kyr BP, retreat of the alpine sector at approximately 9.5 cal kyr BP, and an assigned LGM time that is delayed relative to the LGM of the LIS by 5 kyr. Both ICE-5G and the revised IIS model are shown at their LGM times (26 kyr BP and 21 kyr BP, respectively) in Figure 7.4.

The boundaries of the present-day ice caps on Ellesmere, Axel Heiberg, and Devon islands are approximated from the Randolph Glacier Inventory (RGI, Arendt et al. 2012), although the resolution of the GIA model grid is much coarser than the spatial resolution of the RGI. Constraints on present-day thickness of the ice caps are sparse, although Dowdeswell et al. (2004) estimated the Devon ice cap has a peak central thickness of approximately 700 m with thinner ice around the margins. For simplicity,

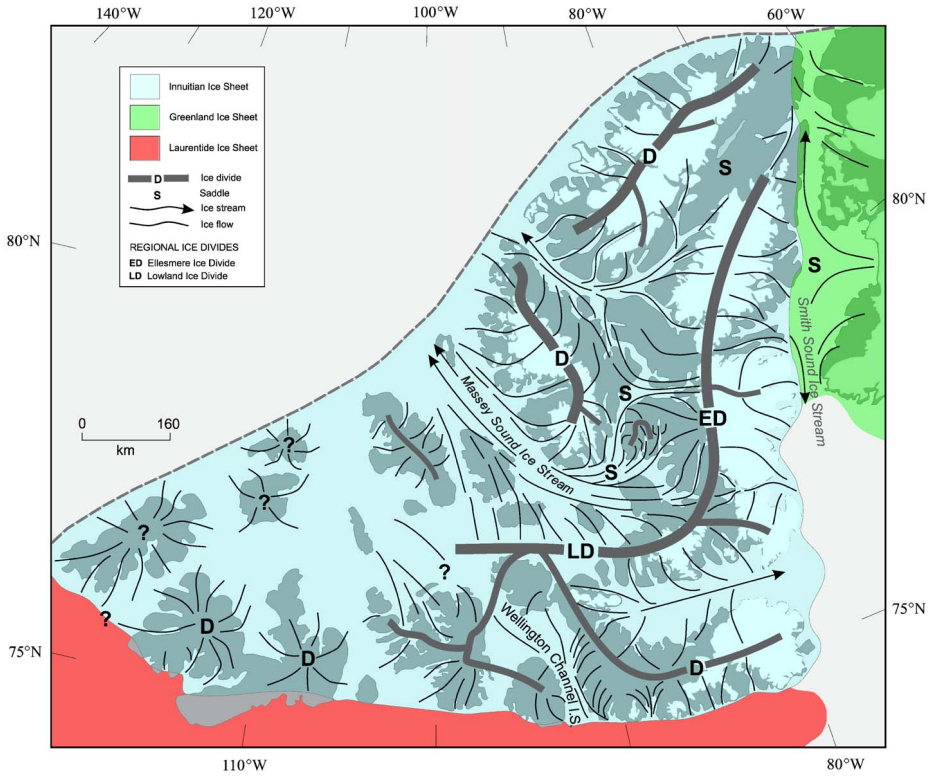

Figure 7.3: Schematic depiction of the Innuitian Ice Sheet. Current glacial-geological constraints indicate continuous ice coverage across the QEI. In the alpine sector, local ice divides formed on the topographic high points and ice flow converged within the alpine interior. Relative to the alpine sector, thinner ice was present in the lowland sector, but covered the islands and filled the inter-island channels. Figure taken from England et al. (2006).

we assume the thicknesses of the present-day ice caps on Axel Heiberg and Ellesmere islands follow a similar distribution. In the results section, we compare the fit to observations of predictions from both the original ICE-5G model to variations of the revised IIS model.

7.2.5 Results

We compare the GIA model predictions to a total of 18 sea-level histories from the QEI (Figure 7.2). From the former alpine sector, we consider the RSL histories from Eureka (EURK), Greely Fiord (GREE), Mokka Fiord (MOKK), Cape Southwest (CaSW), Schei Point (SCHE), Makinson Inlet (MAKI), Clements Markam Inlet (CLEM), Cape Herschel (HERS), and Cape Storm (STOR). From the former lowland sector, we consider the RSL histories from Bere Bay (BERE), Prince Alfred Bay

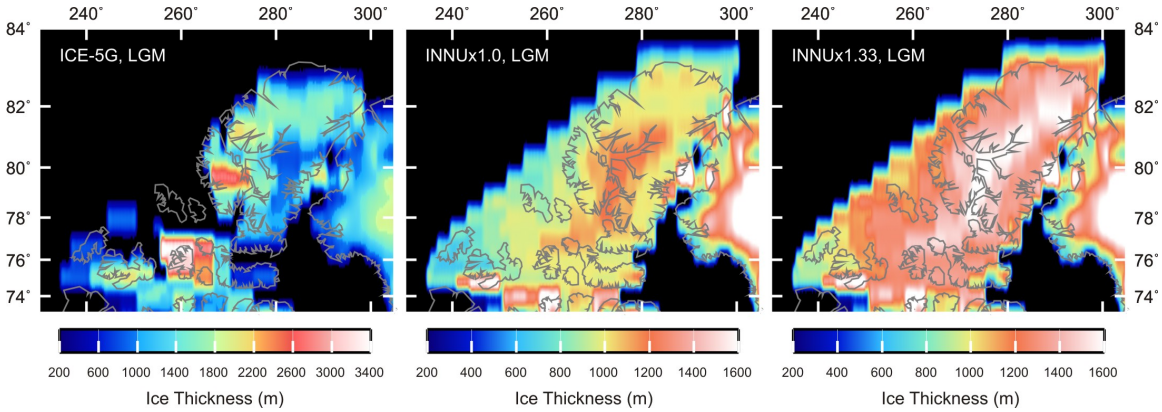

Figure 7.4: Ice thickness maps at LGM of the Innuitian Ice Sheet for ICE-5G (left) and the models developed in this study (middle, right). The initial model developed in this study has peak thicknesses of approximately 1200 m in Eureka and Nansen sounds (middle, INNU×1.0) while the model that best fits the relative sea-level data has peak thicknesses of approximately 1600 m (right, INNU×1.33). Relative to the INNU×1.0 model, the best-fit INNU×1.33 model also has ice locally thickened near Clements Markam Inlet, and thinned near Croker Bay. Both versions of the revised model have continuous ice coverage across the Queen Elizabeth Islands.

(ALFR), Bathurst Island (BAIS), Resolute (RESO), Lovell Point (LOVE), Firkin Point (FIRK), Croker Bay (CROK), Sabine Peninsula (SABI), and Ellef Ringnes Island (ELLE). The fit of the original ICE-5G model to RSL measurements from the Innuitian region is generally good. The main exceptions are that RSL is overpredicted in the Bathurst Island region and underpredicted in the southwestern lowland sector (Figures 7.5, 7.6). However, as discussed in Section 7.2.4, the ICE-5G model does not agree with many of the current constraints on regional ice sheet history.

The revised Innuitian Ice Sheet model discussed in Section 7.2.4 was developed to incorporate these constraints, and has initial peak ice thicknesses of 1200 m in Eureka and Nansen sounds. This model strongly underpredicts RSL throughout both the alpine and lowland sectors (Figures 7.5, 7.6). To improve the fit of the model to the observed sea-level history, we applied uniform scaling factors to the IIS reconstruction. Increasing the thickness of the load by a factor of one-third provides a good fit to most of the sea-level histories from both the alpine and lowland sectors. Clear RSL misfits for this model still exist at Clements Markam Inlet (underpredicted), and Croker Bay (overpredicted). The introduction of locally thicker ice near Clements Markam Inlet and thinner ice near Croker Bay in the thickened IIS model improves, but does not entirely reconcile, the misfit of model-predicted sea level at these sites (Figures 7.5, 7.6).

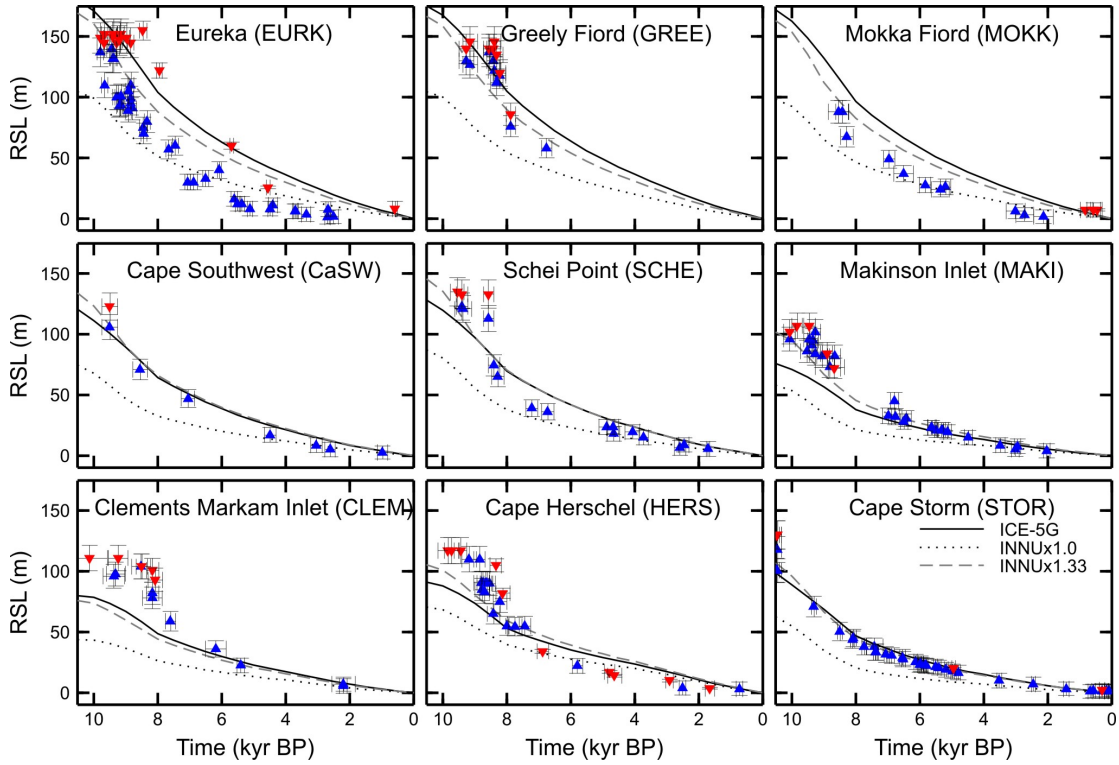

Figure 7.5: Relative sea-level predictions and measurements for the alpine sector of the Innuitian Ice Sheet. Lower observational constraints on the position of sea level are shown by the blue triangles, and upper observational constraints are shown by the red triangles. The triangles point in the direction of the inferred position of sea level. Model predictions of the ICE-5G reconstruction (solid black line) are compared to those from the minimum IIS model developed in this study (black dotted line, INNU×1.0), and the best-fit IIS model, which has ice thicknesses that are one-third larger than the 1.0 model (grey dashed line, INNU×1.33). At most sites, the ICE-5G and the INNU×1.33 models both provide similar and good fits to the RSL data from the alpine sector. The best-fit INNU×1.33 model also has ice locally thickened near Clements Markam Inlet (CLEM) and thinned near Croker Bay (CROK).

Despite the misfits at Clements Markam Inlet and Croker Bay, an IIS reconstruction with most of the ice thicknesses increased by a factor of one-third relative to the first version of the revised IIS model fits the regional RSL data at least as well, or better, than the original ICE-5G model. In the alpine sector, the χ^2 misfit of our best-fit IIS model relative to ICE-5G is modestly decreased at most sites but increased at Clements Markam Inlet and Greely Fiord (Figure 7.7). At Greely Fiord the increase is partly due to scatter on the data points between 8-10 cal kyr BP. Overall, both ICE-5G and the revised IIS model appear to predict sea-level change in the alpine sector reasonably well. Relative to ICE-5G, the change in χ^2 values of the best-fit IIS

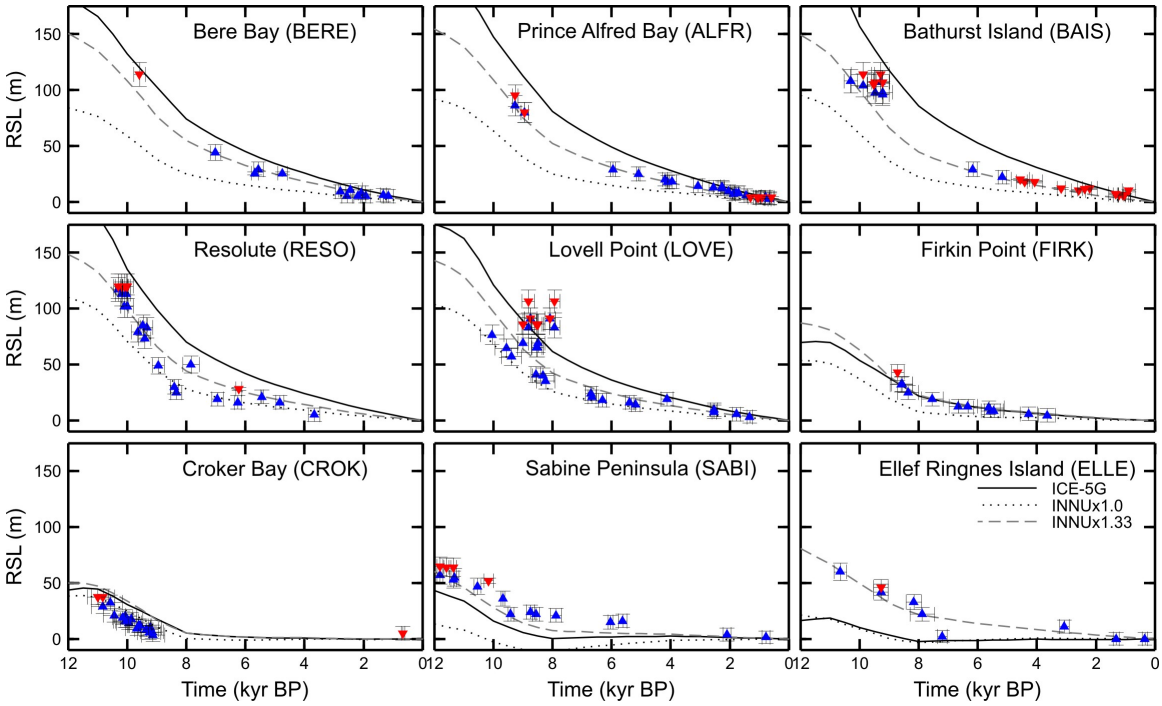

Figure 7.6: Relative sea-level predictions and measurements for the lowland sector of the Innuitian Ice Sheet. The sea-level measurements and model predictions are plotted as described in Figure 7.5. The INNU×1.33 model provides the best fit to the RSL data from the lowland sector, and compared to ICE-5G has thinner ice near Devon, Cornwallis and Bathurst islands (site locations Bere Bay, Prince Alfred Bay, Bathurst Island, Resolute, Lovell Point), and thicker, more continuous ice coverage in the southeastern regions of the QEI (site locations Sabine Peninsula and Ellef Ringnes Island). The best-fit INNU×1.33 model also has ice locally thickened near Clements Markam Inlet (CLEM) and thinned near Croker Bay (CROK).

model is statistically insignificant in the alpine sector ($p = 0.0711$), but this p value is close to the threshold value of 0.05 for significance.

In the lowland sector, the fit of our IIS model is improved relative to ICE-5G (i.e., the χ^2 misfit is decreased, Figure 7.7). This improvement is both the result of decreasing ice thicknesses around Bathurst Island, and including thicker and grounded ice in the southwest near Sabine Peninsula (Melville Island) and Ellef Ringnes Island. At Firkin Point, the χ^2 RSL misfit value is decreased for our model relative to ICE-5G, although both models fit the data at this site very well (Figures 7.6, 7.7). Croker Bay is the only selected site location within the lowland sector for which the fit of predictions to observations is not improved for the revised IIS model. Relative to ICE-5G, the new IIS model yields a statistically significant improvement in fit to RSL data in the lowland sector ($p = 0.0014$).

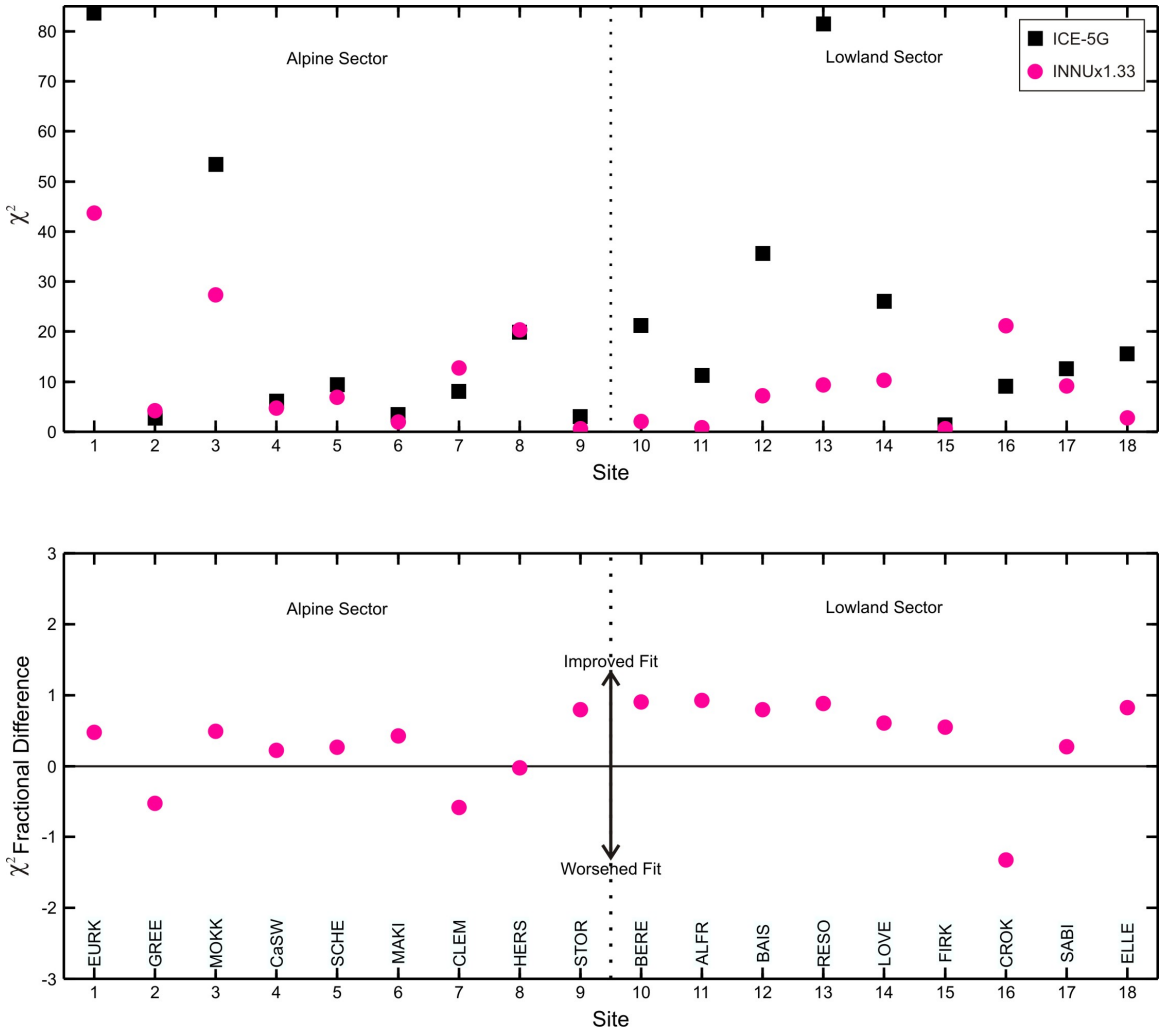

Figure 7.7: Total χ^2 misfit values for the 18 RSL histories from the Innuitian region for both the starting ICE-5G ice model (black squares) and the best-fit IIS model developed in this study (grey circles) (top panel). Fractional difference in χ^2 misfit values relative to ICE-5G for the best-fit IIS model (grey circles) (lower panel). ICE-5G plots at zero because the fractional difference is taken relative to ICE-5G. A positive fractional difference represents a decreased RSL misfit (i.e., improved agreement) for the revised best-fit IIS model, and vice versa. The four-letter site abbreviations for each location are the same as those given in Figure 7.2.

The only four continuous GPS sites in the Queen Elizabeth Islands are located at Resolute, Eureka, and Alert (RESO, EURK and EUR2, ALRT). When only the long-term GIA response is considered, neither the original ICE-5G model nor our best-fit IIS model predict the vertical uplift rates particularly well, and both models have high χ^2 misfit values (Figure 7.7). Both models underpredict the rate of vertical uplift at RESO, EUR2 and ALRT from between ∼0.5-3.5 mm/yr, and overpredict

the rate of vertical uplift at EURK by ∼0.5-2 mm/yr. Addition of the present-day mass loss effect to the predictions from the best-fit IIS model improves the fit between the predicted and observed uplift rates, and reduces the χ^2 misfit value of the four observation points by close to a factor of 5 (Figure 7.8).

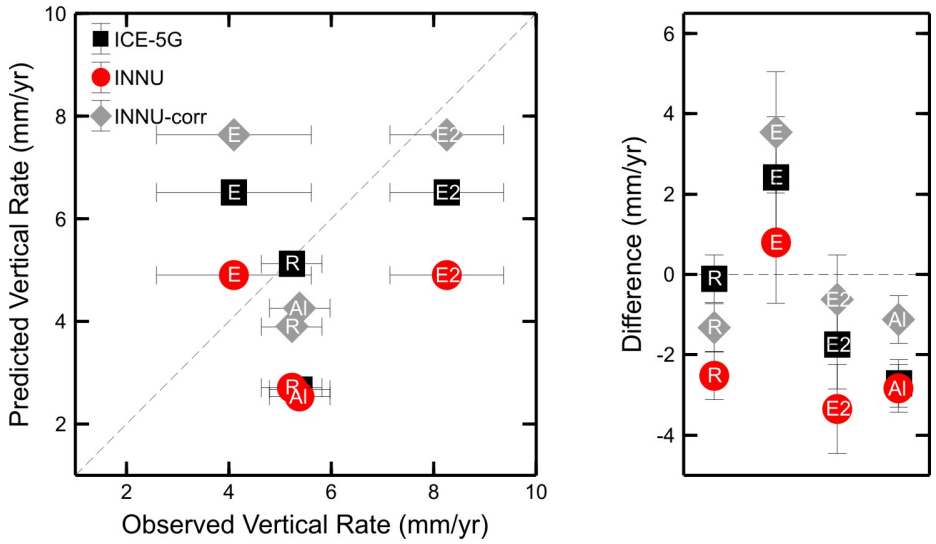

Figure 7.8: Predicted versus GPS-observed vertical uplift rates in the Innuitian region (left), and the differences between the observed and predicted rates (right). The ICE-5G model (black squares) is compared to the best-fit IIS model developed in this study (INNU×1.33). The best-fit INNU×1.33 model is shown both with and without the effect of present-day mass loss of nearby glaciers and ice caps and the Greenland Ice Sheet (grey diamonds and red circles, respectively). Without the inclusion of the present-day mass loss effect, the INNU×1.33 model underpredicts rates of vertical uplift at sites Al, E2 and R (red circles). Compared to not accounting for present-day ice mass change, inclusion of the present-day mass loss effect in the INNU×1.33 model predictions improves the agreement at 3 of the 4 GPS sites (grey diamonds). Al - Alert, E and E2 - Eureka (EURK and EUR2), R - Resolute.

7.2.6 Discussion

The revised Innuitian Ice Sheet reconstruction uses, as a starting basis, the current independent glacial-geological constraints that were summarized in England et al. (2006). The revision features continuous ice coverage throughout both the alpine and lowland sectors of the ice sheet, compared to the isolated ice caps of ICE-5G. Peak ice thicknesses at LGM are approximately one-half of the peak thicknesses in the Innuitian component of ICE-5G, although the peak thickness of 3000 m in ICE-5G is isolated to the region around Bathurst Island. The first version of the IIS model

defined the peak ice thickness to be 1200 m, consistent with the lower bound on peak ice thickness indicated by Ó Cofaigh et al. (2000) and England et al. (2004). This model consistently underpredicts sea-level change throughout the region. A one-third increase to the load provides a much improved fit of the model predictions to regional RSL measurements, and corresponds to peak ice thicknesses in the central alpine sector of ∼1600 m, and peak thicknesses throughout much of the lowland sector of ∼1330 m.

The spatial extent of our best-fit IIS model more closely resembles the ICE-3G model of Tushingham and Peltier (1991) than the ICE-5G model, although, at 1600 m, the peak ice thicknesses are approximately one-third smaller than those in ICE-3G. The ability of our thinner ice sheet reconstruction to fit the regional RSL data may in part be the result of using an Earth model with a slightly thinner lithospheric thickness and a slightly decreased upper mantle viscosity compared to that used for ICE-3G. The global ICE-6G ice sheet reconstruction has been developed as an update to ICE-5G (e.g., Peltier et al. 2012a), and maps of surface elevation and ice cover suggest that ICE-6G also includes more continuous ice coverage in the Innuitian region than ICE-5G ($https://wiki.lsce.ipsl.fr/pmip3/lib/exe/fetch.php/pmip3:design:21k:icesheet:ice-ng_compare_polar.pdf$, Gregoire 2010). As well, maps of ice thickness from Tarasov et al.'s (2012) North American glaciological model (shown in Lecavalier et al. (2014)) show more extensive ice coverage in the Innuitian region than ICE-5G and ice thicknesses that appear comparable to those of the INNU×1.33 model.

The global sea-level equivalent contribution at LGM for the revised version of the IIS model is approximately 2.7 m. Despite the significant differences in ice thickness and distribution compared to ICE-5G, our revision to the IIS reconstruction overall results in only a small net change to the LGM global sea-level budget of +0.6 m (i.e., at LGM the Innuitian component of the revised model is larger than ICE-5G by a global sea-level equivalent contribution of 0.6 m). The small overall change to the global sea-level contribution shows that the effect of expanding the spatial extent of ice cover in the revised model is offset substantially by the overall thinner peak ice thicknesses.

Although the new ice model reproduces the first-order glacial-geological constraints on IIS history summarized by England et al. (2006), the spatial resolution is coarse. The coarseness of the grid allows only approximate definition of the boundaries of certain glacial features, including the present-day ice caps. Future re-

constructions of the Innuitian Ice Sheet could benefit from the use of a finer grid in order to better represent the evolution and configuration of the ice caps. As well, recent glaciological models indicate that the Greenland Ice Sheet was larger than the Greenland component of ICE-5G by up to 2-3 m of global sea-level equivalent at LGM (Simpson et al. 2009, Lecavalier et al. 2014). A larger Greenland Ice Sheet would likely affect prediction of RSL in the eastern alpine sector, such as at Cape Herschel and Clements Markam Inlet. Also, as discussed in Section 4.4, the Innuitian region may be characterized by elastic lithospheric thickness values and (or) upper mantle viscosity values that are less than that of the reference Earth model. Therefore, it would be useful to assess the sensitivity of the model predictions to variations in elastic lithospheric thickness and mantle viscosity in this region. In general, a thinner elastic lithosphere would increase the magnitude of predicted RSL (and thus possibly suggest reduced ice thickness values in order to maintain the fit of the model predictions to the data).

As well, present-day vertical uplift rates may be influenced significantly by recent volume changes to glaciers and ice caps during the retreat of the Little Ice Age, and by observed present-day mass loss to the QEI ice caps and the Greenland Ice Sheet. Addition of the Earth's predicted elastic response to present-day ice mass changes to the predicted long-term viscoelastic GIA response appears to help improve the fit between observed and predicted rates of vertical uplift. However, the estimates of the present-day mass loss effect are preliminary and uncertain; to understand better the short-term vertical uplift signal, a variation of mass loss scenarios as well as spatially non-uniform mass loss should be considered. Because the present-day mass loss signal is uncertain, and likely large, GPS-measured land deformation rates should be used with caution as constraint for GIA models in regions near present-day ice cover.

7.2.7 Conclusion

An ice sheet reconstruction is described here that considers current glacial-geological constraints on Innuitian Ice Sheet history as summarized by England et al. (2006). The revision features continuous ice coverage throughout both the alpine and lowland sectors of the ice sheet compared to the isolated ice caps and limited spatial coverage of ICE-5G. As well, at 1600 m, the peak LGM ice thicknesses of the best-fit IIS model are approximately one-half of those in ICE-5G. The peak ice thicknesses of the best-fit IIS model also cover a larger area than the localized peak ice thicknesses of ICE-5G.

In our first revision of the IIS model, we defined the peak ice thickness to be 1200 m, consistent with the lower bound on peak ice thickness indicated by Ó Cofaigh et al. (2000) and England et al. (2004). However, in order for model predictions to fit regional RSL measurements, peak thicknesses of ∼1600 m are needed. A comparison of our best-fit IIS model to ICE-5G indicates that both models predict RSL histories in good agreement with measurements in the alpine sector of the IIS. The ability of two different models of ice cover to adequately predict the sea-level measurements from the alpine sector underscores the usefulness of incorporating available independent constraints on ice sheet evolution. Conversely, the continuous and thinner ice cover in the lowland sector of the best-fit IIS model significantly improves the fit of RSL predictions relative to ICE-5G. In the Innuitian region, RSL data provide the best constraint for GIA models. Existing GPS data are sparse, but improved agreement between model predictions and measurements is obtained for a majority of locations when the observations are corrected for the Earth's elastic response to present-day ice mass changes. Our best-fit Innuitian ice sheet model provides an additional contribution of 0.6 m to global sea-level at LGM compared to the Innuitian portion of ICE-5G.

Chapter 8

Conclusions

8.1 Summary of Main Results

Most of the research in this dissertation is presented in the format of journal articles and manuscripts in preparation for publication. The main results of this project are summarized briefly below. More detailed results are discussed in the concluding sections of Chapters 5-7.

1. The inclusion of global ocean loading in the glacial isostatic adjustment models has a significant impact on predicted GIA motions, particularly near the Hudson Bay region, which was fully occupied by marine-based ice during the last glaciation. Similar to other work (e.g., Milne 1998, Mitrovica and Milne 2003, Kendall et al. 2005), the inclusion of ocean loading yields a maximum predicted difference to predictions of relative sea-level change of ∼140 m, or approximately 40%. Chapter 3.

2. New measurements of relative sea-level change and present-day vertical land motion obtained near the community of Arviat, Nunavut, provide tight constraint on late Holocene sea-level change and glacial isostatic uplift in the region just west of central Hudson Bay. Following deglaciation, sea level reached a high-stand of nearly 170 m elevation just after 8000 cal yr BP and fell rapidly to 60 m elevation by ∼5200 cal yr BP. The rate of sea-level fall decreased in the mid and late Holocene, with sea level falling 30 m since 3000 cal yr BP. A measurement of present-day vertical uplift obtained by repeat GPS occupations indicates ongoing crustal uplift at Arviat of 9.3 ± 1.5 mm/yr. Chapter 5.

3. The frequently used global ICE-5G ice sheet reconstruction (Peltier 2004) includes ice thickness over- and under-estimates on the North American continent.

GIA modelling suggests that the peak thickness of the Keewatin ice dome west of Hudson Bay was ∼3.4-3.6 km, which corresponds to a 30-35% reduction to ICE-5G in this region. This large reduction to the ice sheet reconstruction decreases the size of the peripheral mantle forebulge to the north, a result which yields an improved fit to relative sea-level data from the southern Canadian Arctic Archipelago. As well, the modelling results indicate that relative to ICE-5G, ice model thicknesses east of Hudson Bay can be increased to up to 4 km. These results are generally compatible with those of Argus and Peltier (2010), who used GPS-measured land motion rates to suggest that similar regional modifications to ICE-5G were needed in regions to the south of the main study area. Chapter 6.

4. A reconstruction of the Innuitian Ice Sheet developed to incorporate the current glacial-geological constraints on ice sheet history reproduces well the regional record of post-glacial sea-level change. The results of the GIA modelling analysis suggest that the peak thicknesses of the Innuitian Ice Sheet may have reached ∼1600 m at LGM. Chapter 7.

5. Relative to the ICE-5G reconstruction, the modifications to the ice sheet history west and east of Hudson Bay correspond to changes to globally-averaged sea-level of -9.8 m and +2.5 m, respectively. The modifications made to Baffin Island ice cover (a change of -0.4 m contribution to global sea-level at LGM) and the Innuitian Ice Sheet (+0.6 m) result in sub-metre changes to the global sea-level budget. The deficit to the global sea-level budget generated from these changes to North American ice sheets may be partially offset by thickening the load in western Canada near the British Columbia-Alberta border and/or within the Cordilleran Ice Sheet. Chapters 6-7.

6. The correction to GPS measurements of vertical crustal motion for the effect of present-day ice mass changes in the High Arctic is large and uncertain. Nevertheless, correction for the present-day mass loss effect helps to reconcile the predicted and observed rates of vertical crustal motion around Baffin Island and in the Innuitian region. Chapters 6-7.

7. The use of relative sea-level data for constraint of GIA models in northern Canada will continue to be important, as they offer the following advantages over GPS measurements: 1) relative insensitivity to present-day ice mass loss

effects, 2) denser spatial coverage throughout the region, although GPS station density is likely to increase with time, and 3) a record of the paleo GIA response, which is useful for constraining past aspects of ice sheet evolution.

8.2 Recommendations for Future Activities and Research

8.2.1 Upgrades to the GIA code

Although the current version of the GIA code can include the rotational contribution from present-day ice and water mass fluctuations, it does not include the time-dependent viscoelastic contribution to the predicted GIA response that occurs as a result of changes to the Earth's rotation vector. Mitrovica and Milne (1998) found that the rotational contribution to sea-level predictions is generally small. Nevertheless, future inclusion of the rotational effect will be an important upgrade to the GIA code.

8.2.2 Earth model variations

In the future, more detailed exploration of Earth model parameters may help to constrain better aspects of regional Earth rheology and structure. These variations could include more comprehensive exploration of the effects of lithospheric thickness and the radial viscosity profile within spherically symmetric Earth models, or the use of Earth models that incorporate three-dimensional variations in Earth structure. For example, because the east coast of Baffin Island is a passive rifted margin, the lithospheric thickness thins substantially from west to east across the island. An Earth model that incorporates this lateral heterogeneity in the lithosphere may help to determine whether increased complexity in the Earth structure significantly influences predicted GIA rates throughout the region.

8.2.3 Additional observational constraints

In the Arviat area, additional measurements of sea-level change may help to constrain better the early Holocene history of regional sea-level change. Given the observed time lag between land emergence and peat formation discussed in Chapter 5, lake coring at higher elevations likely offers the best approach for the collection of constraining measurements. Interpretation of the sea-level history on the Ungava Peninsula may also benefit from additional relative sea-level constraints. In the Kivalliq region to

the west of Hudson Bay, the recent installation of a permanent GPS site at Rankin Inlet, and the planned installation of another GPS site in the Kivalliq interior, will help to constrain better the present-day rates of regional GIA uplift in the next decade. Throughout the region of northern Canada, spatially denser coverage and longer observation periods for both GPS and tide gauge data sets will reduce the uncertainty of measured present-day land deformation and sea-level change, and thus benefit studies of glacial isostatic adjustment. In particular, a GPS site on Foxe Peninsula on Baffin Island would provide measurement of the ongoing uplift from the southeastern margin of the former load centre over Foxe Basin, and would complement the existing data set at Igloolik, which lies near the northwestern margin of this uplift centre. As well, increased GPS station coverage throughout the QEI would provide improved constraint on both long-term and short-term rates of vertical uplift in the High Arctic.

8.2.4 Present-day ice mass change

The predicted elastic response of the Earth to ongoing ice mass changes is large in regions near present-day ice cover. In addition to present-day ice mass loss, measured vertical land motion rates may also be influenced by changes to ice cover during the Little Ice Age. Addition of the present-day mass loss effect to the predicted long-term viscoelastic GIA response helps to reconcile predicted and observed vertical uplift rates on Baffin Island and in the QEI. However, estimation of this effect is subject to large uncertainty, and the present-day mass loss predictions presented in this study should be considered preliminary. More work needs to be done to estimate this effect better, including the examination of different mass loss scenarios, the incorporation of spatially non-uniform mass loss, and consideration of the effects of the Little Ice Age.

8.2.5 The global sea-level budget

This study suggested that a deficit to the LGM global sea-level budget of up to nearly 8 m exists for North America (although this value may be partially offset by thickening ice in western Canada). As well, as discussed in Chapter 6, recent reconstructions of the Antarctic Ice Sheet suggest an additional deficit to global sea level may exist for Antarctica. Therefore, an important avenue for future research is the construction of a global ice sheet model that fits available observational constraints

and simultaneously satisfies the global sea-level budget (as constrained by records of far-field sea-level change).

8.2.6 GIA correction for GRACE

An additional possible application of the updated GIA model developed for North America is the improved prediction of the GIA correction for GRACE measurements. Improved GIA model predictions are needed to correct GRACE measurements in order to isolate variations in present-day hydrological signals, including patterns of continental water storage and ongoing mass loss of glaciers and ice sheets.

References

Ackert R.P., Barclay, D.J., Borns, H.W. Jr, Calkin, P.E., Kurz, M.D., Fastook, J.L., and Steig, E.J., 1999. Measurements of past ice sheet elevations in interior West Antarctica. Science 286, 276-280.

Ackert R.P., Mukhopadhyay, S., Parizek, B.R., and Borns, H.W., 2007. Ice elevation near the West Antarctic Ice Sheet divide during the last glaciation. Geophysical Research Letters 34, doi:10.1029/2007GL031412.

Altamimi, Z., Collilieux, X., and Métivier, L., 2011. ITRF2008: an improved solution of the international terrestrial reference frame. Journal of Geodesy 85, 457-473.

Amalvict M., Willis, P., Wöppelmann, G., Ivins, E.R., Bouin, M.-N., Testut, L., and Hinderer, J., 2009. Isostatic stability of the East Antarctic station Dumont d'Urville from long-term geodetic observations and geophysical models. Polar Research 28, 193-202.

Arendt, A., Bolch, T., Cogley, J. G., Gardner, A., Hagen, J.-O., Hock, R., Kaser, G., Pfeffer, W. T., Moholdt, G., Paul, F., Radić, V., Andreassen, L., Bajracharya, S., Beedle, M., Berthier, E., Bhambri, R., Bliss, A., Brown, I., Burgess, E., Burgess, D., Cawkwell, F., Chinn, T., Copland, L., Davies, B., de Angelis, H. , Dolgova, E., Filbert, K., Forester, R., Fountain, A., Frey, H., Giffen, B., Glasser, N., Gurney, S., Hagg, W., Hall, D., Haritashya, U. K., Hartmann, G., Helm, C., Herreid, S., Howat, I., Kapustin, G., Khromova, T., Kienholz, C., Koenig, M., Kohler, J., Kriegel, D., Kutuzov, S., Lavrentiev, I., LeBris, R., Lund, J., Manley, W., Mayer, C., Miles, E., Li, X., Menounos, B., Mercer, A., Moelg, N., Mool, P., Nosenko, G., Negrete, A., Nuth, C., Pettersson, R., Racoviteanu, A., Ranzi, R., Rastner, P., Rau, F., Rich, J., Rott, H., Schneider, C., Seliverstov, Y., Sharp, M., Sigursson, O., Stokes, C., Wheate, R., Winsvold, S., Wolken, G., Wyatt, F., and Zheltyhina, N., 2012. Randolph Glacier Inventory [v2.0]: a dataset of global glacier outlines. Global Land Ice Measurements from Space, Boulder Colorado, USA, Digital Media.

Arfken, G.B., and Weber, H.J., 2001. Mathematical Methods for Physicists. 5^{th} edition, Harcourt Academic Press, San Diego, 1112pp.

Argus, D.F., Peltier, W.R., and Watkins, M.M., 1999. Glacial isostatic adjustment observed using very long baseline interferometry and satellite laser ranging geodesy. Journal of Geophysical Research 104, 29,077-29,093.

Argus, D.F., and Peltier, W.R., 2010. Constraining models of postglacial rebound using space geodesy: a detailed assessment of model ICE-5G (VM2) and its relatives. Geophysical Journal International 181, 697-723.

Arnold, J.R., and Libby, W.F., 1951. Radiocarbon dates. Science 113, 111-120.

Artemieva, I.M., 2006. Global $1^\circ \times 1^\circ$ thermal model TC1 for the continental lithosphere: Implications for lithosphere secular evolution. Tectonophysics 416, 245-277.

Atkinson, N., 2003. Late Wisconsinan glaciation of Amund and Ellef Ringnes islands, Nunavut: evidence for the configuration, dynamics, and deglacial chronology of the northwest sector of the Innuitian Ice Sheet. Canadian Journal of Earth Sciences 40, 351-363.

Atkinson, N., and England, J., 2004. Postglacial emergence of Amund and Ellef Ringnes islands, Nunavut: implications for the northwest sector of the Innuitian Ice Sheet. Canadian Journal of Earth Sciences 41, 271-283.

Audet, P., and Mareschal, J.C., 2004. Variations in elastic thickness in the Canadian Shield. Earth and Planetary Science Letters 226, 17-31.

Aylsworth, J., Cunningham, C.M., Kettles, I.M., and Shilts, W.W., 1986. Surficial geology, Henik Lakes, District of Keewatin. Map 2-1985, scale 1:125000. Geological Survey of Canada, Ottawa.

Aylsworth, J.M., and Shilts, W.W., 1989. Glacial features around the Keewatin Ice Divide: districts of Mackenzie and Keewatin. Paper 88-24. Geological Survey

of Canada, Ottawa.

Bard, E., 1988. Correction of accelerator mass spectrometry ^{14}C ages measured in planktonic foraminifera: paleoceanographic implications. Paleoceanography 3, 635-645.

Bard, E., Hamelin, B., Arnold, M., Montaggioni, L., Cabioch, G., Faure, G., and Rougerie, F., 1996. Deglacial sea-level record from Tahiti corals and the timing of global meltwater discharge. Nature 382, 241-244.

Bard, E., Hamelin, B., and Delanghe-Sabatier, D., 2010. Deglacial meltwater pulse 1B and Younger Dryas sea levels revisited with boreholes at Tahiti. Science 327, 1235-1237.

Barletta, V.R., Sabadini, R., and Bordoni, A., 2008. Isolating the PGR signal in the GRACE data: impact on mass balance estimates in Antarctica and Greenland. Geophysical Journal International 172, 18-30.

Bassett, S.E., Milne, G.A., Mitrovica, J.X., and Clark, P.U., 2005. Ice sheet and solid Earth influences on far-field sea-level histories. Science 309, 925-928.

Bednarski, J.M., 1998. Quaternary history of Axel Heiberg Island bordering Nansen Sound, Northwest Territories, emphasizing the last glacial maximum. Canadian Journal of Earth Sciences 35, 520-533.

Bevis, M., Alsdorf, D., Kendrick, E., Fortes, L.P., Forsberg, B., Smalley, R., Jr, and Becker, J., 2005. Seasonal fluctuations in the mass of the Amazon River system and Earth's elastic response. Geophysical Research Letters 32, doi:10.1029/2005GL023491.

Blackwell, D.D, and Richards, M.C., 2004. Geothermal map of North America. Map 423, scale 1:6,500,000, American Association of Petroleum Geologists, Tulsa, Oklahoma.

Blake, W. Jr., 1970. Studies of glacial history in Arctic Canada I: pumice, radiocarbon dates, and differential postglacial uplift in the eastern Queen Elizabeth

Islands. Canadian Journal of Earth Sciences, 7, 634-664.

Blake, W., 1983. Radiocarbon dates XXIII. Paper 83-7. Geological Survey of Canada, Ottawa.

Bolch, T., Sørensen, L.S., Simonsen, S.B., Mölg, N., Machguth, H., Rastner, P., and Paul, F., 2013. Mass loss of Greenland's glaciers and ice caps 2003-2008 revealed from ICESat laser altimetry data. Geophysical Research Letters 40, 1-7, doi:10.1002/grl.50270.

Bouin, M.-N., and Vigny, C., 2000. New constraints on Antarctic plate motion and deformation from GPS data. Journal of Geophysical Research 105, 28279-28293.

Calais, E., Han, J.Y., DeMets, C., and Nocquet, J.M., 2006. Deformation of the North American plate interior from a decade of continuous GPS measurements. Journal of Geophysical Research 111, doi:10.1029/2005JB004253.

Capra, A., Mancini, F., and Negusini, M., 2007. GPS as a geodetic tool for geodynamics in northern Victoria Land, Antarctica. Antarctic Science 19, 107-114.

Chao, B.F., and Gross, R.S., 1987. Changes in the Earth's rotation and low degree gravitational field induced by earthquakes. Geophysical Journal of the Royal Astronomical Society 91, 569-596.

Chen, J.L., Wilson, C.R., Blankenship, D.D., and Tapley, B.D., 2006. Antarctic mass rates from GRACE. Geophysical Research Letters 33, doi:10.1029/2006GL026369.

Chen, J.L., Wilson, C.R., Tapley, B.D., Blankenship, D., and Young, D., 2008. Antarctic regional ice loss rates from GRACE. Earth and Planetary Science Letters 266, 140-148.

Clark, P.U., and Mix, A.C., 2002. Ice sheets and sea level of the Last Glacial Maximum. Quaternary Science Reviews, 21, 1-7.

Clark, P.U., Dyke, A.S., Shakun, J.D., Carlson, A.E., Clark, J., Wohlfarth, B., Mitrovica, J.X., Hostetler, S.W., and McCabe, A.M., 2009. The Last Glacial Maximum. Science 325, 710-714.

Conway, H., Hall, B.L., Denton, G.H., Gades, A.M., and Waddington, E.D., 1999. Past and future grounding-line retreat of the West Antarctic ice sheet. Science 286, 280-283.

Cook, G.T., MacKenzie, A.B., Muir, G.K.P., Mackie, G., and Gulliver, P., 2004. Sellafield-derived anthropogenic ^{14}C in the marine intertidal environment on the NE Irish Sea. Radiocarbon 46, 877-883.

Craig, B.G., and Fyles, J.G., 1960. Pleistocene geology of Arctic Canada. Paper 60-10. Geological Survey of Canada, Ottawa.

Craig, B.G., 1969. Late glacial and post-glacial history of the Hudson Bay region. Paper 68-53. Geological Survey of Canada, Ottawa.

Craig, H., 1957. Isotopic standards for carbon and oxygen and correction factors for mass-spectrometric analysis of carbon dioxide. Geochimica et Cosmochimica Acta 12, 133-149.

Craymer, M., Henton, J., and Piraszewski, M., 2006. Sea level change and vertical crustal motion in the Canadian Arctic based on GPS and tide gauges: Challenges and preliminary results. American Geophysical Union Fall Meeting, December 11-15, 2006, G23B-1288.

Craymer, M.R., Henton, J.A., Piraszewski, M., and Lapelle, E., 2011. An updated GPS velocity field for Canada. American Geophysical Union Fall Meeting, December 5-9, 2011, G21A-0793.

Dach, R., Beutler, G., Bock, H., Fridez, P., Gäde, A., Hugentobler, U., Jäggi, A., Meindl, M., Mervart, L., Prange, L., Schaer, S., Springer, T., Urschl, C., and Walser, P., 2007. Bernese GPS Software Version 5.0. Astronomical Institute, University of Bern, Bern, Switzerland.

Dahlen, F.A., 1976. The passive influence of the oceans upon the rotation of the Earth. Geophysical Journal of the Royal Astronomical Society 46, 363-406.

Dal Forno, G., Gasperini, P., and Boschi, E., 2005. Linear or nonlinear rheology in the mantle: a 3D finite-element approach to postglacial rebound modeling. Journal of Geodynamics 39, 183-195.

Daly, R.A., 1925. Pleistocene changes of level. American Journal of Science 10, 281-313.

Darbyshire, F.A., 2003. Crustal structure across the Canadian High Arctic region from teleseismic receiver function analysis. Geophysical Journal International 152, 372-391.

Davis, J.L., Elósegui, P., Mitrovica, J.X., and Tamisiea, M.E., 2004. Climate-driven deformation of the solid Earth from GRACE and GPS. Geophysical Research Letters 31, doi:10.1029/2004GL021435.

de Linage, C., Hinderer, J., and Rogister, Y., 2007. A search for the ratio between gravity variation and vertical displacement due to a surface load. Geophysical Journal International 171, 986-994.

Denton, G.H., and Hughes, T.J., 1981. The Last Great Ice Sheets. John Wiley & Sons Inc., New York, 484pp.

Denton, G.H., and Hughes, T.J., 2002. Reconstructing the Antarctic ice sheet at the last glacial maximum. Quaternary Science Reviews 21, 193-202.

Deschamps, P., Durand, N., Bard, E., Hamelin, B., Camoin, G., Thomas, A.L., Henderson, G.M., Okuno, J., and Yokoyama, Y., 2012. Ice-sheet collapse and sea-level rise at the Bølling warming 14,600 years ago. Nature 483, 559-564.

de Vries, H., 1958. Atomic bomb effect: variation of radiocarbon in plants, shells, and snails in the past 4 years. Science 128, 250-251.

Dietrich, R., Rülke, A., Ihde, J., Lindner, K., Miller, H., Niemeier, W., Schenke, H.W., and Seeber, G., 2004. Plate kinematics and deformation status of the Antarctic Peninsula based on GPS. Global and Planetary Change 42, 313-321.

Donnellan, A., and Luyendyk, B.P., 2004. GPS evidence for a coherent Antarctic plate and for postglacial rebound in Marie Byrd Land. Global and Planetary Change 42, 305-311.

Dowdeswell, J.A., Benham, T.J., Gorman, M.R., Burgess, D., and Sharp, M.J., 2004. Form and flow of the Devon Island Ice Cap, Canadian Arctic. Journal of Geophysical Research 109, doi:10.1029/2003JF000095.

Dyke, A.S., Dredge, L.A., and Vincent, J-S., 1982. Configuration and dynamics of the Laurentide Ice Sheet during the Late Wisconsin maximum. Géographie physique et Quaternaire 36, 5-14.

Dyke, A.S., and Prest, V.K., 1987. Late Wisconsinan and Holocene history of the Laurentide Ice Sheet. Géographie physique et Quaternaire 41, 237-263.

Dyke, A.S., and Dredge, L.A., 1989. Quaternary geology of the northwestern Canadian Shield. In: Fulton, R.J. (Ed.), Quaternary Geology of Canada and Greenland. Geological Survey of Canada, no. 1, Ottawa, pp. 189-214.

Dyke, A.S., Morris, T.F., and Green, D.E.C., 1991. Postglacial tectonic and sea level history of the central Canadian Arctic. Bulletin 397. Geological Survey of Canada, Ottawa, pp. 1-56.

Dyke, A.S., 1999. Last Glacial Maximum and deglaciation of Devon Island, arctic Canada: support for an Innuitian Ice Sheet. Quaternary Science Reviews 18, 393-420.

Dyke, A.S., and Peltier, W.R., 2000. Forms, response times and variability of relative sea-level curves, glaciated North America. Geomorphology 32, 315-333.

Dyke, A.S., Andrews, J.T., Clark, P.U., England, J.H., Miller, G.H., Shaw, J., and Veillette, J.J., 2002. The Laurentide and Innuitian ice sheets during the Last Glacial Maximum. Quaternary Science Reviews 21, 9-31.

Dyke, A.S., 2004. An outline of North American deglaciation with emphasis on central and northern Canada. In: Ehlers, J. and Gibbard, P.L., (Eds.), Quaternary Glaciations - Extent and Chronology, Part II. North America, Developments in Quaternary Science 2. Elsevier, New York, pp. 373-424.

Dyke, A.S., Dredge, L.A., and Hodgson, D.A., 2005. North American deglacial marine- and lake-limit surfaces. Géographie physique et Quaternaire 59, 155-185.

Dziewonski, A.M., and Anderson, D.L., 1981. Preliminary reference Earth model. Physics of the Earth and Planetary Interiors 25, 297-356.

Engelhart, S.E., Peltier, W.R., and Horton, B.P., 2011. Holocene relative sea-level changes and glacial isostatic adjustment of the U.S. Atlantic coast. Geology 39, 751-754.

England, J., 1976. Late Quaternary glaciation of the eastern Queen Elizabeth Islands, northwest Territories, Canada: Alternative models. Quaternary Research 6, 185-202.

England, J., Sharp, M., Lemmen, D.S., and Bednarski, J., 1991. On the extent and thickness of the Innuitian Ice Sheet: a postglacial-adjustment approach: discussion. Canadian Journal of Earth Sciences 28, 1689-1695.

England, J.H., Dyke, A.S., and McNeely, R., 2003. Inter-species, radiocarbon age comparisons on subfossil molluscs from Arctic Canada: the *Portlandia arctica* problem. 33^{rd} Annual Arctic Workshop, Polar Environmental Centre, Tromsø, Norway, April 3-5, 2003, Norsk Polarinstitutt, Internrapport 13, p. 66.

England, J.H., Atkinson, N., Dyke, A.S., Evans, D.J.A., and Zreda, M., 2004. Late Wisconsinan buildup and wastage of the Innuitian Ice Sheet across southern

Ellesmere Island, Nunavut. Canadian Journal of Earth Sciences 41, 39-61.

England, J., Atkinson, N., Bednarski, J., Dyke, A.S., Hodgson, D.A., and Ó Cofaigh, C., 2006. The Innuitian Ice Sheet: configuration, dynamics and chronology. Quaternary Science Reviews 25, 689-703.

England, J., Dyke, A.S., Coulthard, R.D., McNeely, R., and Aitken, A., 2013. The exaggerated radiocarbon age of deposit-feeding molluscs in calcareous environments. Boreas 42, 362-373.

Fairbanks, R.G., 1989. A 17,000-year glacio-eustatic sea level record: influence of glacial melting rates on the Younger Dryas event and deep-ocean circulation. Nature 342, 637-642.

Farrell, W.E., 1972. Deformation of the Earth by surface loads. Reviews of Geophysics and Space Physics 10, 761-797.

Farrell, W.E., and Clark, J.A., 1976. On postglacial sea level. Geophysical Journal of the Royal Astronomical Society 46, 647-667.

Fleming, S., 1976. Dating in Archaeology: a Guide to Scientific Techniques. J.M. Dent & Sons Ltd., London, 272pp.

Gardner, A.S., Moholdt, G., Wouters, B., Wolken, G.J., Burgess, D.O., Sharp, M.J., Cogley, J.G., Braun, C., and Labine, C., 2011. Sharply increased mass loss from glaciers and ice caps in the Canadian Arctic Archipelago. Nature 473, 357-360.

Gardner, A.S., Moholdt, G., Cogley, J.G., Wouters, B., Arendt, A.A., Wahr, J., Berthier, E., Hock, R., Pfeffer, W.T., Kaser, G., Ligtenberg, S.R.M., Bolch, T., Sharp, M.J., Hagen, J.O., van den Broeke, M.R., and Paul, F., 2013. A reconciled estimate of glacier contributions to sea level rise: 2003 to 2009. Science 340, 852-857.

Gasperini, P., Yuen, D.A., Sabadini, R., 1992. Postglacial rebound with a non-Newtonian upper mantle and a Newtonian lower mantle rheology. Geophysical

Research Letters 19, 1711-1714.

Giunchi, C., and Spada, G., 2000. Postglacial rebound in a non-Newtonian spherical Earth. Geophysical Research Letters 27, 2065-2068.

Godwin, H., 1962. Half-life of radiocarbon. Nature 195, 984.

Gomez, N., Mitrovica, J.X., Tamisiea, M.E., and Clark, P.U., 2009. A new projection of sea level change in response to collapse of marine sectors of the Antarctic ice sheet. Geophysical Journal International 180, doi:10.1111/j.1365-246X.2009.04419.x.

Gorham, E., Lehman, C., Dyke, A., Janssens, J., and Dyke, L., 2007. Temporal and spatial aspects of peatland initiation following deglaciation in North America. Quaternary Science Reviews 26, 300-311.

Gray, J., Lauriol, B., Bruneau, D., and Ricard, J., 1993. Postglacial emergence of Ungava Peninsula, and its relationship to glacial history. Canadian Journal of Earth Sciences 30, 1676-1696.

Gregoire, L.J., 2010. Modelling the northern hemisphere climate and ice sheets during the last deglaciation. PhD thesis, University of Bristol, Bristol.

Gregoire, L.J., Payne, A.J., and Valdes, P.J., 2012. Deglacial rapid sea level rises caused by ice-sheet saddle collapses. Nature 487, 219-222.

Griffin, W.L., O'Reilly, S.Y., Doyle, B.J., Pearson, N.J., Coopersmith, H., Kivie, K., Malkovetsa, V., and Pokhilenko, N., 2004. Lithosphere mapping beneath the North American plate. Lithos 77, 873-922.

Grinsted, A., Moore, J.C., and Jevrejeva, S., 2009. Reconstructing sea level from paleo and projected temperatures 200 to 2100 AD. Climate Dynamics, doi:10.1007/s00382-008-0507-2.

Hall, B.L., Baroni, C., and Denton, G.H., 2004. Holocene relative sea-level history of the Southern Victoria Land Coast, Antarctica. Global and Planetary Change 42, 241-263.

Halsey, L.A., Vitt, D.H., and Bauer, I.E., 1998. Peatland initiation during the Holocene in continental western Canada. Climatic Change 40, 315-342.

Hanebuth, T., Stattegger, K., and Grootes, P.M., 2000. Rapid flooding of the Sunda Shelf: a late-glacial sea-level record. Science 288, 1033-1035.

Haskell, N.A., 1935. The motion of a viscous fluid under a surface load. Physics 6, 265-269.

Hughen, K.A., Baillie, M.G.L., Bard, E., Bayliss, A., Beck, J.W., Bertrand, C.J.H., Blackwell, P.G., Buck, C.E., Burr, G.S., Cutler, K.B., Damon, P.E., Edwards, R.L., Fairbanks, R.G., Friedrich, M., Guilderson, T.P., Kromer, B., McCormac, F.G., Manning, S.W., Bronk Ramsey, C., Reimer, P.J., Reimer, R.W., Remmele, S., Southon, J.R., Stuiver, M., Talamo, S., Taylor, F.W., van der Plicht, J., and Weyhenmeyer, C.E., 2004. Marine04 Marine radiocarbon age calibration, 26 - 0 ka BP. Radiocarbon 46, 1059-1086.

Hutchinson, I., James, T.S., Reimer, P.J., Bornhold, B.D., and Clague, J.J., 2004. Marine and limnic radiocarbon reservoir corrections for studies of late- and post-glacial environments in Georgia Basin and Puget Lowland, British Columbia, Canada and Washington, USA. Quaternary Research 61, 193-203.

IPCC, 2014. Summary for Policymakers. In: Edenhofer, O., Pichs-Madruga R., Sokona Y., Farahani E., Kadner, S., Seyboth, K., Adler, A., Baum, I., Brunner, S., Eickemeier, P., Kriemann, B., Savolainen, J., Schlömer, S., von Stechow, C., Zwickel, T., and Minx, J.C., (Eds.), Climate Change 2014, Mitigation of Climate Change. Contribution of Working Group III to the Fifth Assessment Report of the Intergovernmental Panel on Climate Change. Cambridge University Press, Cambridge, United Kingdom and New York, NY, USA.

Ivins, E.R., Sammis, C.G., and Yoder, C.F., 1993. Deep mantle viscous structure with prior estimate and satellite constraint. Journal of Geophysical Research 98, 4579-4609.

Ivins, E.R., and James, T.S., 2005. Antarctic glacial isostatic adjustment: a new assessment. Antarctic Science 17, 541-553.

Ivins, E.R., James, T.S., Wahr, J., Schrama, E.J.O., Landerer, F.W., and Simon, K.M., 2013. Antarctic contribution to sea level rise observed by GRACE with improved GIA correction. Journal of Geophysical Research 118, 1-16, doi:10.1002/jgrb.50208.

James, T.S., 1991. Post-glacial deformation. PhD thesis, Princeton University, Princeton.

James, T.S., and Bent, A.L., 1994. A comparison of eastern North American seismic strain-rates to glacial rebound strain-rates. Geophysical Research Letters 21, 2127-2130.

James, T.S., and Ivins, E.R., 1997. Global geodetic signatures of the Antarctic ice sheet. Journal of Geophysical Research 102, 605-633.

James, T.S., and Ivins, E.R., 1998. Predictions of Antarctic crustal motions driven by present-day ice sheet evolution and by isostatic memory of the Last Glacial Maximum. Journal of Geophysical Research 103, 4993-5017.

James, T.S., Gowan, E.J., Wada, I., and Wang, K., 2009. Viscosity of the asthenosphere from glacial isostatic adjustment and subduction dynamics at the northern Cascadia subduction zone, British Columbia, Canada. Journal of Geophysical Research 144, doi:10.1029/2008JB006077.

James, T.S., Simon, K.M., Forbes, D.L., Dyke, A.S., and Mate, D.J., 2011. Sea-level projections for five pilot communities of the Nunavut Climate Change Partnership. Open File 6715. Geological Survey of Canada, Ottawa.

Jamieson, T.F., 1865. On the history of the last geological changes in Scotland. Quarterly Journal of the Geological Society 21, 161-204.

Johnston, P., 1993. The effect of spatially non-uniform water loads on prediction of sea-level change. Geophysical Journal International 114, 615-634.

Karato, S., and Wu, P., 1993. Rheology of the upper mantle: a synthesis. Science 260, 771-778.

Karato, S., 1998. Micro-physics of post glacial rebound. In: Wu, P. (Ed.), Dynamics of the ice age Earth: a modern perspective. Trans Tech Publications Ltd., Switzerland, pp. 351-364.

Kendall, R.A., Mitrovica, J.X., and Milne, G.A., 2005. On post-glacial sea level - II. Numerical formulation and comparative results on spherically symmetric models. Geophysical Journal International 161, 679-706.

Kouba, J., and Héroux, P., 2001. Precise point positioning using IGS orbit and clock products. GPS Solutions 5, 12-28.

Kovanen, D.J., and Easterbrook, D.J., 2002. Paleodeviations of radiocarbon marine reservoir values for the northeast Pacific. Geology 30, 243-246.

Kuhry, P., and Turunen, J., 2006. The postglacial development of boreal and subarctic peatlands. In: Wieder, R.K., and Vitt, D.H. (Eds.), Boreal Peatland Ecosystems. Springer-Verlag, Berlin, pp. 25-46.

Lambeck, K., 1980. The Earth's Variable Rotation. Cambridge University Press, New York, 449pp.

Lambeck, K., 1993. Glacial rebound of the British Isles - I. Preliminary model results. Geophysical Journal International 115, 941-959.

Lambeck, K., Smither, C., and Johnston, P., 1998. Sea-level change, glacial rebound and mantle viscosity for northern Europe. Geophysical Journal International

134, 102-144.

Lambeck, K., and Chappell, J., 2001. Sea level change through the last glacial cycle. Science 292, 679-686.

Lambert, A., Courtier, N., Sasagawa, G.S., Klopping, F., Winester, D., James, T.S., and Liard, J.O., 2001. New constraints on Laurentide postglacial rebound from absolute gravity measurements. Geophysical Research Letters 28, 2109-2112.

Lambert, A., Courtier, N., and James, T.S., 2006. Long-term monitoring by absolute gravimetry: Tides to postglacial rebound. Journal of Geodynamics 41, 307-317.

Lecavalier, B.S., Milne, G.A., Vinther, B.M., Fisher, D.A., Dyke, A.S., and Simpson, M.J.R., 2013. Revised estimates of Greenland ice sheet thinning histories based on ice-core records. Quaternary Science Reviews 63, 73-82.

Lecavalier, B.S., Milne, G.A., Simpson, M.J.R., Wake, L., Huybrechts, P., Tarasov, L., Kjeldsen, K.K., Funder, S., Long, A.J., Woodroffe, S., Dyke, A.S., and Larsen, N.K., 2014. A model of Greenland Ice Sheet deglaciation constrained by observations of relative sea level and ice extent. Quaternary Science Reviews 102, 54-84.

Lee, H.A., 1959. Surficial geology of southern District of Keewatin and the Keewatin Ice Divide, Northwest Territories. Bulletin 51. Geological Survey of Canada, Ottawa, pp. 1-42.

Lee, H.A., 1962. Method of deglaciation, age of submergence, and rate of uplift west and east of Hudson Bay, Canada. Builetyn Peryglacjalny 11, 239-245.

Lee, H.A., 1968. Quaternary geology. In: Beals, C.S., and Shenstone, D.A. (Eds.), Science, History and Hudson Bay, Volume 2. Department of Energy, Mines and Resources, Ottawa, pp. 503-543.

Lewis, C.A., Reimer, P.J., and Reimer, R.W., 2008. Marine reservoir corrections: St. Helena, South Atlantic Ocean. Radiocarbon 50, 275-280.

Libby, W.F., 1946. Atmospheric Helium Three and radiocarbon from cosmic radiation. Physical Review 69, 671-672.

Libby, W.F., Anderson, E.C., and Arnold, J.R., 1949. Age determination by radiocarbon content: world-wide assay of natural radiocarbon. Science 109, 227-228.

Licht, K.J., 2004. The Ross Sea's contribution to eustatic sea level during meltwater pulse 1A. Sedimentary Geology 165, 343-353.

Lidberg, M., Johansson, J.M., Scherneck, H-.G., and Davis, J.L., 2007. An improved and extended GPS-derived 3D velocity field of the glacial isostatic adjustment (GIA) in Fennoscandia. Journal of Geodesy 81, 213-230.

Lowdon, J.A., and Blake, W., 1979. Radiocarbon dates XIX. Paper 79-7. Geological Survey of Canada, Ottawa.

Lythe, M.B., Vaughan, D.G., and the BEDMAP Consortium, 2001. BEDMAP - a new ice thickness and subglacial topographic model of Antarctica. Journal of Geophysical Research 106, 11335-11351.

Majorowicz, J.A., and Embry, A.R., 1998. Present heat flow and paleo-geothermal regime in the Canadian Arctic margin: analysis of industrial thermal data and coalification gradients. Tectonophysics 291, 141-159.

Mäkinen, J., Amalvict, M., Shibuya, K., and Fukuda, Y., 2007. Absolute gravimetry in Antarctica: status and prospects. Journal of Geodynamics 43, 339-357.

Mareschal, J.C., and Jaupart, C., 2004. Variations of surface heat flow and lithospheric thermal structure beneath the North American craton. Earth and Planetary Science Letters 223, 65-77.

Mareschal, J.C., Nyblade, A., Perry, H.K.C., Jaupart, C., and Bienfait, G., 2004. Heat flow and deep lithospheric thermal structure at Lac de Gras, Slave Province, Canada. Geophysical Research Letters 31, doi:10.1029/2004GL020133.

Mareschal, J.C., Jaupart, C., Rolandone, F., Gariépy, C., Fowler, C.M.R., Bienfait, G., Carbonne, C., and Lapointe, R., 2005. Heat flow, thermal regime, and elastic thickness of the lithosphere in the Trans-Hudson Orogen. Canadian Journal of Earth Sciences 42, 517-532.

Mazzotti, S., and Adams, J., 2005. Rates and uncertainties on seismic moment and deformation in eastern Canada. Journal of Geophysical Research 110, doi:10.1029/2004JB003510.

Mazzotti, S., Lambert, A., Henton, J., James, T.S., and Courtier, N., 2011. Absolute gravity calibration of GPS velocities and glacial isostatic adjustment in mid-continent North America. Geophysical Research Letters 38, doi:10.1029/2011GL049846.

McMartin, I., and Henderson, P.J., 2004a. Evidence from Keewatin (central Nunavut) for paleo-ice divide migration. Géographie physique et Quaternaire 58, 163-186.

McMartin, I., and Henderson, P.J., 2004b. Ice flow history and glacial stratigraphy, Kivalliq region, Nunavut (NTS 55J, K, L, M, N, O; 65I and P): complete datasets, maps and photographs from the Western Churchill NATMAP Project. Open file 4595. Geological Survey of Canada, Ottawa.

McMartin, I., and Dredge, L.A., 2005. History of ice flow in the Schultz Lake and Wager Bay areas, Kivalliq region, Nunavut. Current Research 2005-B2. Geological Survey of Canada, Ottawa.

McMartin, I., Dredge, L.A., Ford, K.L., and Kjarsgaard, I.M., 2006. Till composition, provenance and stratigraphy beneath the Keewatin Ice Divide, Schultz Lake area (NTS 66A), mainland Nunavut. Open file 5312. Geological Survey of Canada, Ottawa.

McNeely, R., and Atkinson, D.E., 1996. Geological Survey of Canada radiocarbon dates XXXII. Current Research 1995-G. Geological Survey of Canada, Ottawa.

McNeely, R., and Brennan, J., 2005. Geological Survey of Canada revised shell dates. Open file 5019. Geological Survey of Canada, Ottawa.

McNeely, R., Dyke, A.S., and Southon, J.R., 2006. Canadian marine reservoir ages, preliminary data assessment. Open file 5049. Geological Survey of Canada, Ottawa.

Milne, G.A., 1998. Refining models of the glacial isostatic adjustment process. PhD thesis, University of Toronto, Toronto.

Milne, G.A., Davis, J.L, Mitrovica, J.X., Scherneck, H.-G., Johansson, J.M., Vermeer, M., and Koivula, H., 2001. Space-geodetic constraints on glacial isostatic adjustment in Fennoscandia. Science 291, 2381-2385.

Milne, G.A., and Mitrovica, J.X., 2008. Searching for eustasy in deglacial sea-level histories. Quaternary Science Reviews 27, 2292-2302.

Mitrovica, J.X., and Peltier, W.R., 1991. On postglacial geoid subsidence over the equatorial oceans. Journal of Geophysical Research 96, 20,053-20,071.

Mitrovica, J.X., Davis, J.L., and Shapiro, I.I., 1994. A spectral formalism for computing three-dimensional deformations due to surface loads, 1, theory. Journal of Geophysical Research 99, 7057-7073.

Mitrovica, J.X., and Milne, G.A., 1998. Glaciation-induced perturbations in the Earth's rotation: a new appraisal. Journal of Geophysical Research 103, 985-1005.

Mitrovica, J.X., Forte, A.M., and Simons, M., 2000. A reappraisal of postglacial decay times from Richmond Gulf and James Bay, Canada. Geophysical Journal International 142, 783-800.

Mitrovica, J.X., and Milne, G.A., 2003. On post-glacial sea level: I. General theory. Geophysical Journal International 154, 253-267.

Mitrovica, J.X., and Forte, A.M., 2004. A new inference of mantle viscosity based upon joint inversion of convection and glacial isostatic adjustment data. Earth and Planetary Science Letters 225, 177-189.

Mitrovica, J.X., Wahr, J., Matsuyama, I., and Paulson, A., 2005. The rotational stability of an ice-age earth. Geophysical Journal International 161, 491-506.

Mitrovica, J.X., and Wahr, J., 2011. Ice age Earth rotation. Annual Reviews of Earth and Planetary Sciences 39, 577-616.

Mooney, W.D., Laske, G., and Masters, T.G., 1998. CRUST 5.1: A global crustal model at 5° × 5°. Journal of Geophysical Research 103, 727-747.

Nettles, M., and Dziewoński, A.M., 2008. Radially anisotropic shear velocity structure of the upper mantle globally and beneath North America. Journal of Geophysical Research 113, doi:10.1029/2006JB004819.

Oakey, G.N., and Stephenson, R., 2008. Crustal structure of the Innuitian region of Arctic Canada and Greenland from gravity modelling: implications for the Palaeogene Eurekan orogen. Geophysical Journal International 173, 1039-1063.

Ó Cofaigh, C., England, J., and Zreda, M., 2000. Late Wisconsinan glaciation of southern Eureka Sound: evidence for extensive Innuitian ice in the Canadian High Arctic during the Last Glacial Maximum. Quaternary Science Reviews 19, 1319-1341.

Ohzono, M., Tabei, T., Doi, K., Shibuya, K., and Sagiya, T., 2006. Crustal movement of Antarctica and Syowa Station based on GPS measurements. Earth Planets Space 58, 795-804.

Okulitch, A.V., Packard, J.J., and Zolnai, A.I., 1991. Late Silurian-Early Devonian deformation of the Boothia Uplift. In: Trettin, H.P. (Ed.), Geology of the Innuitian Orogen and Arctic Platform of Canada and Greenland, Geology of Canada 3. Geological Survey of Canada, Ottawa, pp. 302-307.

Okuno, J., and Nakada, M., 2001. Effects of water load on geophysical signals due to glacial rebound and implications for mantle viscosity. Earth Planets Space 53, 1121-1135.

Paulson, A., Zhong, S., and Wahr, J., 2007. Inference of mantle viscosity from GRACE and relative sea level data. Geophysical Journal International 171, 497-508.

Peltier, W.R., 1974. The impulse response of a Maxwell Earth. Reviews of Geophysics and Space Physics 12, 649-669.

Peltier, W.R., 1976. Glacial-isostatic adjustment-II. The inverse problem. Geophysical Journal of the Royal Astronomical Society 46, 669-705.

Peltier, W.R., 1985. The LAGEOS constraint on deep mantle viscosity: results from a new normal mode method for the inversion of viscoelastic relaxation spectra. Journal of Geophysical Research 90, 9411-9421.

Peltier, W.R., 1994. Ice age paleotopography. Science 265, 195-201.

Peltier, W.R., 1996. Mantle viscosity and ice-age ice sheet topography. Science 273, 1359-1364.

Peltier, W.R., 1998a. 'Implicit ice' in the global theory of glacial isostatic adjustment. Geophysical Research Letters 25, 3955-3958.

Peltier, W.R., 1998b. Postglacial variations in the level of the sea: implications for climate dynamics and solid-earth geophysics. Reviews of Geophysics 36, 603-689.

Peltier, W.R., 2004. Global glacial isostasy and the surface of the ice-age Earth: The ICE-5G (VM2) model and GRACE. Annual Reviews of Earth and Planetary Sciences 32, 111-149.

Peltier, W.R., 2005. On the hemispheric origins of meltwater pulse 1a. Quaternary Science Reviews 24, 1655-1671.

Peltier, W.R., and Fairbanks, R.G., 2006. Global glacial ice volume and Last Glacial Maximum duration from an extended Barbados sea level record. Quaternary Science Reviews 25, 3322-3337.

Peltier, W.R., and Drummond, R., 2008. Rheological stratification of the lithosphere: a direct inference based upon the geodetically observed pattern of the glacial isostatic adjustment of the North American continent. Geophysical Research Letters 35, doi:10.1029/2008GL034586.

Peltier, W.R., 2009. Closure of the budget of global sea level rise over the GRACE era: the importance and magnitudes of the required corrections for global glacial isostatic adjustment. Quaternary Science Reviews 28, 1658-1674.

Peltier, W.R., Argus, D., Drummond, R., Moore, A.W., 2012a. Postglacial rebound and current ice loss estimates from space geodesy: the new ICE-6G (VM5a) global model. American Geophysical Union Fall Meeting, December 3-7, 2012, G23C-02.

Peltier, W.R., Drummond, R., and Roy, K., 2012b. Comment on 'Ocean mass from GRACE and glacial isostatic adjustment' by D.P. Chambers et al. Journal of Geophysical Research 117, doi:10.1029/2011JB008967.

Perry, H.K.C., Eaton, D.W.S., and Forte, A.M., 2002. LITH5.0: a revised crustal model for Canada based on Lithoprobe results. Geophysical Journal International 150, 285-294.

Price, S.F., Conway, H., and Waddington, E.D., 2007. Evidence for late Pleistocene thinning of Siple Dome, West Antarctica. Journal of Geophysical Research 112, doi:10.1029/2006JF000725.

Prinsenberg, S.J., 1987. Seasonal current variations observed in western Hudson Bay. Journal of Geophysical Research 92, 10756-10766.

Rahmstorf, S., 2007. A semi-empirical approach to projecting future sea-level rise. Science 315, 368-370.

Ramillien, G., Lombard, A., Cazenave, A., Ivins, E.R., Llubes, M., Remy, F., and Biancale, R., 2006. Interannual variations of the mass balance of the Antarctica and Greenland ice sheets from GRACE. Global and Planetary Change 53, 198-208.

Ramillien, G., Bouhours, S., Lombard, A., Cazenave, A., Flechtner, F., and Schmidt, R., 2008. Land water storage contribution to sea level from GRACE geoid data over 2003-2006. Global and Planetary Change 60, 381-392.

Ranalli, G., 1987. Rheology of the Earth: Deformation and Flow Processes in Geophysics and Geodynamics. Allen & Unwin Inc., Boston, 366pp.

Raymond, C.A., Ivins, E.R., Heflin, M.B., and James, T.S., 2004. Quasi-continuous global positioning system measurements of glacial isostatic adjustment in the Northern Transantarctic mountains. Global and Planetary Change 42, 295-303.

Reimer, P.J., Baillie, M.G.L., Bard, E., Bayliss, A., Beck, J.W., Bertrand, C.J.H., Blackwell, P.G., Buck, C.E., Burr, G.S., Cutler, K.B., Damon, P.E., Edwards, R.L., Fairbanks, R.G., Friedrich, M., Guilderson, T.P., Hogg, A.G., Hughen, K.A., Kromer, B., McCormac, F.G., Manning, S.W., Ramsey, C.B., Reimer, R.W., Remmele, S., Southon, J.R., Stuiver, M., Talamo, S., Taylor, F.W., van der Plicht, J., and Weyhenmeyer, C.E., 2004. IntCal04 Terrestrial radiocarbon age calibration, 26 - 0 ka BP. Radiocarbon 46, 1029-1058.

Reimer, P.J., Bard, E., Bayliss, A., Beck, J.W., Blackwell, P.G., Bronk Ramsey, C., Buck, C.E., Cheng, H., Edwards, R.L., Friedrich, M., Grootes, P.M., Guilderson, T.P., Haflidason, H., Hajdas, I., Hatté, C., Heaton, T.J., Hoffman, D.L., Hogg, A.G., Hughen, K.A., Kaiser, K.F., Kromer, B., Manning, S.W., Niu, M., Reimer, R.W., Richards, D.A., Scott, E.M., Southon, J.R., Staff, R.A., Turney, C.S.M., and van der Plicht, J., 2013. IntCal13 and Marine13 radiocarbon age calibration curves 0-50000 years cal BP. Radiocarbon 55, 1869-1887.

Ridler, R.H., and Shilts, W.W., 1974. Exploration for Archean polymetallic sulphide deposits in permafrost terrains: an integrated geological/geochemical technique; Kaminak Lake area, District of Keewatin. Paper 73-34. Geological Survey of Canada, Ottawa.

Rignot, E., 2008. Changes in West Antarctica ice stream dynamics observed with ALOS PALSAR data. Geophysical Research Letters 35, doi:10.1029/2008GL033365.

Rignot, E., Velicogna, I., van den Broeke, M.R., Monaghan, A., and Lenaerts, J.T.M., 2011. Acceleration of the contribution of the Greenland and Antarctic ice sheets to sea level rise. Geophysical Research Letters 38, doi:10.1029/2011GL046583.

Rülke, A., Dietrich, R., Fritsche, M., Rothacher, M., and Steigenberger, P., 2008. Realization of the terrestrial reference system by a reprocessed global GPS network. Journal of Geophysical Research 113, doi:10.1029/2007JB005231.

Schmeling, H., 1987. On the interaction between small- and large-scale convection and postglacial rebound flow in a power-law mantle. Earth and Planetary Science Letters 84, 254-262.

Seed, R., and Suchanek, T.H., 1992. Population and community ecology of *Mytilus*. In: Gosling, E. (Ed.), The Mussel *Mytilus*: Ecology, Physiology, Genetics and Culture. Elsevier, Amsterdam, pp. 87-169.

Sella, G.F., Stein, S., Dixon, T.H., Craymer, M., James, T.S., Mazzotti, S., and Dokka, R.K., 2007. Observation of glacial isostatic adjustment in 'stable' North America with GPS. Geophysical Research Letters 34, doi:10.1029/2006GL027081.

Shennan, I., 2007. Sea level studies: overview. In: Elias, S.A. (Ed.), Encyclopedia of Quaternary Science. Elsevier, Amsterdam, pp. 2967-2974.

Shepherd, A., and Wingham, D., 2007. Recent sea-level contributions of the Antarctic and Greenland Ice Sheets. Science 315, 1529-1532.

Shepherd, A., Ivins, E.R., and 45 other IMBIE participants, 2012. A reconciled estimate of ice-sheet mass balance. Science 338, 1183-1189.

Shilts, W., 1973. Drift prospecting; Geochemistry of eskers and till in permanently frozen terrain: District of Keewatin; Northwest Territories. Paper 72-45. Geological Survey of Canada, Ottawa, pp. 1-32.

Shilts, W.W., Dean, W.E., and Klassen, R.A., 1976. Physical, chemical, and stratigraphic aspects of sedimentation in lake basins of the eastern Arctic Shield. Paper 76-1A. Geological Survey of Canada, Ottawa, pp. 245-254.

Shilts, W.W., Aylsworth, J.M., Kaszycki, C.A., and Klassen, R.A., 1987. Canadian Shield. In: Graf, W.L. (Ed.), Geomorphic Systems of North America, Centennial Special Volume 2. Geological Society of America, Boulder, Colorado, pp. 119-161.

Simon, K.M., James, T.S., and Ivins, E.R., 2010. Ocean loading effects on the prediction of Antarctic glacial isostatic uplift and gravity rates. Journal of Geodesy 84, 305-317.

Simon, K.M., James, T.S., Forbes, D.L., Telka, A.M., Dyke, A.S., and Henton, J.A., 2014. A relative sea-level history for Arviat, Nunavut, and implications for Laurentide Ice Sheet thickness west of Hudson Bay. Quaternary Research 82, 185-197.

Simpson, M.J.R., Milne, G.A., Huybrechts, P., and Long, A.J., 2009. Calibrating a glaciological model of the Greenland Ice Sheet from the Last Glacial Maximum to present-day using field observations of relative sea level and ice extent. Quaternary Science Reviews 28, 1631-1657.

Stacey, F.D., 1992. Physics of the Earth. 3^{rd} edition, Brookfield Press, Brisbane, 513pp.

Stanford, J.D., Rohling, E.J., Hunter, S.E., Roberts, A.P., Rasmussen, S.O., Bard, E., McManus, J., and Fairbanks, R.G., 2006. Timing of meltwater pulse 1a and cli-

mate responses to meltwater injections. Paleoceanography 21, doi:10.1029/2006PA001340.

Stuiver, M., and Polach, H.A., 1977. Discussion: Reporting of ^{14}C data. Radiocarbon 19, 355-363.

Stuiver, M., and Braziunas, T.F., 1993. Modeling atmospheric ^{14}C influences and ^{14}C ages of marine samples to 10,000 BC. Radiocarbon 35, 137-189.

Stuiver, M., and Reimer, P.J., 1993. Extended ^{14}C database and revised CALIB 3.0 ^{14}C age calibration program. Radiocarbon 35, 215-230.

Tamisiea, M.E., Mitrovica, J.X., and Davis, J.L., 2007. GRACE gravity data constrain ancient ice geometries and continental dynamics over Laurentia. Science 316, 881-883.

Tamisiea, M.E., 2011. Ongoing glacial isostatic contributions to observations of sea level change. Geophysical Journal International 186, 1036-1044.

Tarasov, L., Dyke, A.S., Neal, R.M., and Peltier, W.R., 2012. A data-calibrated distribution of deglacial chronologies for the North American ice complex from glaciological modeling. Earth and Planetary Science Letters 315-316, 30-40.

Tella, S., Paul, D., Berman, R.G., Davis, W.J., Peterson, T.D., Pehrsson, S.J., and Kerswill, J.A., 2007. Bedrock geology compilation and regional synthesis of parts of the Hearne and Rae domains, western Churchill Province, Nunavut-Manitoba. Open file 5441. Geological Survey of Canada, Ottawa.

Thomas, D., 2008. Development of a coastal community climate change action plan for Arviat, Nunavut. Master of Natural Resource Management thesis, University of Manitoba, Winnipeg.

Thomas, R., Rignot, E., Casassa, G., Kanagaratnam, P., Acuna, C., Akins, T., Brecher, H., Frederick, E., Gogineni, P., Krabill, W., Manizade, S., Ramamoorthy, H., Rivera, A., Russell, R., Sonntag, J., Swift, R., Yungel, J., and Zwally, J., 2004. Accelerated sea-level rise from West Antarctica. Science 306, 255-258.

Tiampo, K.F, Mazzotti, S., and James, T.S., 2012. Analysis of GPS Measurements in eastern Canada using principal component analysis. Pure and Applied Geophysics 169, 1483-1506.

Toscano, M.A., Peltier, W.R., and Drummond, R., 2011. ICE-5G and ICE-6G models of postglacial relative sea-level history applied to the Holocene coral reef record of northeastern St Croix, U.S.V.I.: investigating the influence of rotational feedback on GIA processes at tropical latitudes. Quaternary Science Reviews 30, 3032-3042.

Tregoning, P., Welsh, A., McQueen, H., and Lambeck, K., 2000. The search for postglacial rebound near the Lambert Glacier, Antarctica. Earth Planets Space 52, 1037-1041.

Tregoning, P., Ramillien, G., McQueen, H., and Zwartz, D., 2009. Glacial isostatic adjustment and non-stationary signals observed by GRACE. Journal of Geophysical Research 114, doi:10.1029/2008JB006161.

Trettin, H.P., 1991. Tectonic framework. In: Trettin, H.P. (Ed.), Geology of the Innuitian Orogen and Arctic Platform of Canada and Greenland, Geology of Canada 3. Geological Survey of Canada, Ottawa, pp. 57-66.

Turcotte, D.L., and Schubert, G., 2002. Geodynamics. 2^{nd} edition, Cambridge University Press, Cambridge, 456pp.

Tushingham, A.M., 1991a. On the extent and thickness of the Innuitian Ice Sheet: a postglacial-adjustment approach. Canadian Journal of Earth Sciences 28, 231-239.

Tushingham, A.M., 1991b. On the extent and thickness of the Innuitian Ice Sheet: a postglacial-adjustment approach: reply. Canadian Journal of Earth Sciences 28, 1696-1697.

Tushingham, A.M., and Peltier, W.R., 1991. Ice-3G: A new global model of late Pleistocene deglaciation based upon geophysical predictions of post-glacial relative sea level change. Journal of Geophysical Research 96, 4497-4523.

van der Wal, W., Wu, P., Sideris, M.G., and Shum, C.K., 2008. Use of GRACE determined secular gravity rates for glacial isostatic adjustment studies in North-America. Journal of Geodynamics 46, 144-154.

van der Wal, W., Wu, P., Wang, H., and Sideris, M.G., 2010. Sea levels and uplift rate from composite rheology in glacial isostatic adjustment modeling. Journal of Geodynamics 50, 38-48.

Velicogna, I., and Wahr, J., 2006. Measurements of time-variable gravity show mass loss in Antarctica. Science 311, 1754-1756.

Vettoretti, G., and Peltier, W.R., 2013. Last Glacial Maximum ice sheet impacts on North Atlantic climate variability: the importance of a sea ice lid. Geophysical Research Letters 40, 6378-6383.

Wahr, J., Molenaar, M., and Bryan, F., 1998. Time variability of the Earth's gravity field: hydrological and oceanic effects and their possible detection using GRACE. Journal of Geophysical Research 103, 30205-30229.

Wahr, J., Wingham, D., and Bentley, C., 2000. A method of combining ICESat and GRACE satellite data to constrain Antarctic mass balance. Journal of Geophysical Research 105, 16279-16294.

Walton, A., Trautman, M.A., and Friend, J.P., 1961. Isotopes, Inc. radiocarbon measurements I. Radiocarbon 3, 47-59.

Wang, H., Jia, L., Steffen, H., Wu, P., Jiang, L., Hsu, H., Xiang, L., Wang, Z., and Hu, B., 2012. Increased water storage in North America and Scandinavia from GRACE gravity data. Nature Geoscience 6, 38-42.

Wang, Y., and Mareschal, J.C., 1999. Elastic thickness of the lithosphere in the Central Canadian Shield. Geophysical Research Letters 26, 3033-3035.

Whitehouse, P.L., Bentley, M.J., Milne, G.A., King, M.A., and Thomas, I.D., 2012. A new glacial isostatic adjustment model for Antarctica: calibrated and tested using observations of relative sea-level change and present-day uplift rates. Journal of Geophysical Research 190, 14641482.

Wickert, A.D., Mitrovica, J.X., Williams, C., and Anderson, R.S., 2013. Gradual demise of a thin southern Laurentide Ice Sheet recorded by Mississippi drainage. Nature 502, 668-671.

Willis, M.J., 2008. Crustal motion in the Antarctic interior from a decade of Global Positioning System measurements. PhD thesis, Ohio State University, Columbus.

Witman, J.D., and Dayton, P.K., 2001. Rocky subtidal communities. In: Bertness, M.D., Gaines, S.D., and Hay, M.E. (Eds.), Marine Community Ecology. Sinauer Associates, Massachusetts, pp. 339-366.

Woodward, R.J., 1888. On the form and position of the sea level: with special reference to its dependence on superficial masses symmetrically disposed about a normal to the Earth's surface. United States Geological Survey, Bulletin 48, pp. 87-170.

Wu, P., and Peltier, W.R., 1982. Viscous gravitational relaxation. Geophysical Journal of the Royal Astronomical Society 70, 435-485.

Wu, P., and Peltier, W.R., 1984. Pleistocene deglaciation and the Earth's rotation: a new analysis. Geophysical Journal of the Royal Astronomical Society 76, 753-791.

Wu, P., 1992. Deformation of an incompressible viscoelastic flat earth with power-law creep: a finite element approach. Geophysical Journal International 108, 35-51.

Wu, P., 1993. Postglacial rebound in a power-law medium with axial symmetry and the existence of the transition zone in relative sea-level data. Geophysical Journal International 114, 417-432.

Wu, P., 1995. Can observations of postglacial rebound tell whether the rheology of the mantle is linear or nonlinear? Geophysical Research Letters 22, 1645-1648.

Wu, P., 1998. Postglacial rebound modeling with power-law rheology. In: Wu, P. (Ed.), Dynamics of the ice age Earth: a modern perspective. Trans Tech Publications Ltd., Switzerland, pp. 365-382.

Wu, P., 2001. Postglacial induced surface motion and gravity in Laurentia for uniform mantle with power-law rheology and ambient tectonic stress. Earth and Planetary Science Letters 186, 427-435.

Wu, P., Wang, H., and Schotman, H., 2005. Postglacial induced surface motions, sea-levels and geoid rates on a spherical, self-gravitating laterally heterogeneous earth. Journal of Geodynamics 39, 127-142.

Wu, P., and Wang, H., 2008. Postglacial isostatic adjustment in a self-gravitating spherical earth with power-law rheology. Journal of Geodynamics 46, 118-130.

Zanutta, A., Vittuari, L., and Gandolfi, S., 2008. Geodetic GPS-based analysis of recent crustal motions in Victoria Land (Antarctica). Global and Planetary Change 62, 115131.

Zdanowicz, C., Smetny-Sowa, A., Fisher, D., Schaffer, N., Copland, L., Eley, J., and Dupont, F., 2012. Summer melt rates on Penny Ice Cap, Baffin Island: past and recent trends and implications for regional climate. Journal of Geophysical Research 117, doi:10.1029/2011JF002248.

Zoltai, S.C., 1995. Permafrost distribution in peatlands of west-central Canada during the Holocene warm period 6000 years BP. Géographie physique et Quaternaire 49, 45-54.

Appendix A

An Analytical Expression for $\nabla \overline{Y}^{j}_{nm}$

In order to compute the horizontal displacements, which are a vector quantity, the spherical harmonics must be replaced with the gradient of the spherical harmonics. Mitrovica et al. (1994) derived an analytical expression for the gradient of the spherical harmonics, however, the authors used complex notation. To use the expressions of Mitrovica et al. (1994) would first require conversion from complex spherical coordinates to Cartesian coordinates, and then subsequently to real spherical polar coordinates. Instead of performing these conversions, a direct form of the gradient of the spherical harmonics in real notation was derived.

Recalling equation 2.36, the normalized spherical harmonics are given by

$$\overline{Y}^{j}_{nm}(\theta, \psi) = \overline{P}_{nm}(\cos\theta) c_j(m\psi), \tag{A.1}$$

and if the normalization factors of the associated Legendre polynomials are shown explicitly as N_{nm}, equation A.1 becomes

$$\overline{Y}^{j}_{nm}(\theta, \psi) = N_{nm} P_{nm}(\cos\theta) c_j(m\psi). \tag{A.2}$$

In spherical polar coordinates, the gradient operator is given by

$$\nabla = \frac{\partial}{\partial\theta}\mathbf{e}_\theta + \frac{1}{\sin\theta}\frac{\partial}{\partial\psi}\mathbf{e}_\psi, \tag{A.3}$$

where $\mathbf{e}_\theta$ and $\mathbf{e}_\psi$ are the azimuthal and longitudinal basis vectors, respectively. Using equation A.3 to take the gradient of equation A.2 and explicitly showing the odd and

even parts of $c_j(m\psi)$, yields

$$\begin{aligned}\nabla\overline{Y}^{1,2}_{nm}(\theta,\psi) &= \mathbf{e}_\theta\left[\frac{\partial}{\partial\theta}N_{nm}P_{nm}(\cos\theta)\right](\cos(m\psi),\sin(m\psi)) \\ &+ \mathbf{e}_\psi\frac{1}{\sin\theta}N_{nm}P_{nm}(\cos\theta)(m(-\sin(m\psi),\cos(m\psi))). \qquad \text{(A.4)}\end{aligned}$$

In order to solve the azimuthal component of A.4, the differential operator must first be expressed in terms of $\cos\theta$ as follows

$$\frac{\partial}{\partial\theta} = \frac{\partial}{\partial(\cos\theta)}\frac{\partial(\cos\theta)}{\partial\theta} = -\sin\theta\frac{\partial}{\partial(\cos\theta)}. \qquad \text{(A.5)}$$

Substitution of equation A.5 into A.4 gives

$$\frac{\partial}{\partial\theta}\left(N_{nm}P_{nm}(\cos\theta)\right) = -\sin\theta\left[\frac{\partial}{\partial(\cos\theta)}\left(N_{nm}P_{nm}(\cos\theta)\right)\right]. \qquad \text{(A.6)}$$

By considering only the term in square brackets on the right hand side of equation A.6, and substituting $\cos\theta = x$ for brevity, it is apparent that an expression has to be obtained for

$$N_{nm}\frac{\partial}{\partial x}(P_{nm}(x)). \qquad \text{(A.7)}$$

An explicit expression for associated Legendre polynomials is given by (e.g., Stacey 1992)

$$P_{nm}(x) = \frac{\partial}{\partial x}\left[\frac{1}{2^n n!}(1-x^2)^{\frac{m}{2}}\left(\frac{d}{dx}\right)^{n+m}(x^2-1)^n\right], \qquad \text{(A.8)}$$

which when substituted into equation A.7 gives

$$N_{nm}\frac{\partial}{\partial x}(P_{nm}(x)) = N_{nm}\frac{\partial}{\partial x}\left[\frac{1}{2^n n!}(1-x^2)^{\frac{m}{2}}\left(\frac{d}{dx}\right)^{n+m}(x^2-1)^n\right]. \qquad \text{(A.9)}$$

Differentiating the right hand side of equation A.9 gives

$$\begin{aligned}N_{nm}\frac{\partial}{\partial x}(P_{nm}(x)) &= N_{nm}\left[\frac{1}{2^n n!}(1-x^2)^{\frac{m}{2}}\frac{d}{dx}\left(\frac{d}{dx}\right)^{n+m}(x^2-1)^n\right. \\ &+ \left.\left(\frac{d}{dx}\right)^{n+m}(x^2-1)^n\frac{1}{2^n n!}\frac{m}{2}(1-x^2)^{\frac{m}{2}-1}(-2x)\right]. \qquad \text{(A.10)}\end{aligned}$$

Equation A.10 can be further simplified as

$$\begin{aligned} N_{nm}\frac{\partial}{\partial x}(P_{nm}(x)) &= N_{nm}\left[\frac{1}{2^n n!}(1-x^2)^{\frac{m}{2}}\left(\frac{d}{dx}\right)^{n+m+1}(x^2-1)^n\right. \\ &- \left.\left(\frac{d}{dx}\right)^{n+m}(x^2-1)^n\frac{1}{2^n n!}mx(1-x^2)^{\frac{m}{2}-1}\right] \\ &= N_{nm}\left[P_{n(m+1)}(x)(1-x^2)^{-1/2}-\frac{P_{nm}(x)mx}{1-x^2}\right] \end{aligned} \quad (A.11)$$

where the expression for the associated Legendre polynomials given by equation A.8 has been used. Substituting equation A.11 into equation A.6, replacing x with $\cos\theta$, and making use of the identity $\cos^2\theta + \sin^2\theta = 1$ gives

$$\begin{aligned} \frac{\partial}{\partial\theta}\left(N_{nm}P_{nm}(\cos\theta)\right) &= -\sin\theta N_{nm}\left[P_{n(m+1)}(\cos\theta)\frac{1}{\sin\theta}-P_{nm}(\cos\theta)m\frac{\cos\theta}{\sin^2\theta}\right] \\ &= N_{nm}\left[P_{nm}(\cos\theta)m\cot\theta - P_{n(m+1)}(\cos\theta)\right]. \end{aligned} \quad (A.12)$$

Equation A.12 can be put into equation A.4 to yield an expression for the gradient of the spherical harmonics

$$\begin{aligned} \nabla\overline{Y}^{1,2}_{nm}(\theta,\psi) &= \mathbf{e}_\theta N_{nm}\left(P_{nm}(\cos\theta)m\cot\theta - P_{n(m+1)}(\cos\theta)\right)(\cos(m\psi),\sin(m\psi)) \\ &+ \mathbf{e}_\psi\frac{1}{\sin\theta}N_{nm}P_{nm}(\cos\theta)(m(-\sin(m\psi),\cos(m\psi))). \end{aligned} \quad (A.13)$$

Equation A.13 represents an analytical form of the gradient of the spherical harmonics that can be implemented within the GIA code. The $\cot\theta$ term in the azimuthal component and the $(1/\sin\theta)$ term in the longitudinal component of equation A.13 will cause $\nabla\overline{Y}^{1,2}_{nm}(\theta,\psi)$ to be infinite at the poles, and therefore the computed horizontal displacement will also be infinite at the poles. Since the associated Legendre polynomials only exist for $n \geq m$, $P_{n(m+1)}$ is explicitly set to zero in the code when $n = m$.

All of the associated Legendre polynomials are automatically normalized within the GIA code. Therefore, $P_{n(m+1)}$ is normalized by $N_{n(m+1)}$. However, as equation A.13 indicates, $P_{n(m+1)}$ should be normalized by N_{nm}. Therefore, $P_{n(m+1)}$ must be multiplied explicitly by $\dfrac{N_{nm}}{N_{n(m+1)}}$. A form of the necessary multiplication factor can be

obtained by writing out the standard normalization factors so that all of the factorial terms will cancel upon division

$$N_{nm} = \left(\frac{(2n+1)(n-m)!(2-\delta_{0m})}{(n+m)!} \right)^{1/2} = \left(\frac{(2n+1)(n-m)(n-m-1)!(2-\delta_{0m})}{(n+m)!} \right)^{1/2}$$
$$N_{n(m+1)} = \left(\frac{(2n+1)(n-m-1)!(2-\delta_{0(m+1)})}{(n+m+1)!} \right)^{1/2} = \left(\frac{(2n+1)(n-m-1)!(2)}{(n+m+1)(n+m)!} \right)^{1/2} \tag{A.14}$$

where $\delta_{0(m+1)}$ cancels in the second part of equation A.14 since $m+1 > 0$ for all m. Using equation A.14 therefore gives for the multiplication factor

$$\frac{N_{nm}}{N_{n(m+1)}} = \frac{((n-m)(2-\delta_{0m}))^{1/2}}{\left(\frac{2}{n+m+1} \right)^{1/2}}, \tag{A.15}$$

which reduces to

$$\frac{N_{nm}}{N_{n(m+1)}} = \begin{cases} \dfrac{\sqrt{n}}{\left(\frac{2}{n+1} \right)^{1/2}} & \text{if } m = 0, \\ \dfrac{(2(n-m))^{1/2}}{\left(\frac{2}{n+m+1} \right)^{1/2}} & \text{if } m \neq 0. \end{cases} \tag{A.16}$$

The azimuthal and longitudinal components of equation A.13 are computed separately within the GIA code, and $P_{n(m+1)}$ is multiplied by the appropriate part of equation A.16.

Appendix B

Preliminary Development of Ocean Loading Techniques

B.1 Article Information

B.1.1 Author's and Coauthors' Contributions

Section B.2 is an article that was published in the Journal of Geodesy as part of the PhD research. The author of this thesis performed the numerical modelling calculations, interpreted the results, wrote the original manuscript, and created the figures. Coauthors Thomas James and Erik Ivins developed the IJ05 ice sheet reconstruction used in the study, and also significantly contributed to the formulation of the original research idea and the derivation presented in Appendix B′. All authors read, commented on, and revised earlier versions of the article.

B.1.2 Citation

Simon, K.M., James, T.S., and Ivins, E.R. (2010). Ocean loading effects on the prediction of Antarctic glacial isostatic uplift and gravity rates. Journal of Geodesy 84:305-317, doi:10.1007/s00190-010-0368-4.

B.1.3 Authors' Names and Affiliations

K.M. Simon[1,2*], T.S. James[2,1], E.R. Ivins[3]

[1] School of Earth and Ocean Sciences, University of Victoria, Victoria, BC, V8P 5C2

[2] Geological Survey of Canada, Natural Resources Canada, Sidney, BC, V8L 4B2

[3] Jet Propulsion Laboratory, California Institute of Technology, Pasadena, CA 91190, USA

[*] Corresponding author: ksimon@nrcan.gc.ca

B.1.4 Article Format

Section B.2 consists of a published journal article that appeared in the Journal of Geodesy in 2010. The article has been reformatted to follow the University of Victoria's thesis formatting guidelines and to maintain internal consistency with the rest of the thesis. The formatting changes include the numbering of sections, equations, figures and tables. However, symbols and general notation within mathematical equations remains the same as in the original research article. Since this section is already an appendix, the appendix that originally appeared in the Journal of Geodesy article has been renamed Appendix B′ and appears as section B.2.6 here. The content of the following sections has otherwise been reproduced identically relative to the published article.

B.2 Ocean loading effects on the prediction of Antarctic glacial isostatic uplift and gravity rates

Received: 12 June 2009/ Accepted: 19 January 2010/ Published online: 12 February 2010

B.2.1 Abstract

The effect of regional ocean loading on predicted rates of crustal uplift and gravitational change due to glacial isostatic adjustment (GIA) is determined for Antarctica. The effect is found to be significant for the ICE-3G and ICE-5G loading histories (up to -8 mm/yr and -3 mm/yr change in uplift rate and -3 cm/yr and -1 cm/yr equivalent water height change (EWHC) of surface mass, respectively). The effect is smaller (+1 mm/yr; +0.25 cm/yr) for the IJ05 loading history. The impact of ocean loading on the rate of change of the long-wavelength zonal harmonics of the Earth's gravitational field is also significantly smaller for IJ05 than ICE-3G. A simple analytical formula is derived that is accurate to about 3% in a root-mean-square sense that relates predicted or observed gravitational change at the surface of the Earth ($r = a$) to the EWHC. A fundamental difference in the definition of the load histories accounts for the differing sensitivities to ocean loading. IJ05 defines its surface load history relative to the present-day surface load, rather than specifying an absolute loading history, and thus implicitly approximates the temporal and spatial mass exchange between grounded ice and open ocean. In contrast, ICE-3G and ICE-5G specify an

absolute load history and explicit regional ocean loading substantially perturbs predicted GIA rates. Conclusions of previous studies that used IJ05 predictions without ocean loading are relatively robust.
keywords: glacial isostatic adjustment, Antarctica, GRACE, gravity change, crustal movement, GPS

B.2.2 Introduction

Geodetic measurements of global trends in cryospheric and hydrospheric mass storage are emerging as a critical component of climate change science. For example, Global Positioning System (GPS) determination of crustal motions and satellite gravity observations of the changing gravitational field of the Earth provide new constraints on the sources and sinks of continental-scale water transport (e.g., Davis et al. 2004, Bevis et al. 2005, Ramillien et al. 2008). Glacial isostatic adjustment (GIA) is the on-going response of the Earth to past changes in glaciers and ice sheets. It is a key source of uncertainty in interpreting geodetic observations to discern hydrological changes (e.g., Wahr et al. 2000, Ramillien et al. 2006).

The response of the Earth to changes in the ocean load is an important component of the total GIA response. In near-shore areas formerly covered by grounded marine ice, a significant fraction of the past ice load is replaced by ocean water in the isostatically depressed region. The process is called "water dumping" (Milne 1998). In Hudson Bay, Canada, incorporation of water dumping reduces predicted relative sea-level fall by about 100 m, or 40% (Kendall et al. 2005). The corresponding change in the prediction of the rate of present-day crustal uplift is as large as -5 mm/yr or $+0.75$ μGal/yr and is much larger than measurement uncertainties.

The Antarctic ice sheet has undergone significant mass variation throughout the Holocene (Denton and Hughes 2002) and the West Antarctic ice sheet continues to experience rapid change (e.g., Thomas et al. 2004, Shepherd and Wingham 2007, Rignot 2008). The Ross Sea and Ross Ice Shelf underwent deglaciation and ungrounding of marine-based ice following Last Glacial Maximum (LGM) (e.g., Denton and Hughes 2002, Hall et al. 2004).

The Gravity Recovery and Climate Experiment (GR-ACE) satellite has measured the time-variable gravity field over Antarctica and the data have been used to estimate mass balance for Antarctica and the corresponding contribution to global sea-level change (Chen et al. 2006, 2008, Ramillien et al. 2006, Velicogna and Wahr

2006, Barletta et al. 2008). The magnitude of the GIA-related gravity change is a major source of uncertainty in such estimates. The satellite-derived observations of gravity change are complemented by a limited number of bedrock absolute gravity observations (Mäkinen et al. 2008).

Observations of present-day rates of crustal motion constrain both the Earth's response to surface mass changes and tectonic motion of the Antarctic plate. Several recent GPS campaigns have measured crustal motion in the Transantarctic Mountains (TAM) and Victoria Land (Raymond et al. 2004, Capra et al. 2007, Willis 2008, Zanutta et al. 2008), Marie Byrd Land adjacent to the Ross Sea (Donnellan and Luyendyk 2004), the Antarctic Peninsula (Dietrich et al. 2004), and East Antarctica (Tregoning et al. 2000, Ohzono et al. 2006). As well, continuous GPS sites located around the perimeter of the continent provide further constraints on rates of vertical and horizontal crustal motion (Bouin and Vigny 2000, Rülke et al. 2008, their Figure 17; Amalvict et al. 2009). Much of the observed crustal deformation on the continent is attributed to the GIA process, necessitating accurate model prediction of GIA deformation rates, including the component due to ocean loading.

In this paper we quantitatively assess the effects of regional ocean loading on predicted present-day rates of vertical crustal motion and gravity change for Antarctica. We focus on the IJ05 history, which incorporates recent glacial geological and glaciological constraints on Antarctic ice sheet history (Ivins and James 2005). We also discuss the Antarctic component of the widely used ICE-3G and ICE-5G loading histories (Tushingham and Peltier 1991, Peltier 2004). Their mode of construction differs fundamentally from IJ05 and as a consequence, the response of ICE-3G and ICE-5G to the incorporation of explicit regional ocean loading differs substantially from IJ05. Updated predictions of crustal uplift and gravity change are also given for the IJ05 model. As GIA plays an ever more prominent role in global geodesy, comparisons in this paper offer valuable insight into the differences in predictions that can arise from using different implicit assumptions in the treatment of the forward modelled water-ice load.

B.2.3 Methodology

Sea Level Calculations

Ocean water depth, S, can be expressed by a generalized form of the sea-level equation (e.g., Farrell and Clark 1976, Wu et al. 2005):

$$S(\theta, \phi, t) = [N(\theta, \phi, t) - U(\theta, \phi, t) + c(t)]O(\theta, \phi, t) \tag{B.1}$$

where N is the geoid, U is the position of the solid surface, O is the time dependent ocean function ($O = 1$ for ocean locations, 0 otherwise), θ and ϕ are the spatial coordinates, and t is time. The quantity $c(t)$, which is introduced to conserve mass, approximates global eustatic sea-level change, but is not exact because of vertical motion of the seafloor and perturbations to the gravitational potential. We limit attention to the vicinity of the Antarctic continent. Instead of explicitly computing global model sea surface variations, we have assumed that the Barbados sea-level curve (e.g., Fairbanks 1989, Peltier and Fairbanks 2006) represents global eustatic variations and provides a reasonable approximation for $c(t)$. The sea-level record at Barbados is a widely accepted observation for reconstructing global melt water inundation during glacial transition and Holocene time (e.g., Stanford et al. 2006). As described below, our results are insensitive to the use of this approximation.

To compute the ocean load for each loading history, we iteratively predict the spatial-temporal variation of water depth using equation B.1. For the first iteration, the ocean load is assumed to be the present-day water depth, and for subsequent iterations, a new estimate of water depth, S, is obtained from the sum of the present-day water depth and the predicted change in sea-level relative to present-day. The predicted change to relative sea-level between each iteration contains the perturbations to N and U that arise as the result of the dependence of these quantities on the value of S itself. The method for calculating perturbations to N and U is described by James and Ivins (1998). The convergence criterion for changes to the water depth is one meter.

The effect of ocean loading was incorporated into the surface load of each loading history as discussed below; we do not, however, model more subtle changes to shoreline position due to the on lap and off lap of water over time. Our ocean loading computation is not global and thus does not model effects such as the global redistribution of water due to equatorial ocean syphoning (e.g., Mitrovica and Peltier

1991), or rotational feedback effects which may be important to far-field sea-levels (e.g., Gomez et al. 2009). As discussed later, scaling $c(t)$ uniformly up and down in a sensitivity analysis leads to small changes to predicted present-day crustal motion, showing that the regional response is dominated by Antarctic ice mass change and ocean loading.

Initial Configuration of the Loading Histories

Ivins and James (2005) defined IJ05 as the ice thickness relative to the present-day surface load, rather than as the absolute (total) ice thickness. The choice to construct IJ05 relative to the present load was made in part because information on past ice sheet elevations is often given relative to the present day. In carrying out the reconstruction, the present-day surface load was determined from the present-day ice thickness or water depth, depending on the location. IJ05 thus implicitly includes a regional ocean load in areas that are presently marine but were once ice covered. The main focus of the reconstruction, however, was to incorporate many newly available glacio-geological data that more tightly constrained the history of the grounded ice sheet.

As the necessary first step for incorporating ocean loading into IJ05, the original (differential) IJ05 load thicknesses were converted to absolute thicknesses by adding the present-day surface load to the differential values (Figure B.1). The present-day absolute IJ05 load is defined as either the present-day ice thickness or depth to bedrock (whichever is larger, as floating ice is part of the water load). Ice thickness and bedrock depths were determined by spatially averaging these values from the BEDMAP database (Lythe et al. 2001) using the same grid as the loading history. In contrast to IJ05, the total ice thickness is given for ICE-3G and ICE-5G, and these models do not require conversion to an absolute load.

Prior to performing the ocean loading calculation for the ICE-3G and ICE-5G models, we first check both ice models for the presence of floating ice at each time in the loading history. An initial calculation of sea-level was carried out at each ICE-3G/5G grid point at each model time using the ICE-3G/5G ice loading history, and the ice-thickness values were checked for each model time to see if the ice was floating. Ice floats at any location in the model for which the ice thickness is less than the density scaled predicted water depth (which is, at each time, the sum of the initial predicted relative sea-level (RSL) change and present-day bathymetry).

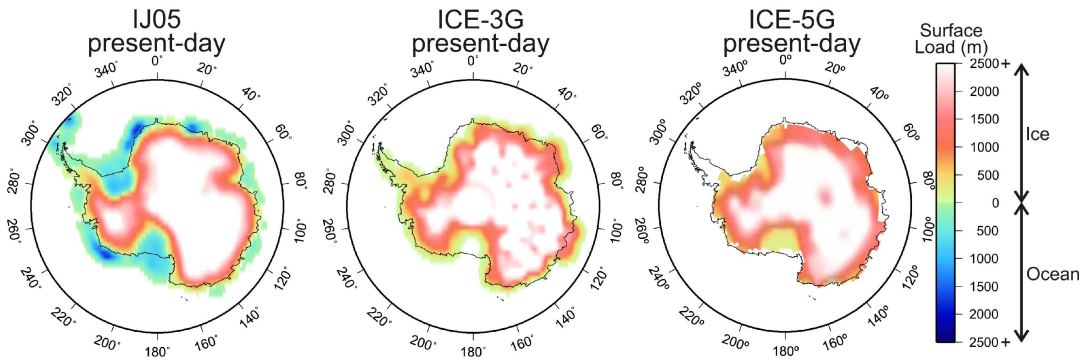

Figure B.1: Absolute present-day surface load thicknesses for glacial loading histories IJ05 (Ivins and James 2005), ICE-3G (Tushingham and Peltier 1991), and ICE-5G (Peltier 2004). IJ05 ice thicknesses are defined relative to the present-day surface load, and thus the present-day absolute IJ05 load includes ocean water loading in formerly glaciated areas. In contrast, ICE-3G and ICE-5G are defined in terms of an absolute ice thickness history.

For a model time and grid point where the ice was found to be floating in this first iteration, the point subsequently was set to be part of the ocean function. The ocean function is also defined by any location and model time for which there is no ice in the model and which is located below the computed sea-level. The ocean function is determined similarly for IJ05. For all loading histories, we have taken into consideration the density difference between water and ice when comparing water depth to ice thickness.

The difference between the two ice model types is illustrated schematically in Figure B.2. The original differential IJ05 model measures its load relative to the present-day surface load. Thus, it includes the local ocean load associated with present-day bathymetry when the differential load is converted to an absolute load, whereas ICE-3G and ICE-5G do not (upper panels). Explicit incorporation of regional ocean loading in IJ05 therefore contributes only the addition of GIA-related RSL change, while in ICE-3G/5G both water dumping and RSL change are added (lower panels). This distinction between the two types of load histories is entirely the result of their initial configuration and is not a consequence of the ocean loading calculation itself. Compared to Peltier's (2004), our implementation of the ICE-5G model does not include rotational effects and has a reduced number of intervals in the timing history in order to reduce computation time. Nevertheless, our computed ICE-5G response reproduces the spatial pattern and magnitude of uplift well. The Antarctic portion of the ICE-3G history is simpler and was utilized here without

modification. The ocean load for all load histories is computed according to the methodology presented in section B.2.3.

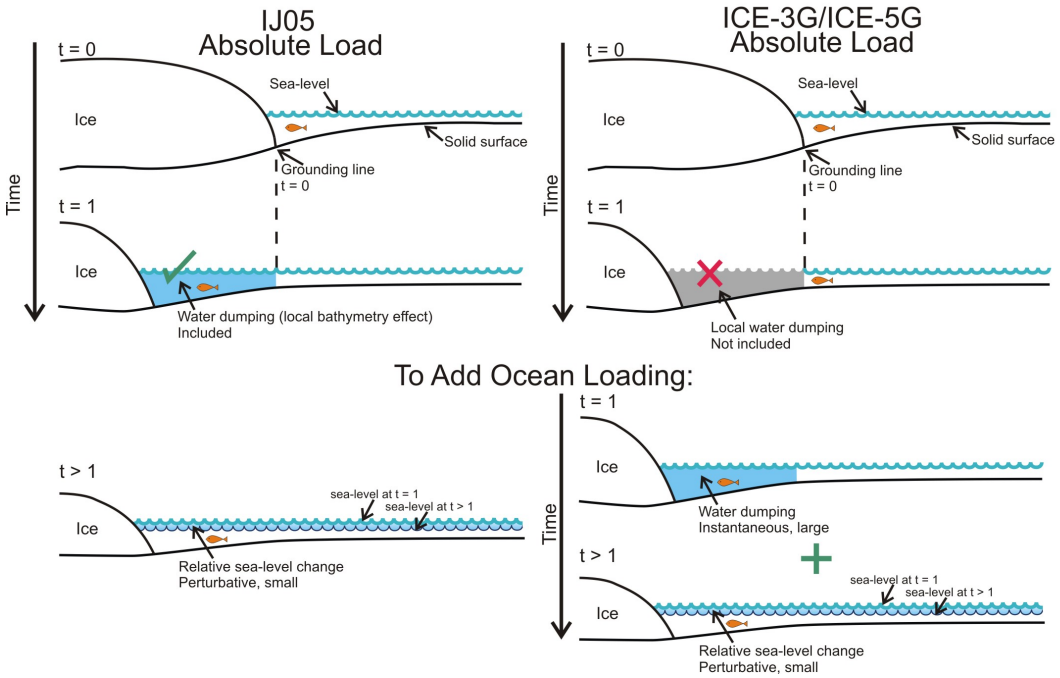

Figure B.2: Conceptual illustration of the configuration for IJ05 and ICE-3G/ICE-5G before and after the explicit incorporation of regional ocean loading in coastal areas. For direct comparison with the ICE-3G/ICE-5G loads, the original IJ05 differential load is shown converted to an absolute load. IJ05 is converted to an absolute load by adding the present-day (density scaled) water depth or ice thickness to the differential load. The generic sequence of events can be considered independent of a specific loading history and is: 1) ablation of grounded marine ice that exists at $t = 0$ leads to water dumping at $t = 1$, and 2) at a later time ($t > 1$), the earth has responded to the removal of ice, perturbing relative sea-level. Figure modified after Mitrovica and Milne (2003).

Earth Model Response

A four-layer Maxwell viscoelastic compressible Earth model with a 90 km thick elastic lithosphere was employed. The upper mantle (90–670 km depth) has a viscosity of 4 $\times$ 10^{20} Pa s. Lower mantle viscosities are 6 $\times$ 10^{21} Pa s (670–1200 km depth) and 8 $\times$ 10^{22} Pa s (1200 km depth to the core-mantle boundary). The model viscosity profile is an average global estimate for mantle viscosity (Mitrovica and Forte 2004) and was employed by Ivins and James (2005, their Figure 6). Earth model responses were computed using methods described by James and Ivins (1998). In terms of dimensionless Love numbers, the response is:

$$\begin{bmatrix} U_l(a,t) \\ V_l(a,t) \\ \Phi_l(a,t) \end{bmatrix} = \frac{ag_0}{M} \begin{bmatrix} h'_l(a,t)/g_0 \\ l'_l(a,t)/g_0 \\ -(k'_l(a,t)+1) \end{bmatrix} \tag{B.2}$$

where U is the vertical displacement, V is the horizontal displacement, Φ is the gravitational potential, l is the degree, a is the radius of the Earth, t is time, g_0 is the unperturbed gravitational acceleration at radius $r = a$, M is the mass of the Earth and h'_l, l'_l, and k'_l are, respectively, the vertical, horizontal and gravitational surface load Love numbers.

The Maxwell viscoelastic rheology features an instantaneous elastic response and a long term delayed response that depends on both the assumed viscosity profile and the elastic structure. In the following, we present both the instantaneous elastic response, the long term response (which we term the viscous response), and the total (summed) response. For the gravitational component of the Earth's response, the elastic component includes the direct mass attraction of the surface load as well as the gravitational effects of the deformed Earth.

Appendix A gives the derivation of an approximate formula that relates the incremental external gravitational acceleration to the thickness of an equivalent surface layer of water. The approximation readily allows conversion of a predicted or observed external gravitational field to the equivalent surface water layer without carrying out an intervening step that involves the summation of Stokes coefficients.

B.2.4 Results

Map Views of Crustal Uplift and Gravity Change

Predicted present-day uplift rates are given in Figure B.3 for IJ05, ICE-3G, and ICE-5G with ocean loading. The predicted spatial patterns differ because of differences in the distribution and thickness of ice in each loading model. Predicted uplift rates for ICE-3G and ICE-5G have a similar spatial distribution, although the reduced load of ICE-5G compared to ICE-3G yields smaller peak rates. The total load size of IJ05 is substantially smaller than both earlier reconstructions of the Antarctic ice sheet. The peak uplift rates for IJ05, observed at the base of the Antarctic Peninsula, are the result of incorporating a large component of recent mass loss from the West Antarctic ice sheet into the loading history. Differential uplift rates were obtained by subtracting ocean-loading predictions from predictions without explicit ocean loading.

For IJ05, the differences in the uplift rates are small and positive, and have a peak value of about 1 mm/yr on the Ross Shelf. A computation of the root-mean-square (RMS) value of the uplift rates for the entire region shown in Figures B.3a and B.3d shows that the differential uplift rates (ocean loading minus no-ocean-loading) are 3% of the uplift rates computed with ocean loading.

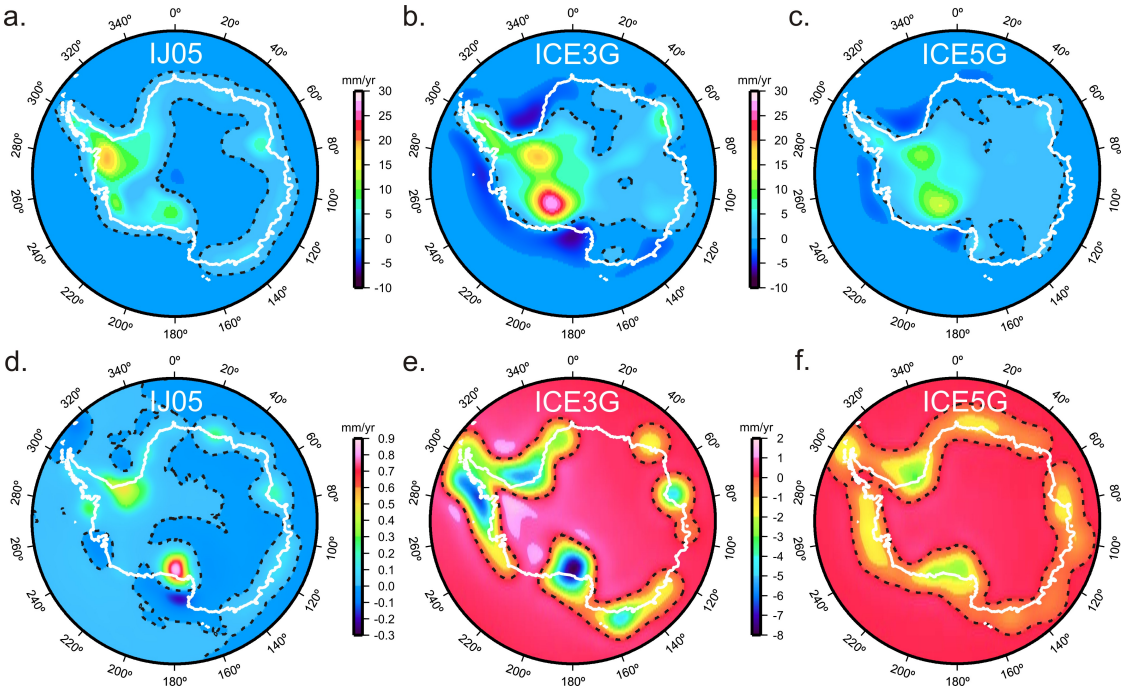

Figure B.3: Predicted present-day crustal uplift rates are shown with regional ocean loading for (a) IJ05, (b) ICE-3G, and (c) ICE-5G. The differential uplift rates obtained by subtracting the 'no ocean loading' case from the 'ocean loading' case are given in panels (d), (e), and (f). A common scale is employed for panels (a), (b) and (c), and a different common scale is used for panels (e) and (f). The black dashed line is the zero contour.

The effect is larger, and of opposite sign, for ICE-3G and ICE-5G. For ICE-3G, ocean loading reduces predicted present-day uplift rates in the Ross and Weddell Seas and the western flank of the Antarctic Peninsula by up to 8 mm/yr, or about a 27% RMS difference over the study area. Some coastal regions in East Antarctica are also affected, but to a lesser degree. Surrounding the ocean-loaded regions of decreased uplift rates is a "halo" or forebulge of slightly increased uplift rates. The largest forebulge values are reached in West Antarctica at the base of the Antarctic Peninsula, where uplift rates are increased by more than 1 mm/yr. The results for ICE-5G are similar to those of ICE-3G, but smaller in magnitude owing to the reduced overall size of ICE-5G's load. The inclusion of ocean loading in ICE-5G

reduces predicted rates of present-day uplift in the Ross and Weddell Seas by up to 3 mm/yr (19% RMS difference).

For both ICE-3G and ICE-5G, ocean loading adds a substantial additional surface load in deglaciated marine areas. The magnitude of unloading is therefore decreased, and the response of the Earth is muted, thus explaining the slower predicted uplift rates when ocean loading is included. In contrast, IJ05 is defined relative to the present-day surface load and thus implicitly incorporates the water dumping effect, even when ocean loading is not explicitly included. For IJ05 with ocean loading, the effect that dominates is perturbative and is due to the gradual reduction in ocean load in regions of uplift. Water flows away from an uplifting region in order to maintain the sea surface as a surface of gravitational equipotential, and the shallower sea in the uplifting region exerts a smaller surface load, which in turn generates more uplift. Consequently, with IJ05, ocean loading generates faster uplift in the Ross Sea. The size of the perturbative effect, however, is small (1 mm/yr, 3% RMS) compared to the -8 mm/yr (-27% RMS) and -3 mm/yr (-19% RMS) (ICE-3G and ICE-5G, respectively) non-perturbative water dumping effect. The ICE-3G/5G models also undergo the perturbative effect, but water dumping dominates.

The predicted present-day rate of gravity change and the corresponding equivalent water height change (EWHC) of surface mass are given in Figure B.4 for IJ05. The time-dependent gravity change predictions, $\dot{g}$, were used to derive the corresponding change in thickness, $\dot{h}$, of an equivalent layer of water using a plane layer approximation ($\dot{g} = 2\pi\rho G\dot{h}$, where ρ is the density of water and G is the universal constant of gravitation; see Appendix A). The predictions in Figures B.4a and B.4b include explicit ocean loading, where the ocean load was first calculated iteratively using the full response of the Earth (i.e., viscous and elastic response). Thus, ocean loading contributes to the present-day elastic loading, although the amplitude and spatial character of the ocean load is dependent upon the Earth's viscous memory. The total surface load was then used to predict separately the viscous and elastic components of the gravity change predictions. The viscous component reflects the long-term response to past surface load changes (Figure B.4a), and gives predictions that may be directly employed to correct satellite gravity observations in order to determine present-day ice mass changes. The elastic component (Figure B.4b) includes the direct effect of present-day mass changes as well as the Earth's instantaneous elastic response to present-day mass changes. These effects are large for IJ05 (Figure B.4b).

For the viscous response, the explicit inclusion of ocean loading gives a small

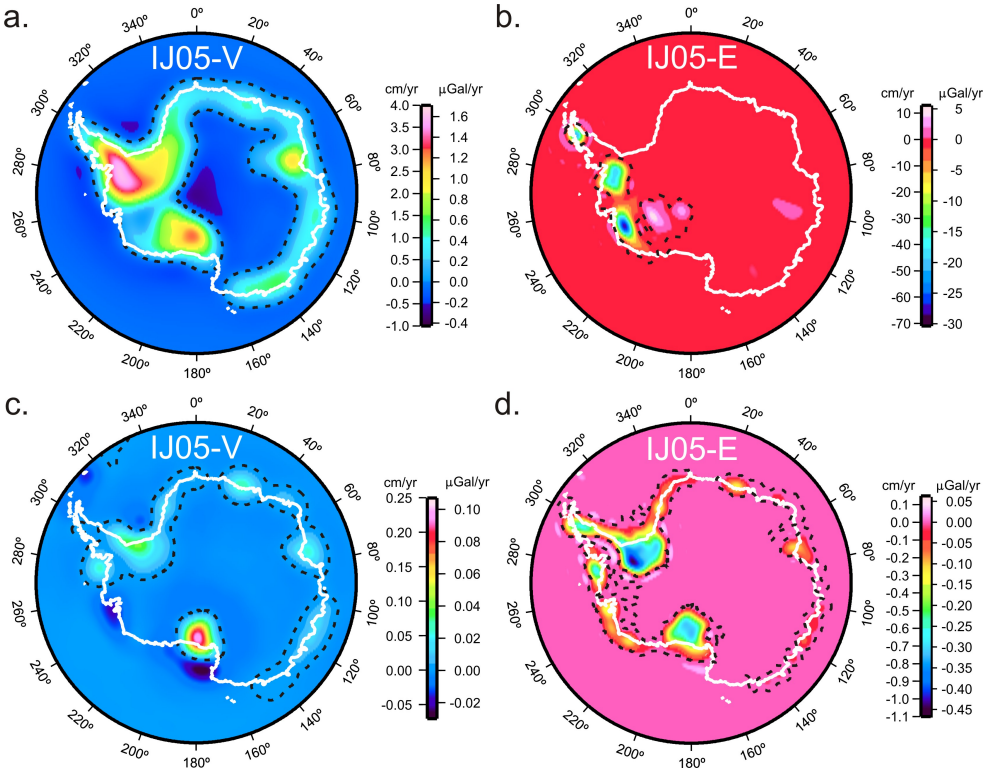

Figure B.4: Predicted present-day rates of gravity change (μGal/yr) and the corresponding EWHC (cm/yr) for the IJ05 load with explicit regional ocean loading for the (a) viscous (V) and (b) elastic (E) response to the load. The black dashed line is the zero contour. The difference between ocean loading and no ocean loading predictions is given in panels (c) and (d) for the viscous and elastic responses. Prior to computing the gravity change and EWHC predictions, the ocean load was calculated to convergence using the full (viscous and elastic) response of the Earth for all predictions including ocean loading; using this ocean load, the viscous and elastic components of gravity change and EWHC were then computed separately.

increase (+0.25 cm/yr EWHC, +0.11 μGal/yr maximum) in gravity rates in the Ross and Weddell Seas (Figure B.4c). The increased viscous rate is a consequence of larger present-day uplift rates driven by a decreasing ocean load. The instantaneous elastic response includes the direct gravitational attraction of the changing load as well as the elastic response of the Earth. The predicted elastic differential rates are larger and of opposite sign (-1.1 cm/yr EWHC, -0.47 μGal/yr maximum, Figure B.4d). The decrease in gravity is due to the decreasing water load in uplifting marine regions. This effect dominates the slight increase in gravity from the elastic response of the Earth. Table B.1 summarizes the maximum predicted differential rates for IJ05, ICE-3G, and ICE-5G.

Table B.1: Maximum Predicted Differential Rates[1]

Load History	Maximum differential uplift rate (mm/yr)	Maximum differential geoid rate (mm/yr)	Maximum differential $\dot{g}$ (μGal/yr) Viscous	Maximum differential EWHC (cm/yr) Viscous	Maximum differential $\dot{g}$ (μGal/yr) Elastic	Maximum differential EWHC (cm/yr) Elastic
ICE-3G	-8.0	-0.5	-0.78	-3.0	+2.28	+5.33
ICE-5G	-3.0	-0.23	-0.43	-1.0	-0.55	-1.28
IJ05	+1.0	-0.14	+0.11	+0.25	-0.47	-1.1

[1]Differential rates are obtained by taking the difference of the 'no ocean loading' and 'ocean loading' predictions.

We tested the sensitivity of our results to the use of the Barbados sea-level curve as an approximation for $c(t)$. Scaling the assumed value of $c(t)$ both up and down by 20% for all times, and carrying out a new ocean loading calculation, results in less than 1% difference in predicted absolute uplift rates for the IJ05 model. For the purposes of computing present-day rates of crustal motion and gravity change, the error associated with the use of this approximation is small.

The selected model viscosity profile remains a significant source of uncertainty in GIA predictions for Antarctica. Viscosity of the upper mantle beneath the Antarctic continent is not well constrained; it is likely, however, that relative to West Antarctica, the upper mantle beneath East Antarctica is more viscous. Approximately doubling the upper mantle viscosity, which is a relatively modest change, gives no appreciable difference in absolute rates for IJ05 and ICE-3G, in agreement with Ivins and James (2005). Larger, and plausible, changes to the viscosity structure would have a more substantial effect.

Zonal Gravity Harmonics

Predictions of the rate of change of the zonal gravitational harmonics (e.g., Lambeck 1980, James and Ivins 1997) are given in Figure B.5 and Table B.2 for spherical harmonic degrees 2 to 8. The predictions reveal the low-degree, or long wavelength, components of the Earth's response to the glacial histories IJ05 and the Antarctic component of ICE-3G. In general, the relative response to the implementation of ocean loading is similar to that described above for the map views of the (spherical

harmonic summed) crustal response and gravitational change. For example, IJ05 predicts smaller zonal harmonics than ICE-3G because its load history features smaller changes to the Antarctic ice sheet. When ocean loading is explicitly introduced, the changes to the predicted zonal harmonics are larger for ICE-3G than for IJ05.

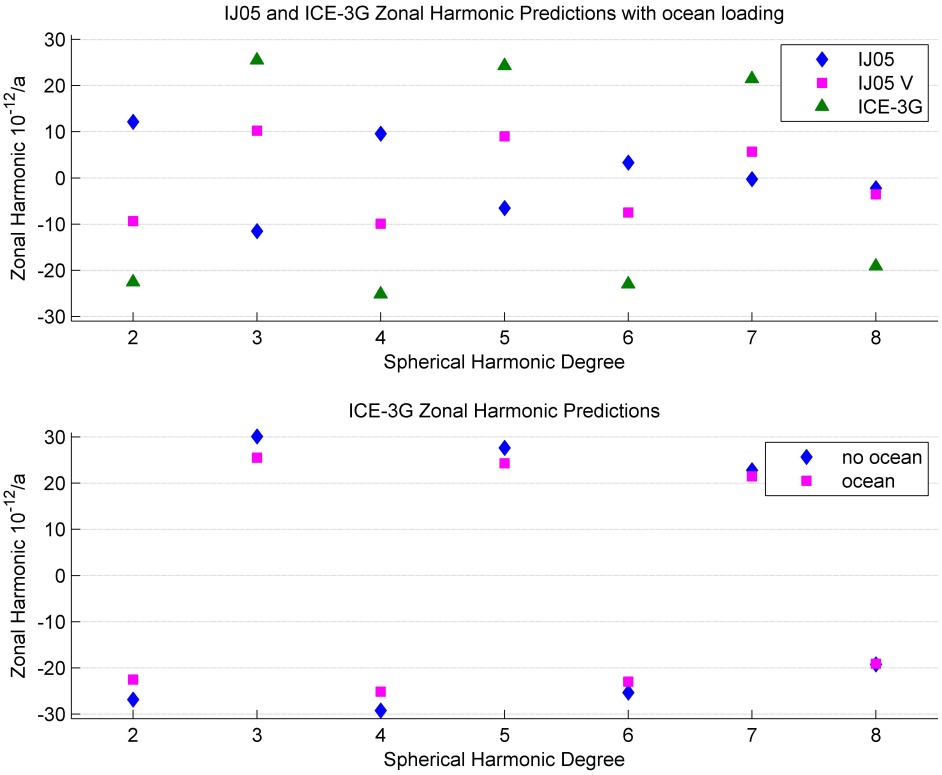

Figure B.5: Predicted rates of change of zonal gravitational harmonics for spherical harmonic degrees 2-8. The top panel shows predictions including ocean loading for the Earth's full response and viscous (V) response to IJ05 (diamonds and squares, respectively), and the full response to the Antarctic component of ICE-3G (triangles). The lower panel contrasts ocean loading versus no ocean loading predictions for ICE-3G (the effect is small for IJ05). Prior to computing the zonal harmonic predictions, the ocean load was calculated to convergence using the full (viscous and elastic) response of the Earth for all predictions in the upper panel. The IJ05-V predictions may be applied as a correction to satellite data. Predictions are specific to the three-layer model viscosity profile: 4×10^{20} Pa s (90-670 km depth), 6×10^{21} Pa s (670-1200 km depth) and 8×10^{22} Pa s (1200 km depth to the core-mantle boundary).

A notable feature of the zonal harmonics is that for degrees two through six the IJ05 predictions change sign at a given degree when the elastic response is included in the calculation, whereas the ICE-3G predictions do not change sign when the elastic

Table B.2: Predictions of the Rate of Change of Zonal Gravitational Harmonics $\dot{J}_l(10^{-12}/a)$

Viscous Response Only	Explicit Ocean Loading	$\dot{J}_2$	$\dot{J}_3$	$\dot{J}_4$	$\dot{J}_5$	$\dot{J}_6$	$\dot{J}_7$	$\dot{J}_8$
IJ05[1]	yes	-9.4	10.2	-9.9	9.0	-7.5	5.7	-3.6
ICE-3G[2]	yes	-21.9	25.0	-24.9	24.3	-23.3	22.0	-19.9
IJ05	no	-9.3	10.2	-9.9	8.9	-7.4	5.6	-3.5
ICE-3G	no	-26.9	30.1	-29.3	27.7	-25.4	22.8	-19.3
Viscous and Elastic Response[3]								
IJ05	yes	12.1	-11.5	9.6	-6.5	3.3	-0.3	-2.2
ICE-3G	yes	-22.5	25.5	-25.1	24.3	-23.0	21.5	-19.1
IJ05	no	10.8	-10.2	8.4	-5.5	2.5	0.3	-2.6
ICE-3G	no	-26.9	30.1	-29.3	27.7	-25.4	22.8	-19.3

[1]IJ05 viscous predictions with ocean loading provide a GIA correction for satellite gravity observations.
[2]As with our other ICE-3G predictions, predicted values are for the Antarctic component only of ICE-3G.
[3]The elastic response includes the gravitational effect of present-day changes to the surface load.

component is incorporated. The sign change is a consequence of the very large present-day ice mass loss that is included in the IJ05 load history. ICE-3G features no such present-day ice mass loss, and the relatively small differences between predictions that only feature the viscous response and predictions with both the viscous and elastic response are due to present-day ocean load mass changes. As mentioned above, for the purposes of "correcting" satellite gravity observations for GIA in order to discern present-day ice mass changes, the IJ05 predictions generated from the purely viscous response should be employed.

B.2.5 Discussion and Conclusions

Compared to ICE-3G and ICE-5G, IJ05 has a markedly different response to the incorporation of explicit regional ocean loading. The difference occurs because IJ05 implicitly contains the present-day ocean load, whereas ICE-3G and ICE-5G do not. Therefore, the changes to the predicted IJ05 rates reflect small perturbative changes to sea-level, while the water dumping effect dominates the changes to the ICE-3G and ICE-5G predictions. The computations with ICE-3G/5G illustrate that significant (up to 19-27%) errors are generated if the ocean load is neglected when computing the Antarctic GIA response. It implies similar errors in the prediction of the Earth's present-day response for other Antarctic GIA and glaciological models that completely neglect ocean loading.

A number of studies have demonstrated the substantial amplitude differences of the responses of GIA models that incorporate ocean loading versus those that do not (Milne 1998, Lambeck et al. 1998, Okuno and Nakada 2001, Mitrovica and Milne 2003). For example, Kendall et al. (2005) document a 20-m difference in predicted relative sea-level at Ottawa Island, Hudson Bay, in the past 4000 years. This difference is equivalent to a reduction in the present-day uplift rate of about 5 mm/yr, approximately midway between the peak reductions of 8 mm/yr and 3 mm/yr documented here for ICE-3G and ICE-5G.

We have compared the widely used ICE-3G model, and its recent successor, ICE-5G, to IJ05 in order to illustrate the effect of ocean loading in absolute and differential load histories. Regardless of whether ocean loading is included, current constraints on the evolution of the Antarctic ice sheet indicate that ICE-3G is not an appropriate candidate for the glacial loading history in Antarctica. Recent geological and glaciological data constraining the growth and deglaciation of the Antarctic ice sheet have converged to suggest that ICE-3G and other earlier reconstructions overestimate the total ice sheet volume and the contribution to global sea-level rise since LGM by at least 60% (Ivins and James 2005, Price et al. 2007, Ackert et al. 2007). ICE-5G is intermediate in total size to the ICE-3G and IJ05 models; its contribution to global sea-level rise since LGM is still larger than IJ05 by approximately 40%. Surface exposure dates constraining past ice sheet elevations in West Antarctica indicate that the maximum reduction of proximal ice thicknesses there has been less than 100 m since LGM (Ackert et al. 1999). Ice volume estimates suggest the total contribution to global sea-level since LGM from the Ross Sea region likely does not exceed 3–6

m (Licht 2004). Sedimentological and chronological data constraining the grounding line position of the ice sheet indicate a prolonged retreat phase in both the Ross and Weddell Seas (e.g., Conway et al. 1999, Licht 2004). The IJ05 model was specifically designed to incorporate many of the current constraints (Ivins and James 2005).

IJ05 has the added value of accounting for most of the regional ocean loading effect. Indeed, maximum predicted differential (ocean loading minus no-ocean-loading) uplift rates, centred in the Ross Sea region, are only +1 mm/yr for IJ05. This value is comparable with the average uncertainty of approximately ±0.9 mm/yr for measured uplift rates in the TAM and West Antarctica (Capra et al. 2007, Willis 2008). The maximum predicted differential EWHC values for IJ05 are also small: +0.25 cm/yr and -1.1 cm/yr, for the viscous and elastic gravity response, respectively (Figure B.4c, d). GRACE measures variations in the gravity field at an accuracy of ∼1.5 cm of equivalent water thickness, and observed long-term mass change rates for Antarctica do not exceed ±3–4 cm/yr (e.g., Chen et al. 2006). The predicted correction to long-term gravity rates therefore is less than the uncertainty associated with observations.

Unless ocean loading is explicitly included, predictions of Antarctic crustal motion and time-dependent gravity that employ ICE-3G (e.g., Barletta et al. 2008), ICE-5G, or similarly derived regional reconstructions, neglect an important component. In contrast, studies that have estimated mass balance from GRACE using GIA corrections predicted by IJ05 (Chen et al. 2006, Ramillien et al. 2006) will not be affected significantly by the implicit ocean loading approximation.

Use of IJ05 without ocean loading provides a reasonable first estimate of Antarctica's present-day GIA response, insofar as the correction for ocean loading is generally less than or equal to the typical measurement accuracy of observations. Nevertheless, implementation of ocean loading in IJ05, which requires the initial conversion of the differential load to an absolute load through addition of present-day bathymetry values, ultimately yields a more accurate prediction. The inclusion of regional ocean loading in the next generation of Antarctic GIA models, including future descendants of IJ05, will therefore provide the best possible GIA correction for analysis of GRACE observations to determine present-day Antarctic mass balance and for interpretation of the growing body of GPS crustal motion observations.

B.2.6 Appendix B′ (Journal of Geodesy Article Appendix)

Here we derive an approximate formula that relates an arbitrary external incremental gravitational field **g** to the thickness h of an equivalent surface water layer. We note that our approach is different from that of de Linage et al. (2007), who considered the spectral properties of gravity change on the deformed surface of the Earth. Although we include the Earth's gravitational response to the equivalent surface water load, our focus is on the external gravitational field, evaluated at the undeformed surface of the Earth ($r = a$).

The gravitational potential Φ is commonly expressed in terms of Stokes coefficients C_{lm} and S_{lm} (e.g., Chao and Gross 1987):

$$\Phi(\mathbf{r}) = \frac{GM}{a}\sum_{l=0}^{\infty}\sum_{m=0}^{l}\left(\frac{a}{r}\right)^{l+1}\tilde{P}_{lm}(\cos\theta) \times(C_{lm}\cos m\phi + S_{lm}\sin m\phi) \qquad \text{(B′.1)}$$

where **r** is the position outside the Earth, G is the universal constant of gravitation, M is the mass of the Earth, a is the radius of the Earth, and the $\tilde{P}_{lm}$ are normalized associated Legendre functions of degree l and order m. In spherical coordinates, the position **r** is defined in terms of the radial distance r from the centre of the Earth, co-latitude θ, and longitude ϕ. The radial acceleration due to gravity **g** is given by the gradient of the potential:

$$\mathbf{g} = \nabla\Phi(\mathbf{r}) = -g\hat{\mathbf{r}} = -\frac{GM}{a^2}\hat{\mathbf{r}}\sum_{l=0}^{\infty}\sum_{m=0}^{l}(l+1)\left(\frac{a}{r}\right)^{l+2} \times\tilde{P}_{lm}(\cos\theta)(C_{lm}\cos m\phi + S_{lm}\sin m\phi) \qquad \text{(B′.2)}$$

with unit radial component $\hat{\mathbf{r}}$. The origin of the reference frame is taken to be the centre of mass of the Earth, and in this case the $l = 1$ Stokes coefficients vanish. Equations (B′.1) and (B′.2) are general and provide a description of the static (background) and the time-varying gravitational field.

Let us now consider the incremental, time-varying portion of the Earth's gravitational field by adding dependence on time, t, to Φ in equation (B′.2). The time-varying component of the Earth's gravitational field may be expressed in terms of changes to

the thickness of an equivalent layer of water at the Earth's surface. This provides a way to readily relate satellite gravity observations to hydrological changes, although it obscures the contribution that other processes, such as GIA, provide to the observed field. Consider a surface mass density $\sigma(\theta,\phi,t) = \rho_w h(\theta,\phi,t)$ at $r = a$ expanded in Legendre functions

$$\begin{aligned}\sigma(\theta,\phi,t) &= \rho_w a \sum_{l=0}^{\infty}\sum_{m=0}^{l} \tilde{P}_{lm}(\cos\theta) \\ &\times (H^C_{lm}(t)\cos m\phi + H^S_{lm}(t)\sin m\phi) \\ &= \rho_w a \sum_{l=0}^{\infty} \bar{h}_l(\theta,\phi,t), \text{ and} \\ h(\theta,\phi,t) &= a\sum_{l=0}^{\infty}\bar{h}_l(\theta,\phi,t) \end{aligned} \tag{B′.3}$$

where ρ_w is the density of water and $\bar{h}_l$ is the normalized degree-l component of the water thickness h. The gravitational potential due to the surface mass density satisfies Laplace's equation inside (Φ^i) and outside (Φ^o) the Earth

$$\nabla^2\Phi^i = \nabla^2\Phi^o = 0. \tag{B′.4}$$

At $r = a$, we have

$$\Phi^o = \Phi^i \tag{B′.5}$$

$$g^o - g^i = 4\pi G\sigma \tag{B′.6}$$

where g^o and g^i give the magnitude of the gravitational acceleration inside and outside the Earth. Outside the Earth ($r > a$) the solution takes the form given by equations (B′.1) and (B′.2). Inside the Earth ($r < a$), the solution has the form

$$\begin{aligned}\Phi^i(\mathbf{r},t) &= \frac{GM}{a}\sum_{l=2}^{\infty}\sum_{m=0}^{l}\left(\frac{r}{a}\right)^l \tilde{P}_{lm}(\cos\theta) \\ &\times (C^i_{lm}(t)\cos m\phi + S^i_{lm}(t)\sin m\phi)\end{aligned} \tag{B′.7}$$

$$\mathbf{g}^i(\mathbf{r},t) = \frac{GM}{a^2}\hat{\mathbf{r}}\sum_{l=2}^{\infty}\sum_{m=0}^{l} l\left(\frac{r}{a}\right)^{l-1}\tilde{P}_{lm}(\cos\theta)$$
$$\times(C^i_{lm}(t)\cos m\phi + S^i_{lm}(t)\sin m\phi) \qquad \text{(B}'.8)$$

Applying the boundary conditions, we obtain, for outside the Earth

$$(C^o_{lm}, S^o_{lm}) = \frac{3\rho_w}{(2l+1)\rho_{ave}}(H^C_{lm}, H^S_{lm}) \qquad \text{(B}'.9)$$

This gives the Stokes coefficients in terms of the spherical harmonic coefficients of the water layer. The Earth yields elastically to the imposed surface load, and the gravitational response is modified by an additional factor of $1 + k'_l$. The quantity k'_l is the surface loading Love number for the gravitational potential, and it varies from -0.303 at degree 2 to -0.051 (degree 20) to -0.014 (degree 100) (e.g., Wahr et al. 1998, Table B′.1). We have

$$(C^o_{lm}, S^o_{lm}) = \frac{3\rho_w(1+k'_l)}{(2l+1)\rho_{ave}}(H^C_{lm}, H^S_{lm}) \qquad \text{(B}'.10)$$

This result is the same as that of Wahr et al. (1998, their equation 12). The complete expression for the acceleration due to gravity of a water layer on the surface of the elastically-yielding Earth is thus

$$\mathbf{g}^o = \nabla\Phi^o(\mathbf{r}) = -g^o\hat{\mathbf{r}}$$

$$= -\frac{GM}{a^2}\hat{\mathbf{r}}\sum_{l=0}^{\infty}(1+k'_l)\sum_{m=0}^{l}\frac{3\rho_w(l+1)}{\rho_{ave}(2l+1)}\left(\frac{a}{r}\right)^{l+2}$$
$$\times\tilde{P}_{lm}(\cos\theta)(H^C_{lm}\cos m\phi + H^S_{lm}\sin m\phi) \qquad \text{(B}'.11)$$

$$= -4\pi G\rho_w a\hat{\mathbf{r}}\sum_{l=0}^{\infty}\left[(1+k'_l)\frac{l+1}{2l+1}\right]\sum_{m=0}^{l}\left(\frac{a}{r}\right)^{l+2}$$
$$\times\tilde{P}_{lm}(\cos\theta)(H^C_{lm}\cos m\phi + H^S_{lm}\sin m\phi) \qquad \text{(B}'.12)$$

where ρ_{ave} is the average density of the Earth and $M = 4/3\pi\rho_{ave}a^3$. At the surface

of the Earth, above the surface load ($r = a^+$), and defining F_l to be

$$F_l = \left[(1 + k'_l)\frac{l+1}{2l+1}\right], \tag{B′.13}$$

we can write

$$\mathbf{g}^o(a^+, \theta, \phi, t) = -4\pi G\rho_w a\hat{\mathbf{r}} \sum_{l=0}^{\infty} F_l \bar{h}_l(\theta, \phi, t). \tag{B′.14}$$

Further simplifying the notation by writing $\mathbf{g}^o = \hat{\mathbf{r}} \sum_{l=0}^{\infty} g_l$, we have, for each degree l

$$g_l(\theta, \phi, t) \equiv -4\pi G\rho_w a F_l \bar{h}_l(\theta, \phi, t) \tag{B′.15}$$

Substituting for $\bar{h}_l$ from (B′.15) into (B′.3),

$$\sigma(\theta, \phi, t) = \rho_w a \sum_{l=0}^{\infty} \bar{h}_l(\theta, \phi, t) = -\sum_{l=0}^{\infty} \frac{g_l(\theta, \phi, t)}{4\pi G F_l}, \text{ or}$$

$$h(\theta, \phi, t) = -\sum_{l=0}^{\infty} \frac{g_l(\theta, \phi, t)}{4\pi G\rho_w F_l} \tag{B′.16}$$

for density and water thickness, respectively. For large degree, the gravitational Love number k'_l approaches zero as a limiting value (e.g., Farrell 1972), and the scale factor F_l asymptotically approaches the value 1/2. Even at low degrees, F_l only deviates from the asymptotic value of 0.5 by about 20% at degree 2 and by less than 3% at degrees 15 and 20 (Table B′.1). This suggests setting F_l equal to 1/2. From (B′.14), this gives the following approximation

$$\mathbf{g}^o \cong -2\pi G\rho_w h\hat{\mathbf{r}} = -2\pi G\sigma(\theta, \phi)\hat{\mathbf{r}} \tag{B′.17}$$

This formula has the same form as the Bouguer attraction of an infinite sheet having surface mass density σ, but it should be kept in mind that the formula (B′.17) includes the elastic response of the Earth to the surface mass load and it is applicable to a surface mass density that varies from location to location on a spherical Earth. Thus, a computed or observed external gravitational field $\mathbf{g}$ reduced to the Earth's surface can be readily expressed in terms of the thickness of a water layer h in the following

manner

$$h = \frac{g^o}{2\pi G\rho_w}; \dot{h} = \frac{\dot{g^o}}{2\pi G\rho_w} \tag{B′.18}$$

The dots indicate time rate of change. Numerically, if the EWHC $\dot{h}$ is in cm/yr and the rate of change of gravitational acceleration $\dot{g}$ is in μGal/yr, then $\dot{h} = 2.386\dot{g}$ (taking the density of water $\rho_w = 1000$ kg/m^3). Equation (B′.18) is an approximation to the exact expression (B′.16).

Table B′.1: Deviation of Scale Factor F_l from its Asymptotic Value of 0.5

Spherical Harmonic Degree l	Gravitational Love Number k'_l	$F_l = (1 + k'_l)\frac{l+1}{2l+1}$	Percentage Deviation $(0.5-F_l)/F_l\times$ 100%
2	-0.306	0.416	20.2
3	-0.197	0.459	8.9
4	-0.134	0.481	4.0
5	-0.105	0.488	2.5
10	-0.069	0.487	2.6
15	-0.058	0.486	2.9
20	-0.051	0.486	2.9
30	-0.041	0.487	2.6
50	-0.028	0.491	1.9
100	-0.015	0.495	1.0
200	-0.008	0.497	0.5
∞	0.0	0.5	0.0

The difference between the exact (B′.16) and approximate (B′.18) relations for converting gravitational change to equivalent water thickness change for the case of the viscous response of IJ05 with ocean loading is shown in Figure B′.1. For comparison, the EWHC, computed using the approximate relation, is shown in Figure B.4a. From Figure B′.1, the peak difference is about 0.1 cm/yr. It occurs where the largest EWHC of 4 cm/yr is attained. This gives a percentage difference of 2.5%, which is consistent with Table B′.1 showing that the percentage deviation is less than 3% for spherical harmonic degrees above $l = 4$. Similarly, the root-mean-square (RMS) of the water-thickness values predicted using the exact relation (B′.16) is 0.79 cm/yr and the RMS difference is 0.025 cm/yr, giving a percentage difference of 3.1%. With a good degree of accuracy, equation (B′.18) provides a way to convert readily

from gravity change to surface mass change without the necessity of converting Stokes coefficients to surface thickness coefficients and performing a summation.

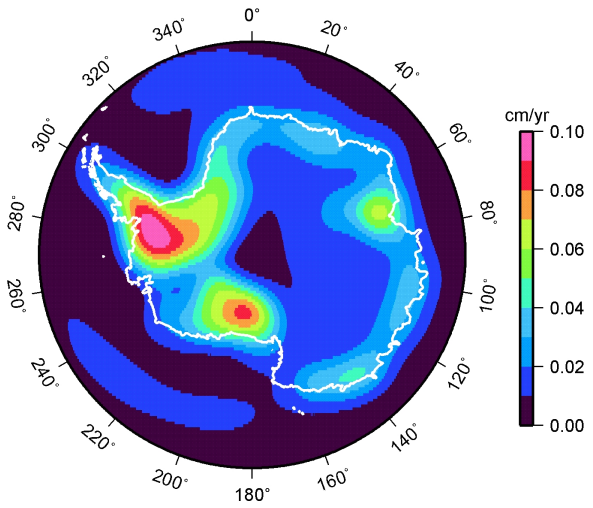

Figure B′.1: The difference between the exact (formula B′.16) and approximate (formula B′.18) relations for converting gravitational change to EWHC, in centimetres of water equivalent per year, for the viscous response of IJ05 with ocean loading. Compare to Figure B.4a, which shows the EWHC computed using the approximate formula.

B.2.7 Acknowledgements

We thank the anonymous reviewers for their detailed comments which helped to substantially improve the manuscript. Karen Simon was supported by the Geomatics for Informed Decision Making Network of Centres of Excellence (GEOIDE NCE) and by ArcticNet. The work of Erik Ivins was preformed at the Jet Propulsion Laboratory, Caltech, and funded by the Solid Earth and Surface Processes Focus Area within NASA's Earth Science Program. This is a product of the Climate Change Geoscience Program of Natural Resources Canada. This is Geological Survey of Canada Contribution Number 20090174.

Appendix C

Supplementary Material for Chapter 5

This appendix provides the supplementary information to the Quaternary Research article in Chapter 5.

This appendix of supplementary information provides detailed descriptions of the other 15 sites that do not provide strong constraints on the position of sea level. All sample ages and site locations are shown in Table 5.1 and Figure 5.2 of the main text.

Site 1, southwest of Arviat I

Excavation of a 35 cm deep hole approximately 90 km southwest of Arviat at an elevation of 158.8 m exposed layers of brown well humified peat to 19 cm depth, underlain by 16 cm of grey-brown, coarse, well sorted sand. A basal peat sample from 17 to 19 cm was obtained (sample 10-50a), as well as an overlying sample from 15 to 16 cm depth (10-50b). *Carex* (sedge) achenes were extracted from both samples, and 10-50a and 10-50b yielded ages of 2855 ± 20 ^{14}C yr BP (2884-3063 cal yr BP) and 1890 ± 25 ^{14}C yr BP (1737-1891 cal yr BP), respectively.

Site 2, southwest of Arviat II

At 149.5 m elevation, site 2 is within 1 km of site 1, and is located at the base of a well defined beach ridge. Excavation of a 45 cm deep pit revealed alternating layers of light and dark brown peat to 35 cm depth underlain by dark brown, organic-rich, coarse sand. A light brown basal peat sample was obtained from 32 to 35 cm (10-51a), as well as an overlying dark brown peat sample from 21 to 23 cm (10-51b). A mixture of *Empetrum nigrum* seeds and *Carex* achenes was extracted from 10-51a, and moss fragments were extracted from 10-51b. Sample 10-51a yielded an age of 1430 ± 45 ^{14}C yr BP (1285-1401 cal yr BP), and sample 10-51b yielded an age of 1360 ± 15 ^{14}C

yr BP (1278-1302 cal yr BP).

Site 5, north of Carr Lake

Site 5 is located at 104.5 m elevation, just north of Carr Lake. Excavation of a 22 cm pit exposed dark brown fibrous peat to 16-17 cm depth, in sharp contact with underlying brown medium-grained sand. *Empetrum nigrum* leaves and charred seeds extracted from a basal peat sample from 16 to 17 cm depth (10-48a) yielded an age of 1950 ± 20 ^{14}C yr BP (1830-1948 cal yr BP). An additional surficial sample was identified as marine algae. The algae appeared partially decomposed, and was matted within grass near the margin of a muddy surface depression. This sample (10-48c) yielded a radiocarbon age of -425 ± 20 ^{14}C yr BP, indicating that the sample is modern and post-dates mid-20th century thermonuclear bomb testing. The origin of the sample is unknown, but it is possible the sample is marine algae that was blown inland by strong winds.

Site 6, north of Maguse Lake

A 50 cm deep pit was excavated north of Maguse Lake at an elevation of 100 m. The pit exposed a layer of brown-black well humified peat intercalated with brown-grey medium-grained sand to a depth of 42 cm, which was underlain by orange-brown medium to coarse sand. A basal organic sample was collected from between 40.5 and 42.0 cm depth (10-46a). Beetle parts, including a worn *Carabidae* fossil head fragment and smaller parts of the ground beetle *Dyschiriodes* sp. were extracted from the sample, and yielded a radiocarbon age of 4155 ± 20 ^{14}C yr BP (4585-4824 cal yr BP). This sample represents the oldest terrestrial sample obtained from higher elevations as a part of this study.

Site 7, southwest of Arviat III

Site 7 is located approximately 85 km southwest of Arviat at an elevation of 81.5 m. Excavation of a 38 cm deep hole exposed layers of peat to 22 cm depth, grading to light brown medium to coarse sand beneath. A basal sample was obtained from 19 to 22 cm depth (10-52). Beetle parts of the genus *Notiophilus* were extracted from the sample, and yielded an age of 1855 ± 20 ^{14}C yr BP (1721-1865 cal yr BP).

Site 10, west of Arviat I

A 35 cm deep pit was excavated at a location approximately 40 km west of Arviat, at

an elevation of 59.6 m. The pit exposed a layer of dark brown to black peat to 20 cm depth, in sharp contact with underlying medium-grained brown sand. A basal peat sample was collected from 18 to 20 cm depth (10-44). Parts of a predaceous diving beetle of the genus *Agabus* were extracted from the sample, and gave an age of 1380 ± 20 ^{14}C yr BP (1279-1331 cal yr BP).

Site 11, south of Carr Lake

A mixture of *Clinocardium ciliatum* and *Macoma* sp. shells were collected south of Carr Lake at an elevation of 59 m (GSC-1626, Lowdon and Blake 1979). The shells yielded an age of 5780 ± 180 ^{14}C yr BP (6247-7086 cal yr BP).

Site 12, active mudboils

Site 12 is located within 2 km of site 10, at 53 m elevation. The site location featured several elliptical mudboils approximately 1 m × 1.6 m across. Several shell fragments were found in one of the active mudboils within a matrix of grey pebbly mud. *Hiatella arctica* shell fragments were collected from the mudboil from the surface to 25 cm depth (10-42b). These shell fragments yielded an age of 5985 ± 15 ^{14}C yr BP (6735-6976 cal yr BP). This site was made known to us by one of the residents of Arviat.

Site 13, Kaminak Lake II

Detrital organic matter was retrieved from a sediment core collected from Kaminak Lake at 51 m elevation (GSC-2688, Blake 1983). Radiocarbon dating of the organic material gave an age of 2370 ± 120 ^{14}C yr BP (2147-2742 cal yr BP).

Site 14, west of Arviat II

Site 14 is approximately 200 m from the active mudboils at site 12, and is at 50.8 m elevation. Excavation of a 52 cm deep hole exposed layers of peat to 43 cm in gradational contact with underlying organic-rich sandy mud. Fossil fragments of the ground beetle *Pterostichus (Cryobius) ventricosus* were extracted from a basal sample from 41 to 43 cm depth (10-43a), and yielded an age of 360 ± 15 ^{14}C yr BP (320-492 cal yr BP).

Site 15, Maguse Road

This site is located alongside Maguse Road, approximately 36 km northwest of Arviat

at an elevation of 44.7 m. A 40 cm deep pit was dug, exposing a layer of thick fibrous peat in sharp contact with underlying grey muddy sand at 35 cm depth. The grey muddy sand was in turn in sharp contact with brown, pebbly, medium sand. A basal peat sample was obtained from 32 to 35 cm depth (10-53a). A mixture of *Carex* achenes, *Empetrum nigrum* seeds, and *Andromeda polifolia* (bog rosemary) seeds was extracted from this sample, and yielded an age of 2540 ± 40 ^{14}C yr BP (2488-2750 cal yr BP).

Site 22, Arviat gully I

This site is a gully that drained the former town reservoir in 1970, and is located on the outskirts of Arviat. Whole valves of *Hiatella arctica* were collected at the top of the gully at 8.9 m elevation (09-07a). These shells gave an age of 4420 ± 15 ^{14}C yr BP (4965-5263 cal yr BP).

Site 23, Maguse Road gravel pit III

Shell fragments were collected on the floor of a gravel pit at 6.5 m elevation. Radiocarbon dating one of these shell fragments (10-71) yielded an age of 4480 ± 15 ^{14}C yr BP (5039-5300 cal yr BP).

Site 24, Maguse Road gravel pit IV

Articulated valves of *Mya truncata* were collected in growth position (09-18a) from a gravel pit with abundant shells at 4.3 m elevation. The shells yielded an age of 3475 ± 15 ^{14}C yr BP (3700-3965 cal yr BP).

Site 25, Arviat gully II

Site 25 lies just south of site 22, and is located in the same gully that catastrophically drained the town reservoir in 1970 (W.W. Shilts in Lowdon and Blake 1979). The sample (GSC-1427) is a *Mya truncata* shell with an age of 3000 ± 220 ^{14}C yr BP (2737-3808 cal yr BP) that was collected approximately 2 m above the high tide line, two days after the reservoir drained.